Direct Numerical Simulation of the Flow over a Golf Ball

by

Clinton E. Smith

A Dissertation Presented in Partial Fulfillment
of the Requirements for the Degree
Doctor of Philosophy

Approved November 4, 2011 by the
Graduate Supervisory Committee:

Kyle D. Squires, Chair
E. Balaras
M. Herrmann
R. Adrian
D. Stanzione
R. Calhoun

ARIZONA STATE UNIVERSITY

December 2011

ABSTRACT

The flow around a golf ball is studied using direct numerical simulation (DNS). An immersed boundary approach is adopted in which the incompressible Navier-Stokes equations are solved using a fractional step method on a structured, staggered grid in cylindrical coordinates. The boundary conditions on the surface are imposed using momentum forcing in the vicinity of the boundary. The flow solver is parallelized using a domain decomposition strategy and message passing interface (MPI), and exhibits linear scaling on as many as 500 processors. A laminar flow case is presented to verify the formal accuracy of the method. The immersed boundary approach is validated by comparison with computations of the flow over a smooth sphere. Simulations are performed at Reynolds numbers of 2.5×10^4 and 1.1×10^5 based on the diameter of the ball and the freestream speed and using grids comprised of more than 1.14×10^9 points. Flow visualizations reveal the location of separation, as well as the delay of complete detachment. Predictions of the aerodynamic forces at both Reynolds numbers are in reasonable agreement with measurements. Energy spectra of the velocity quantify the dominant frequencies of the flow near separation and in the wake. Time-averaged statistics reveal characteristic physical patterns in the flow as well as local trends within dimples. A mechanism of drag reduction due to the dimples is confirmed, and metrics for dimple optimization are proposed.

ACKNOWLEDGEMENTS

At the completion of any effort, it can sometimes be difficult to identify each person who has contributed, either directly or indirectly to the quality and content of my doctoral dissertation. I will attempt to detail my gratitude herein, and apologize for any omissions.

First and foremost, I want to thank my thesis advisor and friend, Professor Kyle Squires. As a seasoned computationalist and fluids physicist, he demonstrated great vision in this work by recognizing an area of fluid mechanics where an application of Direct Numerical Simulation would have a significant impact. Many conversations with Professor Squires throughout this effort provided guidance not only for running the simulations, but also for correct interpretation of the results.

I am indebted to Professor Elias Balaras, who not only provided assistance for understanding and running parallel research codes on supercomputers, but also for his technical expertise and guidance with regard to immersed boundary methods and fluid mechanics. Conversations with Professor Marcus Herrmann at various instances throughout the research have been very helpful, in particular with regard to numerical methods and verification and validation. I also want to thank Dr. Daniel Stanzione, who provided me with opportunities to explore methods for parallelizing numerical algorithms. Correspondence and conversation with Dr. Phillipe Spalart have provided clarity with regard to modeling approaches and results.

I have benefited greatly from working with past and present members of Professor Squires' research group. In particular, I acknowledge Dr. Nikolaos Beratlis, whose assistance with immersed boundary methods and resistless logic proved invaluable throughout this project.

During my time at Arizona State University, I have benefited greatly from knowing a very unique group of people, both within and outside of the department. For the friendships, assistance, and unforgettable experiences I want to thank Dr. Lynn

Cozort, Mr. Jeevan Rajaram, Dr. Kringan Saha, Dr. Vivek Krishnan, Dr. Heath Lorzel, Dr. Philip Wheat, Mr. Ben Watson, Mr. Sachin Badarayani, Dr. Gil Speyer, and Dr. Stephen Wheat, to name a few.

Finally, at the conclusion of writing this PhD thesis, I realize how much I owe to my family. They have been a constant source of support during this effort. I am extraordinarily grateful to my parents, Jim and Diana Smith, for their wise counsel, encouragement toward academic achievement, and for teaching me how to work. My wife, Erin, has provided me with unwavering support, encouragement, and love from the beginning of my doctoral studies, and has devoted herself to the care of our children while I have completed this task. I can never repay her or our children, Jackson and Claire Marie, for all that they have given me. As a token of payment and my love, I dedicate this thesis to them.

Soli Deo gloria.

To: Erin, Jackson, and Claire Marie

TABLE OF CONTENTS

LIST OF FIGURES

Figure Page

Figure Page

LIST OF TABLES

Table Page

Chapter 1

Introduction

1.1 Literature Survey

External flows over bluff bodies are frequently encountered in a diverse spectrum of applications, spanning from space launch vehicles to skyscrapers to sports equipment. Many flow phenomena are present, including boundary layer development, separation, wake formation, and vortex shedding. When investigated over a range of Reynolds numbers, the drag on the body drops dramatically, producing what is widely known as the "drag crisis". This reduction in the drag on a bluff body occurs in different physical regimes for different geometries, and much work has been devoted to an understanding of the flow in these physical regimes. Efforts have been placed into an understanding of the mechanisms that produce a reduction in drag, with the expectation that methods of flow control will be produced from such study. Passive flow control is one such method, and is often achieved by modifying the surface of the bluff body by adding roughness. Surface roughness is used effectively to modify the flight characteristics of a sphere by reducing the drag. It was implemented in golf ball design after early golfers observed better flight performance from scratched, nicked, and dented rubber balls. This discovery has led to the dimpling techniques used for modern golf balls, but questions remain regarding how the dimples produce the dramatic drag reduction we now observe. The current work presents a numerical examination of the flow within and around dimples on a golf ball in the supercritical regime, and is intended to build upon existing literature which have suggested a mechanism of drag reduction due to the dimples. In particular, the contribution of this work is to illuminate physics of the flow that are related to geometric details of the dimples, and to quantify how the geometric features of the dimples affect the flow over the golf ball.

Understanding of the flow over bluff bodies has been advanced by investigation of simple objects, with the purpose of extending the acquired knowledge to realistic ones. A widely-studied geometry is the circular cylinder, as its two-dimensionality allows straightforward configuration for measurements and calculations, and has geometrical characteristics that are similar to realistic bluff body flows. The flow over a circular cylinder has been investigated by many workers over a range of Reynolds numbers. A comprehensive survey of contributions in the study of circular cylinder flows was produced by Williamson [109]. Some representative contributions are cited herein: Hiemenz [44] was one of the first measurement-based studies of the flow over a circular cylinder. Roshko [79] measured the flow over a circular cylinder and quantified the recovery of the drag coefficient when the Reynolds number increases from order of $Re = 1 \times 10^6$ to $Re = 1 \times 10^7$. Achenbach [1] measured the flow over a circular cylinder up to $Re = 5 \times 10^6$ and measured local pressure and skin friction distributions therein. Gerrard [38] quantified the modes and frequencies associated with vortex formation in the wake of a cylindrical bluff bodies up to $Re = 2 \times 10^3$. Unal & Rockwell [102] used measurements to quantify the shear layer instabilities, vortex shedding, and wake dynamics around a circular cylinder from $Re = 440$ to $Re = 5040$. Lin *et al.* [56] examined instanteous structures in the near-wake from $Re = 1 \times 10^3$ to $Re = 1 \times 10^4$. Norberg [65] measured the lift coefficients on circular cylinders by integrating the RMS pressure on the cylinder in the subcritical regime ($Re = 47$ to $Re = 2 \times 10^5$). Computations of the flow over a cylinder have also been conducted by many workers, one of the first of whom was Thoman [100]. Karniadakis & Triantafyllou [50] applied direct simulation to cylinder flows in the wake-transitional range ($Re = 200$ to $Re = 400$) in order illuminate the physical mechanisms of this transition. Henderson [43] calculated the flow in the subcritical range ($Re = 1000$) using a two-dimensional spectral method. Mittal & Balachandar [59] used Fourier spectral methods to compute

the flow over three-dimensional cylinders, and quantified the source of discrepancies between two-dimensional and three-dimensional simulations of a cylinder. Travin *et al.* [101] computed the flow over a cylinder using DES for $Re = 5 \times 10^4$, $Re = 1.4 \times 10^5$ and $Re = 3 \times 10^6$. Most recently, Squires *et al.* [95] calculated the supercritical flow over a circular cylinder at $Re = 8 \times 10^6$ in order to compare variations in turbulence models.

Knowledge of the flow over three-dimensional objects has been advanced by studying the sphere. Studies of the flow over a stationary sphere have contributed to the understanding of drag reduction by turbulent separation. Maxworthy [57] measured the flow characteristics of a stationary sphere for $Re = 2 \times 10^3$ to $Re = 6 \times 10^4$ and investigated the effects of placing a trip wire on the sphere upstream of the location at which natural transition occurs. Roos & Willmarth [78] measured the flow field from $Re = 5$ to $Re = 1 \times 10^5$) to obtain detailed drag coefficient results. Achenbach [3] and Schlichting [81] measured aerodynamic forces, pressure, and skin friction in the subcritical and supercritical regimes ($Re = 5 \times 10^4$ to $Re = 6 \times 10^6$). The calculations of Johnson & Patel [48] of the flow over a sphere in the subcritical regime ($Re = 300$) compared very well with previous measurements. Computations of the flow over a sphere have been conducted by Constantinescu & Squires [26], Constantinescu & Squires [28] and Constantinescu & Squires [29], in which large eddy simulation (LES) and detached eddy simulation (DES) were used to accurately predict the fluid motion in the near wake and capture many of the characteristic features of the flow in the subcritical and supercritical regimes.

Another commonly-studied three-dimensional geometry is the prolate spheroid, as it closely resembles a variety of objects affected by external flows (watercraft and aircraft). Measurements of the flow over a prolate spheroid have been conducted by many workers. Significant contributions were made by Chesnakas and Simpson at $Re = 4.2 \times 10^6$ for flow over a 6:1 prolate spheroid using a LDV (Laser Doppler

Velocimetry) technique (see Chesnakas & Simpson [21] and Chesnakas & Simpson [22]) to obtain results for the Reynolds stresses, skin friction, and mean pressures. Fu [36] applied PIV (Particle Image Velocimetry) to quantify flow over a 6:1 prolate spheroid for a range of Reynolds numbers (4.2×10^5 to 2.1×10^6) and quantified (among other results) the integrated forces and moments on the body. Gee [37] applied turbulence modeling to solve the flow over a prolate spheroid at $Re = 7.2 \times 10^6$. Constantinescu *et al.* [27] calculated the solution for flow over a 6:1 prolate spheriod at $Re = 4.2 \times 10^6$ that compared very well with the measurements of Wetzel [108].

Principles derived from the study of cylinder-type and ellipsoidal geometries has been applied to more realistic geometrical configurations such as trains (Hemida & Krajnovic [42], Schetz [80]); cars (Diasinos & Gatto [31] and Katz [52]); trucks (Menter & Kuntz [58]); aircraft forebodies (Pauley *et al.* [69], Squires *et al.* [93], Wurtzler [110], and Viswanathan *et al.* [107]); aircraft wings (Forsythe & Woodson [34], Shur *et al.* [82]); and the actual aircraft themselves (Forsythe *et al.* [35], Squires *et al.* [94], Spalart [89], and Spalart [90]).

Studies of the flow over canonical geometries (the cylinder, sphere, and spheroid) as well as more realistic bodies have quantified flow characteristics and the physical regime(s) associated with the drag crisis, but questions remain about how the flow around bluff bodies can be controlled optimally. This generally implies drag reduction, but other possibilities include increasing/decreasing vortex shedding and heat transfer. The review by Choi [23] has summarized flow control methods from active loop control to passive flow control. Active flow control methods can include motion of the bluff body, as well as suction and blowing as in Krishnan *et al.* [55], Wygnanski [111] and many others. The current work is primarily concerned with passive flow control, since the focus is on drag reduction for a projectile object. One such method of passive flow control is surface roughening. This approach was dis-

covered accidentally by early golfers, who noticed that their rubber golf balls that were chipped, scratched, and nicked flew further than the new, smooth golf balls (see Smits & Ogg [85]). Achenbach explored effects of sand-grain roughness on the flow over a cylinder (Achenbach [2]) and a sphere (Achenbach [4]) in the range of Reynolds numbers spanning the drag crisis ($Re = 5 \times 10^4$ to $Re = 6 \times 10^6$). Son *et al.* [87] investigated the effect of a trip wire on the flow over a sphere (a single instance of surface roughness) for subcritical Reynolds numbers ($Re = 0.5 \times 10^5$ to $Re = 2.8 \times 10^5$). Other workers have investigated the usefulness of surface roughness (namely, dimples) to modify and improve heat transfer coefficents in turbine engines (see Moon *et al.* [63], Bunker & Donnellan [19]), increase load-carrying capacity of thrust bearings (Brizmer *et al.* [18]), and to reduce friction in lubricated journal bearings (Ausas *et al.* [7]). Since the accidental discovery of drag reduction by surface roughening, golfers and equipment manufacturers have sought to optimize the surface roughening (dimples) on a sphere to reduce drag (e.g., see Smits & Ogg [85]). Optimization of dimple patterns - their density, shape, and size - requires a fundamental understanding of the mechanisms that lead to drag reduction by surface dimpling.

Measurements of flow over a golf ball have produced some understanding of the mechanism of drag reduction by dimpling. Davies [30] measured the aerodynamic forces of a spinning golf ball at $Re = 9.4 \times 10^4$ by noting the impact point after the ball was dropped through the horizontal flow in a wind tunnel. Bearman & Harvey [11] made the next major contribution by measuring the aerodynamic forces of a spinning golf ball over a range of Reynolds numbers, and compared these results for spherically- and hexagonally-dimpled golf balls. Smits & Smith [86] measured the flight performance of a spinning golf ball in an indoor range and developed an aerodynamic model for golf ball flight. Most recently, Choi *et al.* [25] measured the aerodynamic forces on a non-rotating golf ball and gathered turbulent

statistics of the flow in order to understand how dimples generate turbulence and their relationship to the reduction of drag on a golf ball. Choi *et al.* [25] have proposed that the drag reduction mechanism is related to the development of a shear layer instability that produces higher momentum near the wall, causing local flow reattachment and a delay in complete separation, which reduces drag significantly. This proposition was confirmed by the direct simulations of Smith *et al.* [84], which reported results in the subcritical ($Re = 2.5 \times 10^4$) and supercritical ($Re = 1.1 \times 10^5$) regimes for a stationary golf ball.

From the literature survey above, it is clear that progress has been made in understanding the basic mechanisms of drag reduction in bluff body flows. Central to this process appears to be the development of shear layer instabilities over dimples that increase momentum transport near the surface of the golf ball. Local flow separation from shear layer instability along with other mechanisms (e.g., turbulent boundary layer separation) influencing drag reduction are excellent candidates for study using simulations. The over-arching objective of the current contribution is the application of DNS to study and understand the flow over a golf ball and the influence of dimples on drag reduction. Since drag reduction occurs over an established flow regime, it is necessary to investigate the physical characteristics of the flow in the range of this regime. Therefore, in the present work DNS is used to study the flow around a golf ball in the subcritical ($Re = 1.0 \times 10^4$, $Re = 2.5 \times 10^4$) and supercritical regimes ($Re = 1.1 \times 10^5$).

1.2 Background

Since DNS will be used to investigate the flow around a golf ball, a framework for the DNS must be selected. Two general categories of methods exist: boundary-conforming methods, and non-boundary conforming methods. Consider an arbitrary body around which flow is to be calculated. Boundary-conforming methods

involve the generation of structured or unstructured grids which conform to the boundary. The grid generation process usually involves specification of sizing details on the surface(s), which are then used to generate grid cells in the volume. The governing equations are then discretized and solved on the boundary-conformed grid using the appropriate technique. For non-boundary conforming methods, the process is distinctly different. First, a surface grid is created on the arbitrary body. Next, the grid in the volume is generated without regard to the body; e.g., the geometry of the volume grid cells are not modified in the vicinity of the body. The arbitrary body effectively cuts through the volume grid, or is immersed into the volume grid; which is why this class of methods is often labeled *immersed boundary methods*. This term was first used by Peskin [70] when he simulated the flow of blood in the heart on a Cartesian grid which did not conform to the shape of the heart. The effect of the body on the flow is represented by modifying the governing equations in the vicinity of the boundary. The details of how the boundary condition is applied to the governing equations by these modifications is generally what distinguishes one type of immersed boundary approach from another. A thorough review of immersed boundary methods is presented by Mittal & Iaccarino [60], in which the authors discuss the current status of these methods and compare them with boundary-conforming approaches.

As noted by Mittal & Iaccarino [60], immersed boundary methods have their own unique set of advantages and disadvantages. Perhaps the most obvious is that applying the boundary conditions through a modification of the equations in the vicinity of the boundary is not straightforward. Also, questions could be raised about the effect of these modifications on the order of accuracy and the conservative properties of the numerical scheme. Furthermore, when the grid aligns with the boundary (as in boundary-conforming approaches) it is generally easier to control the resolution near the boundary, which can imply greater control over the toal

size of the grid as the Reynolds number increases. Volume grids used with non-boundary conforming methods can grow more quickly in total size than boundary-conformal grids for the same geometry with increasing Reynolds number, but this greater size does not necessarily imply greater computational cost. This is mainly due to the fact that the grid points inside the immersed body may not require the same amount of computational effort as those actually in the flow. Additionally, the application of simple Cartesian or cylindrical coordinate grids with non-boundary conforming methods can reduce the amount of machine operations per grid point, as there are no additional terms associated with grid transformations (as in the case of boundary-conforming methods with structured grids) or local geometrical details (face centroids, local normals; this information must be stored for each cell when using an unstructured grid with a boundary-conforming method) that add cost.

Thus, the primary advantange of immersed boundary techniques is that the process of grid generation is greatly simplified. The process of grid generation for body-conformal structured or unstructured grids can be an iterative process, often requiring a lot of input from the user. Even with recent advances in body-conformal grid generation algorithms, care must be exercised in order to obtain a grid with sufficient resolution near the wall. Often, body-conformal grid generation is iterative because of the conflicting requirements of adequate resolution near the walls and minimization of the total grid size (to reduce computational cost). Conversely, the complexity and/or quality of non-body conforming grids in Cartesian or cylindrical coordinates are generally not affected by immersed complex geometry. A secondary (though not insignificant) advantage of non-boundary conforming methods is that their implementation for moving boundaries is relatively straightforward and low (computational) cost when compared with analogous boundary-conforming approaches.

Non-boundary conforming methods (immersed boundary methods) are generally divided into two categories (following Mittal & Iaccarino [60]): continuous-forcing methods and discrete forcing methods. The distinction between the two is the way that the governing equations are modified to represent the effect of the immersed body in the flow. Essentially, immersed boundary methods require that a forcing term is introduced into the governing equations to represent the effect of the boundary on the flow.

The continuous forcing approach applies forcing functions for the momentum and the pressure to the governing equations, which are then solved on the entire domain. It has been implemented by Peskin [70], and promising results have been reported by many workers (see Peskin [71], Beyer [16], Unverdi & Tryggvason [103], and Zhu & Peskin [115]) for biological flows in which the immersed boundary is flexible; solution of flows over rigid immersed bodies with the continuous forcing approach have had limited success.

The discrete forcing technique establishes the set of governing equations for the entire domain without additional forcing terms in the equations. The discretization in the grid cells near the boundary is adjusted to account for the presence of the boundary, producing a modified set of equations in these cells which are then solved along with the entire solution domain. This methodology is advantageous because it leads to a sharp representation of the immersed boundary, which is desirable with increasing Reynolds number. No extra stability constraints are introduced with the discrete forcing technique. The discrete forcing approach has been applied successfully by many workers to variety of problems including internal flows (Verzicco *et al.* [105], Fadlun *et al.* [33], Iaccarino *et al.* [46], and Balaras [9]), bluff body flows (Ye *et al.* [114], Kim *et al.* [54], Verzicco *et al.* [104], Gilmanov *et al.* [40], Kalitzin *et al.* [49], Mittal *et al.* [61], and Ghias *et al.* [39]), and biological flows (Balaras & Yang [10], Beratlis *et al.* [15], and Beratlis *et al.* [14]).

Since the objective of this contribution is the application of DNS to study the flow around a golf ball, and DNS presents very high computational costs (based on the size of the grids and time needed to create such grids with a boundary-conforming method), an immersed boundary technique is selected as the framework within which DNS will be applied. A body-conforming approach with unstructured grids (reference Appendix A) was tested for the flow over a golf ball, but the cost of the simulations was high even without resorting to DNS. For the grid resolutions and models studied, the most promising result was reasonable convergence of the aerodynamic forces with measurements, but the cost limitations of this approach motivated a more efficient technique. Application of an immersed boundary method will not only simplify the generation of the grids needed for this study, but will also allow highly efficient flow solvers to be employed. The boundary-conforming approach for the flow over a golf ball required an unstructured grid (due to the geometry near the ball), and this presented additional computational cost in terms of the flow solver. Furthermore, an immersed boundary framework will allow for future implemention of rigid body motion, and it is well-known that rotation as well as translation is present during golf ball flight. Within the class of immersed boundary methods, the discrete-forcing approach is selected for this work, since (as noted above and in Mittal & Iaccarino [60]) it allows for a sharp representation of the boundary even with increasing Reynolds numbers, and has very stable properties with respect to the numerics.

1.3 Present Contribution

Having summarized significant efforts toward understanding of bluff body aerodynamics, and also discussed available methods for analysis, a summary of the primary contributions of this work are presented as follows:

- Direct numerical simulation (DNS) of laminar, transitional, and turbulent flow around a golf ball.
- Development of an approach for calculating wall shear, pressure and turbulent statistics on complex immersed bodies.
- Quantification of the effect of the dimples on the flight performance of golf balls.

Chapter 2

Computational Approach

In this Chapter, the implementation of the governing equations is presented in Section 2.1, where 2.1.1 presents the implementation of the governing equations in cylindrical coordinates, the time-advancing scheme is outlined in 2.1.3, and the solution of the Poisson equation is presented in 2.1.4. The immersed boundary approach is discussed in detail in Section 2.2, outlining the relationship of the boundary with the grid (Section 2.2.1), and Sections 2.2.2 and 2.2.3 which present details of different reconstruction schemes. The parallelization approach for the code is presented in Section 2.3. Post-processing methods for reconstruction of the wall stress (pressure and viscous contributions) are presented in Section 2.5. An approach for calculation of momentum fluxes is detailed in Section 2.6.

2.1 Navier-Stokes Solver

2.1.1 Governing Equations

The governing equations for unsteady, incompressible, viscous flow of a Newtonian fluid with constant density are given in Cartesian coordinates as follows:

$$\frac{\partial u_i}{\partial x_i} = 0 \tag{2.1}$$

$$\frac{\partial u_i}{\partial t} + \frac{\partial \left(u_i u_j\right)}{\partial x_j} = -\frac{\partial p}{\partial x_i} + \frac{1}{Re}\frac{\partial^2 u_i}{\partial x_j x_i} \tag{2.2}$$

where x_i and x_j $i, j = 1, 2, 3$ are the Cartesian coordinates; u_i and u_j are the velocity components in their respective directions, non-dimensionalized by a reference velocity U; t is the time non-dimensionalized by D/U, where D is a reference length scale (the sphere or golf ball diameter in the current work); p is the pressure non-dimensionalized by ρU^2 where ρ is the fluid density; and Re is the Reynolds number defined as $Re = \rho UD/\mu$, where μ is the dynamic viscosity of the fluid.

In the current work, the governing equations are solved in cylindrical coordinates. Cylindrical coordinates are implemented because they are a convenient choice for the external flow problem of flow around a bluff body. Additionally, cylindrical coordinates allow for ease of grid adaptation when combined with immersed boundary formulations. Therefore, the Navier-Stokes equations are written in cylindrical coordinates in the conservative formulation as follows:

$$\frac{1}{r}\frac{\partial(ru_r)}{\partial r}+\frac{1}{r}\frac{\partial u_\theta}{\partial \theta}+\frac{\partial u_z}{\partial z}=0 \tag{2.3}$$

$$\begin{aligned}&\frac{\partial u_r}{\partial t}+\frac{1}{r}\frac{\partial(ru_ru_r)}{\partial r}+\frac{1}{r}\frac{\partial(u_\theta u_r)}{\partial \theta}+\frac{\partial u_z u_r}{\partial z}-\frac{{u_\theta}^2}{r}\\&\quad=-\frac{\partial p}{\partial r}+\frac{1}{Re}\left[\frac{\partial}{\partial r}\left(\frac{1}{r}\frac{\partial}{\partial r}(ru_r)\right)+\frac{1}{r^2}\frac{\partial^2 u_r}{\partial \theta^2}+\frac{\partial^2 u_r}{\partial z^2}-\frac{2}{r^2}\frac{\partial u_\theta}{\partial \theta}\right]\end{aligned} \tag{2.4}$$

$$\begin{aligned}&\frac{\partial u_\theta}{\partial t}+\frac{1}{r}\frac{\partial(ru_ru_\theta)}{\partial r}+\frac{1}{r}\frac{\partial(u_\theta u_\theta)}{\partial \theta}+\frac{\partial(u_z u_\theta)}{\partial z}+\frac{u_r u_\theta}{r}\\&\quad=-\frac{1}{r}\frac{\partial p}{\partial \theta}+\frac{1}{Re}\left[\frac{1}{r}\frac{\partial}{\partial r}\left(r\frac{\partial u_\theta}{\partial r}\right)-\frac{u_\theta}{r^2}+\frac{1}{r^2}\frac{\partial^2 u_\theta}{\partial \theta^2}+\frac{\partial^2 u_\theta}{\partial z^2}+\frac{2}{r^2}\frac{\partial u_r}{\partial \theta}\right]\end{aligned} \tag{2.5}$$

$$\begin{aligned}&\frac{\partial u_z}{\partial t}+\frac{1}{r}\frac{\partial(ru_ru_z)}{\partial r}+\frac{1}{r}\frac{\partial(u_\theta u_z)}{\partial \theta}+\frac{\partial(u_z u_z)}{\partial z}\\&\quad=-\frac{\partial p}{\partial z}+\frac{1}{Re}\left[\frac{1}{r}\frac{\partial}{\partial r}\left(r\frac{\partial u_z}{\partial r}\right)+\frac{1}{r^2}\frac{\partial^2 u_z}{\partial \theta^2}+\frac{\partial^2 u_z}{\partial z^2}\right]\end{aligned} \tag{2.6}$$

where r represents the radial direction, θ represents the azimuthal (spanwise) direction, and z represents the axial (streamwise) direction.

2.1.2 Spatial Discretization

A second-order central-differencing scheme on a staggered grid is applied in the present study. An illustration of a typical grid cell and a grid cell near the axis is shown below in Figure 2.1, with the velocity components located at the cell face

centers and pressure located at the center of the grid cell. Since the grid variables are staggered, it is evident that only the radial velocity component exists at the centerline. In order to preserve consistency with the numerical indexing scheme in the code, the standard half cell notation typically applied in the literature ($i \pm \frac{1}{2}, j \pm \frac{1}{2}, k \pm \frac{1}{2}$) is not used.

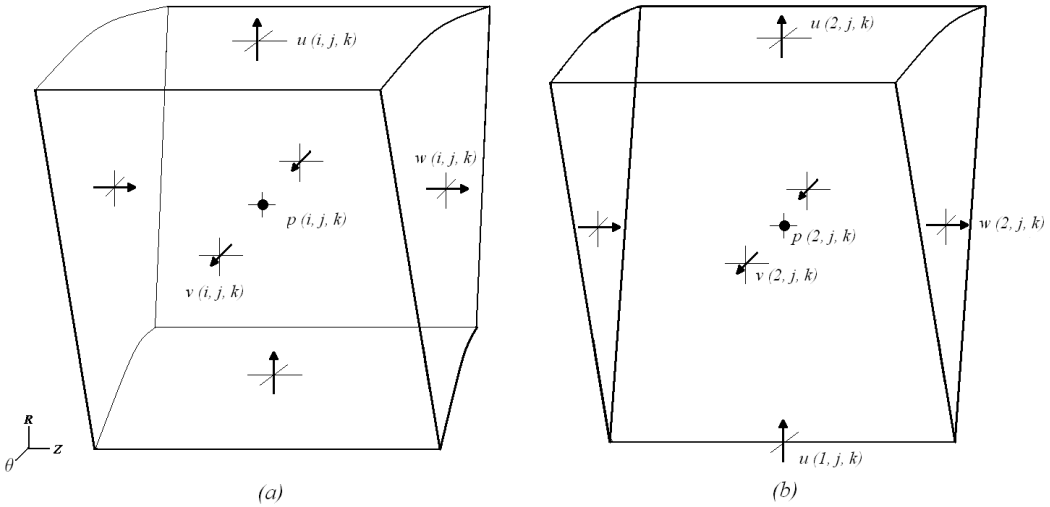

Figure 2.1: Illustration of staggered grid cell and variable locations in cylindrical coordinates (a) typical grid cell; (b) a grid cell at the centerline.

The finite difference schemes can be constructed either in physical space or computational space. It becomes advantageous to construct the finite differences in computational space when a non-uniform grid in physical space may be transformed to a uniformly-spaced grid in computational space. In the current work, the grid is uniform in the azimuthal direction, but non-uniform in the radial and axial directions. The mapping between physical and computational space is described mathematically as:

$$r = r(\xi), \quad \theta = \theta(\eta), \quad z = z(\zeta) \tag{2.7}$$

$$\xi = \xi(r), \quad \eta = \eta(\theta), \quad \zeta = \zeta(z) \tag{2.8}$$

where ξ, η, and ζ are the variables in computational space, which correspond to the physical variables r, θ, and z, respectively. Thus, derivatives in physical space are transformed to computational space in following manner:

$$\frac{\partial}{\partial r} = \frac{\partial}{\partial \xi}\xi_r, \quad \frac{\partial}{\partial \theta} = \frac{\partial}{\partial \eta}\eta_\theta, \quad \frac{\partial}{\partial z} = \frac{\partial}{\partial \zeta}\zeta_z \tag{2.9}$$

where the operators ξ_r, η_θ, ζ_z, are defined as:

$$\xi_r = \frac{2\Delta\xi}{r_{i+1} - r_{i-1}}, \quad \eta_\theta = \frac{2\Delta\eta}{\theta_{i+1} - \theta_{i-1}}, \quad \zeta_z = \frac{2\Delta\zeta}{z_{i+1} - z_{i-1}} \tag{2.10}$$

The cell sizes in computational space set to 1, e.g., $\Delta\xi = \Delta\eta = \Delta\zeta = 1$. The introduction of this transformation implies that Eq.s 2.3, 2.4, 2.5, 2.6 can be rewritten as follows:

$$\frac{1}{r}\xi_r \frac{\partial (r u_r)}{\partial \xi} + \frac{1}{r}\eta_\theta \frac{\partial u_\theta}{\partial \eta} + \zeta_z \frac{\partial u_z}{\partial z} = 0 \tag{2.11}$$

$$\begin{aligned} &\frac{\partial u_r}{\partial t} + \frac{1}{r}\xi_r \frac{\partial (r u_r u_r)}{\partial \xi} + \frac{1}{r}\eta_\theta \frac{\partial (u_\theta u_r)}{\partial \eta} + \zeta_z \frac{\partial (u_z u_r)}{\partial \zeta} - \frac{{u_\theta}^2}{r} \\ &\quad = \frac{1}{Re}\left[\xi_r \frac{\partial}{\partial \xi}\left(\frac{1}{r}\xi_r \frac{\partial (r u_r)}{\partial \xi}\right) + \frac{1}{r^2}\eta_\theta \frac{\partial}{\partial \eta}\left(\eta_\theta \frac{\partial u_r}{\partial \eta}\right)\right] \\ &\quad + \frac{1}{Re}\left[\zeta_z \frac{\partial}{\partial \zeta}\left(\zeta_z \frac{\partial u_r}{\partial \zeta}\right) - \frac{2}{r^2}\eta_\theta \frac{\partial u_\theta}{\partial \eta}\right] - \xi_r \frac{\partial p}{\partial \xi} \end{aligned} \tag{2.12}$$

$$\begin{aligned} &\frac{\partial u_\theta}{\partial t} + \frac{1}{r}\xi_r \frac{\partial (r u_r u_\theta)}{\partial \xi} + \frac{1}{r}\eta_\theta \frac{\partial (u_\theta u_\theta)}{\partial \eta} + \zeta_z \frac{\partial (u_z u_\theta)}{\partial \zeta} + \frac{u_r u_\theta}{r} \\ &\quad = \frac{1}{Re}\left[\frac{1}{r}\xi_r \frac{\partial}{\partial \xi}\left(r\xi_r \frac{\partial u_\theta}{\partial \xi}\right) - \frac{u_\theta}{r^2} + \frac{1}{r^2}\eta_\theta \frac{\partial}{\partial \eta}\left(\eta_\theta \frac{\partial u_\theta}{\partial \eta}\right)\right] \\ &\quad + \frac{1}{Re}\left[\zeta_z \frac{\partial}{\partial \zeta}\left(\zeta_z \frac{\partial u_\theta}{\partial \zeta}\right) + \frac{2}{r^2}\eta_\theta \frac{\partial u_r}{\partial \eta}\right] - \frac{1}{r}\eta_\theta \frac{\partial p}{\partial \eta} \end{aligned} \tag{2.13}$$

$$\begin{aligned}
&\frac{\partial u_z}{\partial t} + \frac{1}{r}\xi_r \frac{\partial (r u_r u_z)}{\partial \xi} + \frac{1}{r}\eta_\theta \frac{\partial (u_\theta u_z)}{\partial \eta} + \zeta_z \frac{\partial (u_z u_z)}{\partial \zeta} \\
&\quad = \frac{1}{Re}\left[\frac{1}{r}\xi_r \frac{\partial}{\partial \xi}\left(r\xi_r \frac{\partial u_z}{\partial \xi}\right) + \frac{1}{r^2}\eta_\theta \frac{\partial}{\partial \eta}\left(\eta_\theta \frac{\partial u_z}{\partial \eta}\right)\right] \\
&\quad + \frac{1}{Re}\left[\zeta_z \frac{\partial}{\partial \zeta}\left(\zeta_z \frac{\partial u_z}{\partial \zeta}\right)\right] - \zeta_z \frac{\partial p}{\partial \zeta}
\end{aligned} \tag{2.14}$$

Two examples of the discretization scheme are presented here. The discretization of these equations on a staggered grid is presented in detail in [8]. In order to simplify this description of the discretization scheme, the following redefinitions for the velocity components are applied: $u_r = u$, $u_\theta = v$, $u_z = w$. This (u, v, w) notation will be used in the discrete form of the equations, while (u_r, u_θ, u_z) will be used in the continuous form of the equations. Since the grid variables are staggered, an arithmetic average is applied to obtain variables at the grid locations between where the variables are defined (see Figure 2.1). The first representative example is given by presenting the discretization of the convective u_z term from the u_z equation in computational space.

$$\begin{aligned}
\zeta_z \frac{\partial (u_z u_z)}{\partial \zeta}\bigg|_{i,j,k}^{w} &\approx \zeta_z|_k^w \frac{\delta (ww)}{\delta \zeta}\bigg|_{i,j,k}^{w} \\
&= \zeta_z|_k^w \frac{1}{\Delta \zeta}\left[\frac{(ww)_{i,j,k} + (ww)_{i,j,k+1}}{2} - \frac{(ww)_{i,j,k-1} + (ww)_{i,j,k}}{2}\right]
\end{aligned} \tag{2.15}$$

The second representative example is given by the discretization of the diffusive term from the u_z equation in computational space.

$$\begin{aligned}
\zeta_z \frac{\partial}{\partial \zeta}\left(\zeta_z \frac{\partial u_z}{\partial \zeta}\right)\bigg|_{i,j,k}^{w} &\approx \zeta_z|_k^w \frac{\delta}{\delta \zeta}\left(\zeta_z \frac{\delta w}{\delta \zeta}\right)\bigg|_{i,j,k}^{w} \\
&= \zeta_z|_k^w \frac{1}{\Delta \zeta}\left[\left(\frac{w_{i,j,k+1} - w_{i,j,k}}{\Delta \zeta}\right)\bigg|_{i,j,k+1}^{p} - \left(\frac{w_{i,j,k} - w_{i,j,k-1}}{\Delta \zeta}\right)\bigg|_{i,j,k}^{p}\right]
\end{aligned} \tag{2.16}$$

In these discrete equations described above, the symbols $|_{i,j,k}^{w}$ and $|_{i,j,k}^{p}$ represent quantities evaluated at the location of the pressure p grid points (cell centers) and

at the location of the streamwise velocity w points (cell faces) as shown in Figure 2.1 above.

Discrete solution of the governing equations in cylindrical coordinates presents a complication when the centerline is considered. The centerline presents a mathematical singularity which is not present in Cartesian coordinates. This singularity implies that the radial (u) and azimuthal (v) components cannot be defined at the centerline, even though the flow field itself does not have a singularity problem at the centerline. Several approaches (Eggels *et al.* [32], Akselvoll & Moin [5], Verzicco & Orlandi [106] Morinishi *et al.* [64]) have been suggested for treatment of this singularity at the centerline. The approach proposed in Pierce [72] and implemented successfully in Yang [112] is applied in the current work. The radial and azimuthal velocity components are assumed to have multiple values at the centerline, and a linear averaging of two symmetrical points over the centerline provides the value there. For the radial velocity component, this is an average over two grid cells and has a decreased order of accuracy, which requires finer grid spacing near the centerline to obtain good resolution of the flow field near the singularity point.

The treatment of the solution variables at the centerline is shown in Figure 2.2. Ghost cells are used to implement the centerline boundary conditions, and these required boundary conditions are given in Figure 2.2 a. Figure 2.2 b demonstrates the variable collocation on the grid cell across the centerline.

As demonstrated in Figure 2.2, the variable value for the ghost cell may be obtained from the grid cell across the centerline. This implies mathematically that:

$$\begin{aligned} v_{1,j,k} &= -v_{2,N\theta/2+j,k}, \\ w_{1,j,k} &= w_{2,N\theta/2+j,k}, \\ p_{1,j,k} &= p_{2,N\theta/2+j,k} \end{aligned} \tag{2.17}$$

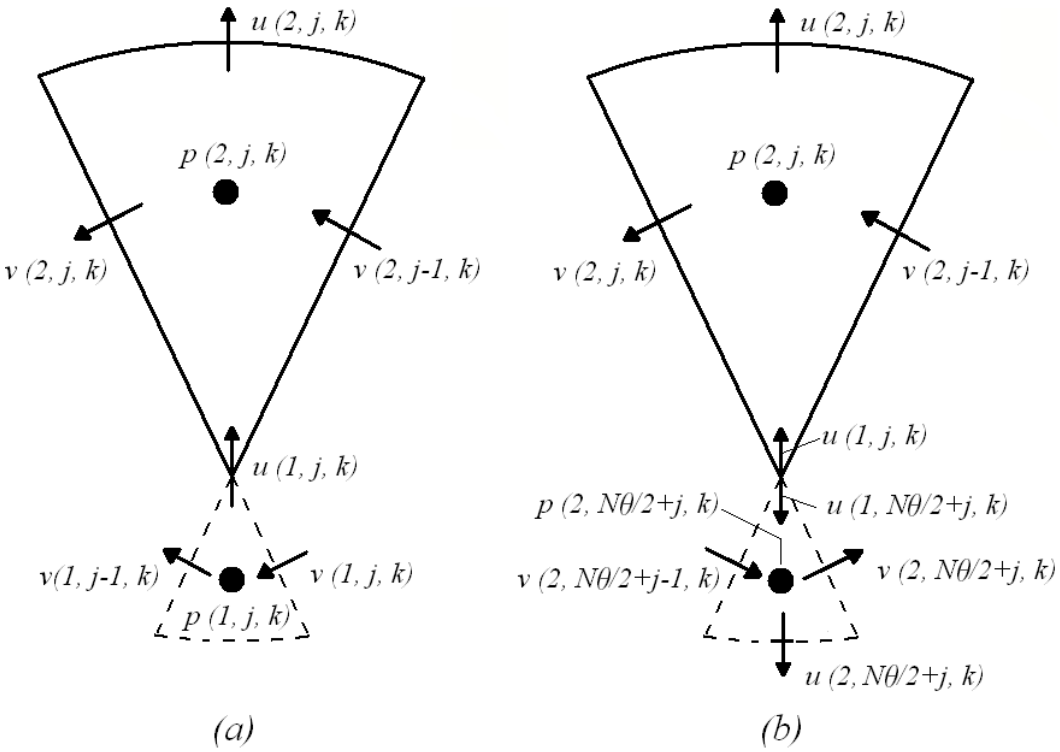

Figure 2.2: Treatment of the centerline in cylindrical coordinates (a) required boundary conditions and variable location for the ghost cell; (b) variables defined across the centerline on an $r-\theta$ plane.

where the boundary condition for the pressure (although reported above) is not directly utilized in the current formulation.

The boundary condition for the radial velocity component (u) is obtained by averaging the values of the opposing u across the centerline:

$$u_{1,j,k} = \frac{1}{2}\left(u_{2,j,k} - u_{2,N\theta/2+j,k}\right) \tag{2.18}$$

This approximation is a linear interpolation over a distance of $2\Delta\xi$, therefore the grid must maintain good resolution in the vicinity of the centerline to avoid large errors due to the discretization scheme. This centerline boundary condition implementation has been used successfully in the current work (as reported in Yang

[112]), and no problems have been encountered as a result of this centerline treatment.

2.1.3 Time-Advancement Schemes

In the code, there are several choices for the time-advancement scheme. Specfically, a second-order Adams-Bashforth (AB2) approach or a low-storage, third-order Runge-Kutta (RK3) method are available. If the equations are solved in Cartesian coordinates, an explicit scheme would typically be used, although the implicit scheme, which is outlined below in 2.1.3.2, provides a significant advantage when the equations are solved in cylindrical coordinates, as in the current work. The time-advancing scheme applied for this work is a combination of the RK3 explicit scheme with a second-order Crank Nicholson scheme applied for the terms treated implicitly. An overview of the low-storage RK3 scheme applied to a fractional step method is described in 2.1.3.1. The implicit implementation is presented in 2.1.3.2.

2.1.3.1 Explicit Approach

The governing equations are integrated in time using a fractional step approach. Here, the methodology of the fractional step method is presented within the framework of the RK3 scheme. The fractional step integration in the current work is performed three times within one timestep, producing the characteristic third-order temporal accuracy of the RK3 approach. The discrete equations below represent the solution process at any one substep: 1, 2, or 3. Therefore, the solution process at **any** substep k represented in equation 2.19 by solving for the provisional velocity in the radial direction, $\widehat{u}^k$. Then the provisional velocity is used to calculate a scalar (ϕ) in equation 2.20, which projects the velocity back into divergence-free space (reference 2.21) and corrects the pressure as in 2.22.

$$\frac{\widehat{u}^k - u^{k-1}}{\Delta t} = \gamma_k A\left(u^{k-1}\right) + \rho_k A\left(u^{k-2}\right) - \alpha_k \xi_r \frac{\delta p^{k-1}}{\delta \xi} \tag{2.19}$$

$$\xi_r^2 \frac{\delta^2 \phi^k}{\delta \xi^2} = \frac{1}{\alpha_k \Delta t} \xi_r \frac{\delta \widehat{u}^k}{\delta \xi} \tag{2.20}$$

$$u^k = \widehat{u}^k - \alpha_k \Delta t \xi_r \frac{\delta \phi^k}{\delta \xi} \tag{2.21}$$

$$p^k = p^{k-1} - \phi^k \tag{2.22}$$

Here, k is the substep index, ranging from 1 to 3 for the RK3 method. A is a spatial operator containing the convective and viscous terms. Δt represents the timestep, which can be specified at a constant value or calculated at each timestep by selecting a constant value of the stability criterion. As stated above, this fractional step process is carried out in the code at each substep k, implying that the A operator (which contains the convective and viscous terms) must be retained in memory at the two previous substeps, $k-1$ and $k-2$.

The RK3 coefficients are:

$$\begin{aligned} &\alpha_1 = 8/15, \quad \gamma_1 = 8/15, \quad \rho_1 = 0 \\ &\alpha_2 = 2/15, \quad \gamma_2 = 5/12, \quad \rho_2 = -17/60 \\ &\alpha_3 = 1/3, \quad \gamma_3 = 3/4, \quad \rho_3 = -5/12 \end{aligned} \tag{2.23}$$

with

$$\sum_{k=1}^{3} \alpha_k = \sum_{k=1}^{3} (\gamma_k + \rho_k) \tag{2.24}$$

The stability criterion (or the CFL number including the timestep constraint from the viscous terms) for the code is adopted from Akselvoll & Moin [5].

$$CFL = \Delta t \left[\frac{|u|}{\Delta r} + \frac{|v|}{r\Delta\theta} + \frac{|w|}{\Delta z} + 4Re\left(\frac{1}{\Delta r^2} + \frac{1}{\Delta z^2} \right) \right] \tag{2.25}$$

where

$$\Delta r = r_i - r_{i-1}, \quad \Delta\theta = \theta_j - \theta_{j-1}, \quad \Delta z = z_k - z_{k-1} \tag{2.26}$$

The theoretical stability limit for the RK3 scheme is $\sqrt{3}$. Since the cross derivative terms are not included in the above equation, the actual CFL number in the simulations is lower. $CFL = 1.5$ was used in most of the simulations in this work with the RK3 time-advancing scheme.

2.1.3.2 Implicit Approach

The governing equations in cylindrical coordinates are integrated in time using the fractional step method outlined in the previous section. In cylindrical coordinates, the grid spacing at the centerline is extremely small, and imposes severe restrictions on the timestep in the azimuthal direction. This computational penalty can be avoided by applying an implicit method for the diffusive terms in the azimuthal direction. Specfically, the explicit RK3 approach is used for all convective terms and the viscous terms in the streamwise and radial directions, while an implicit second-order Crank-Nicholson (CN2) approach is used for the viscous terms in the azimuthal direction. This implementation is described in terms of the discrete operators (δ) in computational space as follows:

$$\begin{aligned} \left[1 - \frac{\alpha_k \Delta t}{2} \frac{1}{Re} \frac{1}{r^2} \eta_\theta \frac{\delta}{\delta\eta} \left(\eta_\theta \frac{\delta}{\delta\eta} \right) \right] \widehat{u}^k &= RHS_\xi{}^{k-1} \\ &= u^{k-1} + \gamma_k \Delta t A_\xi{}^{k-1} + \rho_k \Delta t A_\xi{}^{k-2} + \frac{\alpha_k \Delta t}{2} B_\xi{}^{k-1} - \alpha_k \Delta t \xi_r \frac{\delta p^{k-1}}{\delta\xi} \end{aligned} \tag{2.27}$$

$$\left[1-\frac{\alpha_k\Delta t}{2}\frac{1}{Re}\frac{1}{r^2}\eta_\theta\frac{\delta}{\delta\eta}\left(\eta_\theta\frac{\delta}{\delta\eta}\right)\right]\widehat{v}^k = RHS_\eta{}^{k-1}$$
$$= v^{k-1}+\gamma_k\Delta t A_\eta{}^{k-1}+\rho_k\Delta t A_\eta{}^{k-2}+\frac{\alpha_k\Delta t}{2}B_\eta{}^{k-1}-\alpha_k\Delta t\frac{1}{r}\eta_\theta\frac{\delta p^{k-1}}{\delta\eta} \quad (2.28)$$

$$\left[1-\frac{\alpha_k\Delta t}{2}\frac{1}{Re}\frac{1}{r^2}\eta_\theta\frac{\delta}{\delta\eta}\left(\eta_\theta\frac{\delta}{\delta\eta}\right)\right]\widehat{w}^k = RHS_\zeta{}^{k-1}$$
$$= w^{k-1}+\gamma_k\Delta t A_\zeta{}^{k-1}+\rho_k\Delta t A_\zeta{}^{k-2}+\frac{\alpha_k\Delta t}{2}B_\zeta{}^{k-1}-\alpha_k\Delta t\zeta_z\frac{\delta p^{k-1}}{\delta\zeta} \quad (2.29)$$

The coefficients are the same as were defined above in Section 2.1.3.1, and the A and B operators are defined as follows:

$$A_\xi = -\left[\frac{1}{r}\xi_r\frac{\delta(ruu)}{\delta\xi}+\frac{1}{r}\eta_\theta\frac{\delta(vu)}{\delta\eta}+\zeta_z\frac{\delta(wu)}{\delta\zeta}-\frac{v^2}{r}\right]$$
$$+\frac{1}{Re}\left[\xi_r\frac{\delta}{\delta\xi}\left(\frac{1}{r}\xi_r\frac{\delta(ru)}{\delta\xi}\right)+\zeta_z\frac{\delta}{\delta\zeta}\left(\zeta_z\frac{\delta u}{\delta\zeta}\right)-\frac{2}{r^2}\eta_\theta\frac{\delta v}{\delta\eta}\right] \quad (2.30)$$

$$A_\eta = -\left[\frac{1}{r}\xi_r\frac{\delta(ruv)}{\delta\xi}+\frac{1}{r}\eta_\theta\frac{\delta(vv)}{\delta\eta}+\zeta_z\frac{\delta(wv)}{\delta\zeta}+\frac{uv}{r}\right]$$
$$+\frac{1}{Re}\left[\frac{1}{r}\xi_r\frac{\delta}{\delta\xi}\left(r\xi_r\frac{\delta v}{\delta\xi}\right)+\zeta_z\frac{\delta}{\delta\zeta}\left(\zeta_z\frac{\delta v}{\delta\zeta}\right)+\frac{2}{r^2}\eta_\theta\frac{\delta u}{\delta\eta}-\frac{v}{r^2}\right] \quad (2.31)$$

$$A_\zeta = -\left[\frac{1}{r}\xi_r\frac{\delta(ruw)}{\delta\xi}+\frac{1}{r}\eta_\theta\frac{\delta(vw)}{\delta\eta}+\zeta_z\frac{\delta(ww)}{\delta\zeta}\right]$$
$$+\frac{1}{Re}\left[\frac{1}{r}\xi_r\frac{\delta}{\delta\xi}\left(r\xi_r\frac{\delta w}{\delta\xi}\right)+\zeta_z\frac{\delta}{\delta\zeta}\left(\zeta_z\frac{\delta w}{\delta\zeta}\right)\right] \quad (2.32)$$

$$B_\xi = \frac{1}{r^2}\frac{1}{Re}\eta_\theta\frac{\delta}{\delta\eta}\left(\eta_\theta\frac{\delta u}{\delta\eta}\right) \quad (2.33)$$

$$B_\eta = \frac{1}{r^2}\frac{1}{Re}\eta_\theta\frac{\delta}{\delta\eta}\left(\eta_\theta\frac{\delta v}{\delta\eta}\right) \quad (2.34)$$

$$B_\zeta = \frac{1}{r^2}\frac{1}{Re}\eta_\theta \frac{\delta}{\delta\eta}\left(\eta_\theta \frac{\delta w}{\delta\eta}\right) \tag{2.35}$$

The discretization scheme for the spatial coordinates in the above equations results in a set of cyclic tridiagonal equations, which are solved using the solver for cyclic tridiagonal systems from *Numerical Recipes* (Press *et al.* [75]).

2.1.4 Poisson Equation

Now that the implementation of the provisional velocity calculation has been described, the treatment of the Poisson equation can be discussed. The Poisson equation Eq. 2.20 can be rewritten in vector form as

$$\begin{aligned} \nabla^2\phi = f = \frac{1}{\alpha_k \Delta t}\nabla\cdot\widehat{u}_i^k \\ \phi = p^k - p^{k-1} \end{aligned} \tag{2.36}$$

where k is the substep index for the RK3 time advancing scheme. The discrete form of Eq. 2.37 in cylindrical coordinates is

$$\left[\frac{1}{r}\frac{\delta}{\delta r}\left(r\frac{\delta}{\delta r}\right) + \frac{1}{r^2}\frac{\delta^2}{\delta\theta^2} + \frac{\delta^2}{\delta z^2}\right]\phi_{i,j,k} = f_{i,j,k} \tag{2.37}$$

It is imperative that the discrete spatial operators used for the Poisson equation are the same as those used for the previous spatial differences, otherwise mass conservation is not guaranteed. If discrete (δ) operators are expanded, the discrete Poisson equation is described by adding together Eq.s 2.38 (represents the ξ term), 2.39 (represents the η term), 2.40 (represents the ζ term):

$$\frac{1}{r|_i^p}\xi_r|_i^p \frac{1}{\Delta\xi^2}\left[\left[r|_i^u \xi_r|_i^u \left(\phi_{i+1,j,k} - \phi_{i,j,k}\right)\right] - \left[r|_{i-1}^u \xi_r|_{i-1}^u \left(\phi_{i,j,k} - \phi_{i-1,j,k}\right)\right]\right] \tag{2.38}$$

$$\frac{1}{r^2|_i^p}\eta_\theta|_j^p \frac{1}{\Delta\eta^2}\left[\left[\eta_\theta|_j^v\left(\phi_{i,j+1,k}-\phi_{i,j,k}\right)\right]-\left[\eta_\theta|_{j-1}^v\left(\phi_{i,j,k}-\phi_{i,j-1,k}\right)\right]\right] \tag{2.39}$$

$$\zeta_z|_k^p \frac{1}{\Delta\zeta^2}\left[\left[\zeta_z|_k^w\left(\phi_{i,j,k+1}-\phi_{i,j,k}\right)\right]-\left[\zeta_z|_{k-1}^w\left(\phi_{i,j,k}-\phi_{i,j,k-1}\right)\right]\right]=f_{i,j,k} \tag{2.40}$$

This equation is solved using a combination of a fast Fourier transform (FFT) method from FFTPACK (Swarztrauber [98]) and a direct solution procedure from FISHPACK (Swarztrauber [97]). The direct solver can converge the solution to machine accuracy within one iteration, which provides a significant advantage over iterative solvers. In order to utilize the FFT approach, the computational grid must be uniform in the direction in which the FFT is performed. The current work utilizes a grid that is uniformly spaced in the azimuthal (spanwise) direction. Thus, the fast Fourier transform in the azimuthal direction causes Eq. 2.37 to change into a set of two-dimensional Helmholtz equations in uncoupled wavenumber space:

$$\left[\frac{1}{r}\frac{\delta}{\delta r}\left(r\frac{\delta}{\delta r}\right)+\frac{\delta^2}{\delta z^2}+\frac{1}{r^2}k'_l\right]\widehat{\phi}_{i,l,k}=\widehat{f}_{i,l,k} \tag{2.41}$$

and the modified wavenumber is

$$k'_l=\frac{2}{\Delta\theta^2}\left[1-cos\left(\frac{2\pi l}{N_\theta}\right)\right] \tag{2.42}$$

where l is the wavenumber, N_θ is the number of grid cells (not including ghost cells) $\Delta\theta$ is the cell size in the spanwise direction. This implies that the discrete Poisson equation can be rewritten as follows:

$$\frac{1}{r|_i^p}\xi_r|_i^p \frac{1}{\Delta\xi^2}\left[\left[r|_i^u\xi_r|_i^u\left(\widehat{\phi}_{i+1,l,k}-\widehat{\phi}_{i,l,k}\right)\right]-\left[r|_{i-1}^u\xi_r|_{i-1}^u\left(\widehat{\phi}_{i,l,k}-\widehat{\phi}_{i-1,l,k}\right)\right]\right] \tag{2.43}$$

$$-\frac{k_l^{'}}{r^2|_i^p}\widehat{\phi}_{i,l,k} \tag{2.44}$$

$$\zeta_z\,|_k^p\,\frac{1}{\Delta\zeta^2}\left[\left[\zeta_z\,|_k^w\left(\widehat{\phi}_{i,l,k+1}-\widehat{\phi}_{i,l,k}\right)\right]-\left[\zeta_z\,|_{k-1}^w\left(\widehat{\phi}_{i,l,k}-\widehat{\phi}_{i,l,k-1}\right)\right]\right]=\widehat{f}_{i,l,k} \tag{2.45}$$

The above equations are solved separately for each wavenumber, with the real and imaginary part of each wavenumber being solved using "BLKTRI" routine, in which a generalized cyclic reduction algorithm (Swarztrauber [97]) is employed from the FISHPACK library.

2.1.5 Boundary Conditions

Ghost cells are used to implement all boundary conditions in the current work. The ghost cell approach provides a specific advantage because it the same stencil can be used for all points in the domain; e.g.; no modification of the discretization stencil is needed at the boundaries. Ghost cells are also a natural choice for a parallel implementation of the solver.

2.1.5.1 Dirichlet and Neumann Boundary Conditions

An illustration of a $\xi-\zeta$ computational plain near the lower left boundary is depicted in Figure 2.3.

It can be observed that the Dirichlet boundary condition for the velocity component normal to the wall (u for the lower boundary in Figure 2.3 and w for the left boundary in Figure 2.3) can be directly enforced, since the in these cases, the velocity is defined on the wall itself. Thus,

$$u_{1,j,k}=u_b, \qquad w_{i,j,1}=w_b \tag{2.46}$$

where u_b and w_b are the prescribed conditions on the boundary.

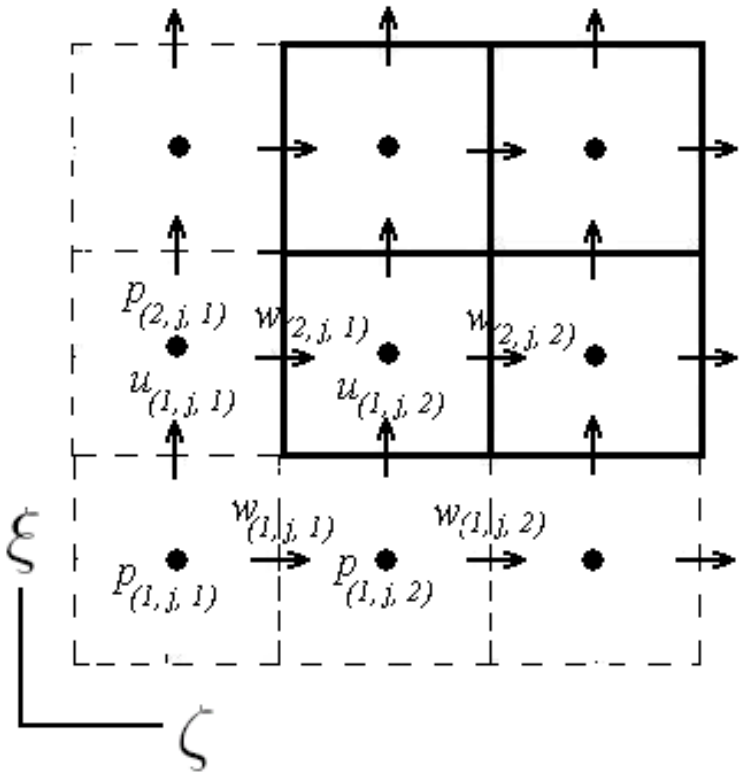

Figure 2.3: Dirichlet and Neumann boundary conditions in ξ - ζ plane at the lower left boundary of the computational domain.

The non-slip conditions for the velocity components tangent to the wall in Figure 2.3 (v and w) are implemented through the use of ghost cells.

$$v_{1,j,k} = 2v_t - v_{2,j,k} \qquad w_{1,j,k} = 2w_t - w_{2,j,k} \tag{2.47}$$

where v_t and w_t are the prescribed components tangent to the wall in the y and z directions. The Neumann boundary condition for an arbitrary variable ϕ can be written as:

$$\frac{\delta\phi}{\delta n} = f \tag{2.48}$$

where n is the direction normal to the boundary, and f is a known function. For the lower boundary in Figure 2.3, the normal direction is ξ, and this condition can be written with the help of ghost cells as follows:

$$\phi_{1,j,k} = \phi_{2,j,k} - f\Delta\xi \tag{2.49}$$

For a homogeneous boundary condition, $f = 0$.

2.1.5.2 Convective Boundary Condition

In the present work, the outflow boundary condition is implemented from Orlanski [66]. This condition has proved successful in convecting structures out of the domain without distorting the flow therein. In this case, the boundary condition can be calculated from the following equation:

$$\frac{\partial u_i}{\partial t} + U_{convec}\frac{\partial u_i}{\partial z} = 0 \tag{2.50}$$

where u_i is any velocity component, and U_{convec} is the convective velocity, which is set to the mean streamwise velocity at the exit plane. In the present work, the outflow boundary is normal to the streamwise direction, which is the z direction for cylindrical coordinates. Equation 2.50 is discretized using an explicit Euler scheme in time, with a one-sided spatial difference for the streamwise w component, and central differences in space for the other two velocity components. Furthermore, the predicted streamwise velocity is updated at each timestep in order to presernve mass conservation. The discrete form of the convective boundary condition is represented here by writing the streamwise version:

$$wb_{i,j,1} = w_{i,j,1} - U_{mean}\alpha_k\Delta t\frac{w_{i,j,2} - w_{i,j,1}}{z_k - z_{k-1}} \tag{2.51}$$

where wb is the desired condition on the boundary.

2.1.5.3 Periodic Boundary Conditions

The implementation of periodic boundary conditions using ghost cells is straightforward. The solution values in the periodic direction (which is the θ direction in the current work) are imposed as follows:

$$u_{i,1,k} = u_{i,N\theta+1,k} \quad v_{i,1,k} = v_{i,N\theta+1,k} \quad w_{i,1,k} = w_{i,N\theta+1,k} \tag{2.52}$$

$$u_{i,2,k} = u_{i,N\theta+2,k} \quad v_{i,2,k} = v_{i,N\theta+2,k} \quad w_{i,2,k} = w_{i,N\theta+2,k} \tag{2.53}$$

This approach guarantees that the periodicity and the derivative of the function of interest are imposed.

2.2 Immersed Boundary treatment

In this section, the immersed boundary approach is introduced and explained. Implementation of an immersed boundary method requires two crucial steps: first, the relationship between the immersed body and the background fluid grid must be established; next, a discrete-forcing reconstruction must be applied in the grid cells within the vicinity of the body. Section 2.2.1 presents a discussion of the relationship between the immersed body and the fluid grid. Then, two discrete-forcing reconstruction schemes are presented in Section 2.2.2 and Section 2.2.3. A brief introduction to moving immersed boundaries is discussed in Section 2.2.4.

2.2.1 Immersed Boundary - Fluid Grid Relationship

There are two methods that are commonly used for describing the boundary between two or more objects: Eulerian and Lagrangian approaches. Eulerian approaches, such as Level Set methods (Osher & Fedkiw [68]), provide an implicit definition of the interface which is usually defined by the isocontour of a function; typically, the signed shortest distance function to the interface. Conversely, in Lagrangian methods the interface is described explicitly, and is independent of the

underlying grid. In the present work a Lagrangian tracking scheme is employed. The independence with respect to the underlying Eulerian grid yields an advantage in the current work, as it implies that the surface resolution of the interface need not be of the same resolution as the Eulerian grid, which is refined at high Reynolds numbers.

The surface of the body is represented by a set of unstructured triangular elements and nodes as applied in Gilmanov *et al.* [40]. These vertices (points) are formed on the geometrical database of the immersed body, as depicted in Figure 2.4 using the commercial grid generation software GAMBIT. The process by which the triangles were formed on the surface of the golf ball is as follows:

- Discretize the connectors which comprise the CAD geometry obtained from the manufacturer.
- Generate unstructured triangular mesh via an unstructured solver in GAMBIT.

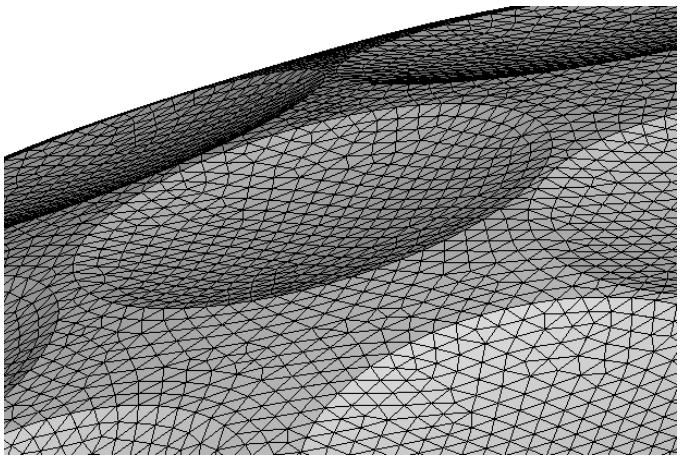

Figure 2.4: Discretization of the golfball surface (the Lagrangian body) using an unstructured mesh of surface triangles.

Now, the relation between the points on the surface and the Eulerian fluid grid must be determined. Figure 2.4 shows the surface of the golfball discretized by triangular elements. This set of vertices is then immersed in the Eulerian (fluid) grid. The approach used in the current work is similar to that applied in [9], and is summarized here and in Figure 2.5 as:

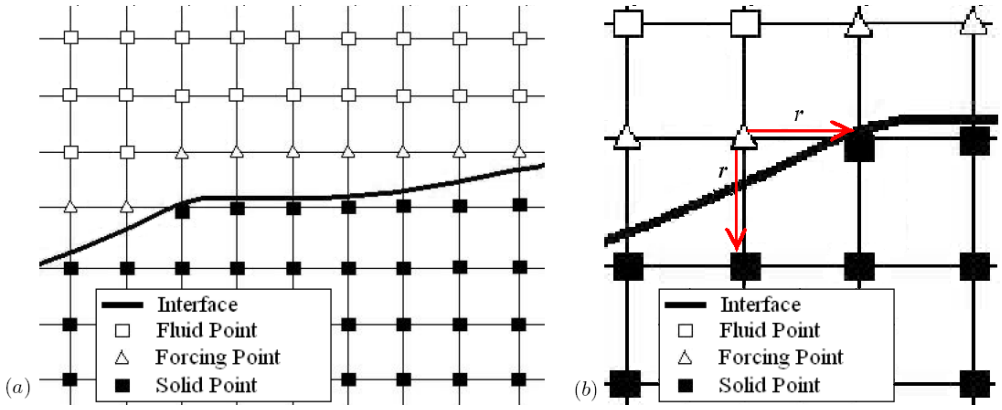

Figure 2.5: Interface-Grid relationship (*a*) Tagging of the Eulerian points as fluid points, solid points or forcing points; (*b*) Intersection of a ray projected from a forcing point toward the immersed body.

1. Determine the location of the interface in the grid using **all** the known vertices of triangles on the immersed body (as mentioned above). All Eulerian points are tagged as either interior(solid) or exterior(fluid) points.

2. Find the Eulerian points closest to the immersed body, which are defined as the points in the fluid phase with at least one neighboring point in the solid phase.

3. For these grids points, a search for the closest intersection on the surface of the immersed object is performed. A ray **r** (shown in Figure 2.5 b) is shot from the point in the fluid phase to its neighboring point in the solid phase along a gridline in the vertical and horizontal directions. The intersection point of the ray with the triangle on the surface of the immersed body is

stored. The smallest distance between the Eulerian point in the fluid phase and its intersection with the immersed boundary are then selected and stored.

The information about the closest intersection of the ray from the Eulerian grid point to the body is central to the reconstruction procedure outlined in 2.2.2. An example of the result of the tagging process is presented in Figure 2.5 *a*. The Eulerian grid points are classified with respect to the body as *forcing points* (points which have at least one neighbor in the solid phase), *solid points* (which are the points inside the body), and *fluid points* (those remaining points outside the body in the fluid phase). During the solution procedure, the fluid points are unknowns, the forcing points are boundary points, and the solid points do not affect the remainder of the computation. For solution of flow around a stationary immersed body, this procedure is performed once at the beginning of the calculation.

2.2.2 Discrete Forcing: Linear Reconstruction

The fundamental philosophy of immersed boundary methods can be demonstrated by considering the following special case, in which the immersed boundary (Ψ) coincides with an Eulerian (fluid) grid point, on which a Dirichlet boundary condition (u_Ψ) must be enforced. Now, consider a slightly modified form of Eq. 2.19 that is written for the boundary point itself, in which a forcing term f_i^k is added for this demonstration case.

$$\frac{\widehat{u}^k - u^{k-1}}{\Delta t} = \gamma_k A\left(u^{k-1}\right) + \rho_k A\left(u^{k-2}\right) - \alpha_k \xi_r \frac{\delta p^k}{\delta \xi} + f_i^k \tag{2.54}$$

The magnitude of the forcing term needed at this point which will satisfy the Dirichlet boundary condition can be found by setting $\widehat{u}^k = u_\Psi$ and solving for f_i^k from Eq.2.54. The result is

$$f_i^k = \frac{u_\Psi - u^{k-1}}{\Delta t} - RHS^k \tag{2.55}$$

For the explicit fractional-step approach presented, the use of f_i^k in Eq. 2.55 enforces the proper boundary conditions on the predicted velocity $\widehat{u}^k$ (e.g., substitution of 2.55 into 2.54 will yield $\widehat{u}^k = u_\Psi$). This approach does not compromise the overall temporal accuracy of the splitting scheme; u^k will satisfy the boundary condition to the order of Δt^2 as described in Kim *et al.* [54].

The evaluation of f_i^k for the immersed boundary formulation presents a specific problem when the implicit time-advancement scheme is used. The momentum forcing f_i^k can no longer be obtained from the provisional velocity field $\widehat{u}$, which was obtained using the explicit approach outlined in the previous section. This is why the momentum forcing term is omitted in these equations above (2.2, 2.13, 2.14, 2.15). A solution has been proposed by Kim *et al.* [54], in which a provisional explicit step is added for the evaluation of f_i^k, which uses the RK3 approach for A_i and a forward Euler scheme for B_i in the above equations:

$$\frac{\widehat{u}^k - u^{k-1}}{\Delta t} = \gamma_k A\left(u^{k-1}\right) + \rho_k A\left(u^{k-2}\right) + \alpha_k B\left(u^{k-1}\right) - \alpha_k \xi_r \frac{\delta p^k}{\delta \xi} + f_i^k \tag{2.56}$$

This implementation works well and is applied within the code.

For the purpose of clarification, the above idealized example rarely occurs in practice, e.g., the interface rarely coincides with an Eulerian grid point. Thus, in this work and several others (Yang [112], Balaras [9], Gilmanov *et al.* [40]) the immersed boundary approach is implemented by using known information from the boundary condition on the interface and the fluid to "force" the velocity components at Eulerian points which have at least one neighbor in the solid phase, and have been previously referred to as forcing points. This forcing procedure involves an interpolation scheme to "force" the velocity (u, v, w) to be what is needed to satisfy the boundary condition at the interface.

A successful, robust implementation has been proposed by Balaras [9], in which the interpolation has been performed along a well-defined line normal to the boundary. Additionally, Yang [112] has extended the approach of Balaras [9] by applying a compact interpolation scheme in the normal direction to the boundary which is better suited to problems with moving immersed boundaries and allows efficient parallelization of the solver.

Some preliminary validation cases for the flow over a smooth sphere were calculated with reasonable success using the scheme reported in Balaras [9] (results are reported in 3.3). Application of this approach to an immersed object with complex geometry (e.g., the dimpled surface of a golf ball) proved troublesome, however. The definition of the line normal to the wall (along which interpolation was performed) would overlap with another line normal to the wall when the interface geometry became concave (as in a dimple).

The reconstruction scheme used in the present work is similar to those introduced above, but eliminates the overlapping problem by applying a linear interpolation along a gridline. As will be demonstrated in Chapter 3, this proposed reconstruction approach is as accurate, robust and stable as the methods proposed in Balaras [9] and Yang [112]. In the current work, a linear interpolation is applied in either the radial or axial direction. The selection of the interpolation direction is based on the minimum distance between the forcing point and the intersection with immersed body itself, as discussed above in 2.2.1. Therefore, for a given forcing point, the minimum distance (along either the radial or axial gridline) to an intersection with the immersed body is the metric needed for selection of the interpolation direction. Once the direction of interpolation is known, a one-dimensional, linear interpolation in the direction of the gridline is applied to the forcing point using information from the intersection point on the immersed body and information from the next Eulerian (fluid) point. This approach is illustrated in Figure 2.6.

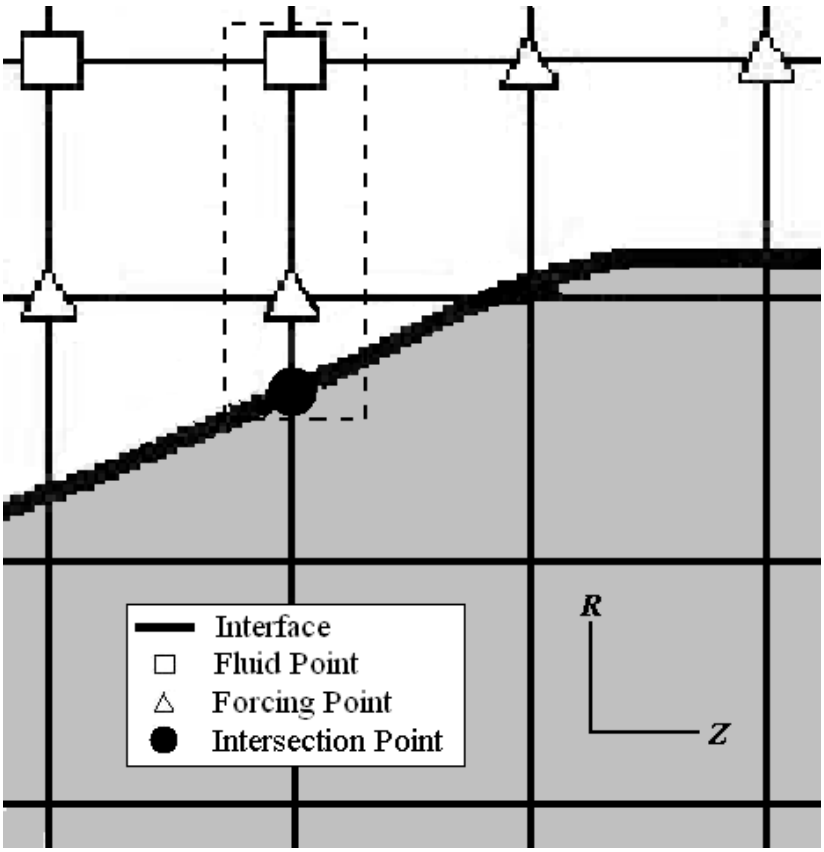

Figure 2.6: Reconstruction scheme at a forcing point. Discrete forcing uses a stencil of two points (the fluid and intersection points) to obtain the value of the velocity field at the forcing point.

The dashed rectangle around the fluid point, forcing point, and intersection point represents the selected interpolation. The direction of interpolation is the radial direction, **R**, since the smallest distance between the boxed forcing point and the interface is in the radial direction. The coefficients for this linear interpolation can be computed as follows: if we assume that any variable in the R direction can be represented as,

$$\phi = b_1 + b_2 x \tag{2.57}$$

The coefficients b_1 and b_2 in Eq. 2.57 can be found by solving the system of equations in Eq. 2.58:

$$\begin{bmatrix} \phi_1 \\ \phi_2 \end{bmatrix} = \begin{bmatrix} 1 & x_1 \\ 1 & x_0 \end{bmatrix} \begin{bmatrix} b_1 \\ b_2 \end{bmatrix} \tag{2.58}$$

where (x_0, x_1) are the R direction coordinates of the fluid point and the intersection point used in the stencil shown in Figure 2.6. The inversion of the 2×2 matrix on the right-hand side of equation 2.58 will yield the solution at the forcing point. As previously mentioned, calculation of the flow over a stationary immersed body requires this step to be performed only once, at the beginning of the calculation. The interpolation stencils are then saved once for each forcing point, and referenced in the code at each time step. This linear reconstruction scheme is both stable and robust, and therefore it has been used for simulations of the flow over a golf ball which are reported in Chapters 4 and 5.

2.2.3 Discrete Forcing: Quadratic Reconstruction

To complement the linear reconstruction scheme presented in Section 2.2.2, a quadratic reconstruction scheme has been proposed by Beratlis [13]. This approach is based on a reconstruction along the local normal, and thus the expression for a variable (*phi*) at the forcing point is comprised of a normal and tangential component (reference eqs. 2.59, 2.60). Here, x_n represents the direction that points outward normally from the wall, while u_t and u_n are the tangential and wall normal velocity components. The coefficients (a_n,a_t), (b_n,b_t), and (c_n,c_t) are to be determined.

$$\phi_t(x_n) = a_t \cdot {x_n}^2 + b_t \cdot x_n + c_t \tag{2.59}$$

$$\phi_n(x_n) = a_n \cdot {x_n}^2 + b_n \cdot x_n + c_n \tag{2.60}$$

In order to solve for the coefficients, three boundary conditions are needed for each equation. The first boundary condition is the velocity at the surface of the immersed boundary. Then, values of the solution at two fluid points along the outward normal are used as boundary conditions. Following Beratlis [13], the boundary conditions can be written as (see eqs. 2.61, 2.62). Here ${\phi_t}^b$ and ${\phi_n}^b$ are the tangential and normal components of the velocity at the surface of the immersed boundary. The variables dF_1 and dF_2 are the extension distances from the immersed body outward along the normal direction for two different velocity stencil points.

$$\phi_t(x_n = 0) = {\phi_t}^b, \quad \phi_t(x_n = dF_1) = \phi_{t1}, \quad \phi_t(x_n = dF_2) = \phi_{t2} \tag{2.61}$$

$$\phi_n(x_n = 0) = {\phi_n}^b, \quad \phi_n(x_n = dF_1) = \phi_{n1}, \quad \phi_n(x_n = dF_2) = \phi_{n2} \tag{2.62}$$

Applying the boundary conditions to equations 2.59 and 2.60 produces the resulting system of equations (see eq. 2.63, 2.64).

$$\begin{bmatrix} dF_1 & {dF_1}^2 \\ dF_2 & {dF_2}^2 \end{bmatrix} \begin{bmatrix} b_t \\ a_t \end{bmatrix} = \begin{bmatrix} \phi_{t1} - {\phi_t}^b \\ \phi_{t2} - {\phi_t}^b \end{bmatrix} \tag{2.63}$$

$$\begin{bmatrix} dF_1 & {dF_1}^2 \\ dF_2 & {dF_2}^2 \end{bmatrix} \begin{bmatrix} b_n \\ a_n \end{bmatrix} = \begin{bmatrix} \phi_{n1} - {\phi_n}^b \\ \phi_{n2} - {\phi_n}^b \end{bmatrix} \tag{2.64}$$

The coeffients can be calculated by taking the inverse of the 2×2 matrices on the left-hand side of equations 2.63 and 2.64, and once they are known the velocity values at the forcing point can be determined analytically using the distance from the immersed boundary to the forcing point as the input for equations 2.59 and 2.60.

The approach is displayed graphically in Figure 2.7. This quadratic reconstruction is based on two Dirichlet conditions for the velocity at the two stencil points shown in Figure 2.7. It is also possible to create a scheme which uses a Neumann

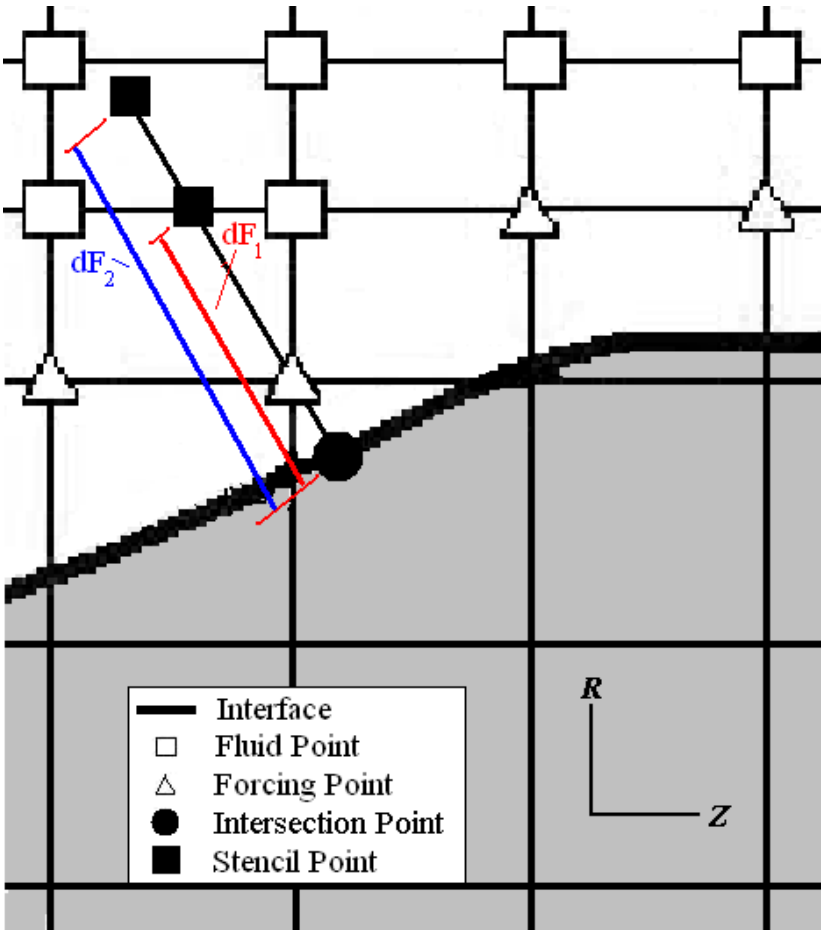

Figure 2.7: Quadratic reconstruction scheme along the local normal: velocities at the stencil points in the fluid and at the immersed boundary are used to derive the coefficients for a quadratic representation of the velocity along the normal. Once the coefficients are known, the forcing point value is solved using the distance between the forcing point and the immersed boundary.

boundary condition at the outermost stencil point as reported in Beratlis [13]. Both variations of the quadratic approach provide improvements over a linear reconstruction scheme in terms of the local order of the interpolation polynomial. This quadratic reconstruction method was validated as reported in Beratlis [13], and was used for the simulations of the golf ball reported in Chapter 6.

2.2.4 *Moving immersed boundaries*

In the case of a moving immersed body, the tagging process is repeated at each timestep. In addition, another set of points is introduced for the field-extension treatment, which is shown in Figure 2.8(a). As in the previous discussion, the Eulerian grid points are classified into three groups: field-extension points (grid points in the solid which have at least one neighbor in the fluid phase), solid points (which comprise the rest of the points inside the body), and fluid points (the points outside the body in the fluid phase). In the case of a moving body, the solution at the field-extension points is extrapolated using the the intersection point and the closest neighboring point in the fluid. The proper treatment of the forcing points (points in the fluid phase closest to the interface) and the field-extension points (points in the solid phase closest to the interface) is critical to the successful implementation of this immersed boundary method for moving bodies.

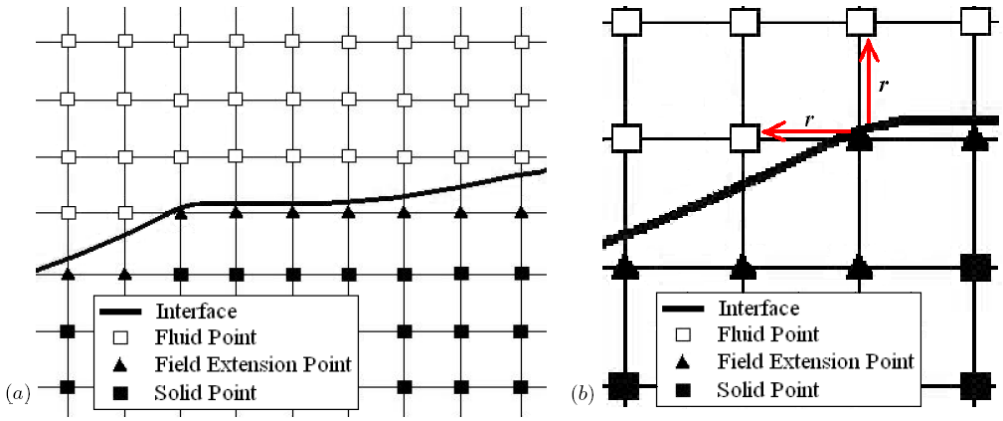

Figure 2.8: Interface-Grid relationship (*a*) Field Extension Tagging; (*b*) Field Extension Intersections.

The algorithm for the treatment of stationary immersed bodies outlined above in Sections 2.2.1, 2.2.2 and 2.2.3 is directly applicable to moving immersed body problems, provided that the interface-grid relationship and the forcing point reconstruction are re-calculated each time the location of the interface is updated. This

requirement imposes certain computational costs, as the search for intersections with the interface involves looping through all the vertices on the body at each substep. Initial estimates indicated that it could be nearly 1 and a half times as much as the current cost per time step. A promising alternative is the application of an optimized searching algorithm known as the Approximate Nearest Neighbor (ANN) libraries (Arya *et al.* [6]). This algorithm is a type of KD-tree searching approach, and is highly optimized for speed. In the current work, the approach has been implemented as follows:

1. Specify a narrow band of Eulerian grid points(base on the known location of the body) in which to search.

2. Initialize a small set of "neighbor" Eulerian grid points which are near each Eulerian point in the narrow band.

3. Search these gridpoints using ANN to determine the interface-grid relationship (tagging, reference Section 2.2.1).

4. Initialize a small set of "neighbor" triangles on the surface of the interface which are near the established forcing points.

5. Search these triangles with ANN to find an intersection point along a gridline as in 2.2.2.

6. Establish the reconstruction stencil (as detailed above in 2.2.2).

Additionally, moving boundary problems often pose certain complications which are typically related to the time-advancement scheme. A specific problem is the fact that the Eulerian grid points near the immersed boundary can change from fluid points to forcing points, and vice-versa as the solid immersed body moves through grid. In the present study, the RHS of the momentum equation must be evaluated

at each Runge-Kutta substep k, requiring that the velocity and pressure (as well as their derivatives) at the previous substep $(k-1)$ have physical values (see Eq.s 2.27, 2.28, 2.29) at all fluid points. Since the interface changes locations at each substep, it is possible that some of the required derivatives are not physical, as they involve points from the solid phase. These unphysical values can induce large errors in the pressure and the vorticity fields.

This problem has been addressed successfully in Yang & Balaras [113], and a similar implementation is used here. The proposed solution is known as "field extension", in which the velocity and pressure fields are "extended" into the solid phase at the end of each substep. In the code, this implies that the velocity components are extrapolated onto the field-extension points mentioned above in 2.2.1. The pressure field is also extended into the solid domain in regions where the solution is unphysical, so that not only the velocity and pressure, but also their derivatives, will have physical values at the forcing points at substep $k-1$, thus eliminating problems with calculation of the RHS in the next substep. The value of the velocity at the field-extension points is reconstructed using a similar approach to that developed in 2.2.2. This reconstruction procedure uses information from the closest point on the interface along a gridline, as discussed in 2.2.1. Additionally, the reconstruction also uses information from the next point in the fluid phase along that particular gridline. This methodology is illustrated in Figure 2.9.

The dashed rectangle around the fluid point, field extension point, and intersection point represents the selected extrapolation. The direction of extrapolation is the radial direction, **R**, since the smallest distance between the boxed forcing point and the interface is in the radial direction. The stencil is formed in the same manner as outlined above in 2.2.2. This approach uses known values of the velocity and pressure on the interface and in the fluid to extrapolate onto the field extension point. The application of the ANN algorithm for the field extension points is

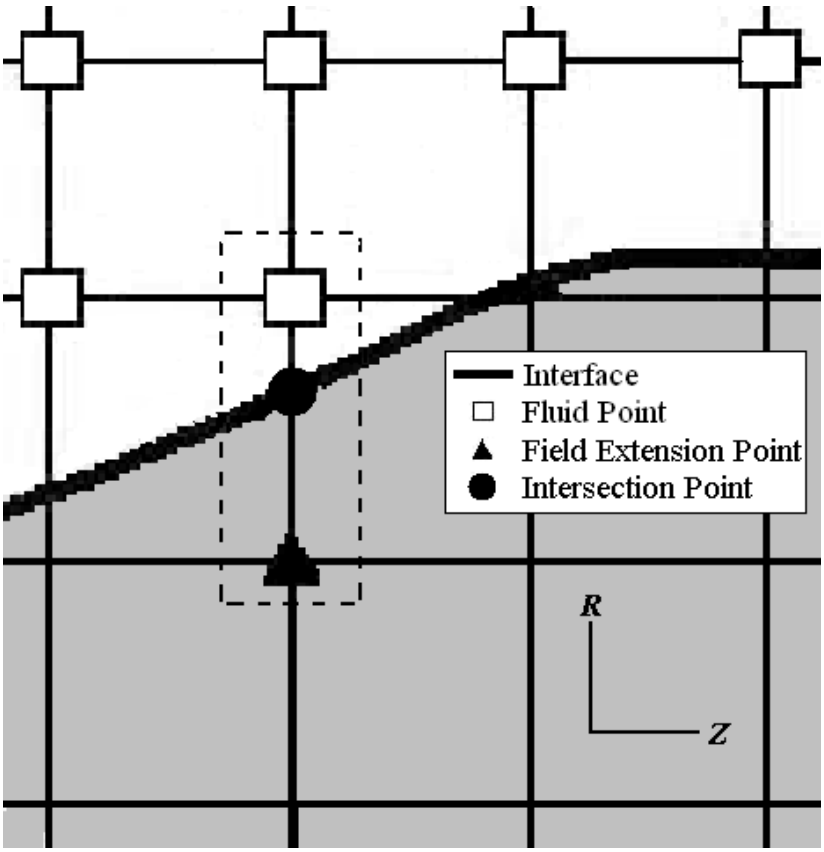

Figure 2.9: Extrapolation at a Field Extension Point. Discrete forcing uses a stencil of two points (the fluid and intersection points) to obtain the value of the velocity field at the field-extension point.

straightforward, and a simple search can be conducted in a narrow band of Eulerian grid points near the interface in order to establish the reconstruction scheme.

2.3 Parallelization: Flow Solver

Since the grid size increases exponentially with the Reynolds number, the flow solver has been parallelized to maintain decent performance with large grids across multiple processors. This parallelization was accomplished by previous workers (Beratlis [12]) and used to obtain results for a variety of flows reported in Balaras & Yang [10] and Beratlis *et al.* [14]. However, the present application of this parallel scheme presented new challenges, as its performance across hundreds of processors

was untested. Herein are details of how linear parallel performance was preserved for large simulations using more than 500 processors.

2.3.1 Implementation

The parallelization is implemented using a classical domain decomposition approach. Message passing interface (MPI) is used for the communication. To minimize the amount of communication needed, the domain decomposition is applied in the direction with the most points, which is typically the streamwise direction. Figure 2.10 shows a sample domain decomposition in the streamwise (Z) direction.

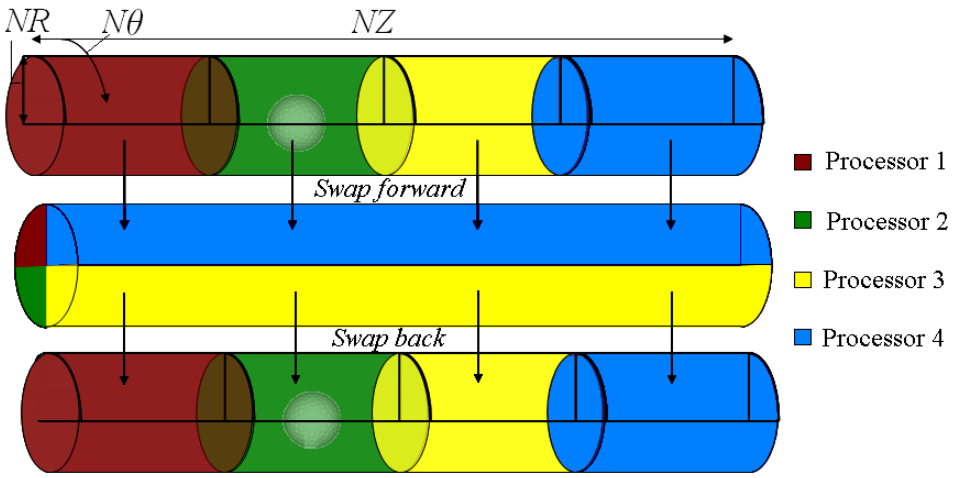

Figure 2.10: Domain decomposition approach for the flow solver. A swap into the slice decomposition is required for the direct solution of the pressure Poisson equation.

Each block is equally sized, which allows for optimum load balancing. Ghost cells are implemented at the block boundaries to account for the needed information from neighboring blocks. The message-passing scheme at the block boundaries is illustrated in Figure 2.11. Since a second-order central difference scheme is used for all spatial discretizations, only one layer of ghost cells is needed at the block boundary.

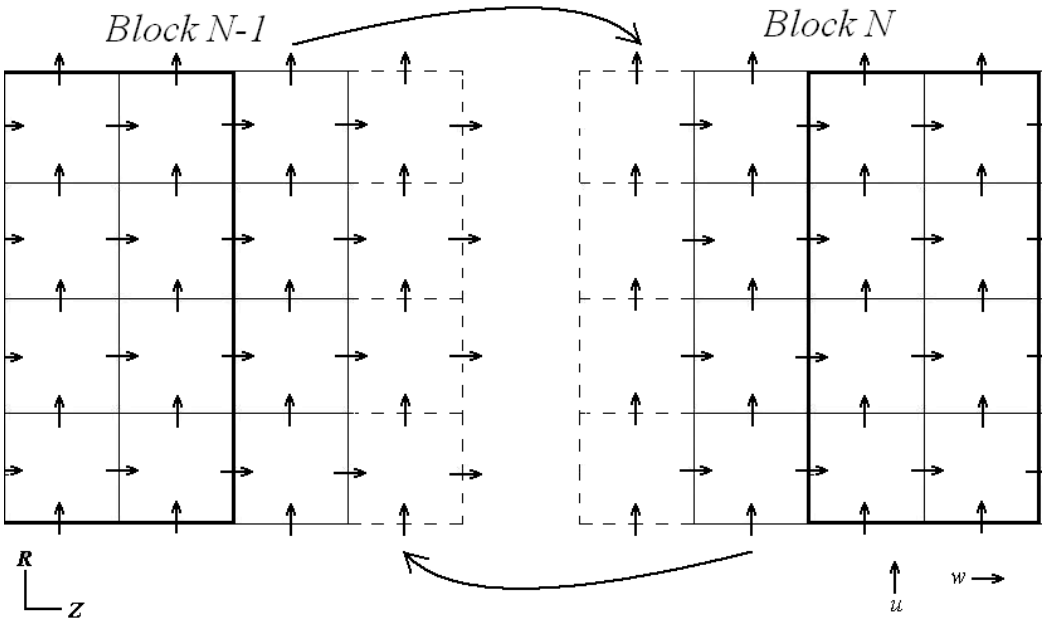

Figure 2.11: Ghost cell approach for parallel implementation (slab or slice decomposition). Only one layer of ghost cells is required due to central differencing scheme.

Typically, the most expensive part of a Navier-Stokes solver is the solution of the pressure Poisson equation. In the current work, the computational grid is always uniform in the azimuthal direction, thus allowing a fast Fourier transform (FFT) to be applied to the Poisson equation in the azimuthal (θ) direction, providing a series of decoupled, two-dimensional equations in wavenumber space that can be directly solved in one iteration using the direct solver from FISHPACK (Swarztrauber [97]). This implementation of the direct solver requires global communication, in which the domain decomposition is changed from block decomposition in the Z direction to block decomposition in the θ direction, which is illustrated in Figure 2.10. The blocks in the Z direction are swapped and become blocks in the θ direction instead. Furthermore, after solution of the Poisson equation, these blocks must be swapped back to the original domain decomposition in the Z direction.

2.3.2 *Performance*

The parallel performance of this immersed boundary approach has been tested on the *Saguaro* high performance computing cluster at Arizona State University. *Saguaro* is comprised of 5000 Intel Xeon EM64T processors. Each node has 8 cores and at least 16 gigabytes of RAM (some have 24 gigabytes); communication between the nodes is conducted via Infiniband high speed interconnects from Cisco.

Prelminary profiling of the solver was conducted using the Java-based commercial visualization tool called JUMPSHOT. The code is compiled with certain flags that track the parallel communication when the code runs. The primary objective was to assess the most costly portions of the code so that an optimal parallel scheme could be achieved. A plot from the JUMPSHOT tool is shown below in Figure 2.12.

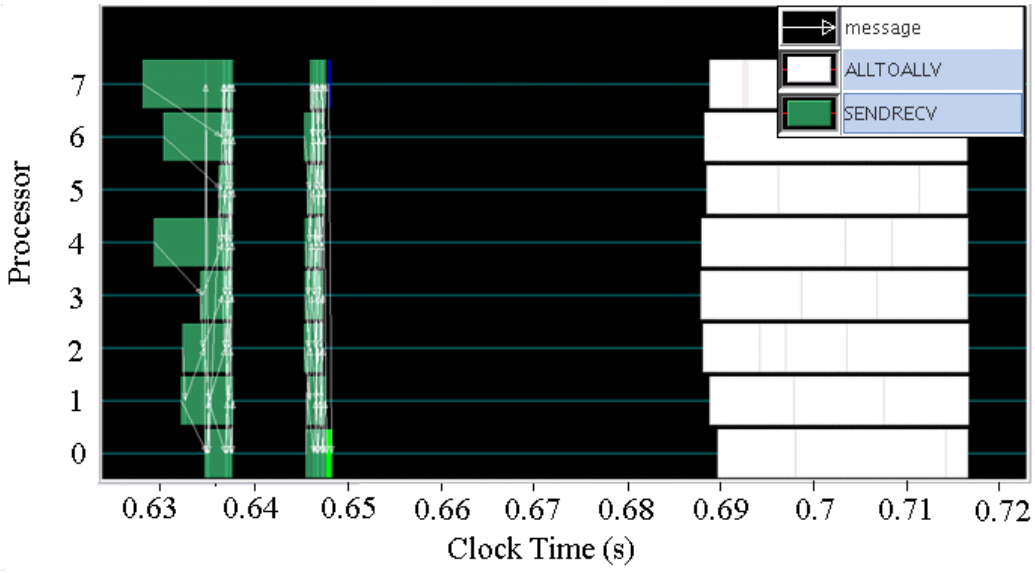

Figure 2.12: Clock time of eight processors calling $MPI\_ALLTOALLV$ in the Poisson solver at one RK3 substep.

Each of the eight processes is visualized on the vertical axis, and clock time is plotted on the horizontal axis. This particular plot is a detail view of the call to the Poisson solver at one Runge-Kutta substep. As mentioned above, the Poisson

solver is typically the most costly portion of the code, which is confirmed by the JUMPSHOT plot in Figure 2.12, but the latency is primarily caused by unstable behavior of the collective call $MPI\_ALLTOALLV$.

Collective MPI communication calls, such as $MPI\_ALLTOALLV$, have shown decent performance when grid sizes are less than 100 million points; e.g., the solver demonstrates linear scaling across processors. However, as the grid sizes increase with increasing Reynolds numbers, $MPI\_ALLTOALLV$ becomes unstable in terms of its timing performance.

In order to overcome this computational penalty, an alternative has been implemented by applying a set of $MPI\_SENDRECV$ calls for the domain decomposition swap from the Z to the θ direction. For the calculations conducted using a stationary immersed body, the code has demonstrated **linear scaling**, as shown by the representative plot in Figure 2.13.

Scalability in parallel computing can be subdivided into two categories: strong scaling and weak scaling. Strong scaling implies that the computational cost of the solution is reduced when the problem size is constant and the number of processors increases. Weak scaling means that the computational cost of the solution remains constant when the problem size and number of processors are increased by the same factor.

1. **Strong scaling**: For a fixed grid size, doubling the number of processors used to compute the solution produces a factor-of-two reduction in the cost.

2. **Weak scaling**: Increasing both the grid size AND number of processors by a constant factor produces a computational cost that remains constant.

This has been verified by monitoring the computational timing of the code for a range of grid sizes. As shown in Table 2.1, both strong and weak linear scaling

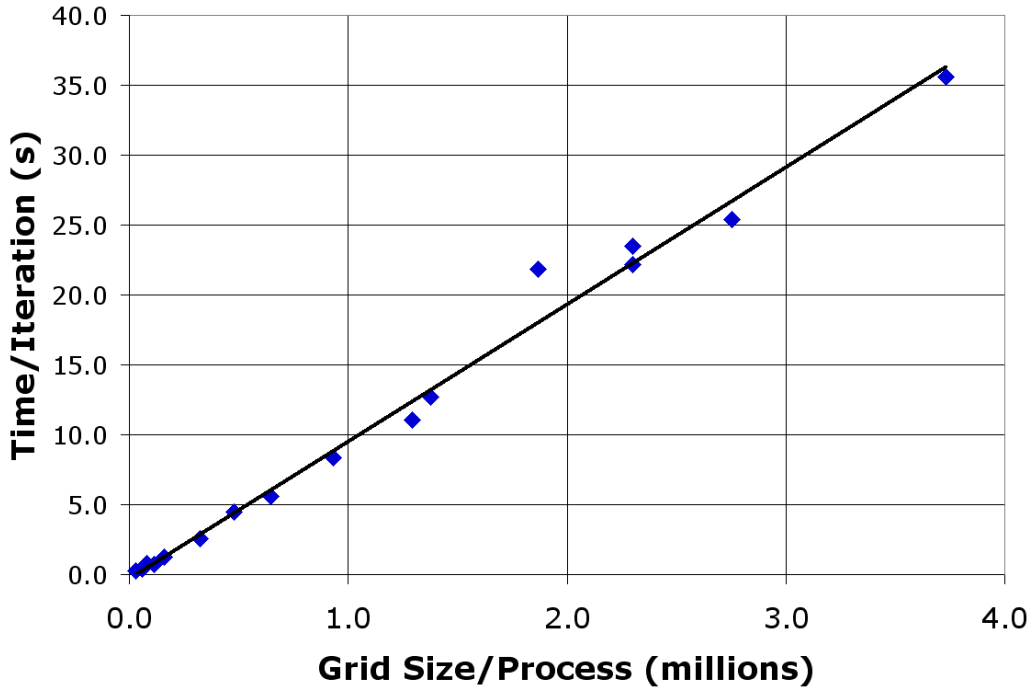

Figure 2.13: Grid size per processor versus averaged iteration time: slab decomposition of the flow solver with linear discrete-forcing immersed boundary scheme. $\diamond$ Flow solver performance; – Ideal linear scaling.

are present. Examples of strong scaling would be the results from the 5.2×10^6 grid points and 30×10^6 grid points models. For a fixed problem size at 5.2 million points, the computational cost (time per iteration) decreased from 11.1 seconds on 4 processors to 5.6 seconds on 8 processors, and then decreased again to 2.5 seconds on 16 processors. The reduction in the time per iteration followed an approximate factor-of-two decreasing trend as the number of processors increased from 4 to 16. Similar results are observed for the 30 million points model; as the number of processors is doubled from 8 to 16, and then from 16 to 32, there is an accompanying reduction in the time per iteration.

Some results in Table 2.1 also demonstrate weak scaling behavior. For instance, increasing the grid size from 575×10^6 points to 1.2×10^9 points (an increase by a factor of two) in conjunction with doubling the number of processors from 250

Table 2.1: Strong and Weak Linear scaling results: slab decomposition of the Navier-Stokes solver with the linear discrete-forcing immersed boundary scheme.

Grid Points	Processors	Grid Points/Process	Time/Iteration (s)
0.5 million	4	0.10 million	0.7
0.5 million	8	0.06 million	0.4
0.5 million	16	0.03 million	0.3
5.2 million	4	1.30 million	11.1
5.2 million	8	0.60 million	5.6
5.2 million	16	0.30 million	2.5
5.2 million	32	0.15 million	1.2
30 million	8	3.70 million	35.6
30 million	16	1.90 million	21.8
30 million	32	0.90 million	8.4
60 million	125	0.48 million	4.5
172 million	125	1.38 million	12.7
337 million	125	2.75 million	25.4
575 million	250	2.30 million	22.2
1.2 billion	500	2.30 million	23.5

to 500 produces approximately constant values for the computational cost (time per iteration). Thus, since the flow solver exhibits both strong and weak scaling performance for grids as large as 1.2×10^9 points, it has been used for all of the simulations in the current work.

2.4 Parallelization: Interface-Tracking

As discussed above in Section 2.2.4, the computational cost in the case of a moving immersed boundary is substantial. The primary cause is the implementation of interface-tracking at each of the three Runge-Kutta substeps (since the immersed

body moves at each of these substeps). The addition of the Approximate Nearest Neighbor (ANN) libraries (Arya *et al.* [6]) presented in the current work has greatly reduced the cost associated with the search for ray-intersections between each forcing point and the immersed boundary, and has produced large increases in performance.

Preliminary scaling analysis of the interface-tracking algorithm (via ANN) coupled with the flow slover indicates that this performance improvement is significant for problem sizes in which the number of grid points, and thus, the number of processors required are few (on the order of 2 or 4). Scaling analysis reveals that the performance actually decreases for a certain grid size as the number of processors increases. Thus, the algorithm runs progressively slower as the number of processors increases. This is effectively demonstrated in Figure 2.14, where the grid size per processor is held constant, but the number of processors increases, leading to a startling slowdown.

2.4.1 Implementation

The reason for this decrease in performance is related to the domain decomposition approach used for the flow solver: a "slab" decomposition in the streamwise (Z) direction. Each processor has a portion of the domain divided up along the streamwise direction (shown in Figure 2.10), which implies that not every processor's Z-coordinates will correspond to the Z-coordinates of the immersed body; e.g., only a few processors will actually perform the majority of the work needed to complete the interface-tracking at each substep. The algorithm is designed to have all processors call the subroutines which do the interface-tracking, but this is trivial if the Z-coordinates of the Eulerian (fluid) grid do not "contain" the Z-coordinates of the Lagrangian (immersed body) grid. This imbalance of work among the processors in the parallel decomposition is the direct cause of the decrease in performance,

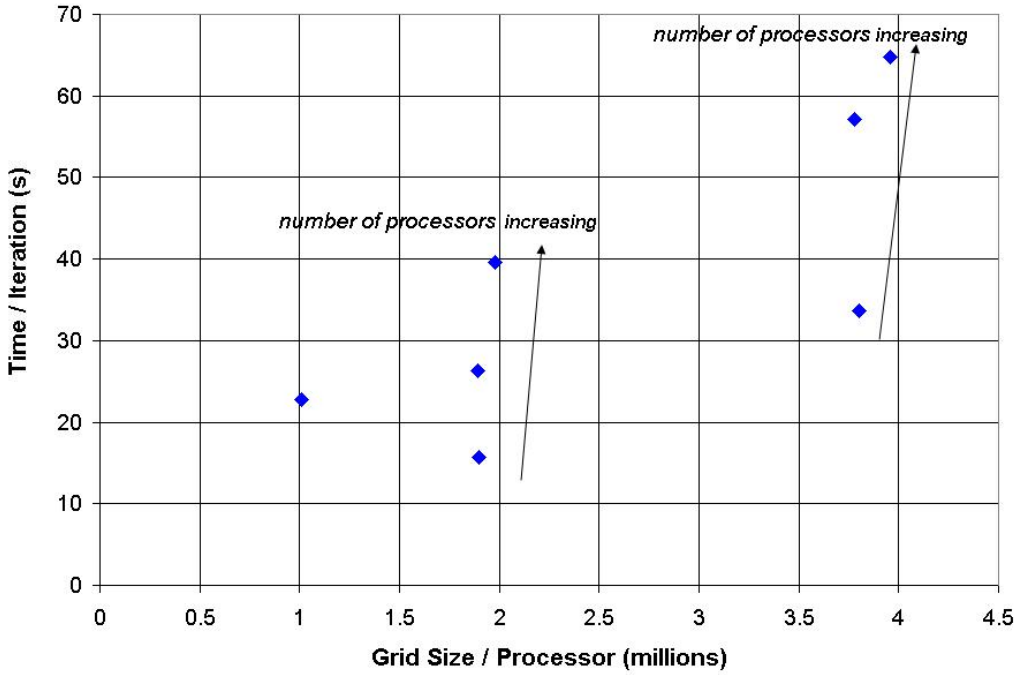

Figure 2.14: Grid size per processor versus averaged iteration time for moving immersed boundary: slab decomposition of the flow solver with the linear discrete-forcing immersed boundary scheme. ⋄ Flow solver performance without parallelized interface-tracking scheme.

notwithstanding the performance increase gained with the implementation of the ANN search algorithm. Therefore, in order to proceed with calculation of the solution on large grids at high Reynolds numbers (with large processor counts), a reorganization of the domain decomposition for the interface-tracking algorithm is required, in which the computational work done by each of the tagging routines will be distributed evenly across all processors.

In an effort to evenly divide the work required for the interface-tracking across processors, the domain decomposition is organized in the azimuthal (θ) direction. Using this approach, each process now has an even "slice" of the domain along the azimuth. This approach is displayed below in Figure 2.15. Organization of the domain decomposition for the interface-tracking requires that the results of the

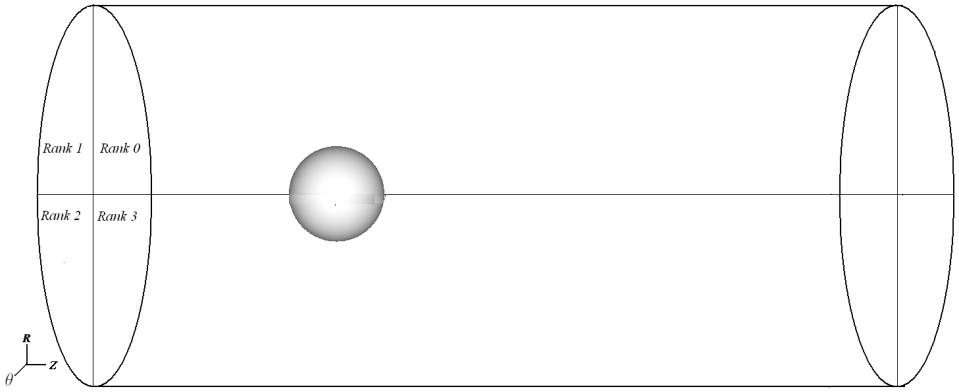

Figure 2.15: Slice (azimuthal) domain decomposition for the parallelization of the interface-tracking scheme.

interface-tracking algorithm (the outputs) be mapped back to the domain decomposition of the flow solver (the slab decomposition in the streamwise direction). This is required because the outputs of the interface-tracking are used in the flow solver to account for the effect of the immersed body in the flow. Message passing interface (MPI) is used for the communication between processes and the forward and reversed mapping steps. The details of this implementation are discussed extensively in Appendix C.

2.4.2 Performance

Once the algorithmic details were applied into the code, the performance of the parallel interface-tracking scheme was tested in conjunction with the parallel scheme already applied to the flow solver. Performance tests were conducted with a simulation of a smooth sphere mesh (comprised of $71,938$ triangles) rotating about the streamwise axis within a fluid grid of 19×10^6 points on the *Saguaro* supercomputer. The new algorithm was tested using as many as 80 processors, and demonstrated strong linear scaling as shown in Figure 2.16 and Table 2.2. As the grid size per processor decreased from 1.9 million points (using 10 processors) to 0.24 million points (on 80 processors) for a fixed total grid size of 19 million points, the time per

iteration decreased (approximately linearly) as well. These results are very promising, and indicate that linear performance is possible even for a moving immersed boundary implementation with the linear discrete-forcing reconstruction.

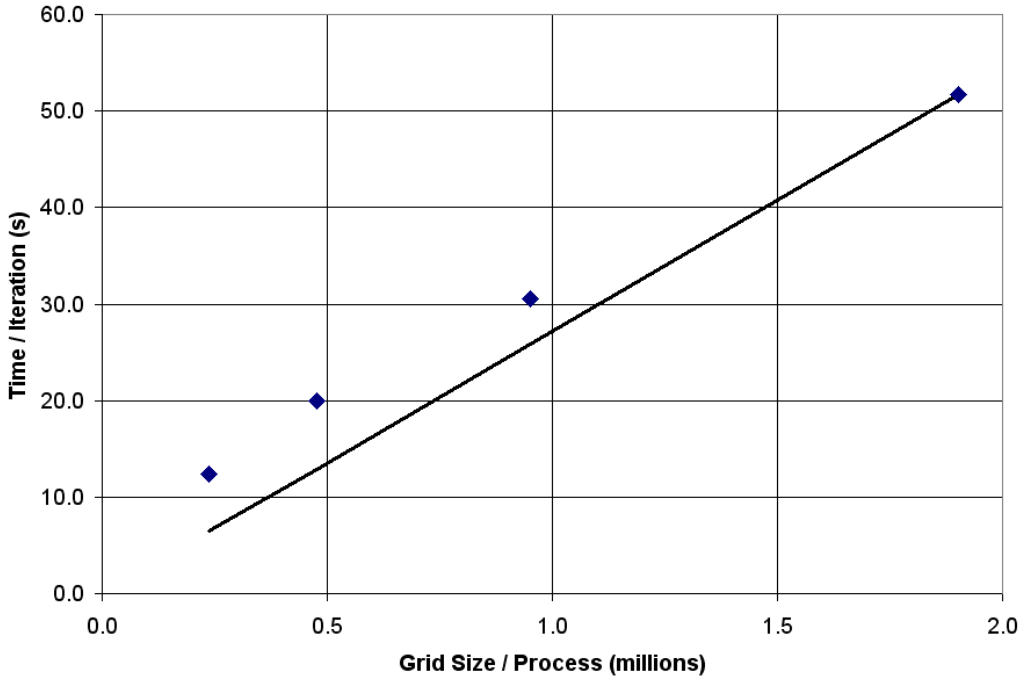

Figure 2.16: Grid size per processor versus averaged iteration time for moving immersed boundary: slab decomposition of the flow solver and slice decomposition of the interface-tracking with the linear discrete-forcing immersed boundary scheme. $\diamond$ Flow solver with parallelized interface-tracking performance; $-$ Ideal linear scaling.

2.5 Calculation of Wall Stress on an Immersed Boundary

In bluff body flows, it is often critical to assess the relative contribution of the pressure drag and the viscous drag. The contribution of each can be understood by integrating the wall stress (which is comprised of the normal stress (pressure) and the shear stress) on the body. Calculation of the wall stress for a flow computed with an immersed boundary method can be challenging. Since the grid does not conform to the body, the fluid stress on the body must be recovered from the Eulerian flow

Table 2.2: Strong Linear scaling results: slab decomposition of the flow solver and slice decomposition of the interface-tracking with the linear discrete-forcing immersed boundary scheme.

Grid Points	Processors	Grid Points/Process	Time/Iteration (s)
19 million	10	1.9 million	51.7
19 million	20	0.95 million	30.5
19 million	40	0.48 million	19.9
19 million	80	0.24 million	12.4

solution. The purpose of this section is to present the method developed by the author for recovering the pressure and shear stress results on an immersed body. A preliminary approach based on a linear extrapolation of the pressure from Eulerian grid points directly onto the body yielded favorable results when compared with available measurements. The method was extended using an interpolation of the Eulerian solution onto the local normal of each triangle on the (Lagrangian) body, and the shear stress results obtained with this method matched well with computations using a body-fitted solver at the same Reynolds number. The validation of the both methods is presented in Chapter 3.

2.5.1 Preliminary reconstruction approach

The preliminary approach for the calculation of the wall stress on an immersed body was applied primarily to the reconstruction of the pressure. The Eulerian values of the pressure in cells near the body were extrapolated directly onto the immersed body using similar ideas as used for the reconstruction of the momentum field at the forcing points. An inverse-distance weighted interpolation was used to calculate pressure values at the vertices of the triangular surface mesh for plotting purposes.

The first step in the reconstruction was to establish the intersection of a ray from the Eulerian points nearest the body (forcing points) to the surface of the body

in the direction of the gridline, as displayed in Figure 2.17. This is accomplished by projecting a ray in the direction of the gridline toward the body, searching the database of the Lagrangian mesh for the closest coordinate points on the surface, then performing a few geometrical tests to see if an intersection between the ray and the body (in particular, the plane of the triangle which the ray intersects) exists.

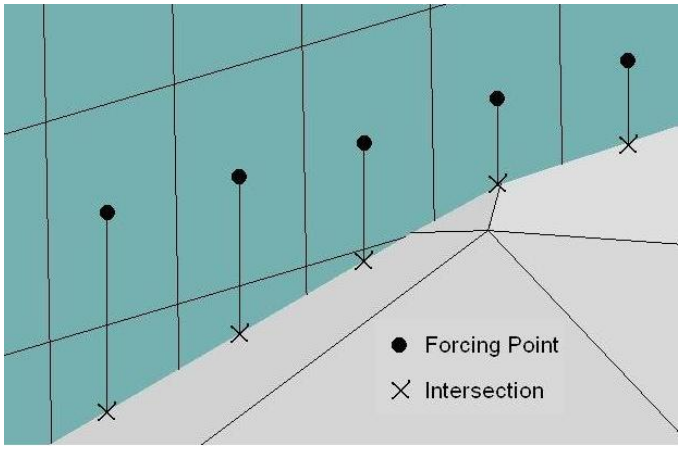

Figure 2.17: Intersection points of ray(s) from the forcing points with the Lagrangian surface. Rays are projected from a forcing point along both gridlines.

Once the Cartesian coordinates of the intersection are established, the pressure is extrapolated onto the body at the intersection point using a stencil comprised of the pressure at the nearest forcing point and the next Eulerian point in the fluid (also in the direction of a gridline). This is illustrated in Figure 2.18.

Since pressure values are now known on the Lagrangian surface at all the extrapolation points, the final step is to organize this information according to the vertices of the triangles which comprise the surface mesh (in order to visualize the result in a post-processing software). This organization step is accomplished by building a searchable data structure which contains coordinates of the extrapolation points. Then, the data structure is queried for the coordinates and indices of five

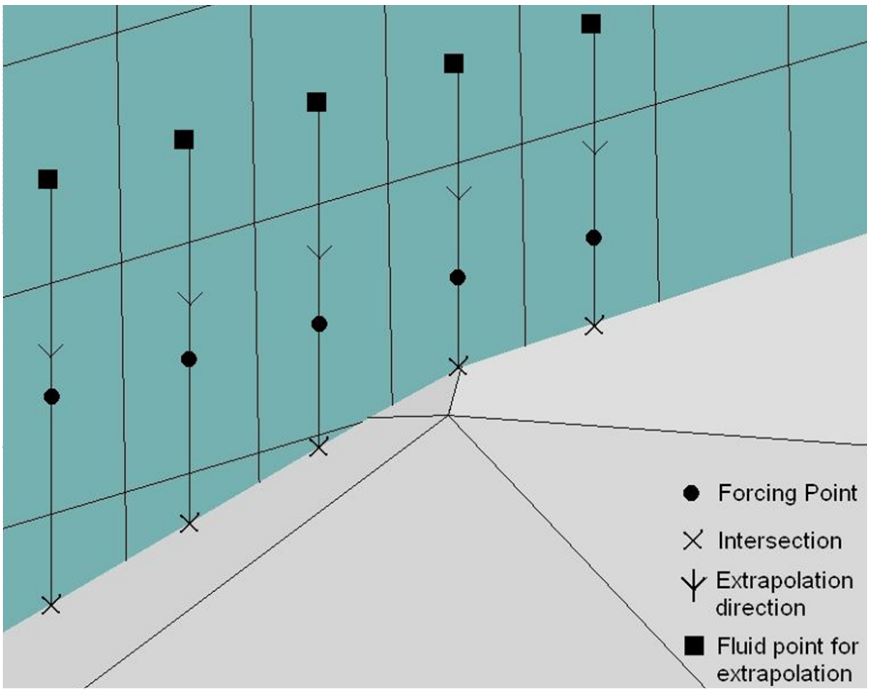

Figure 2.18: One-dimensional reconstruction stencil comprised of a fluid point and a forcing point.

extrapolation points that are nearest to the first triangle vertex (the same process is repeated for all vertices on the Lagrangian surface), as shown in Figure 2.19.

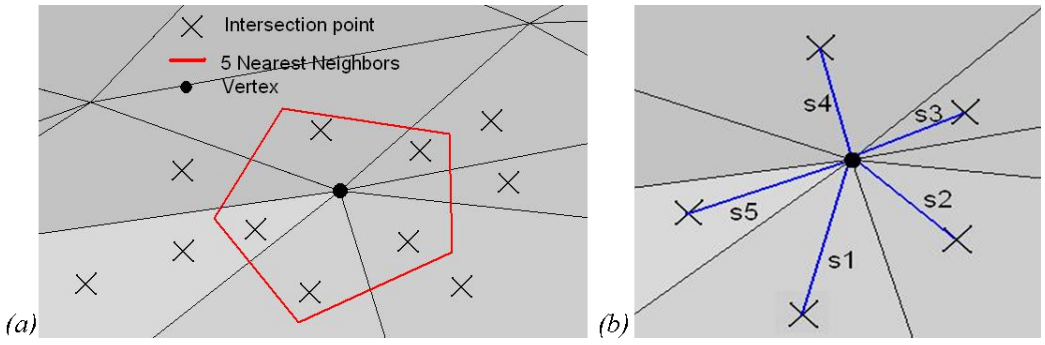

Figure 2.19: (*a*) Triangle vertex with five nearest-neighbors; (*b*) Inverse-distance weighted interpolation at vertices.

Efficient queries are made possible by utilizing the search algorithm in the Approximate Nearest Neighbor (ANN) library (Arya *et al.* [6]). Once the coordinates

and indices of the five nearest neighbors are known, a weighted interpolation of the pressure from the neighbor points to the triangle vertex is applied using the inverse-distance method (Figure 2.19).

Mathematically, the inverse-distance weighted interpolation is implemented by calculating the distance from each of the five neighbors (denoted by the subscript "i") to the vertex in question (subscript "v"). Next, take the inverse of the distance as the weighting coefficient, and compute the value of the pressure (ϕ) at that vertex.

$$s_i = \sqrt{(x_v - x_i)^2 + (y_v - y_i)^2 + (z_v - z_i)^2} \qquad i = 1,2,3,4,5 \tag{2.65}$$

$$a_i = \frac{1}{s_i} \tag{2.66}$$

$$\phi_v = \frac{\sum_{i=1}^{5} a_i \phi_i}{\sum_{i=1}^{5} \phi_i} \tag{2.67}$$

2.5.2 Extended reconstruction approach

An extension of the preliminary reconstruction technique used for the pressure on the Lagrangian surface is presented. This extension is applied for the shear stress. Calculation of the shear stress requires computation of the scalar (dot) product between the stress tensor and the local normal vector at the plane of interest. In general, the plane of interest is each triangle that comprises the surface mesh. Therefore, a reconstruction approach which is based on the Lagrangian mesh is warranted. Since extrapolation is required to reconstruct the solution on the immersed (Lagrangian) surface, pursuing an improvement in the accuracy of the extrapolation is one goal of this extended reconstruction approach. An additional motivation is

to provide more accuracy in the organization of the solution on the Lagrangian surface; namely, in the way that the solution is interpolated to the vertices of surface triangles.

First, two coordinate points outside the immersed body are found by projecting outward along the local normal vector from the centroid of each triangle. The points are separated by a value of Δ, which corresponds to the minimum of the streamwise and radial grid spacings near the Lagrangian body (Figure 2.20).

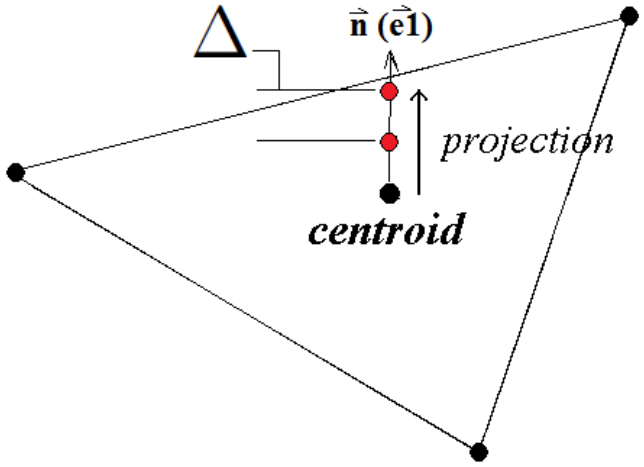

Figure 2.20: Calculation of projected coordinate points along local normal vector using $\Delta = \min(\Delta_x, \Delta_z)$.

Next, the time-averaged Eulerian stress tensor in cylindrical coordinates,

$$\vec{\sigma}_{cyl} = \begin{bmatrix} s_{rr} & s_{r\theta} & s_{rz} \\ s_{\theta r} & s_{\theta\theta} & s_{\theta z} \\ s_{zr} & s_{z\theta} & s_{zz} \end{bmatrix} \tag{2.68}$$

is interpolated onto these points from the surrounding grid cells (see Figure 2.21).

The Eulerian stress tensor is then transformed from cylindrical coordinates to Cartesian coordinates (the coordinate system of the Lagrangian surface). This is accomplished using the transformation matrix $\mathbf{R}$ and its transpose $\mathbf{R}^T$ to pre-multiply and post-multiply the cylindrical coordinates stress tensor.

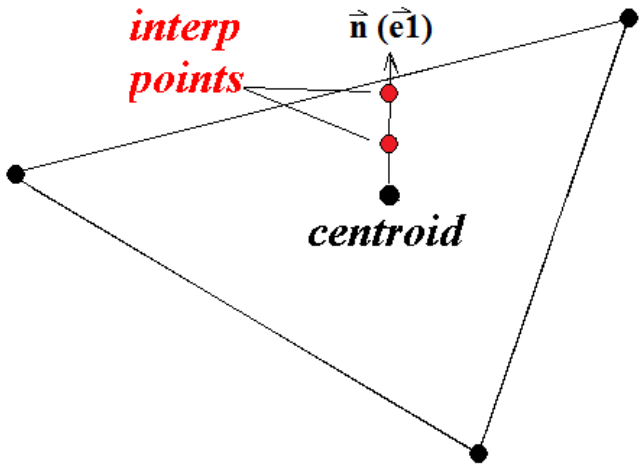

Figure 2.21: Discretized local normal used for interpolation of the stress tensor from surrounding cells.

$$\vec{\sigma}_{cart} = \vec{R}\vec{\sigma}_{cyl}\vec{R}^{T} \tag{2.69}$$

$$\vec{R} = \begin{bmatrix} \cos\theta & -\sin\theta & 0 \\ \sin\theta & \cos\theta & 0 \\ 0 & 0 & 1 \end{bmatrix} \tag{2.70}$$

$$\vec{\sigma}_{cart} = \begin{bmatrix} s_{xx} & s_{xy} & s_{xz} \\ s_{yx} & s_{yy} & s_{yz} \\ s_{zx} & s_{zy} & s_{zz} \end{bmatrix} \tag{2.71}$$

Rather than extrapolating onto an intersection with the Lagrangian surface in the direction of the grid lines, the current approach extrapolates the Eulerian stress tensor onto the centroid of each triangle on the surface in the direction of the local normal vector as illustrated in Figure 2.22.

The shear stress on the surface of a triangle is approximated by calculating the scalar product of the extrapolated stress tensor (at the centroid of each triangle) and

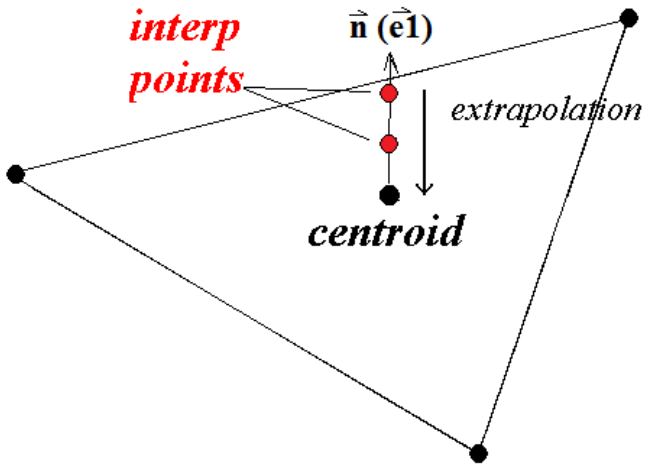

Figure 2.22: Extrapolation using two points onto triangle centroids in the normal direction.

the local normal vector. The scalar product of a second-order tensor with a first-order tensor yields a first-order tensor with components in the x, y, and z directions, which, when properly scaled, represent the shear stress in each of the global Cartesian coordinate directions. Since the preceding operation yields the shear stress at the centroid of each triangle, the final step is to organize the information according to the vertices of the triangles, which is required for visualizations and averaged plots.

$$\vec{\tau}_k = \begin{bmatrix} s_{xx} & s_{xy} & s_{xz} \\ s_{yx} & s_{yy} & s_{yz} \\ s_{zx} & s_{zy} & s_{zz} \end{bmatrix}_k \begin{bmatrix} n_x \\ n_y \\ n_z \end{bmatrix}_k \qquad k = 1,2,3,...,N_{triangles} \tag{2.72}$$

The organization of the shear stress components at the vertices of the surface triangles is accomplished by interpolation. Since an arbitrary vertex is shared by all of the triangles that use it as one of the three necessary vertices, the value of the shear stress at that vertex should take into account the shear stress values in each of the triangles that share it. The index of each surrounding triangle (for an

arbitrary vertex) is found and stored in an integer data structure which is sized by the number of vertices. The data structure is utilized for an inverse-distance weighted interpolation method that is applied to calculate the shear stress components at a vertex using the centroid value of the shear stress from each surrounding triangle. The data structure is constructed using 4 nested loops: an outermost loop over the number of triangles, followed by a loop over the number of vertices per triangle (3). The coordinates of each vertex owned by a certain triangle are then compared with all other vertex coordinates on the Lagrangian body, which involves another loop over the number of triangles and the vertices per triangle. When a match between the x, y, and z components of one vertex with another vertex is found, the index of the triangle with the matching vertex is stored in the data structure to be used later for the inversed distance weighted interpolation.

2.6 Calculation of Momentum Flux through Dimpled Surfaces

Since drag reduction appears to be related to momentum transport near the body, quantification of this effect is critical. In the following section, an approach is presented for calculating the flux of momentum through sampling surfaces. First, the concept of momentum flux is introduced and explained. Next, the actual implementation is discussed. Results using this approach are present in Chapter 6.

2.6.1 Momentum Flux Definition

The term *flux* is commonly in reference to transport phenomena. Mathematically, it is the rate of transfer of a physical quantity across a surface. There are different physical quantities which are dynamic, and thus their motion can be quantified with the concept of flux. This is evident in the many constitutive relationships observed in the study of the physical world. Consider, for example, conservation of mass (2.1), which implies mass flux:

$$\dot{m} = \rho\left(\vec{U}\cdot\vec{n}\right)A \tag{2.73}$$

This expression has units of $[kg/s]$; essentially, the rate of mass transfered across a surface of area A. Another example is the heat conduction equation (Fourier's Law), which implies heat flux:

$$\dot{q} = -kA\frac{\partial T}{\partial x} \tag{2.74}$$

This expression has units of $[J/s]$; essentially, the rate of energy transfered across a surface of area A. Thus, the rate of transfer of momentum across a surface can be quantified in a similar manner.

$$\dot{p} = \left(\rho\vec{U}\right)\left|\vec{U}\cdot\vec{n}\right|A \tag{2.75}$$

In which the units are $[kg\cdot m/s/s]$; the rate of momentum transfered across a surface of area A.

2.6.2 Momentum Flux Approach

First, start with the computed Eulerian velocity solution in cylindrical coordinates.

$$\vec{U} = \begin{bmatrix} u_r \\ v_\theta \\ w_z \end{bmatrix} \tag{2.76}$$

The second step is to define the surface(s) through which the momentum is being transported. This is accomplished by creating a smooth sphere with the same radius as the golf ball. When the smooth sphere is superimposed on the golf ball, it creates a set of surfaces which exactly overlay the dimples. As in the case of the golf ball surface, the spherical surface is composed of triangular elements as shown in Figure 2.23.

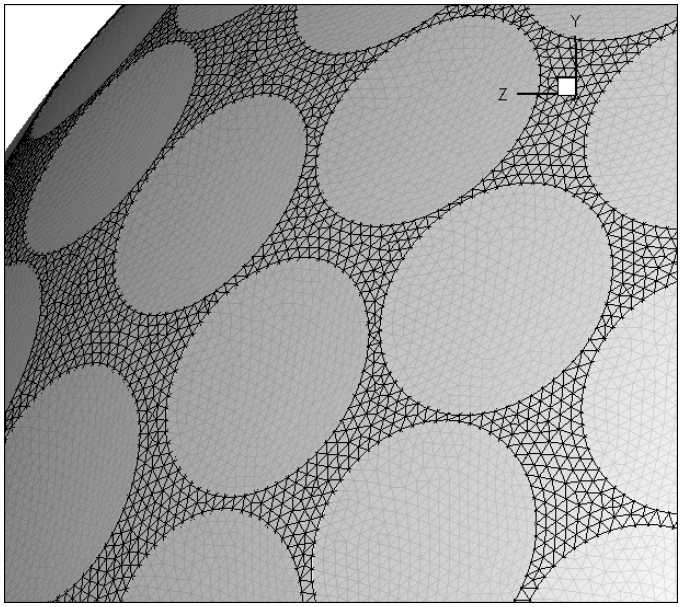

Figure 2.23: Smooth sphere superimposed on golf ball - specification of surfaces for momentum flux calculation.

Third, the Eulerian velocity field is interpolated onto the centroid of each triangle on the spherical (Lagrangian) surface. This is represented in Figure 2.24.

Fourth, the velocity field (now stored at the triangle centroids) is converted to Cartesian coordinates using tensor operations:

$$\vec{U}_{Cartesian} = \vec{R}\vec{U}_{cyl} = \begin{bmatrix} cos\theta & -sin\theta & 0 \\ sin\theta & cos\theta & 0 \\ 0 & 0 & 1 \end{bmatrix} \begin{bmatrix} u_r \\ v_\theta \\ w_z \end{bmatrix} = \begin{bmatrix} u \\ v \\ w \end{bmatrix} \tag{2.77}$$

where $\vec{R}$ is the tensor transformation matrix going from cylindrical coordinates to Cartesian coordinates.

The fifth step involves finding the contribution of the velocity vector in the direction normal to the local triangle; thus, the scalar (dot) product of the (newly-computed) Cartesian velocity vector (stored at the centroid of the local triangle) with the local unit normal vector is computed.

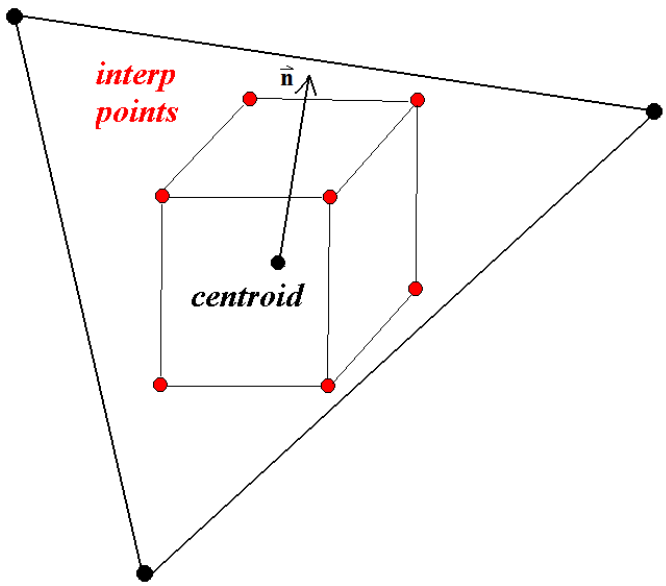

Figure 2.24: Interpolation of the velocity field on local triangle centroids - momentum flux calculation.

$$\vec{U}_{Cartesian} \cdot \vec{n} = \begin{bmatrix} u \\ v \\ w \end{bmatrix} \begin{bmatrix} n_x \\ n_y \\ n_z \end{bmatrix} \tag{2.78}$$

Sixth, the Cartesian velocity field stored at the triangle centroids is converted to spherical coordinates via tensor transformation (see Bower [17]) in equations 2.79 and 2.80. The primary motivation for using spherical coordinates is that the radial (u_r) and axial (v_θ) components of velocity in spherical coordinates align with the flow entering and exiting the dimples on the golf ball. For reference, see Figure 2.25 from Bower [17].

$$\vec{U}_{spherical} = \vec{R}\vec{U}_{Cartesian} = \begin{bmatrix} sin\theta cos\phi & sin\theta sin\phi & cos\theta \\ cos\theta cos\phi & cos\theta sin\phi & -sin\theta \\ -sin\phi & cos\phi & 0 \end{bmatrix} \begin{bmatrix} u \\ v \\ w \end{bmatrix} = \begin{bmatrix} u_r \\ v_\theta \\ w_\phi \end{bmatrix} \tag{2.79}$$

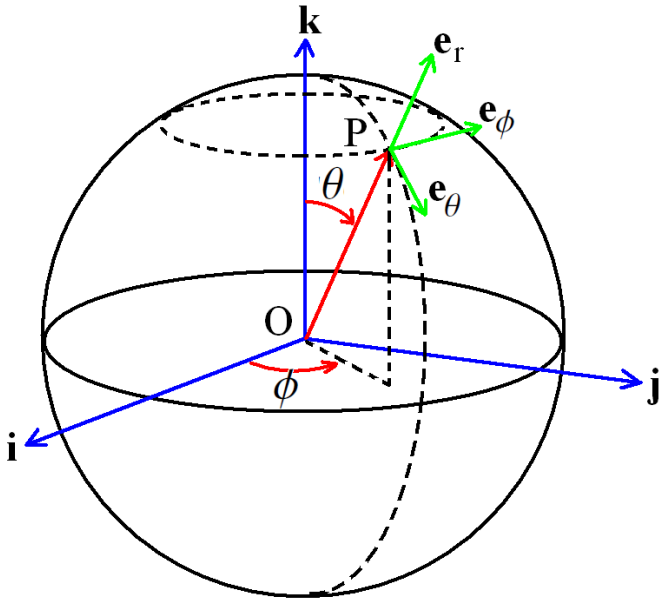

Figure 2.25: Spherical coordinate system from Bower [17] - momentum flux transformation.

$$r = \sqrt{x^2 + y^2 + z^2}, \qquad \theta = cos^{-1}\left(\frac{z}{r}\right), \qquad \phi = tan^{-1}\left(\frac{y}{x}\right) \tag{2.80}$$

The seventh step is to calculate the area of the local triangle (reference equation 2.81). Finally, the components of the momentum flux are calculated as shown in equations 2.82, 2.83, and 2.84.

$$A_{triangle} = \frac{1}{2} base \cdot height \tag{2.81}$$

$$mflux, u_r = u_r \left|\vec{U} \cdot \vec{n}\right| A_{triangle} \tag{2.82}$$

$$mflux, v_\theta = v_\theta \left|\vec{U} \cdot \vec{n}\right| A_{triangle} \tag{2.83}$$

$$mflux, w_\phi = w_\phi \left|\vec{U} \cdot \vec{n}\right| A_{triangle} \tag{2.84}$$

Chapter 3

Verification and Validation

In this Chapter, verification and validation studies are presented. Section 3.1 presents a verification of the accuracy of the method. Section 3.2 verifies convergence of solutions with respect to the grid using the present immersed boundary approach for DNS. Section 3.3 presents a validation of the immersed boundary approach at subcritical Reynolds numbers. Finally, Section 3.4 presents a validation of the post-processing methods discussed in Section 2.5 for reconstruction of the wall stress on an immersed boundary.

3.1 Verification - Formal Accuracy of the Immersed Boundary Method

Though the individual accuracy of the spatial and temporal differencing schemes in the present work are known to be second- and third-order, respectively; the formal, global accuracy of the method must be tested. Therefore, a numerical accuracy study for the present immersed boundary method has been conducted. This test case has been designed with a stationary immersed body in a fixed Eulerian grid. Specfically, a sphere is placed inside a three-dimensional cylindrical domain which is given a rotational velocity of V = 1 (azimuthal velocity) at the outer wall boundary. The computational domain and configuration of the boundary conditions are shown in Figure 3.1.

Computations were performed on four uniform grids: $90\times90\times90$ (*coarse* grid), $150\times150\times150$ (*intermediate* grid), $210\times210\times210$ (*fine* grid), and $270\times270\times270$ (*reference* grid). In this case, the grid refinement was conducted without the typical doubling of the grid points. Since the velocities are solved on a staggered grid, the simulations were designed so that every node on each subsequently coarser grid can be directly located on the reference mesh (see Figure 3.2). This approach alleviates any interpolation error when comparing solutions.

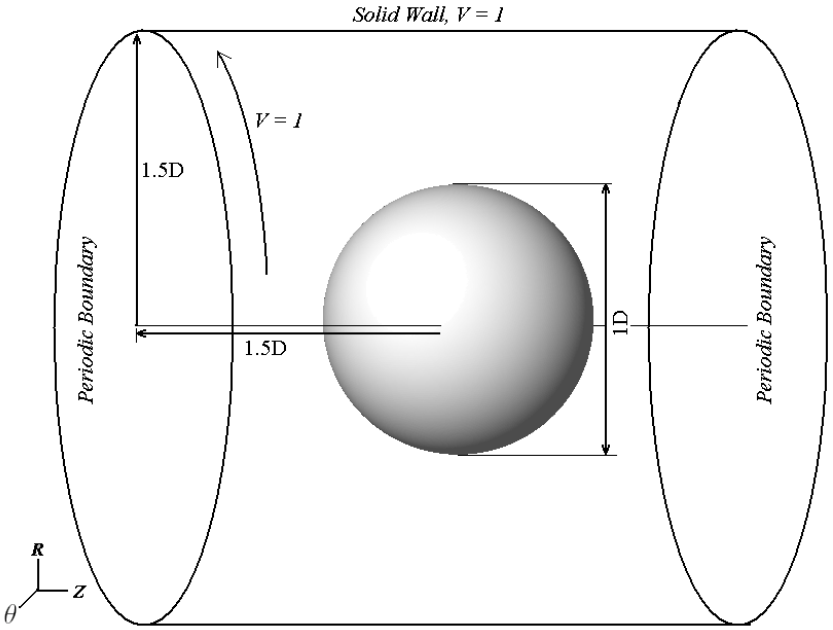

Figure 3.1: Computational domain: formal accuracy verification with a smooth sphere inside a domain with a moving outer wall.

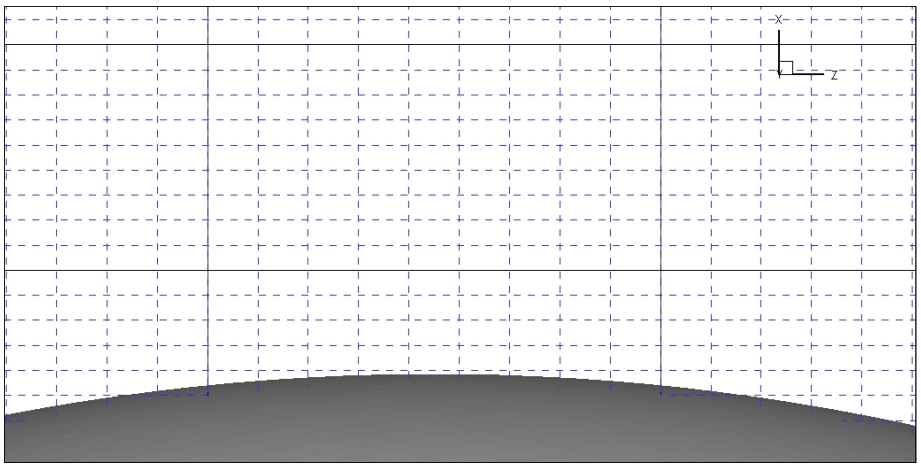

Figure 3.2: Design of computational grid accuracy study; marginal mesh ($N = 30^3$) imposed on reference mesh ($N = 270^3$).

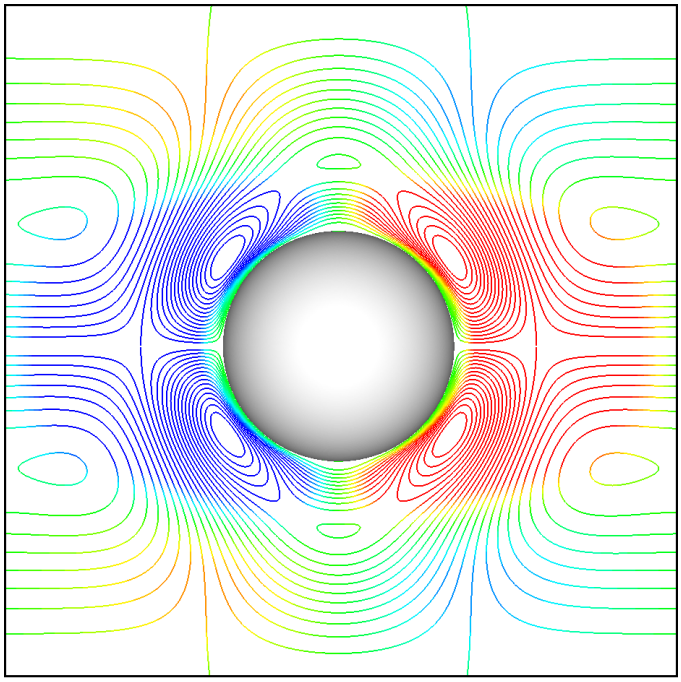

Figure 3.3: Radial (U) velocity contours colored by axial (W) velocity; $Re = 25$, $N = 270^3$.

The Reynolds number (based on the diameter of the sphere and the velocity of the moving wall) is 25. A visualization of the flow field is shown in Figure 3.3. As momentum is diffused from the moving outer boundary, regions of recirculation form on either side of the sphere. The $root - mean - square$ (RMS) of the error, which is calculated as:

$$RMS = \left[\frac{1}{NR * N\theta * NZ} \left(\sum_{k=1}^{NZ} \sum_{j=1}^{N\theta} \sum_{i=1}^{NR} \left(e_{i,j,k} \right)^2 \right) - \left(\bar{e}_{i,j,k} \right)^2 \right]^{1/2} \tag{3.1}$$

measures the difference between the converged reference solution and each coarser converged solution and is plotted in Figure 3.4 versus the corresponding grid resolution. The solutions on the $N = 90^3$, $N = 150^3$, and $N = 210^3$ were integrated until the change in the material derivative, $D\bar{u}/Dt$, (where $\bar{u}$ represents the velocity vector) converged to 10^{-9}. The reference solution ($N = 270^3$) has con-

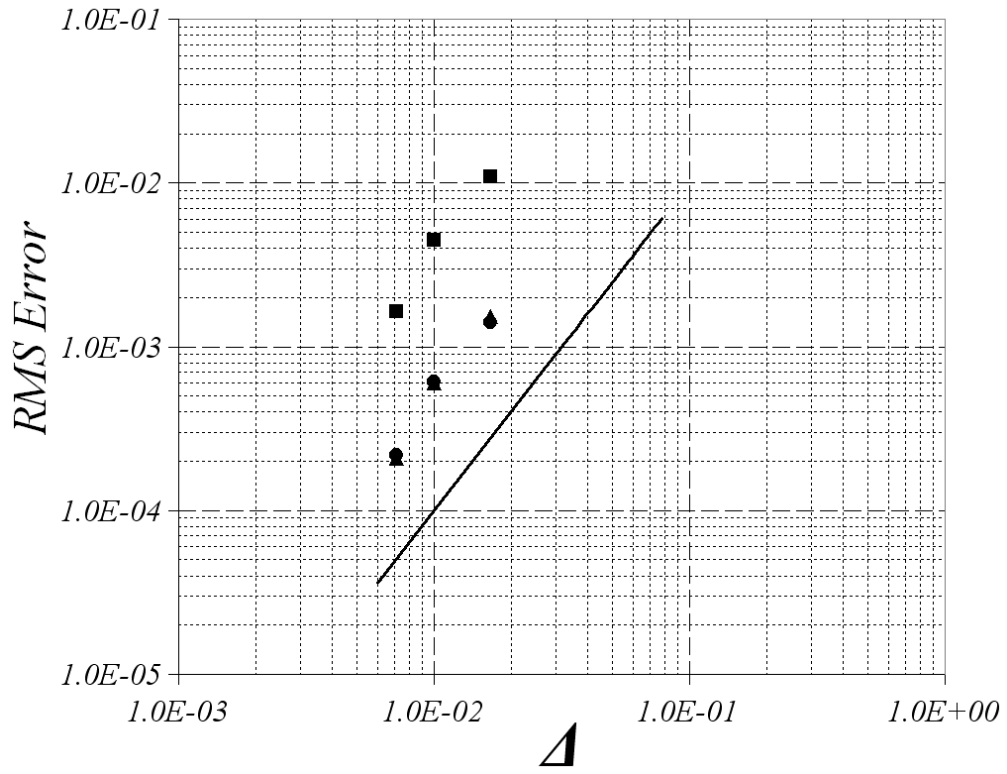

Figure 3.4: *RMS* norm of the error versus grid resolution: ● radial velocity; ■ azimuthal velocity; ▲ axial velocity.

verged to 10^{-9}. The linear trend in the plot represents second-order accuracy. The error decreases with Δ^2 for the $N = 210^3$, $N = 150^3$, and $N = 90^3$ data points on the plot, implying that the immersed body is represented exactly, within the order of accruacy of the present discretization scheme.

3.2 Verification - Grid Convergence Study

Since the accuracy of the present method has been verified in Section 3.1, a grid convergence study is used as verification of the solution's correctness. First, the technique for determining grid convergence will be outlined. Next, grid convergence results for simulations of the flow over a golf ball at $Re = 7.5 \times 10^4$ and $Re = 1.1 \times 10^5$ will be discussed.

3.2.1 Grid convergence approach

This technique is based on Richardson extrapolation (proposed in Roache & Knupp [77], applied in Roache [76]), and assumes the comparison of two or more simulation results on differing grid sizes. The analysis can be conducted on every grid point, or solution functionals (representative results) can be used. A symbolic example will be presented to outline the method, with the necessary symbols displayed in Table 3.1.

Table 3.1: Representative example of Grid Convergence using three grids per the method of Roache & Knupp [77].

Grid	Grid lengthscale	Result
1	h_1	f_1
2	h_2	f_2
3	h_3	f_3

First, the lengthscale ratio between different grids ($r = h_1/h_2$) is determined (ideally, for factor-of-two refinement r should be equal to a constant value of 2.0). Assuming a constant r, the order of convergence (labeled p), is computed as shown in equation 3.2:

$$p = \ln\left(\frac{f_3 - f_2}{f_2 - f_1}\right) / \ln(r) \tag{3.2}$$

Now, apply Richardson extrapolation with the two finest grids to estimate the solution as the grid spacing goes to zero ($f_{h=0}$) as shown in equation 3.3.

$$f_{h=0} \approx f_1 + \frac{f_1 - f_2}{r^p - 1} \tag{3.3}$$

The original intent of the method is that the grid lengthscale is the actual mesh spacing. However, in cases where factor-of-two refinement is not strictly enforced,

the grid lengthscale can be estimated using the cube root of the number of grid points (see equation 3.4).

$$h_1 = \sqrt[3]{NR_1 \times N\theta_1 \times NZ_1}, \qquad h_2 = \sqrt[3]{NR_2 \times N\theta_2 \times NZ_2} \tag{3.4}$$

Furthermore, the ratio of the grid lengthscales r may not be constant between the subsequent grid refinement levels; e.g., there may two different ratios as in equation 3.5:

$$r_1 = \frac{h_1}{h_2}, \qquad r_2 = \frac{h_2}{h_3} \tag{3.5}$$

In this situation, an equation for the order of convergence (p) may be derived using the expression from Richardson extrapolation (equation 3.3). Since Richardson extrapolation provides an estimate of the solution as the grid spacing goes to zero (the exact solution), then this expression in terms of grid 1 and grid 2 (as in 3.3) must equal the expresssion written in terms of grid 2 and grid 3 (see equation 3.6). Notice that equation 3.6 includes different ratios (r_1 and r_2).

$$f_{h=0} \approx f_1 + \frac{f_1 - f_2}{{r_1}^p - 1} = f_2 + \frac{f_2 - f_3}{{r_2}^p - 1} \tag{3.6}$$

This equation can be rearranged (equation 3.7), then solved numerically for the order of convergence (p) in a case where the ratio of the grid length scales are not equal.

$${r_2}^p \left(\frac{f_1 - f_2}{f_3 - f_1} \right) - {r_1}^{-p} \left(\frac{f_3 - f_2}{f_3 - f_1} \right) + 1 = 0 \tag{3.7}$$

Next, compute the Grid Convergence Index (GCI, from Roache [76]) comparing solutions on grids 1 and 2, then on grids 2 and 3. This is accomplished using the following definition in equation 3.8 for the GCI corresponding to the solutions on

grids 1 and 2 (a similar expression would be calculated for the solution on grids 2 and 3):

$$GCI_{12} = F_{sec}\frac{|\epsilon|}{r^p - 1}, \qquad F_{sec} = 1.25, \qquad \epsilon = \frac{f_1 - f_2}{f_1} \tag{3.8}$$

The value of the constant F_{sec} should have a value of 3.0 for an analysis comprised of two results, but can be reduced to a value of 1.25 when comparing three or more results. The last step is essentially a ratio of the Grid Convergence Indices for the cases considered to ascertain whether the results are in the asymptotic range of convergence (implied by this ratio being close to a value of 1.0; ref. equation 3.9). For the case in which $r_1 \neq r_2$, the most logical approach would be to use r_1, since the purpose of equation 3.9 is to determine whether the change in the results between grids 1 and 2 approaches the asymptotic range.

$$\frac{GCI_{12}}{GCI_{23}}r^p \approx 1 \tag{3.9}$$

3.2.2 Grid convergence results

Results are presented in which a solution functional (in this case, the mean drag coefficient (C_D, reference equation 3.10)

$$C_D = \frac{F_z}{\frac{1}{2}\rho {U_\infty}^2 A} \tag{3.10}$$

is used as the metric for the grid convergence verification. The drag coefficient is a non-dimensionalization of the axial force on the golf ball (F_z) by the fluid density (ρ), the bulk velocity (U_∞) squared, and the cross-sectional area of the golf ball (A). The first set of results is comprised of a set of simulations of the flow over a non-rotating golf ball at $Re = 7.5 \times 10^4$; the second set of results are computed at $Re = 1.1 \times 10^5$. A summary of the simulations is presented Tables 3.2 and 3.3. Here,

since the grid is not refined uniformly in each principle direction, the cube root of the total number of grid points is used to calculate the ratio of the grid lengthscales; e.g., h_1 is the cube root of the total number of grid points on the finest mesh, while h_2 is the cube root of the total number of grid points on the intermediate mesh. Furthermore, equation 3.7 was solved numerically for the order of convergence (p) using the bi-section method. Now, applying the methodology presented in section 3.2.1, the following results are obtained (see Table 3.4).

Table 3.2: Simulations of the flow over a golf ball, $Re = 7.5 \times 10^4$. Grid information, lengthscales, and solution functional (drag coefficient) used for the grid convergence study.

Grid	Number of grid points	$\sqrt[3]{NR \times N\theta \times NZ}$	C_D
1	$760 \times 252 \times 3002$	8.315×10^2	0.376
2	$536 \times 127 \times 2502$	5.543×10^2	0.398
3	$315 \times 102 \times 1502$	3.640×10^2	0.451

Table 3.3: Simulations of the flow over a golf ball, $Re = 1.1 \times 10^5$. Grid information, lengthscales, and solution functional (drag coefficient) used for the grid convergence study.

Grid	Number of grid points	$\sqrt[3]{NR \times N\theta \times NZ}$	C_D
1	$760 \times 502 \times 3002$	1.046×10^3	0.26
2	$760 \times 252 \times 3002$	8.315×10^2	0.27
3	$315 \times 102 \times 1502$	3.640×10^2	0.39

The values obtained for the (p) are within the range of what would be expected for grid convergence. The solutions are calculated on structured grids using second-order centered-differences for the spatial discretization, and the reconstruction scheme applied to the velocity field at the immersed boundary is strictly second-order. Thus, the orders of convergence indicate that the fine meshes for

Table 3.4: Results of the grid convergence study for simulations of the flow over a golf ball at $Re = 7.5 \times 10^4$ and $Re = 1.1 \times 10^5$. Lengthscale ratios (r_1,r_2), order of convergence (p), Richardson extrapolation of C_D, Grid Convergence Indices, and the assessment of the asymptotic range.

Metric	$Re = 7.5x10^4$	$Re = 1.1x10^5$
$r_1 = \frac{h_1}{h_2}$	1.50	1.258
$r_2 = \frac{h_2}{h_3}$	1.522	2.284
p	**2.037**	**2.075**
$f_{h=0}$, C_D	0.358	0.244
GCI_{12}	0.056	0.078
GCI_{23}	0.122	0.122
$\frac{GCI_{12}}{GCI_{23}} {r_1}^p$	**1.058**	**1.038**

both Reynolds numbers presented are sufficiently resolved to approach the asymptotic range of the solution(s). This is confirmed by the values for the ratio of the Grid Convergence Indices multiplied by ${r_1}^p$: 1.058 for $Re = 7.5 \times 10^4$ and 1.038 for $Re = 1.1 \times 10^5$. The asymptotic convergence of the mean drag coefficient (C_D) is illustrated in Figure 3.5.

3.3 Validation - Smooth sphere cases

The flow around a smooth sphere is a well-documented case in the literature, as discussed in Chapter 1. It is an important validation benchmark for calculations of flow around bluff bodies. The key parameter in the (incompressible) flow over a sphere is the Reynolds number, as it largely determines the nature of the boundary-layer development, wake dynamics, and fluid forces on the sphere. Drag forces on bluff bodies generally decrease sharply at a critical Reynolds number, producing the drag crisis. For the sphere, the drag crisis occurs around $Re = 4 \times 10^5$ (reference Figure 3.6).

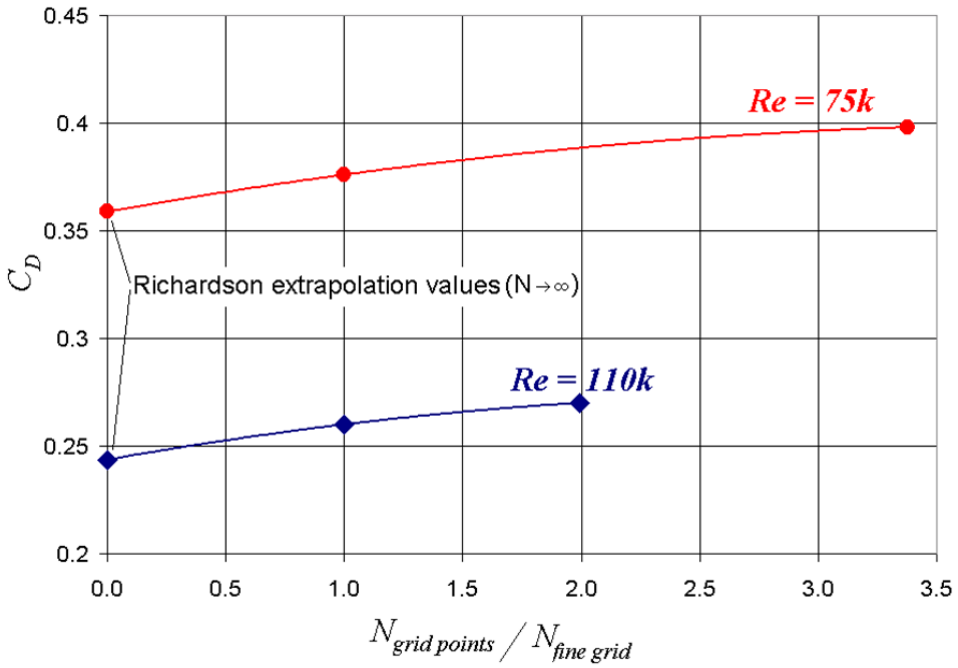

Figure 3.5: Asymptotic convergence of the mean drag coefficient toward the Richardson extrapolated value. ● $Re = 7.5 \times 10^4$; ⋄ $Re = 1.1 \times 10^5$.

In order to validate the immersed boundary approach, flows of differing Reynolds numbers (based on the diameter of the sphere and the freestream velocity) were studied. Some representative examples are discussed herein. The first case is the calculation of the flow over a sphere at $Re = 300$. The flow was computed using a grid of NR = 213, Nθ = 34, and NZ = 706, and is visualized in Figure 3.7, in which the **Q** criterion method of vortex indentification Hunt *et al.* [45] is used to identify the large, coherent vortices which are generated in the wake of the sphere. The aerodynamic forces were averaged for the $Re = 300$ case, and show decent comparison with computations (Johnson & Patel [48], Constantinescu & Squires [29]) and measurements (Roos & Willmarth [78]), as is demonstrated in Table 3.5.

Other validation cases was computed for sphere over a range of Reynolds numbers consisting of $Re = 0.5 \times 10^4$, $Re = 1.0 \times 10^4$, $Re = 2.5 \times 10^4$, $Re = 5.0 \times 10^4$, and $Re = 1.0 \times 10^5$. A representative example is the $Re = 1.0 \times 10^4$ simulation. The solu-

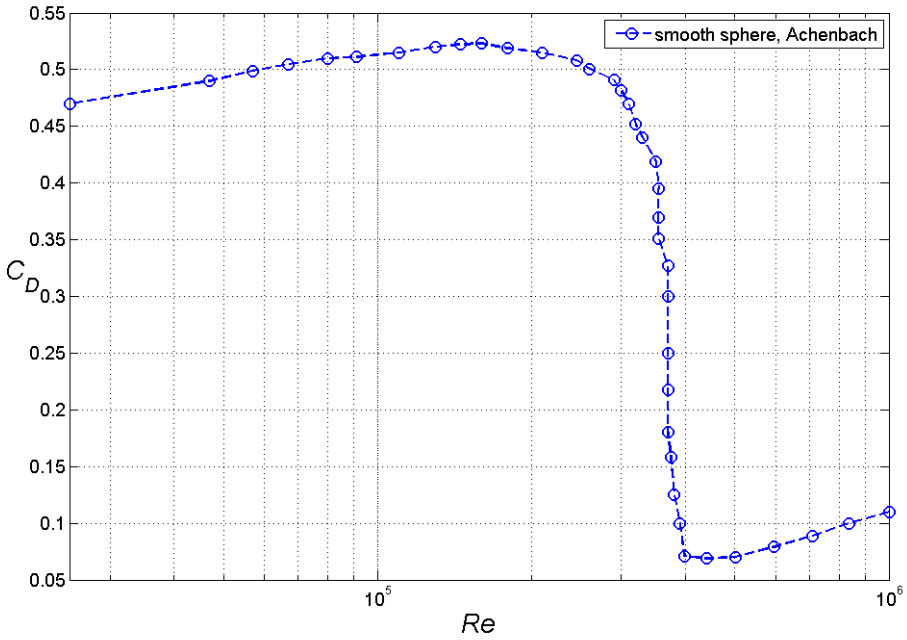

Figure 3.6: Drag coefficient (C_D) as a function of Reynolds number; smooth sphere results of Achenbach [3].

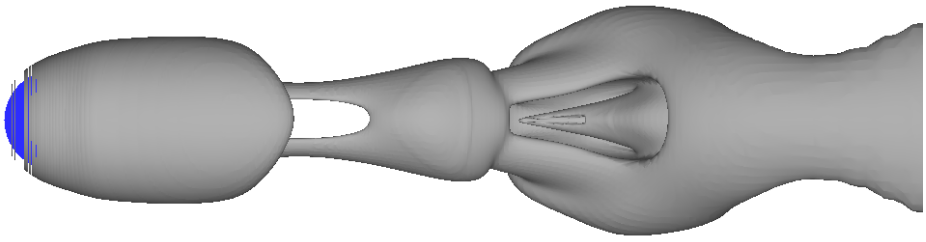

Figure 3.7: Isosurface using the Q-criterion method of Hunt *et al.* [45]: smooth sphere, $Re = 300$.

Table 3.5: Comparison of the drag coefficent (C_D) between the present immersed boundary method and previous work for a validation case at Re = 300.

Results	Drag Coefficient
Present DNS	0.655
Johnson and Patel (1999)	0.656
Constantinescu and Squires (2004)	0.655
Roos and Willmarth, Exp. (1971)	0.629

tion was integrated for 25 Ut/D time units on grids up to a size of 105×10^6 points. Contours of the spanwise vorticity are presented in Figure 3.8. Time-averaged values of the drag coefficient compares well with previous computations and measurements, as shown below in Table 3.6.

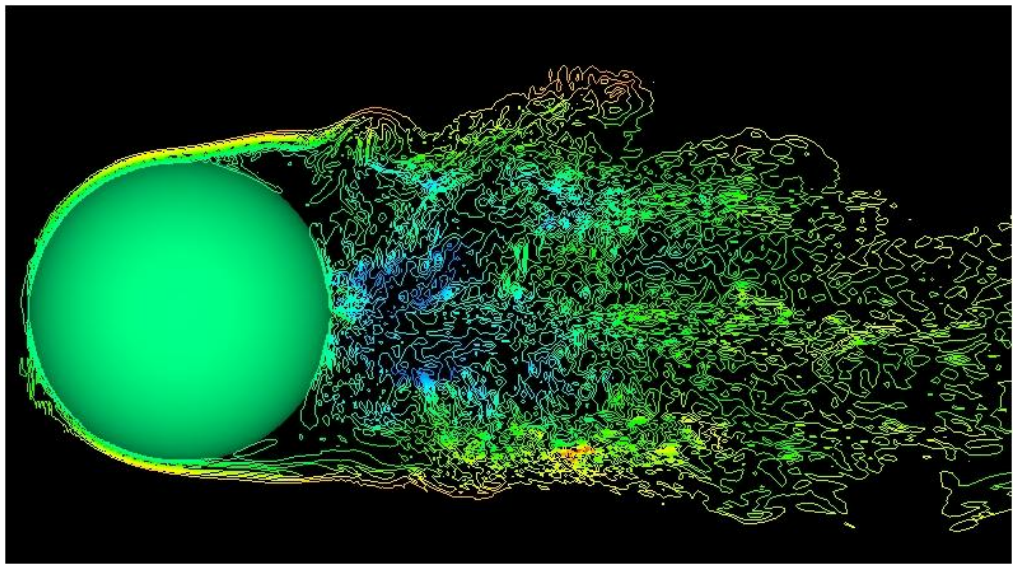

Figure 3.8: Instantaneous contours of spanwise vorticity (Ω_θ), $Re = 1.0\times10^4$. NR = 122, Nθ = 66, and NZ = 642.

Table 3.6: Comparison of the drag coefficent (C_D) between the present immersed boundary method and previous work for a validation case at $Re = 1.0 \times 10^4$.

Results	Drag Coefficient
Present DNS	0.4
Constantinescu and Squires (2004)	0.393
Achenbach, Exp. (1972)	0.4

3.4 Validation of Methods for Calculating the Pressure and Shear Stress on an Immersed Boundary

Validation data are presented for the preliminary and extended reconstruction approaches discussed in Chapter 2. The preliminary reconstruction approach is validated using the computations of flow over a sphere by Kim & Choi [53] at $Re = 300$. The extended reconstruction approach is validated using a computation (by the author) of flow over a sphere at $Re = 300$ with a body-fitted solver.

3.4.1 Preliminary reconstruction approach

A smooth sphere validation case was calculated using the present immersed boundary approach and compared with the stationary (non-rotating) result reported by [53] at $Re = 300$. The grid resolution used in Kim & Choi [53] was $161 \times 40 \times 289$; the grid resolution in the present simulation was $183 \times 66 \times 642$, and is illustrated in Figure 3.9. The immersed boundary solution was integrated for 350 Ut/D time units to reach statistically-stationary state before computing the pressure on the surface using the preliminary reconstruction approach. The pressure on the surface of the sphere is scaled to yield the pressure coefficient (C_P, reference equation 3.11)

$$C_P = \frac{P - P_\infty}{\frac{1}{2}\rho {U_\infty}^2} \tag{3.11}$$

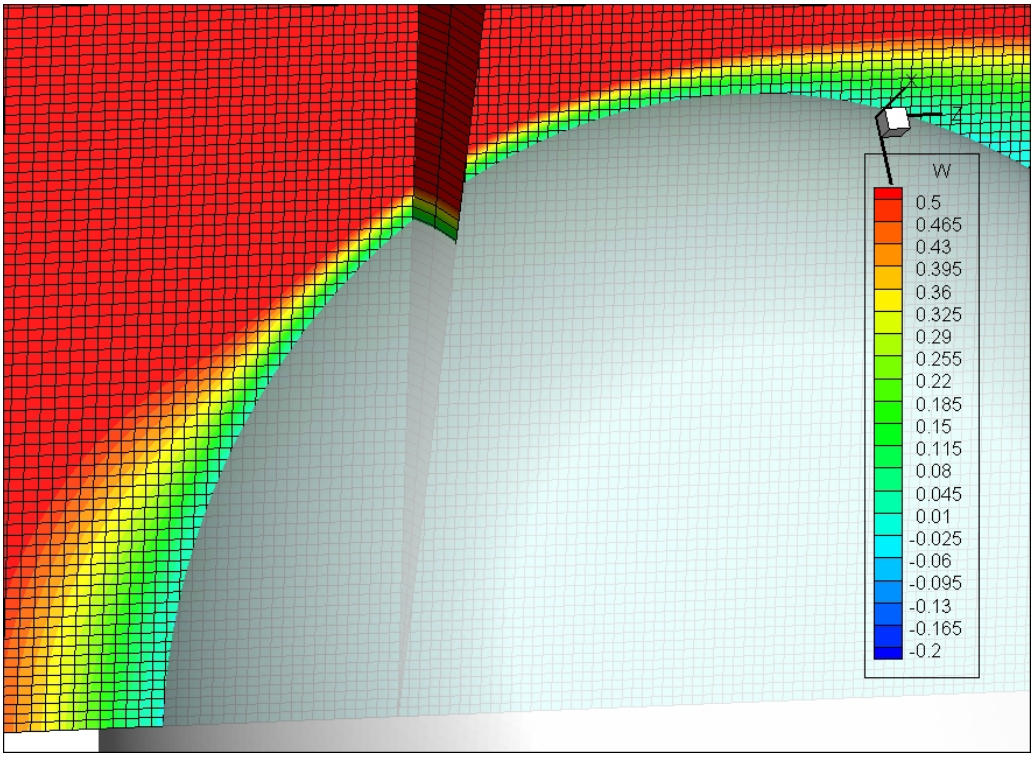

Figure 3.9: Instantaneous contours of streamwise velocity (W) of the flow around a smooth sphere at $Re = 300$ using an immersed boundary approach (mesh superimposed on the contours).

and is plotted at a representative line from the stagnation point to the back of the sphere in Figure 3.10. The pressure coefficient is a dimensionless pressure scale defined as the relative pressure ($P - P_\infty$) divided by the fluid density (ρ) and the bulk velocity (U_∞) squared. Reasonable comparison with the computations of Kim & Choi [53] is illustrated in Figure 3.10. Around 40° and 60° the reconstructed pressure results deviate slightly from the simulation of Kim & Choi [53], which is due to the fact that the result is presented along a single line intersecting the immersed sphere; averaging in the azimuthal direction would have produced a smoother result. Nevertheless, the agreement between a result along a line and the reference result suggest that the preliminary reconstruction approach can be used to approximate the pressure on the surface of an immersed boundary.

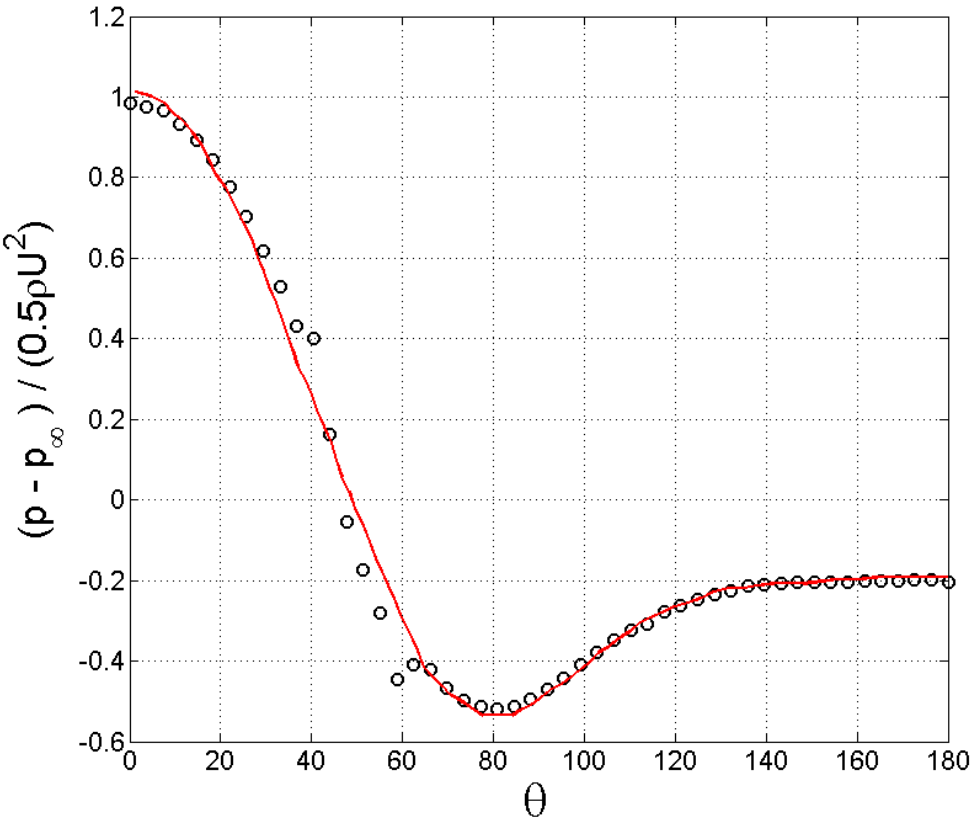

Figure 3.10: Preliminary reconstruction approach applied to compute the pressure coefficient (C_p) on a smooth sphere at $Re = 300$: − simulation result of Kim & Choi [53]; ◯ immersed boundary method with preliminary reconstruction approach.

3.4.2 Extended reconstruction approach

A smooth sphere validation case was calculated using the present immersed boundary approach and compared with a result computed using a body-fitted approach in the industry solver *Cobalt* (reference Strang *et al.* [96]) at $Re = 300$. Since *Cobalt* is an unstructured finite-volume solver, the grid topology was comprised of tetrahedral and prism elements. The total size of the grid was approximately 413000 points and 2.01×10^6 cells. The unstructured, body-fitted grid was constructed to maintain the same cell size near the wall of the sphere as that which is used in the immersed

boundary solution, in which the grid resolution was comprised of $183 \times 42 \times 402$ points. Contours of the friction coefficient (C_f, reference equation 3.12) (defined as the ratio of the wall stress (τ_w) with the fluid density (ρ) and the bulk velocity (U_∞) squared) for both approaches are illustrated in Figure 3.11a (body-fitted) and Figure 3.11b (immersed-boundary). The friction coefficient (C_f) is multiplied by the square root of the Reynolds number in order to allow comparison with results over a range of Reynolds numbers. Both solutions were integrated for approximately 340 Ut/D time units, and quantitative results for the friction coefficient are displayed in Figure 3.12.

$$C_f = \frac{\tau_w}{\frac{1}{2}\rho {U_\infty}^2} \sqrt{Re} \tag{3.12}$$

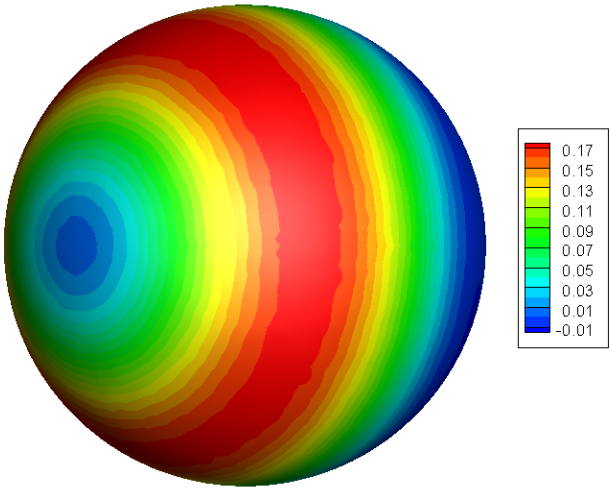

(*a*)

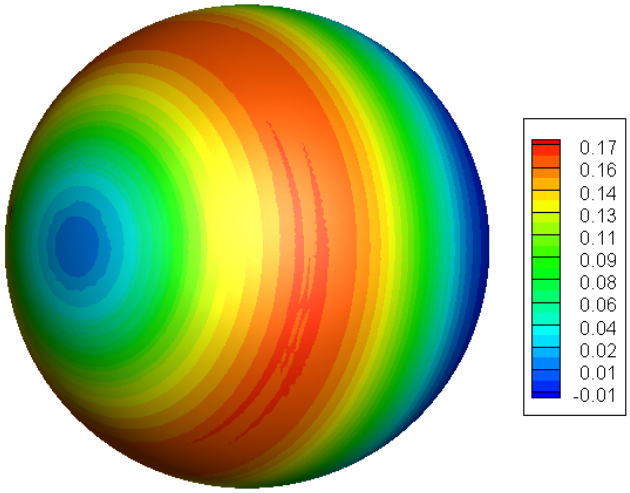

(*b*)

Figure 3.11: Contours of the friction coefficient (C_f) for Re = 300. (*a*) Body-conformal calculation with *Cobalt* - 413000 points and 2.01×10^6 cells; (*b*) Immersed-boundary calculation - $183 \times 42 \times 402$ points.

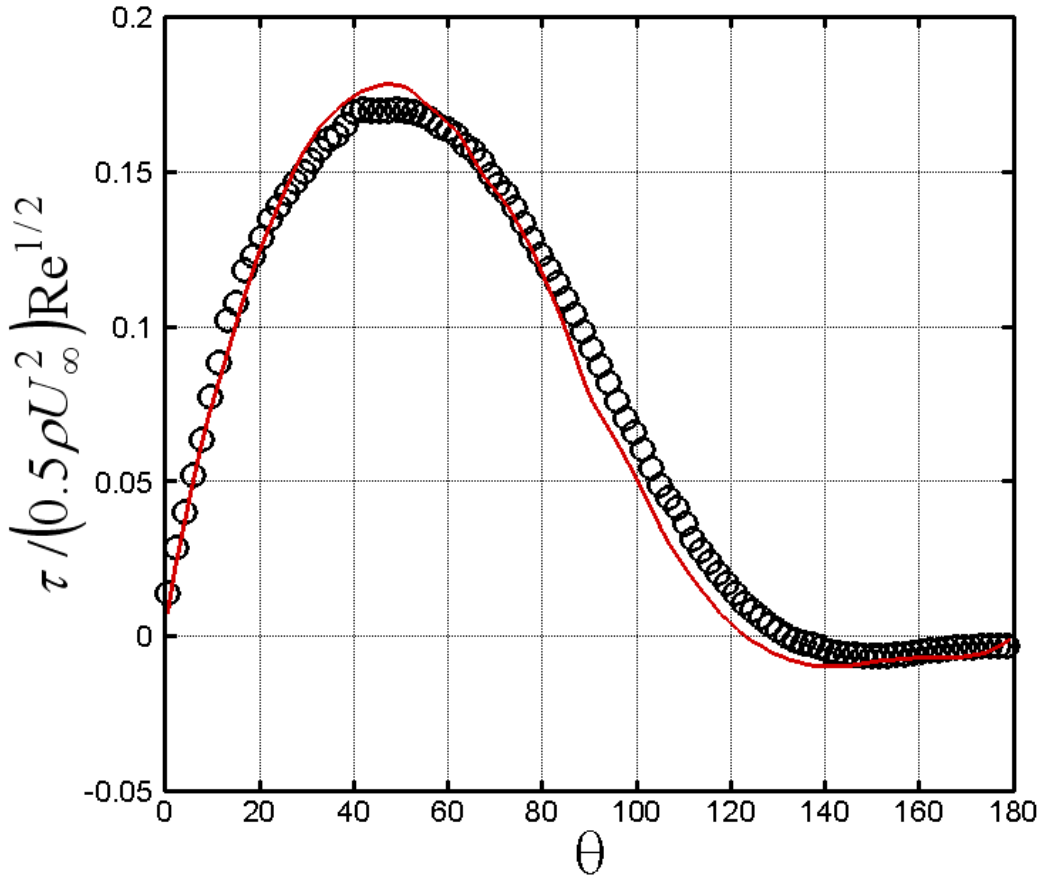

Figure 3.12: Extended reconstruction approach applied to the friction coefficient (C_f) on a smooth sphere at $Re = 300$: – simulation result with *Cobalt*; ◯ immersed boundary method with extended reconstruction approach.

Chapter 4

Subcritical and Supercritical Regimes: arbitrarily-aligned golf ball

In the present study, DNS results are reported for simulations performed pre- and post-drag crisis; in particular, for computations around a golf ball in the subcritical ($Re = 1.0 \times 10^4$, $Re = 2.5 \times 10^4$) and supercritical regimes ($Re = 1.1 \times 10^5$). In this work, the golf ball is oriented arbitrarily with respect to the flow (flight direction); e.g., no attempt was made to align the axes of symmetry with the direction of the flow. The primary reason is that a rotating golf ball is not aligned with the flow in any way; its axes of symmetry are moving and thus the orientation of the ball is transient as well.

4.1 Geometry and Grid

A geometry supplied by Srixon and comprised of approximately 300 spherical dimples is used in this study. The surface of the ball is discretized with a mesh of surface triangles connected by nodes. The orientation of the golf ball is shown in Figure 4.1; the view shown is of the X-Y plane with the observer looking from directly upstream. As noted, no symmetry axes are aligned with the flow or are visible here.

In the present work, several grid resolutions used to study the flow at Reynolds numbers of 1.0×10^4, 2.5×10^4, and 1.1×10^5. Preliminary results were computed on a coarse grid of 172×10^6 points at subcritical Reynolds numbers ($Re = 1.0 \times 10^4$, $Re = 2.5 \times 10^4$), and the mesh was progressively refined for the higher Reynolds number cases ($Re = 1.1 \times 10^5$). The mesh refinement progression is displayed in Figure 4.2.

The grid sizes in the radial, azimuthal, and axial directions are summarized in Table 4.1. Grid refinement studies for both Reynolds numbers indicated that qualitative flow features (e.g., visualizations) as well as quantitative measures such

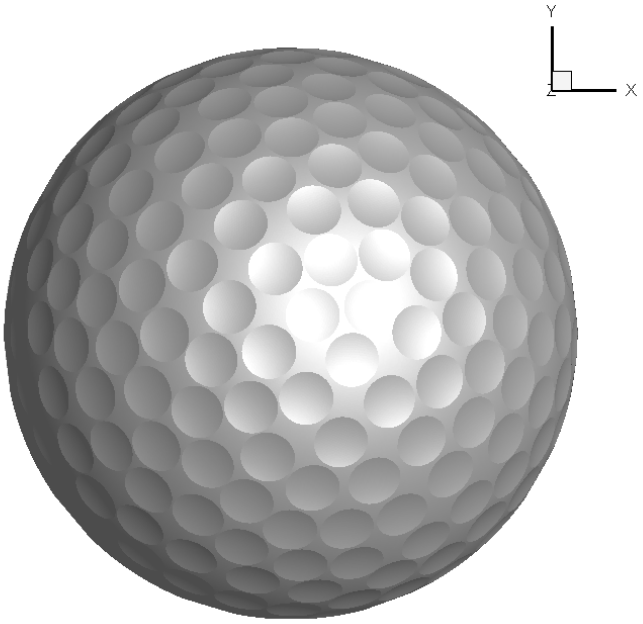

Figure 4.1: Orientation with respect to the flow direction, 300-dimple golfball; present view looking from upstream of the golf ball toward the downwind direction.

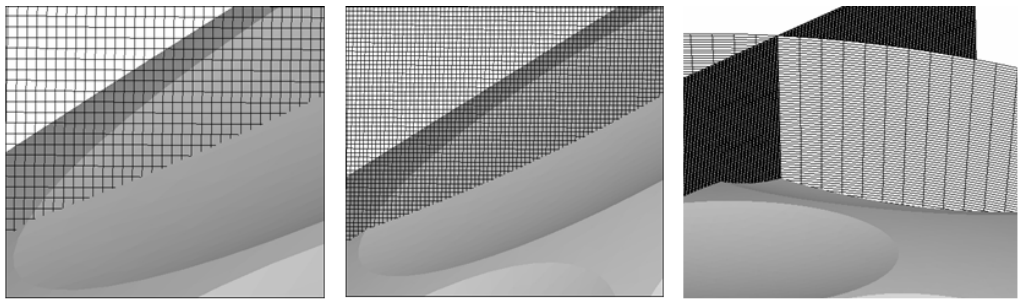

Figure 4.2: Example grid resolutions used in this study: (*a*) Coarse resolution (172 million points); (*b*) Intermediate resolution (575 million points); (*c*) Fine resolution (1.1 billion points).

as the aerodynamic forces could be accurately captured using the grid resolutions presented in Table 4.1.

Table 4.1: Grid resolution for present DNS: subcritical ($Re = 1.0 \times 10^4$, $Re = 2.5 \times 10^4$) and supercritical regimes ($Re = 1.1 \times 10^5$).

Coordinate	$Re = 1.0 \times 10^4$	$Re = 2.5 \times 10^4$	$Re = 1.1 \times 10^5$
Radial (R)	544	536	760
Azimuthal (θ)	127	252	252 / 502
Axial (Z)	2502	2502	3002
Total grid points	172×10^6	337×10^6	575×10^6 / 1.1×10^9

The radial and axial grid point distributions were clustered to refine the grid near the golf ball. This was accomplished using stretching ratios for the grid spacing near the critical regions (near the centerline to the region of flow detachment). The radial and axial grids were then smoothed in order to avoid abrupt changes in spacing using a stencil that weighted the coordinate value of a particular point twice as much as the point before and after it.

4.2 Flow Visualization: Near-Wall Region

Visualizations of the instantaneous flow field near the point of flow detachment illustrate the effect of the Reynolds number on flow separation characteristics. The results plotted in Figure 4.3 were computed on the 337×10^6 point mesh (subcritical case) and the 575×10^6 point mesh (supercritical case).

In the subcritical case (Figure 4.3a), the roll-up of the shear layer occurs after the boundary layer has detached from the golf ball. The reason is that the lower Reynolds number flow has less near-wall momentum, and is therefore able to resist separation longer. In the supercritical case (Figure 4.3b), flow visualization of the vorticity reveals truly intriguing structures, and the roll-up of the shear layer occurs in a manner that seems that echo the proposal of Choi *et al.* [25]. As the flow

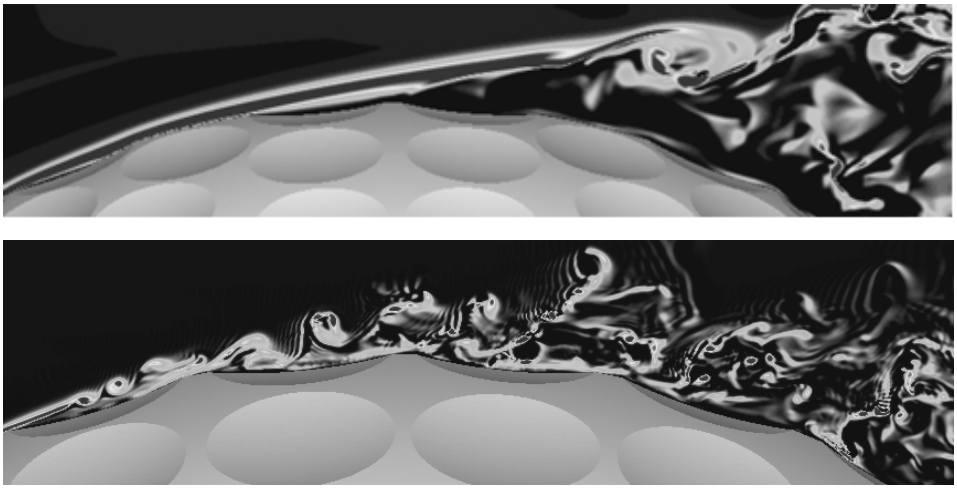

Figure 4.3: Instantaneous contours of spanwise vorticity (a) $Re = 2.5 \times 10^4$; (b) $Re = 1.1 \times 10^5$.

evolves from the front to the rear of the left-most dimple in Figure 4.3b, local detachment leads to flow structures generated by a developing shear layer instability. The structures generated by the shear layer instability increase the momentum of the near-wall flow and lead to local reattachment of the flow within the dimple. This process repeats through several dimples in the streamwise direction until complete flow detachment occurs downstream of the initial flow detachment.

Furthermore, the three-dimensionality of the flow structures may be observed by investigating the velocity contours for the fine mesh solution. Here, the azimuthal grid spacing is 1/2 the grid spacing of the intermediate mesh for the same Reynolds number, and the effect of this grid refinement is illustrated in Figure 4.4.

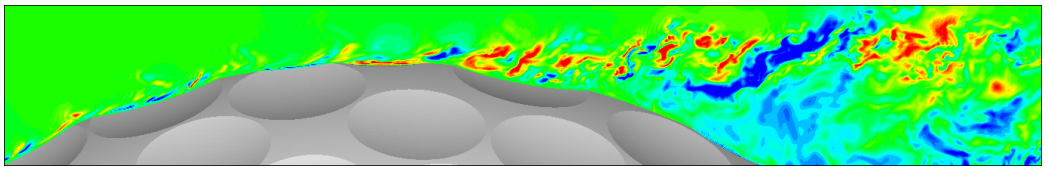

Figure 4.4: Instantaneous spanwise (out-of-plane) velocity contour, $Re = 1.1 \times 10^5$, 1.14×10^9 points.

The alternating color changes (from red to blue) in the contours near the golf ball reveal the helical motion of the small flow structures near the dimples. These flow patterns emerge upstream (at the left of the figure) around 60 degrees (measured from the stagnation point at the front of the ball), and progress downstream, increasing in size as they are convected by the bulk flow.

The time-averaged flow patterns are visualized using contours of the streamwise velocity in Figure 4.5.

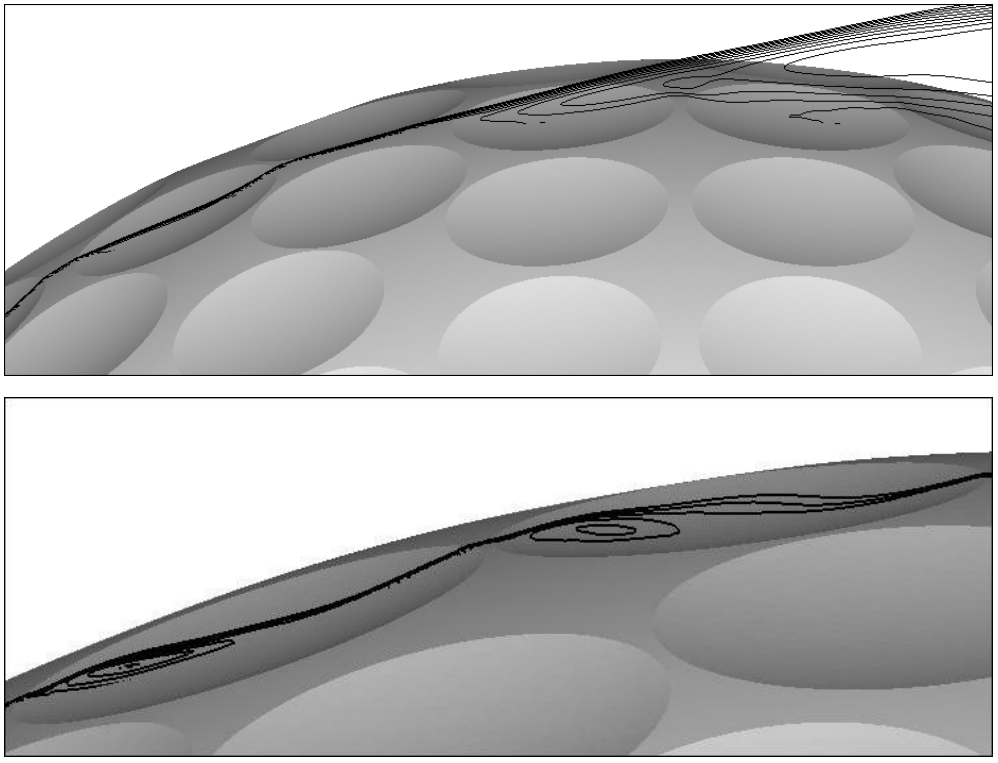

Figure 4.5: Time-averaged contours of streamwise velocity (a) $Re = 2.5 \times 10^4$; (b) $Re = 1.1 \times 10^5$.

The flow patterns within dimples and in the region of complete flow separation are depicted in Figure 4.5. The subcritical case displays the mean flow which follows the boundary until flow separation at an angle of 80 degrees (calculated from the stagnation point at the front of the ball). This separation region is characterized

by the recirculation apparent in Figure 4.5 *a*. The supercritical case shows regions of local flow detachment within individual dimples in Figure 4.5 *b*. Fluid recirculation within dimples transports momentum into the near-wall region, energizing the flow and delaying separation.

4.3 Flow Visualization: Wake

Some contour results demonstrating the effect of the Reynolds number are presented in Figure 4.6. As the Reynolds number increases from $Re = 1.0 \times 10^4$ to $Re = 1.1 \times 10^5$,(and the local grid spacing necessarily decreases), the size of the flow structures in the wake decrease significantly, the separation point moves aft, and the mechanism of separation is modified.

Statistics of the flow for the subcritical and supercritical cases have been computed by averaging over approximately 6 Ut/D time units. Flow patterns corresponding to the turbulent kinetic energy ($\bar{k}$) are illustrated in Figure 4.7 for the supercritical case. The turbulent kinetic energy (which is defined as one half the trace of the mean Reynolds stress tensor as shown in 4.1 per Pope [74]) is plotted along radial lines at points in the wake. These line plots are superimposed on a contour of the averaged streamwise (W) velocity.

$$\bar{k} = \frac{1}{2}\langle u_i u_j \rangle \tag{4.1}$$

where the mean Reynolds stress tensor is defined as:

$$\langle u_i u_j \rangle = \begin{bmatrix} \langle uu \rangle & \langle uv \rangle & \langle uw \rangle \\ \langle uv \rangle & \langle vv \rangle & \langle vw \rangle \\ \langle uw \rangle & \langle vw \rangle & \langle ww \rangle \end{bmatrix} \tag{4.2}$$

As demonstrated in Figure 4.7, the velocity statistics in the region of the dimples appear to be close to convergence. The plot of kinetic energy imposed on the

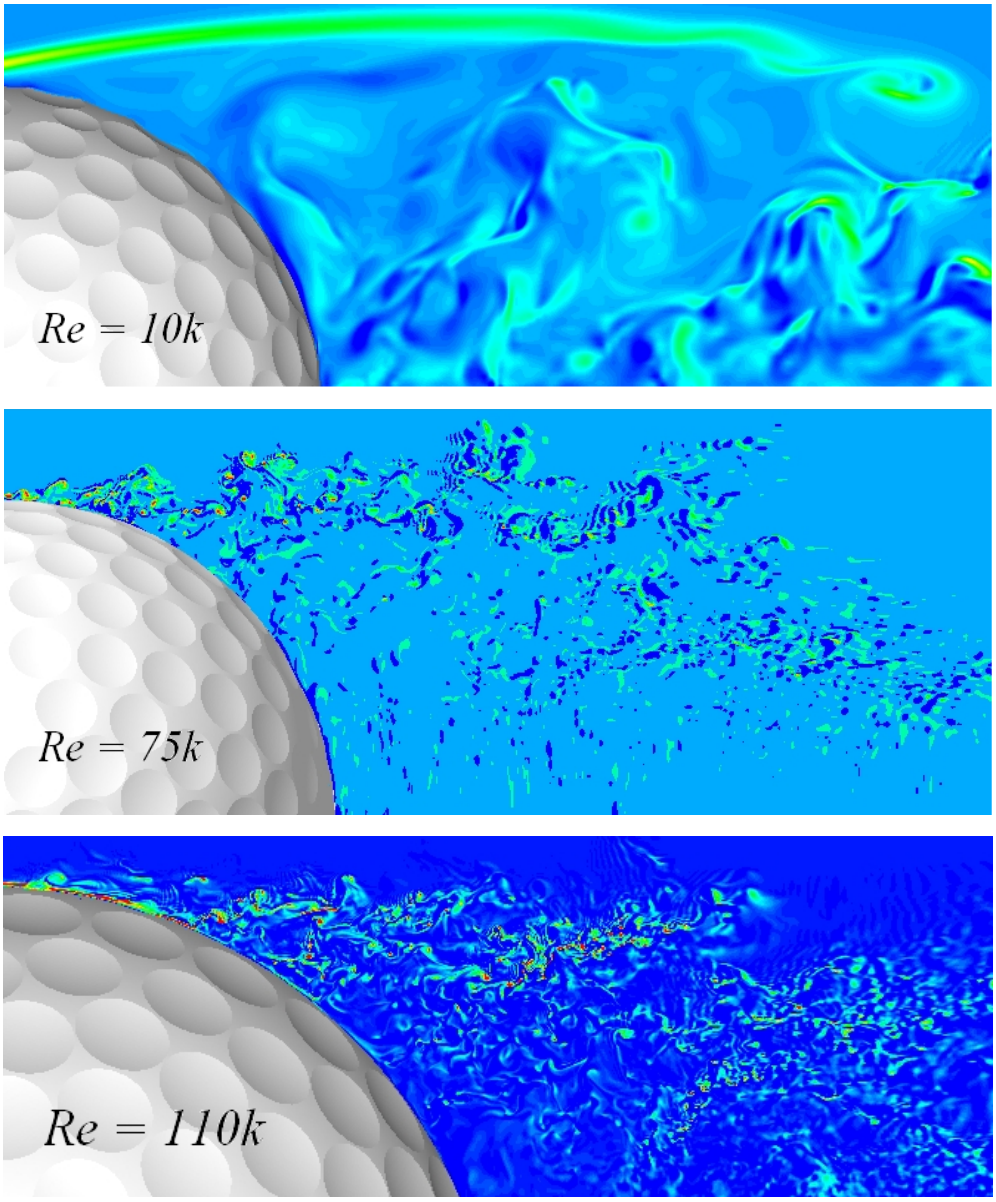

Figure 4.6: Contours of spanwise vorticity (a) $Re = 1.0 \times 10^4$; (b) $Re = 7.5 \times 10^4$; (c) $Re = 1.1 \times 10^5$.

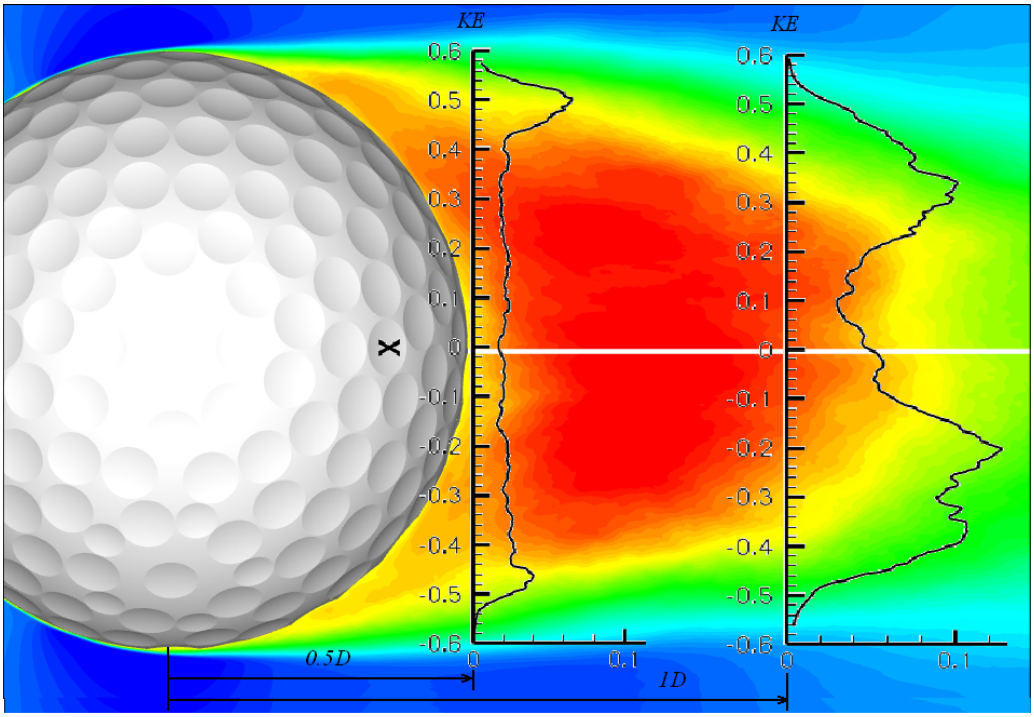

Figure 4.7: Time-averaged kinetic energy at selected locations in the wake superimposed on contours of mean streamwise velocity, $Re = 1.1 \times 10^5$.

streamwise velocity contour demonstrates these statistics in the wake are not converged yet, as the time scales of the flow structures in the wake are much longer than those within individual dimples. The solution field for the non-rotating case will be integrated further to converge the statistics in the wake.

A reasonable question which may be posed is the degree to which these results represent a DNS; e.g., is the mesh resolution sufficient to capture the smallest lengthscales in the flow (even to the level of the viscous lengthscale)? Some indication of this can be evaluated by looking at the level of the the eddy viscosity in the flow. Following the explanation in Pope [74], the eddy viscosity hypothesis (introduced by Boussinesq in 1877) presents a mathematically-similar expression to the relationship between the viscous stress and rate of strain in a Newtonian fluid; the hypothesis contends that the Reynolds stress tensor is linearly proportional to the

mean rate of strain by some positive scalar coefficient (namely, the *eddy viscosity* or *turbulent viscosity* ν_T) as expressed in equation 4.3.

$$-\rho\langle u_i u_j\rangle + \frac{2}{3}\rho k\delta_{ij} = 2\rho\nu_T\overline{S_{ij}} \tag{4.3}$$

where $\overline{S_{ij}}$ is defined as:

$$\overline{S_{ij}} = \frac{1}{2}\left(\frac{\partial\langle U_i\rangle}{\partial x_j} + \frac{\partial\langle U_j\rangle}{\partial x_i}\right) \tag{4.4}$$

This hypothesis was applied by Smagorinsky [83] as a closure for the filtered velocity equations in the large-eddy simulation (LES) approach (reference Pope [74] for a comprehensive explanation of LES). Smagorinsky applied the eddy viscosity hypothesis to relate the sub-grid (residual) stresses to the filtered rate of strain using the eddy viscosity, where the eddy viscosity is defined as shown in equation 4.5.

$$\nu_T = (C_S\Delta)^2\,\overline{S} \tag{4.5}$$

Here, C_S is the Smagorinsky coefficient and together with Δ (in equation 4.6) forms the Smagorinsky lengthscale (which is assumed to be proportional to the filter width for the LES). The S term is the mean-squared value of the filtered rate of strain tensor (4.6).

$$\Delta = \sqrt[3]{\Delta_x\Delta_y\Delta_z}, \quad \overline{S} = \sqrt{2\overline{S_{ij}}\,\overline{S_{ij}}} \tag{4.6}$$

These ideas from LES can be applied to the current effort, in the sense that the degree to which the current simulation is a DNS can be estimated by computing the eddy viscosity levels by calculating the rate of strain tensor from the mean velocity field. If equation 4.5 is evaluated using current statistics for the velocity field at the supercritical Reynolds number ($Re = 1.1\times10^5$), an estimate of ν_T is obtained

for each cell in the computational domain, and the maximum value is shown in equation 4.7 for a cell downstream of the golf ball in the wake:

$$\nu_{T\,max} = 6.29 \times 10^{-5} \tag{4.7}$$

The molecular viscosity (due to the non-dimensional formulation) is simply $\nu = 1/Re$, thus the ratio of the eddy viscosity to the molecular viscosity is as follows (ref. equation 4.8). This result implies that the resolution of the mesh in the wake is not sufficient to capture all of the viscous scales, as the simulation may be reasonably labeled a DNS if this ratio is less than 0.1. In this work, the simulations were designed to concentrate the mesh resolution near the golf ball in order to resolve the flow scales in the dimples and to capture the aerodynamic forces; the mesh requirements for DNS far from the golf ball in the wake were relaxed in order to minimize the computational cost.

$$\frac{\nu_T}{\nu} = \frac{6.29 \times 10^{-5}}{9.09 \times 10^{-6}} \approx 6.93 > 0.1 \tag{4.8}$$

4.4 Statistical Features - Aerodynamic forces

Time-histories of the lift and drag for both Reynolds number cases are presented in Figure 4.8. Mean values of the force coefficients ($C_D = F_Z/\frac{1}{2}\rho U^2 A$) are presented in Table 4.2. These statistics results show reasonable agreement with measurements of Bearman & Harvey [11] and Choi *et al.* [25].

4.5 Statistical Features - Frequency spectra

The flow field was sampled at several points near the ball and in the wake to extract the high-frequency vortex shedding in the shear layer as well as to assess the

Table 4.2: Mean drag coefficients - present work compared with previous measurements.

Result	C_D
$Re = 2.5\times10^4$, 172×10^6 points	0.47
Bearman & Harvey [11]	0.25
Choi *et al.* [25]	0.21
$Re = 1.1\times10^5$, 575×10^6 points	0.27
$Re = 1.1\times10^5$, 1.1×10^9 points	0.26

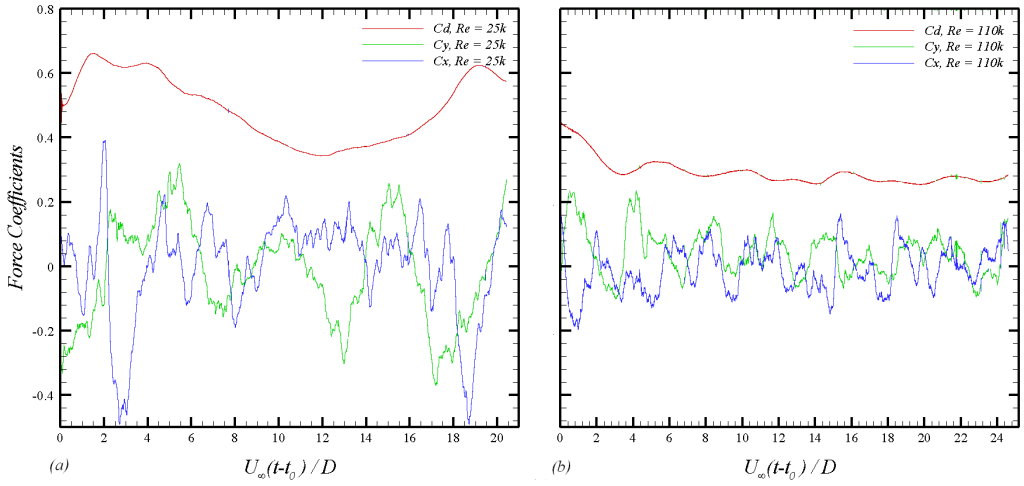

Figure 4.8: Time-history of aerodynamic force coefficients for a non-rotating golf ball: (a) $Re = 2.5\times10^4$; (b) $Re = 1.1\times10^5$.

lower frequency motion in the wake. Sampling locations (represented by white circles) are shown in Figure 4.9 superimposed on contours of spanwise vorticity and streamwise velocity from the $Re = 1.1\times10^5$ DNS.

The locations of the probes used for the spectral analysis are specified in terms of the ball diameter, and represent the radial and axial coordinates. For each Reynolds number, a location near the golf ball is contrasted with a location in the wake. The locations are labeled as follows:

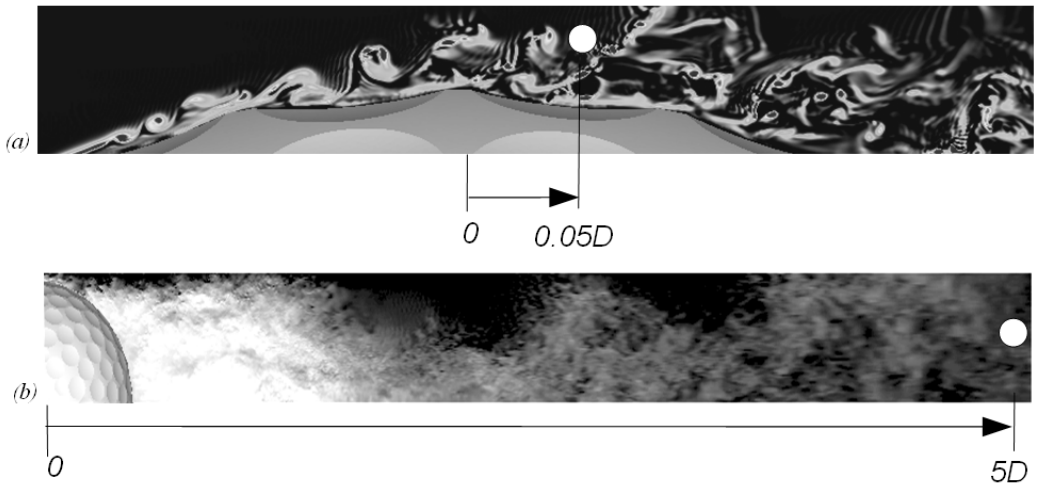

Figure 4.9: Sampling locations superimposed on contours of (a) spanwise vorticity (b) streamwise velocity, $Re = 1.1 \times 10^5$.

1. Subcritical case: a_1 = (0.51D, 0.05D); a_2 = (0.55D, 5D).

2. Supercritical case: b_1 = (0.52D, 0.05D); b_2 = (0.36D, 5D).

The spectra indicate the quantitative differences between the physics of the flow before and after the drag crisis. The subcritical case (Figure 4.10 *a*) has nearly the same spectral distribution for the shear layer near the ball and in the wake. The supercritical case (Figure 4.10 *b*), however, shows a significant difference between the dominant frequency of the flow in the shear layer (b_1) and the flow in the wake (b_2). The spectra of the wake flow has a Strouhal number of St = 5, while the spectra of the flow near the ball has a Strouhal number of St = 12. Another dominant, lower-energy high-frequency peak is apparent in Figure 4.10 *b* at a Strouhal number of St = 70. This frequency mode is most likely linked with the break-up of the small structures in the shear layer. This probe (b_1), which is represented by the white dot in Figure 4.9 *a*, is placed strategically to capture the decay of these coherent structures.

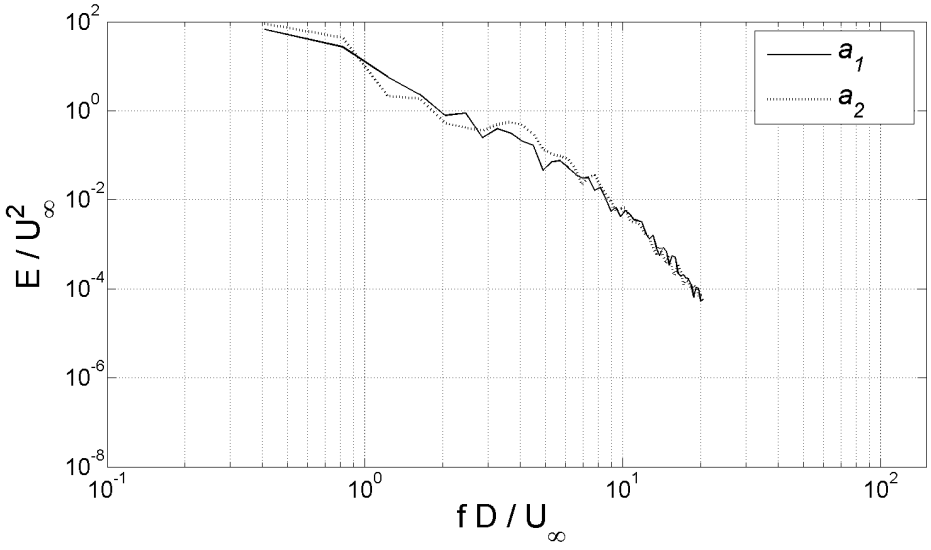

(*a*)

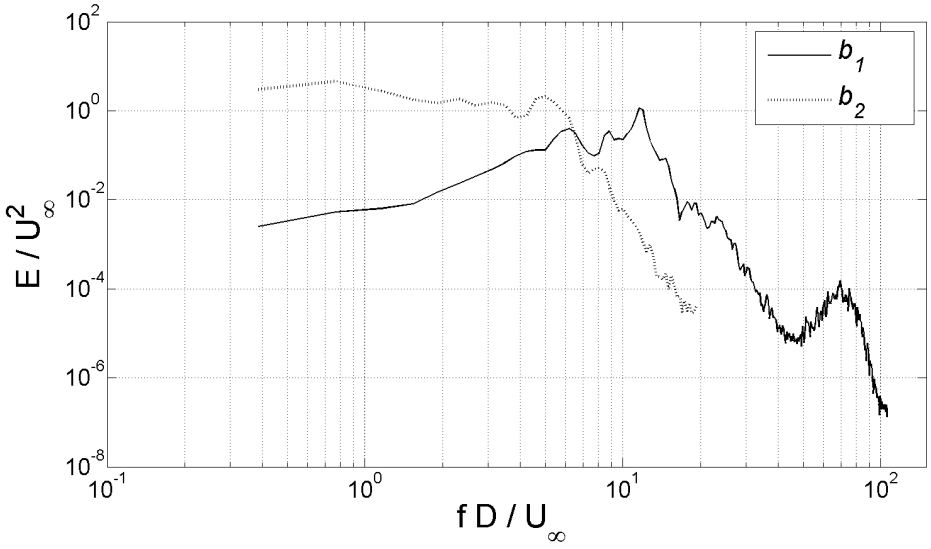

(*b*)

Figure 4.10: Energy spectra of radial velocity at selected locations (a) $Re = 2.5 \times 10^4$; (b) $Re = 1.1 \times 10^5$.

4.6 Summary

Direct numerical simulation (DNS) has been used to investigate the flow over an arbitrarily-oriented golf ball in the subcritical ($Re = 1.0 \times 10^4$, $Re = 2.5 \times 10^4$) and supercritical ($Re = 1.1 \times 10^5$) regimes. The simulations were performed using an

immersed boundary approach in which the golf ball is represented using momentum forcing applied on a background grid in a cylindrical coordinate system.

Flow visualizations in the near-wall region and in the wake reveal differences in the separation characteristics of the flow. The lengthscales of structures in the subcritical regime are generally larger than the diameter of the dimples, making local detachment within dimples impossible. Global flow separation occurs further upstream in the subcritical case, as would be expected for this physical regime. For supercritical flow, the lengthscales of vortical structures are smaller than the geometrical details of the dimples, leading to local detachment with dimples even in the mean.

Integrated forces on the golf ball compare reasonably well with existing measurements, and energy spectra of the velocity fluctuations reveal frequencies of with small-scale flow structures associated with a shear layer instability over the dimples.

This work will be extended in the following chapter. In order to increase the statistical sample, a symmetry axis of the golf ball is aligned with the flow, so that statistics can be averaged spatially and temporally. Further effort is devoted to high-fidelity visualizations of the wake and the dimples. Implementation of the preliminary reconstruction scheme is applied to study the pressure distribution on the golf ball. Velocity profiles and Reynolds stress profiles illuminate mean flow trends in the dimples.

Chapter 5

Subcritical and Supercritical Regimes: symmetrically-aligned golf ball

The over-arching objective of this work is the application of DNS to prediction of the flow over a golf ball in order to gain insights into the role of surface dimpling on flow physics. In the present study DNS results are reported for simulations performed pre- and post-drag crisis; in particular, for computations around a non-rotating ball in the subcritical ($\mathrm{Re} = 2.5 \times 10^4$) and supercritical regimes ($\mathrm{Re} = 1.1 \times 10^5$) that has the $1/5$ symmetry axis of the ball aligned with the flow direction.

5.1 Geometry and Grid

A geometry supplied by Srixon and comprised of approximately 300 spherical dimples is used in this study. The surface of the ball is discretized with a mesh of surface triangles connected by nodes. The dimple geometry on the golf ball has an axis of one-fifth symmetry. The symmetry axis is aligned with the freestream direction (c.f. Figure 5.1). The existence of the symmetry axis and its alignment with the freestream coordinate is advantageous since statistical sample can be improved by averaging over azimuthal planes, as well as time. For the statistics presented in the current work, samples were collected in the five azimuthal planes shown in Figure 5.1.

Simulations are conducted for a subcritical case at a Reynolds number of 2.5×10^4 and a supercritical case at a Reynolds number of 1.1×10^5. The grid sizes in the radial, azimuthal, and axial directions are summarized in Table 5.1. Grid refinement studies for both Reynolds numbers indicated that qualitative flow features (e.g., visualizations) as well as quantitative measures such as the aerodynamic forces could be accurately captured using the grid resolutions presented in Table 5.1.

The radial and axial grid point distributions were clustered to refine the grid near the golf ball. This was accomplished by modifying stretching ratios, e.g.,

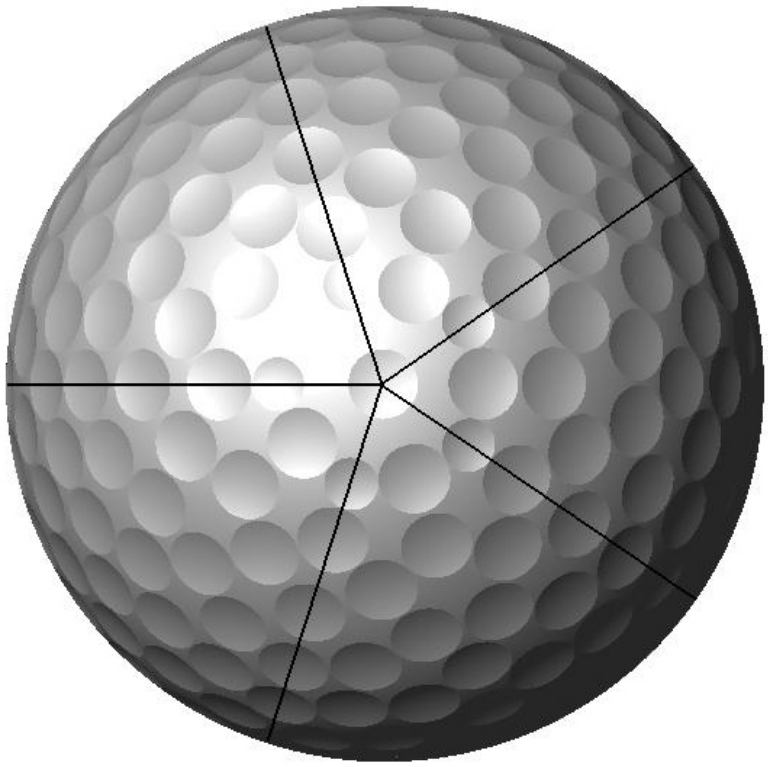

Figure 5.1: One-fifth symmetry of the 300-dimple golfball; present view looking from upstream of the golf ball toward the downwind direction.

Table 5.1: Grid resolution for present DNS: subcritical ($Re = 2.5\times10^4$) and supercritical regimes ($Re = 1.1\times10^5$).

Coordinate	Re = 2.5×10^4	Re = 1.1×10^5
Radial (R)	536	814
Azimuthal (θ)	252	502
Axial (Z)	2502	3002
Total grid points	337×10^6	1.2×10^9

a radial stretching ratio in the Re = 2.5×10^4 case changes from 0.984 ($\Delta R/D \approx 1.0\times10^{-2}$) near the center-line to 0.999 ($\Delta R/D \approx 8.0\times10^{-4}$) near the region of flow detachment. The radial and axial grids were then smoothed in order to avoid abrupt changes in spacing using a stencil that weighted the coordinate value of

a particular point twice as much as the point before and after it. As depicted in Figure 5.2, the grid near the dimple surface maintains an approximately uniform resolution in order to capture the velocity gradients and small-scale structures that develop over the ball. This approximate uniformity of the grid near the surface is maintained for both Reynolds numbers. For either Reynolds number, the azimuthal grid spacing is constant, finer by a factor of two at the higher Reynolds number. For the low Reynolds number flow there are approximately 120 points across the dimple at the top/bottom of the ball (90 degrees from the stagnation point) while for the high Reynolds number case the mesh resolution at the top/bottom of the ball is approximately 160 points across the dimple.

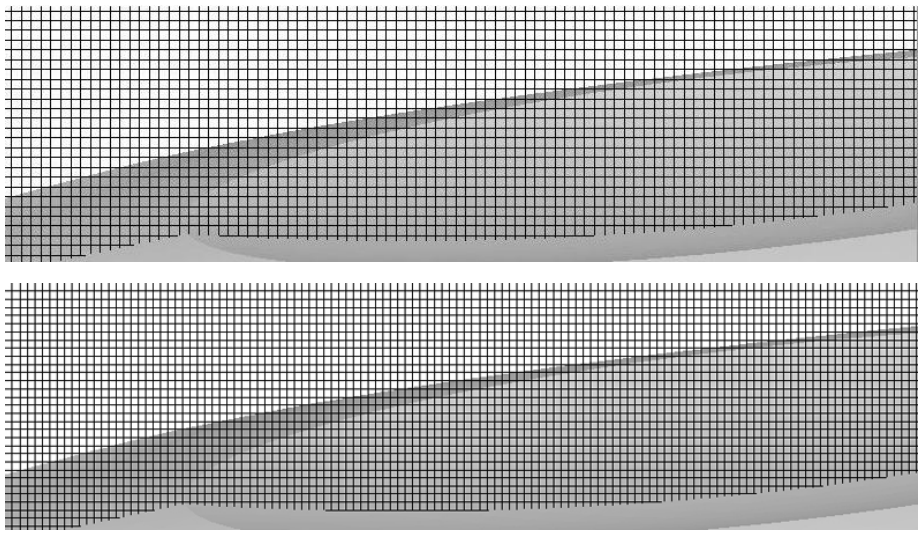

Figure 5.2: Example grid resolution in a dimple near 84 degrees (measured from the stagnation point at the front of the golf ball) (a) $Re = 2.5 \times 10^4$; (b) $Re = 1.1 \times 10^5$.

Solutions are obtained in a domain that extends 10 D (where D is the golf ball diameter) in the radial direction and 40 D in the axial direction. The center of the golf ball is 10 D from the inlet to the computational domain (corresponding to the front stagnation point at 9.5 diameters from the inlet), as illustrated in Figure 5.3.

The *R-Z* plane shown in Figure 5.3 is revolved about the centerline in the azimuthal dimension, θ.

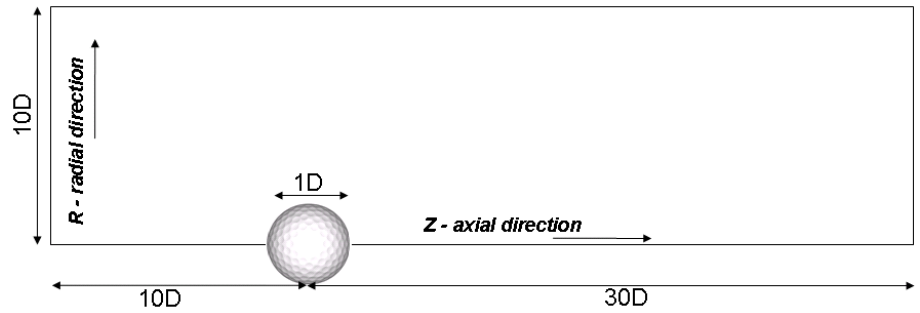

Figure 5.3: Computational domain, cylindrical coordinates. The *R-Z* slice shown in revolved about the centerline to create the entire domain.

5.2 Flow Visualization: Near-Wall Region

Visualizations of the instantaneous azimuthal vorticity near the golf ball in Figure 5.4 provide one illustration of the effect of the Reynolds number on separation characteristics. In the subcritical case (Figure 5.4a), separation does not appear strongly influenced by the dimples, and roll-up of the shear-layer occurs following boundary layer detachment. In the supercritical case (Figure 5.4b), visualization of the instantaneous vorticity reveals intriguing structures that have length scales comparable to the dimple dimensions. Figure 5.4b shows that within dimples there are shear layers that develop following detachment of the flow from the leading edge of the dimple, a similar feature being advanced by Choi *et al.* [25] based on their measurements. The development of these shear layers over and within individual dimples appears qualitatively similar to the wavering shear layer results of Spalart & Strelets [92].

Further magnification of the near-wall flow for both regimes is depicted in Figure 5.5. Contours of the azimuthal vorticity are plotted on an axial plane along with contours of the streamwise velocity in azimuthal planes. For the subcritical case

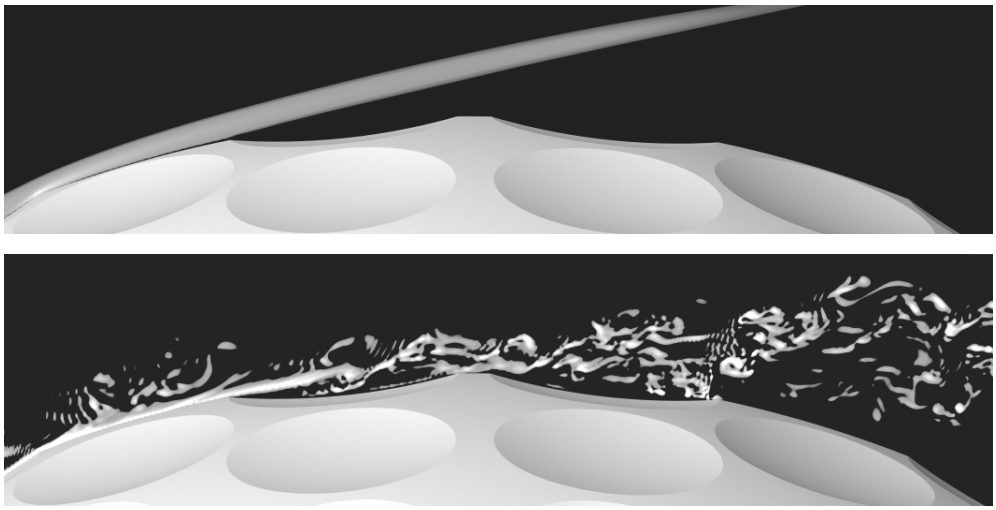

Figure 5.4: Instantaneous contours of spanwise (azimuthal) vorticity (a) $Re = 2.5 \times 10^4$; (b) $Re = 1.1 \times 10^5$.

(Figure 5.5a), the azimuthal vorticity exhibits relatively little variation as the flow evolves across a dimple near the location of flow detachment. As the flow evolves from the front to the rear of the same dimple in the supercritical case (Figure 5.5b), local detachment leads to small-scale structures resulting from the shear-layer development over the dimple. These small-scale structures (produced by the shear layer over the center of the dimple in Figure 5.4b) are being advected downstream by the bulk flow.

The structures highlighted in Figure 5.4b and Figure 5.5b for the high Reynolds number increase the momentum of the near-wall flow and lead to local reattachment as the flow exits the dimple. This process repeats through several dimples until complete detachment occurs, as displayed in Figure 5.6. Here, time-averaged contours of the streamwise velocity are displayed at increasing angles from the stagnation point in an azimuthal plane.

Figure 5.6b shows that the flow at 52 degrees and 63 degrees detaches downstream of the leading edge of the dimple. The flow appears to reattach to the surface

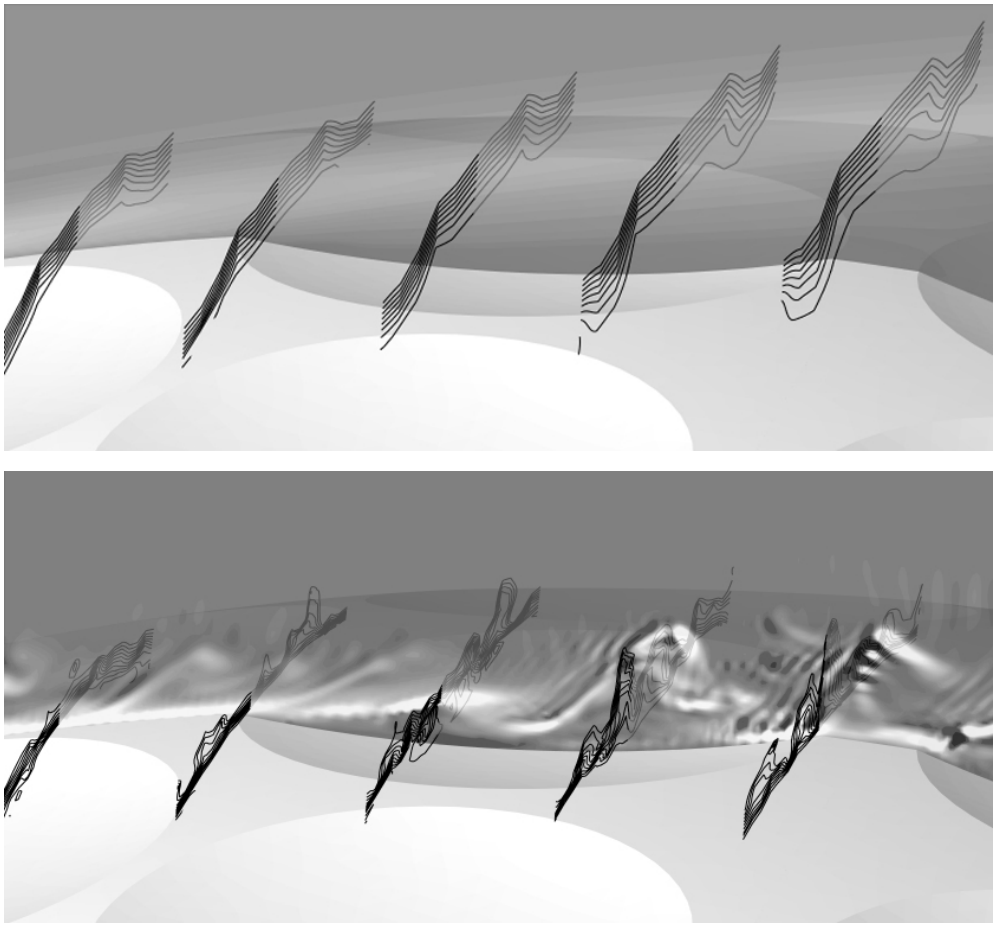

Figure 5.5: Contours of azimuthal vorticity in an axial plane (background) and streamwise velocity in azimuthal planes in dimples near flow detachment; (a) $Re = 2.5 \times 10^4$; (b) $Re = 1.1 \times 10^5$.

as it exits the dimple at 63 degrees, as depicted in Figure 5.6b. Around 74 degrees, the flow remains attached until it traverses the dimple at 84 degrees. Even as the flow exits the dimple at 84 degrees, it appears to reattach to the leeward side of the dimple surface before it detaches again around 96 degrees (not shown).

The flow patterns within dimples and in the region of complete detachment are depicted in Figure 5.7. The subcritical case depicts the mean flow which follows the boundary until detachment at around 84 degrees. This separation region is characterized by the recirculation apparent in Figure 5.7a. The supercritical case

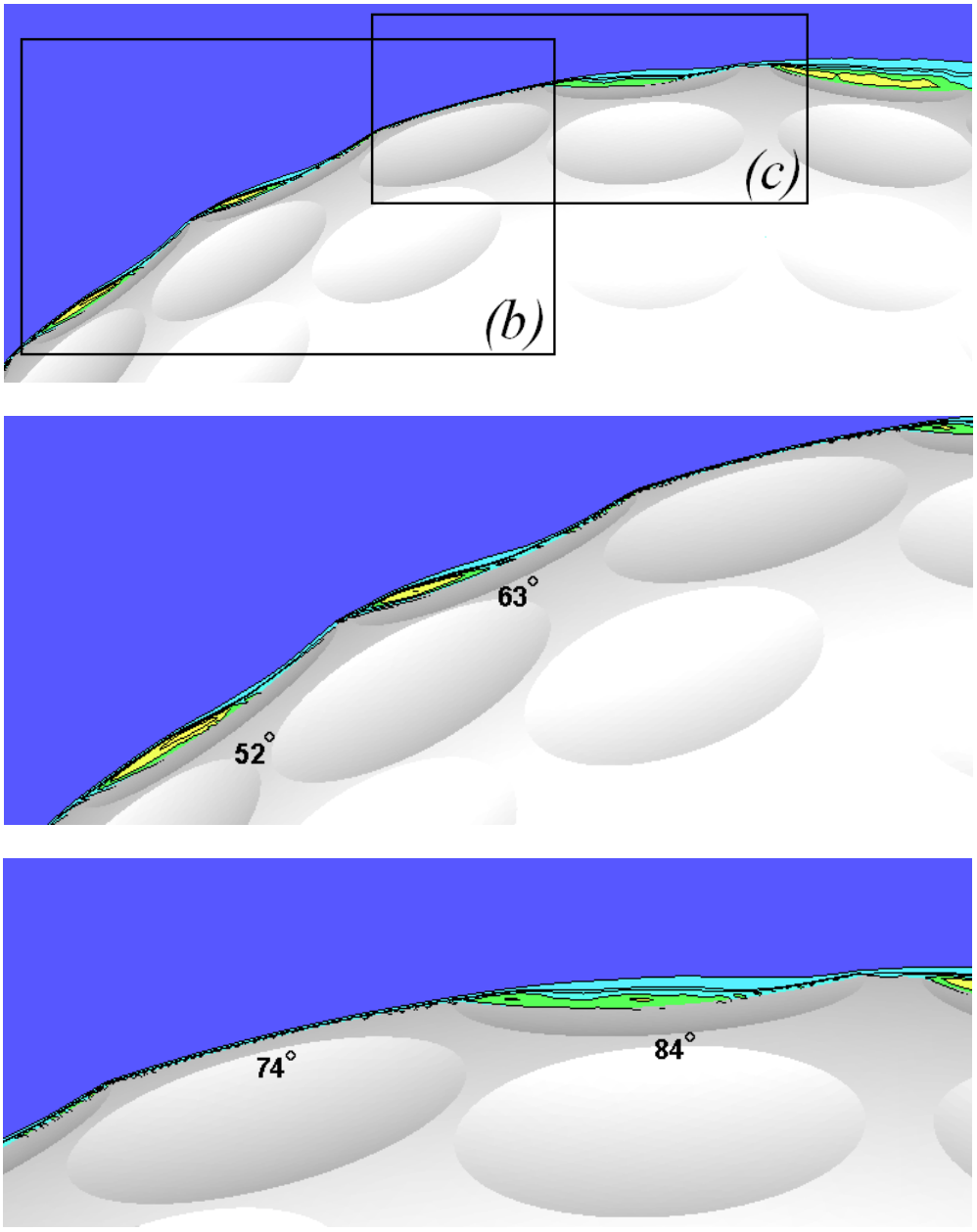

Figure 5.6: Time-averaged contours of the streamwise velocity, $Re = 1.1 \times 10^5$: (a) complete view (b) view at 52°, 63°; (c) view at 74°, 84° (angles measured from stagnation point at the front of the golf ball to the dimple centers).

shows regions of local recirculation within individual dimples in Figures 5.6a-c and 5.7b which transport momentum into the near-wall region and ultimately delay complete detachment until around 110 degrees.

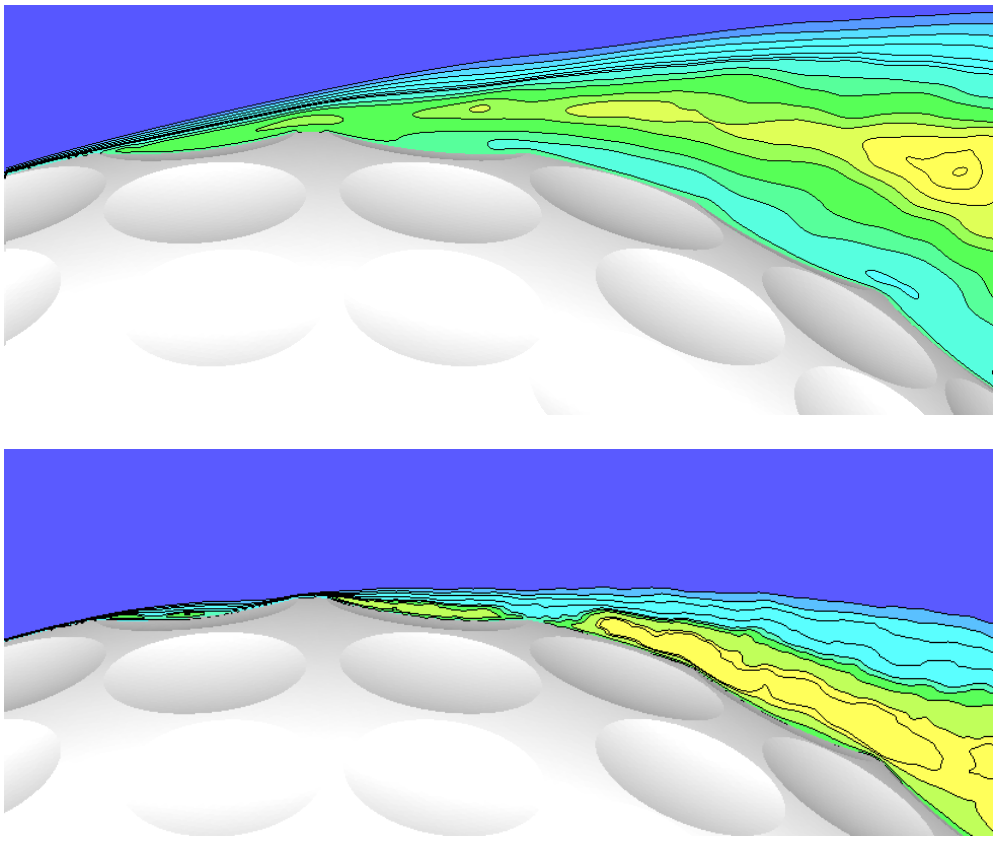

(*a*)

(*b*)

Figure 5.7: Time-averaged contours of streamwise velocity (a) $Re = 2.5 \times 10^4$; (b) $Re = 1.1 \times 10^5$.

5.3 Flow Visualization: Wake

Contours of the instantaneous azimuthal vorticity are displayed in Figure 5.8 for both Reynolds numbers. As suggested by visualizations in the near-wall region, complete detachment occurs much earlier for the subcritical case (prior to 90 degrees) in this particular plane. A Kelvin-Helmholtz rollup of the separated shear

layers is observed downstream of flow detachment at the subcritical Reynolds number. Similar Kelvin-Helmholtz-type behavior occurs upstream of complete flow detachment for the supercritical Reynolds number (even occurring within individual dimples; c.f., Figures 5.4, 5.5), illustrating one of clearest differences between the two physical regimes. The supercritical Reynolds number result displays flow detachment which is delayed further into the region of adverse pressure gradient, and the shed vortices are difficult to distinguish due to their small size.

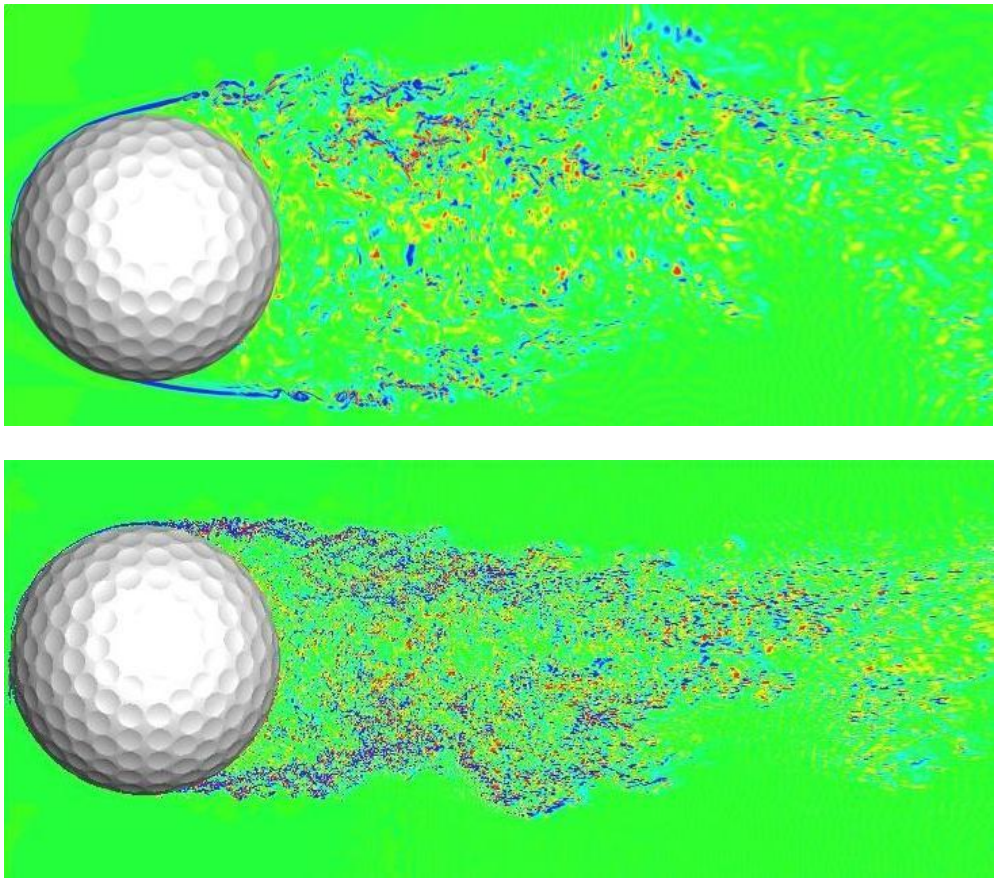

(*a*)

(*b*)

Figure 5.8: Instantaneous contours of spanwise (azimuthal) vorticity (a) $Re = 2.5 \times 10^4$; (b) $Re = 1.1 \times 10^5$.

Further insight into the shed structures for both regimes is provided by isosurfaces depicted in Figures 5.9 and 5.10 using the Q-criterion method of Hunt *et al.*

[45]. This vortex identification approach identifies convex, low-pressure tubes, which are usually associated with coherent vortices. Prior to the drag crisis (Figure 5.9), the vortical structures in the wake originate approximately 0.25 D downstream of complete flow detachment. Finger-like striations in the isocontour surface are also apparent between complete detachment and the point where smaller structures form in the wake. For the supercritical Reynolds number, the generation of vortical structures occurs within dimples, forming "streets" of small vortices which are shed from the leading edge of dimples. The supercritical results in Figure 5.10 also show clear evidence of large-scale shedding, particularly in Figure 5.10a. There also appears to be some large-scale spiral motion of the wake, which is mostly evident in Figure 5.10b. The orientation of the shed vortices appears to change further downstream, and this is confirmed by investigation of streamwise vorticity contours at select crossflow locations (ref. Figure 5.11).

Further details of the wake structure for the two regimes are illustrated in the streamwise vorticity contours in planes normal to the freestream direction, shown in Figure 5.11 at $1.0D$ and $2.0D$ from the center of the golf ball. An interesting difference in the wake structure is observed for the subcritical and supercritical flow at $z/D = 1.0D$. In particular, the size of the wake for the subcritical Reynolds number (Figure 5.11a) is larger than the diameter of the golf ball, extending beyond the ball in an approximately symmetric fashion. In contrast, the supercritical result demonstrates that the wake is comparable to, if not smaller, than the golf ball, as indicated in Figure 5.11c. Even further downstream ($z/D = 2.0D$), there are other interesting differences in the vorticity contours. The scale of the structures clearly differs, while some degree of asymmetry in the wake is illustrated in the subcritical vorticity contours (Figure 5.11b). The vorticity contours for the supercritical flow indicate that the wake is approximately symmetric at that location as well, although the wake has grown as the structure grow outward (Figure 5.11d).

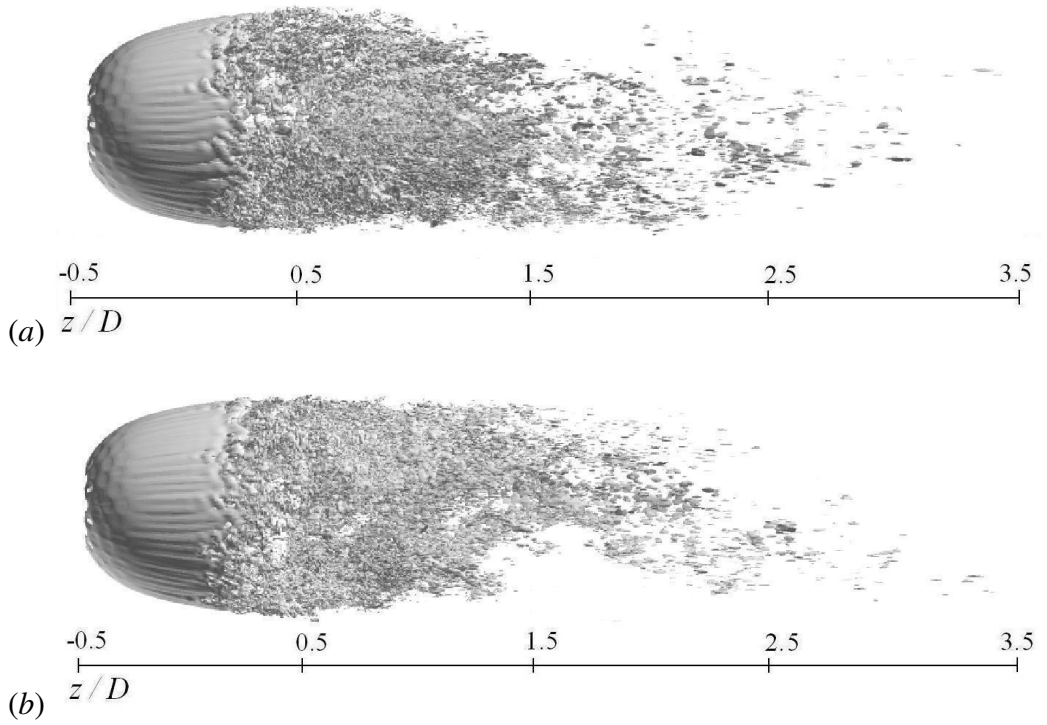

Figure 5.9: Visualization of vortical structures using the Q-criterion method of Hunt *et al.* [45], $Re = 2.5 \times 10^4$ (a) $\phi = 0°$ plane; (b) $\phi = 90°$ plane.

5.4 Statistical Features - Aerodynamic Forces

Averaged values of the drag are summarized together with experimental measurements for both Reynolds numbers in Figure 5.12. The values shown in Figure 5.12 have been obtained from averages of the force history acquired over approximately 20 D/U time units from the subcritical case, and 15 D/U time units from the supercritical case. For the subcritical regime, 20 time units corresponds to 3-4 vortex-shedding cycles. In the supercritical case, 15 time units corresponds to 8-10 vortex-shedding cycles, in which a vortex-shedding cycle is characterized by one oscillation period of the lift force history.

As shown in Figure 5.12, the DNS results are in the range of the measurements reported by Achenbach [3], [11], and Choi *et al.* [25]. DNS of the subcritical case

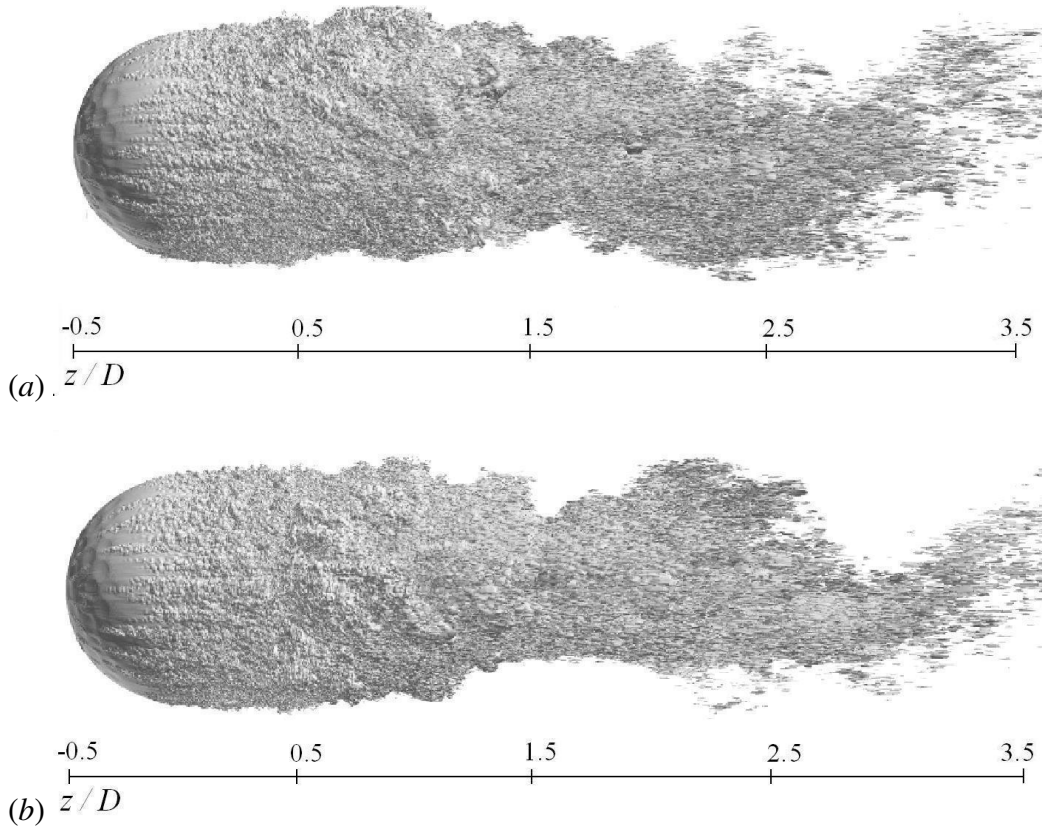

Figure 5.10: Visualization of vortical structures using the Q-criterion method of [45], $Re = 1.1 \times 10^5$ (a) $\phi = 0°$ plane; (b) $\phi = 90°$ plane.

at $Re = 2.5 \times 10^4$ yields $C_D = 0.47$, close to the value for a smooth sphere of $C_D = 0.45$ reported by Achenbach at the same Reynolds number, implying a similar separation process in the flow around a golf ball at this Reynolds number. DNS of the supercritical case at $Re = 1.1 \times 10^5$ leads to $C_D = 0.26$ that is nominally higher than the measurements of Bearman and Harvey ($Re = 4.0 \times 10^4$ to $Re = 2.4 \times 10^5$) and approximately two percent higher than the measurements of Choi *et al.* [25] ($Re = 5.0 \times 10^4$ to $Re = 2.8 \times 10^5$). An important distinction between the studies in the number of dimples on each golf ball. Bearman and Harvey studied a golf ball that had 330-336 spherical dimples arranged in rows. The golf ball used by Choi *et al.* [25] had 392 spherical dimples, while the golf ball used in the current

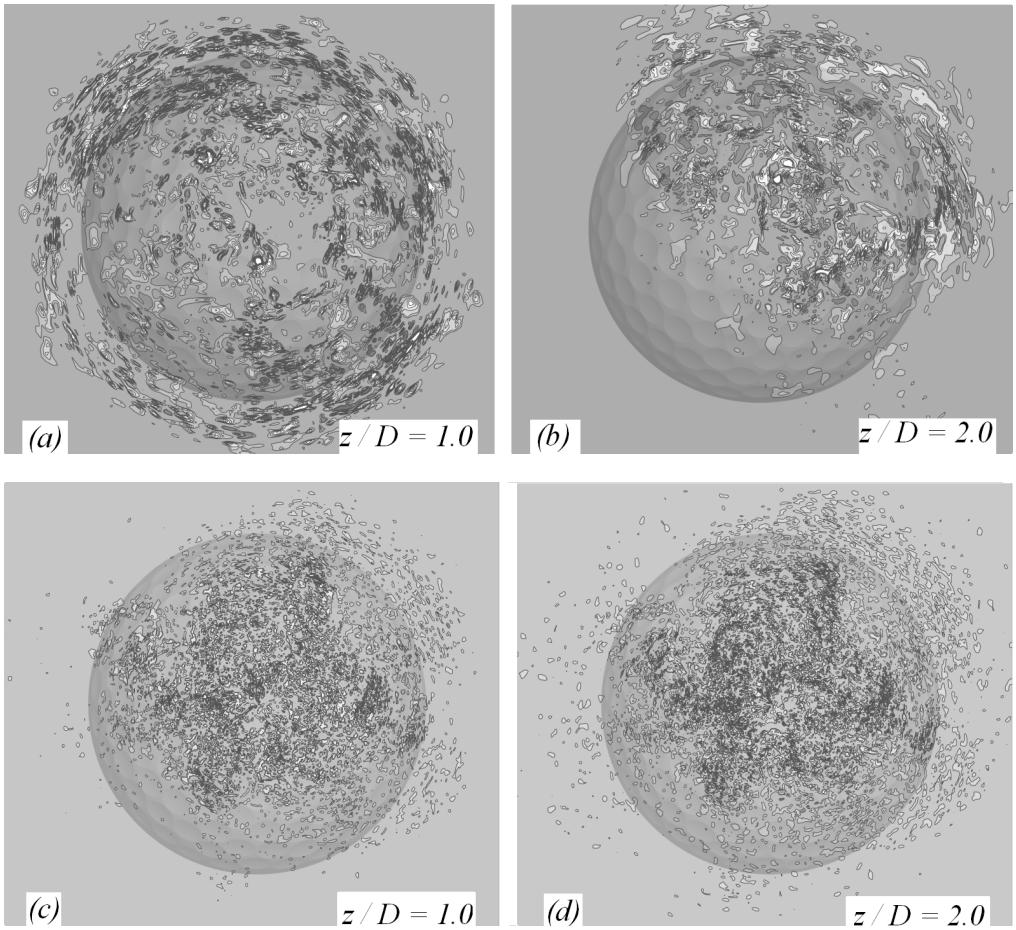

Figure 5.11: Streamwise vorticity component in the crossflow plane at z/D = 1.0 and z/D = 2.0, (a),(b) $Re = 2.5\times10^4$; (c),(d) $Re = 1.1\times10^5$.

work has approximately 300 spherical dimples. Another metric that characterizes the geometries, and differs among the studies, is the dimensionless dimple depth, k/D, where k represents the depth of a dimple and D is the ball diameter (c.f., Figure 5.13). In Bearman and Harvey, $k/D = 9.0\times10^{-3}$, for Choi et al. $k/D = 4.0\times10^{-3}$, and the present DNS has $k\ /\ D_{max} = 6.0\times10^{-3}$. The dimple geometry, along with related factors such as the overall number and distribution of dimples for the different cases, contribute to the changes in the drag between the experiments and simulations.

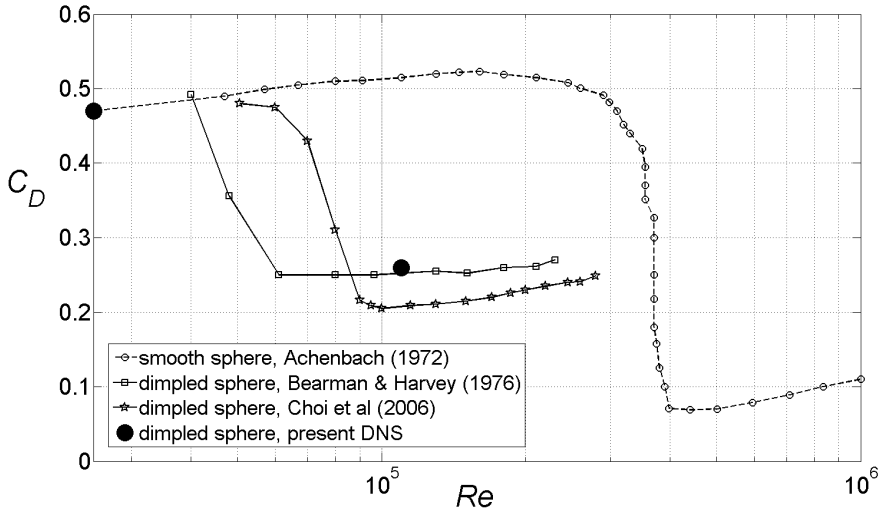

Figure 5.12: Drag coefficient from current DNS along with measurements from Achenbach [3], Bearman & Harvey [11], and Choi *et al.* [25].

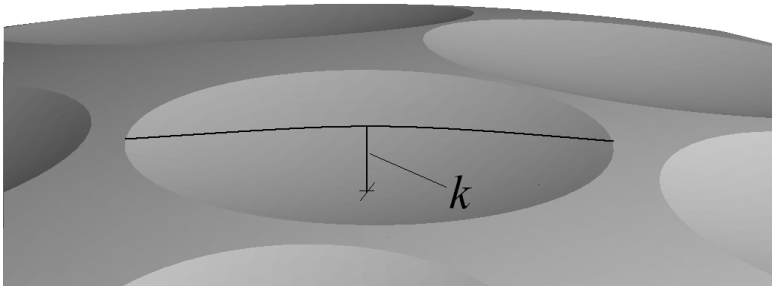

Figure 5.13: Example of dimple depth, k for the present 300-dimple golf ball oriented symmetrically.

5.5 Statistical Features - Pressure

Distributions of the pressure coefficient C_p are presented in Figures 5.14, 5.15, and 5.16 for the subcritical and supercritical regimes. Calculation of C_P using an immersed boundary approach is non-trivial since the pressure is not computed or stored on the immersed object during integration of the governing equations. In the current work, the pressure is projected onto the golf ball using an extrapolation from points directly outside the surface as described in Chapter 3.

The subcritical case from the present DNS compares reasonably well with the results of Constantinescu & Squires [29] in the subcritical flow around a smooth sphere at $Re = 1.0 \times 10^4$, indicating a similarity in the normal force distribution between the two flows in their respective pre-drag crisis states. The supercritical pressure distribution in the current work compares reasonably well with the measurements of Achenbach [3], in which the flow over a smooth sphere was measured at $Re = 3.18 \times 10^5$, again suggesting similarity in the normal force distribution for the flow over a golf ball and a smooth sphere. The delay in complete separation for the supercritical case substantially decreases the minimum C_P as compared to the subcritical case. Interestingly, prior to 90 degrees, C_P for both flow regimes exhibits small local increases at approximately the same angular positions of 40, 50, and 60 degrees (measured from the front stagnation point). Further investigation of this effect indicates that these small increases in C_P correspond to the local deceleration of the flow as it exits the trailing edge of the dimples at these angular positions. This is confirmed by observation of the inset of Figure 5.14, which displays time-averaged contours of the pressure coefficient in a plane near the angular positions of 40, 50, and 60 degrees. The subcritical result shown in Figure 5.14 (mean C_P versus the angle measured from the stagnation point) at 40, 50, and 60 degrees yields $C_P = 0.2$, $C_P = -0.1$, and $C_P = -0.35$, respectively, which correspond to the contours in Figure 5.14, inset a. Pressure coefficients for the supercritical regime in Figure 5.14 at 40, 50, and 60 degrees are $C_P = 0.15$, $C_P = -0.2$, and $C_P = -0.45$, respectively, as confirmed by comparison with the contours of Figure 5.14, inset b. Small local increases in C_P are also observed upstream at approximately 18 and 25 degrees for the supercritical regime.

Contours of the mean pressure coefficient (C_P) on the surface of the golf ball reveal another view of the effect of the dimples in both flow regimes. The stagnation point and associated region of high pressure is displayed in Figure 5.15a

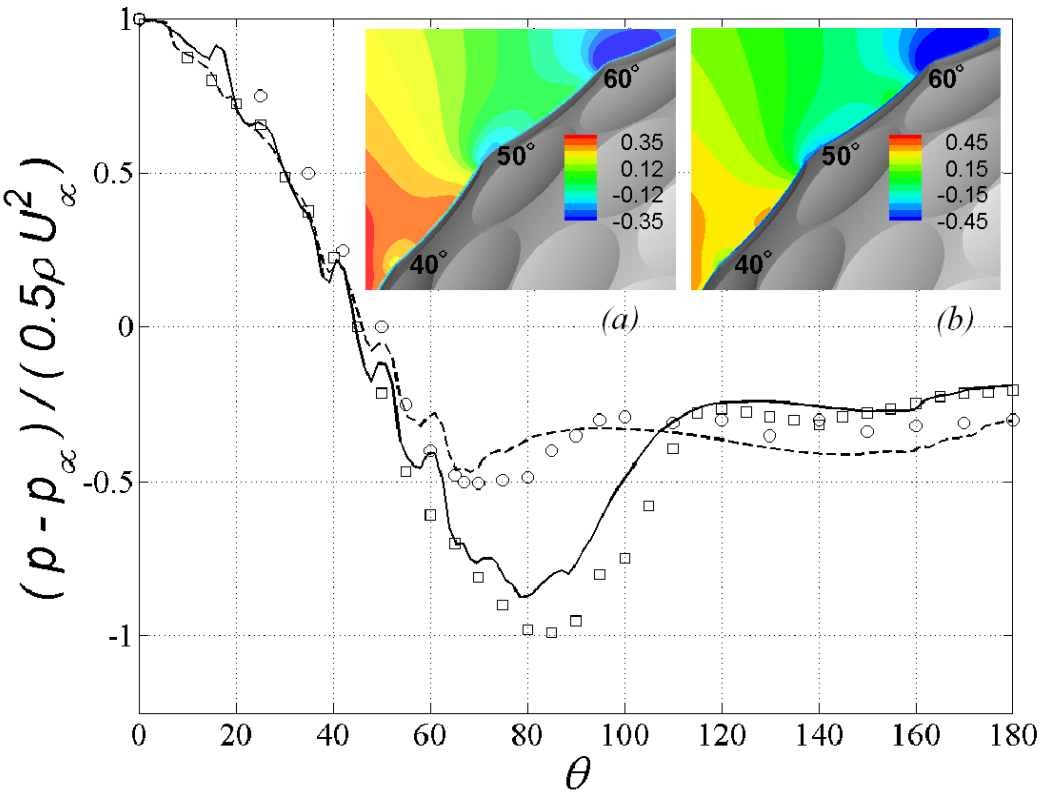

Figure 5.14: Mean pressure coefficient: −− $Re = 2.5 \times 10^4$ golf ball, present DNS; — $Re = 1.1 \times 10^5$ golf ball, present DNS; ◯ $Re = 1.0 \times 10^4$ sphere, subcritical calculation of Constantinescu & Squires [29]; □ $Re = 3.18 \times 10^5$ sphere, supercritical measurement of Achenbach [3]. Inset, C_P contours: (a) $Re = 2.5 \times 10^4$, present DNS; (b) $Re = 1.1 \times 10^5$, present DNS.

for the subcritical case, and in Figure 5.15b for the supercritical Reynolds number. The pressure coefficient decreases as the flow accelerates from the front stagnation point around the ball. C_P decreases to its minimum around 65 degrees from the stagnation point for the subcritical regime ($C_P = -0.49$), and around 80 degrees for the supercritical regime ($C_P = -0.8$). In the subcritical regime, the pressure coefficient increases from -0.49 at 65 degrees to approximately -0.3 on the leeward side of the golf ball, corresponding to the behavior for a smooth sphere at a subcritical Reynolds number (reference Achenbach [3]). In the supercritical case, the pressure coefficient eventually recovers to $C_P = -0.25$ on the leeward side of the golf ball.

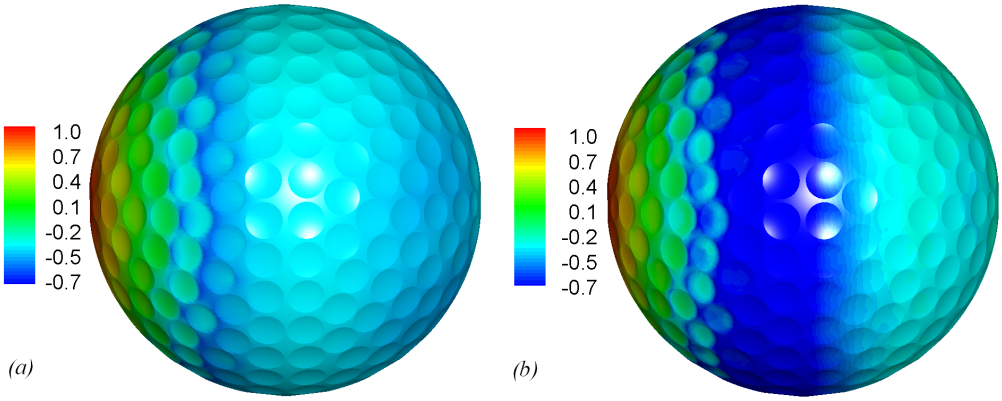

Figure 5.15: Contours of the mean pressure coefficient on the surface (side view): (a) $Re = 2.5 \times 10^4$; (b) $Re = 1.1 \times 10^5$.

Contours of the pressure coefficient on the leeward side of the golf ball for a single instant in time (Figure 5.16a,b) display the chaotic effects from the impinging turbulent structures being generated downstream of separation and in the near wake. Vorticity contours in Figure 5.8 illustrate planar perspectives of these structures on the leeward side of the golf ball, and corroborate the pressure coefficient results of Figure 5.16. Figures 5.8 and 5.16 indicate the increased presence of small scale structures on the leeward side of the golf ball for the supercritical regime, while larger-scale, less frequent structures dominate the leeward flow in the subcritical case. As with the side views shown in Figure 5.15, the differences in flow separation characteristics are apparent in the pressure distribution on the leeward side of the ball.

5.6 Statistical Features - Velocity profiles

Velocity profiles in a tangent-normal coordinate system shown in Figure 5.18 were acquired at several locations in the symmetry planes (c.f., Figure 5.1). The location of the profiles are shown in Figure 5.17 and numbered 1 through 7; the profile is acquired at 90 points along each of the surface-normal lines shown. The sampling locations within dimples (locations 1, 2, 4, 6) and on the outer surface of the golf

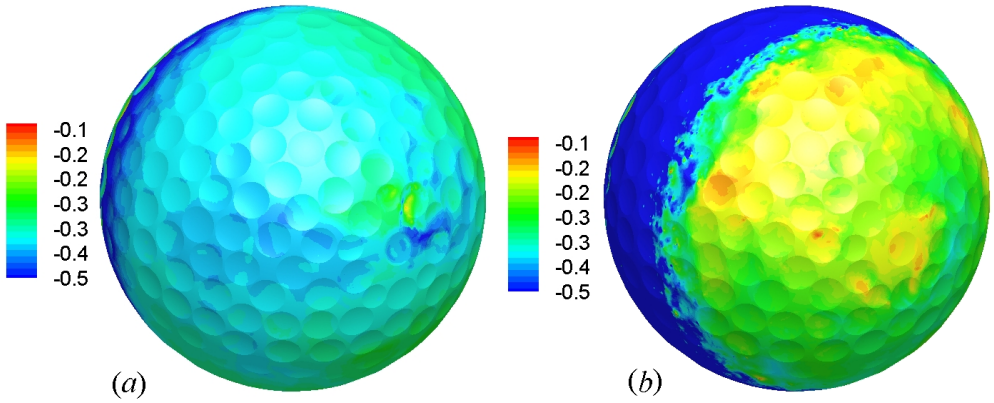

Figure 5.16: Contours of the instantaneous pressure coefficient on the surface (leeward view): (a) $Re = 2.5 \times 10^4$; (b) $Re = 1.1 \times 10^5$.

ball (locations 3, 5, 7) were chosen to gather statistics at the locations where the flow is locally detaching and reattaching (c.f. Figure 5.6).

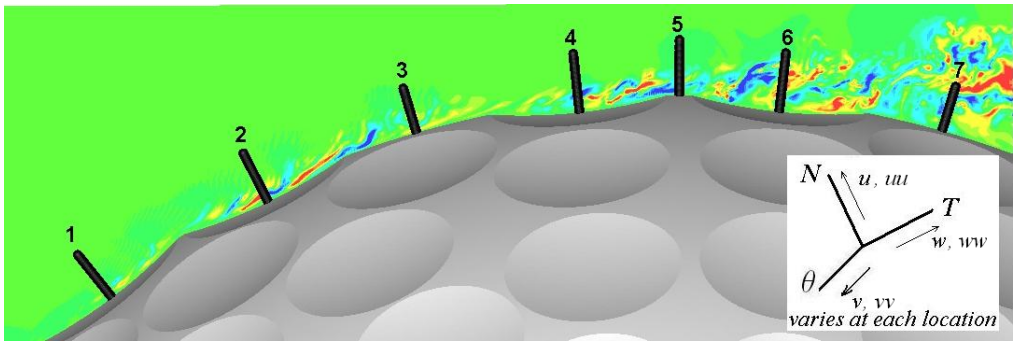

Figure 5.17: Profile locations in each of the symmetry planes; background contour shows the azimuthal velocity at $Re = 1.1 \times 10^5$ (angle measured from stagnation point in a symmetry plane): location 1 - 52°; location 2 - 63°; location 3 - 74°; location 4 - 84°; location 5 - 90°; location 6 - 96°; location 7 - 106°.

Statistics of the velocity field acquired at these locations are averaged in time and in space (azimuthally). For each location, the velocity components are displayed in tangent-normal coordinates along a scaled wall-normal coordinate in Figure 5.18a-f. The azimuthal component is nearly zero for both Reynolds numbers, and is therefore not shown.

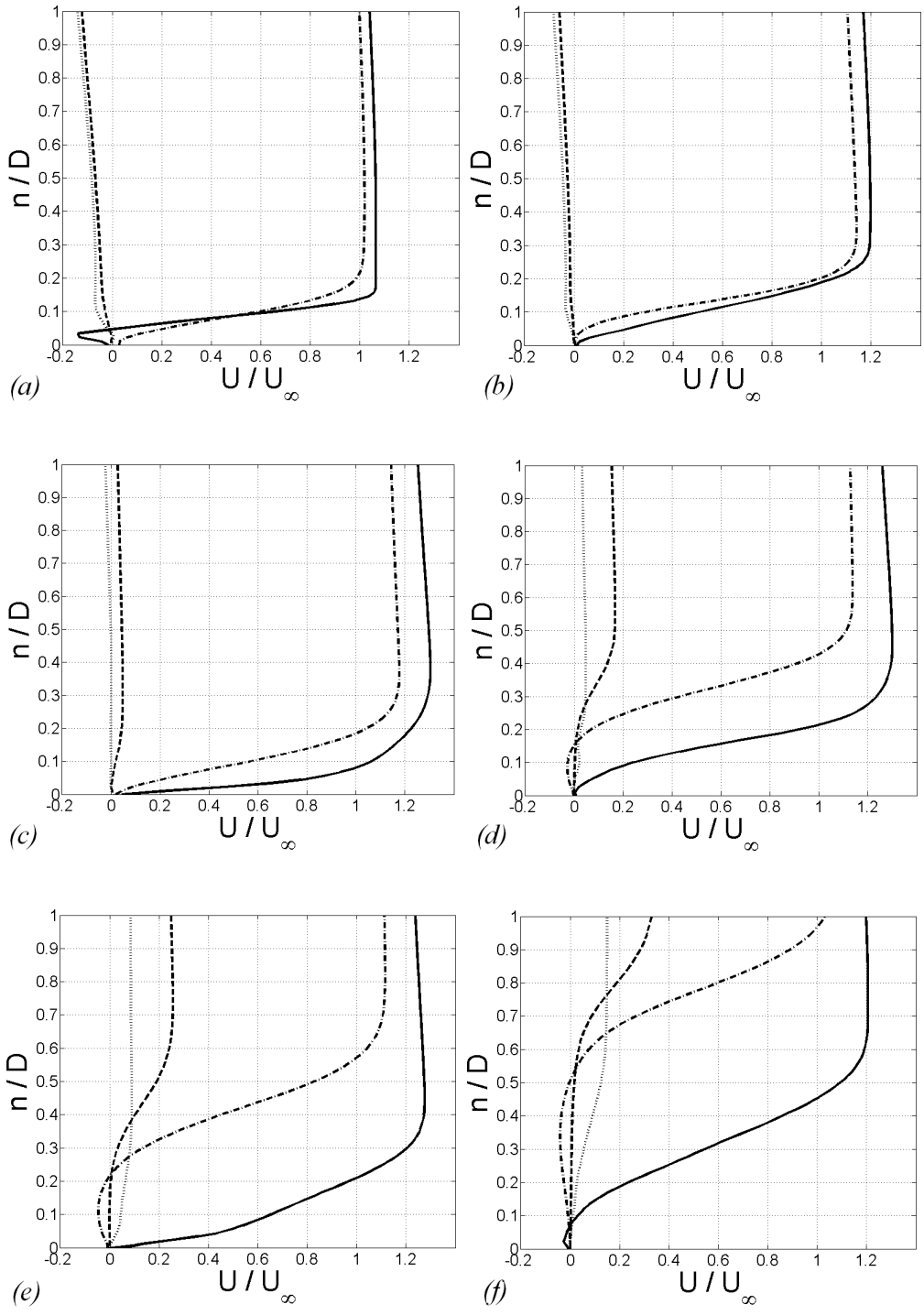

Figure 5.18: Mean velocity profiles at locations 1-6 in frames (a)-(f), respectively. $---$ u (normal) $Re = 2.5 \times 10^4$; $-.-$ w (tangential) $Re = 2.5 \times 10^4$; $\cdots$ u (normal) $Re = 1.1 \times 10^5$; — w (tangential) $Re = 1.1 \times 10^5$.

Mean velocity profiles for the subcritical case in Figure 5.18 quantify the behavior suggested by the visualizations. Locations 1-3 (Figure 5.18a-c) depict velocity profiles that are analogous to a laminar boundary layer. Slight reversal of the flow is observed in the tangential average at location 4 (Figure 5.18d), with increasing reversal at locations 5 and 6 (Figure 5.18e,f). Non-zero values of the wall-normal component become more prominent at location 5, owing to the complex structure of the flow at and past the point of detachment. For the subcritical case, flow detachment begins as early as location 4 (prior to 84 degrees) and appears to be complete around 90 degrees (c.f. Figure 5.7a).

For the high Reynolds number case, the mean velocity profiles also quantify the behavior illustrated by the flow visualizations. For the supercritical flow, it is locations 1-2 (Figure 5.18a-b) that have velocity profiles similar to those of a laminar boundary layer. Location 1 exhibits a small region of reversed flow in the wall-tangent component, corresponding to the local separation bubble observed at the same location in Figure 5.6b. The velocity field at location 4 (Figure 5.18d) may be affected by the Kelvin-Helmholtz type instabilities in the dimple, as shown by the slight reduction of the tangential component at approximately $n/D = 0.1$. Profiles at locations 3 and 5 (Figure 5.18c,e) suggest high rates of momentum transfer. These mean profiles indicate that the flow detachment begins further into the wake for the supercritical case (approximately 110 degrees, c.f., Figure 5.7b). The profile at location 6 (Figure 5.18f) also captures a local flow reversal.

5.7 Statistical Features - Frequency spectra

Additional insight into the flow physics is provided by the frequency spectra of the velocity. The solution was sampled at locations near the ball to extract the frequencies of vortex formation in the shear layers. Time series were acquired in the shear layer that develops over the dimple at 96 degrees from the stagnation

point (Location 6) (c.f. Figure 5.18, 5.19) in the symmetry planes. This is the same location at which flow reversal is observed in the average (Figure 5.18f). The resulting spectra of the radial and axial velocity are shown in Figure 5.20a,b.

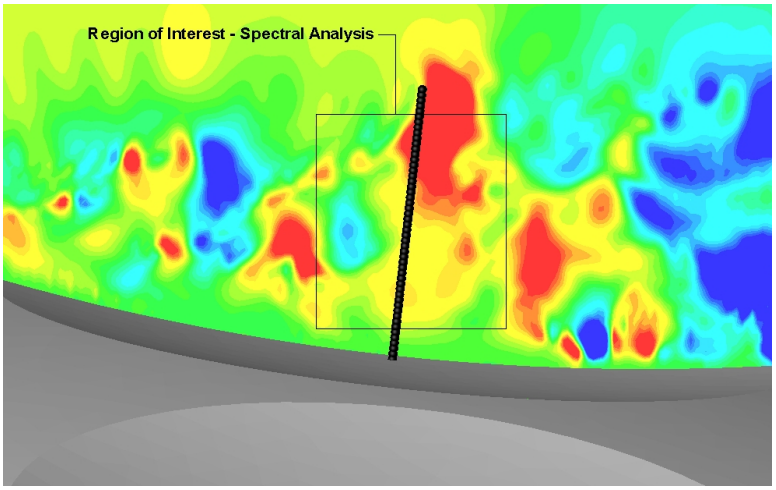

Figure 5.19: Sampling location of energy spectra within the shear layer (superimposed on instantaneous contours of radial velocity) at 96°, $Re = 1.1 \times 10^5$.

The spectra highlight the energy of the flow near complete detachment for the supercritical Reynolds number. The figure indicates two peaks at higher Strouhal numbers around 40 and 60. The first peak is associated with the K-H instability in the shear layer. The latter is comparable to estimates of the frequencies associated with the small structures over the dimples deduced from visualizations. Estimates of the Kolmogorov time scale yields a non-dimensional frequency of $f_\eta \approx 77$, which is in the range of the spectral peaks depicted in Figure 5.20.

5.8 Statistical Features - Reynolds stresses

Momentum transport from the fluctuating velocity field is analyzed via investigation of the Reynolds stresses. Statistics of the flow for the subcritical case have been computed from averages over approximately 20 time units and for the supercritical case over approximately 4.5 time units, sufficient to elucidate trends though not statistically converged. As with the mean velocity, the Reynolds stresses are

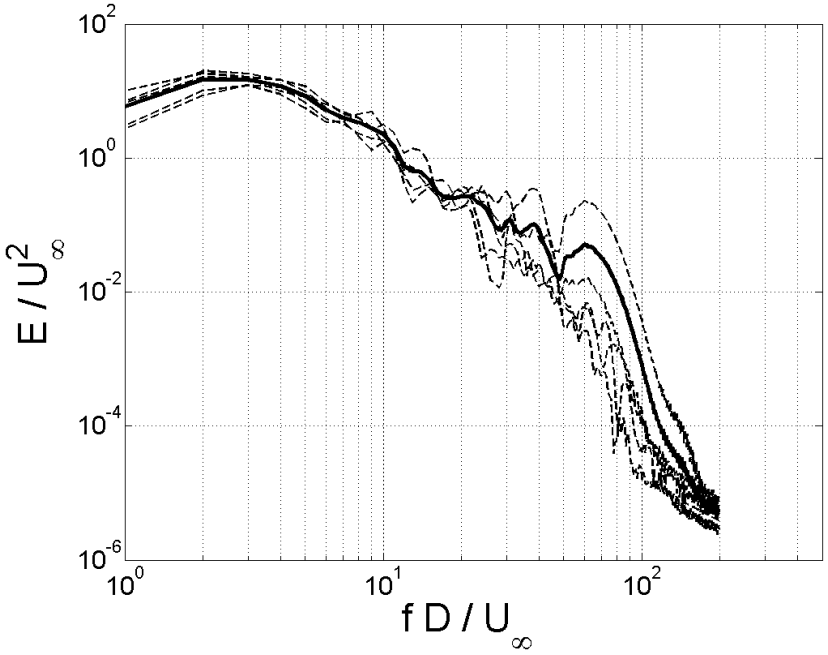

(*a*)

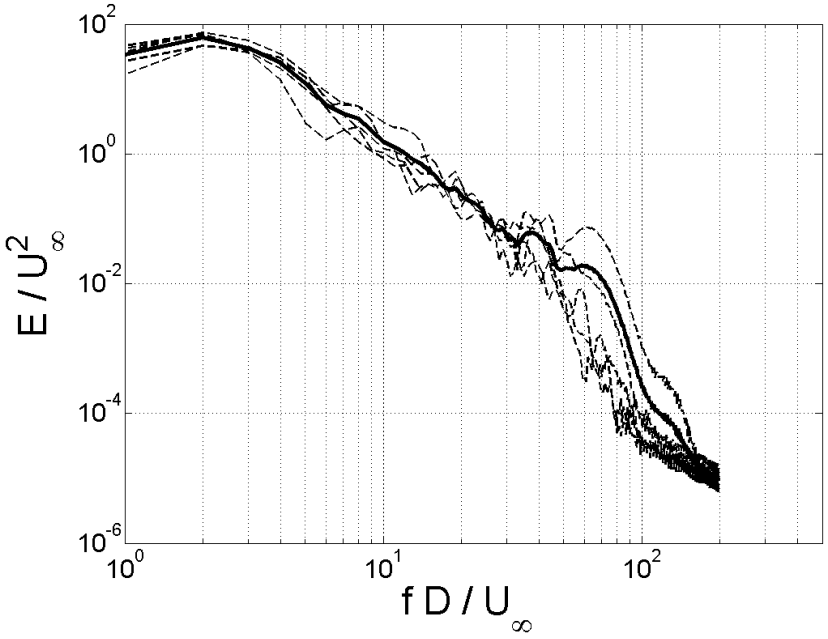

(*b*)

Figure 5.20: Energy spectra of radial, axial velocity at 96°, $Re = 1.1 \times 10^5$: – – – individual plane results, — spatially-averaged result (a) U (radial) spectra; (b) W (axial) spectra.

averaged in the azimuth (again exploiting the symmetry of the geometry) and are plotted in wall-normal coordinates. The Reynolds stresses are non-dimensionalized by the free-stream velocity and the wall-normal coordinate is scaled by the golf ball diameter. Reynolds stress trends for the subcritical and supercritical regimes are displayed in Figures 5.21-5.22.

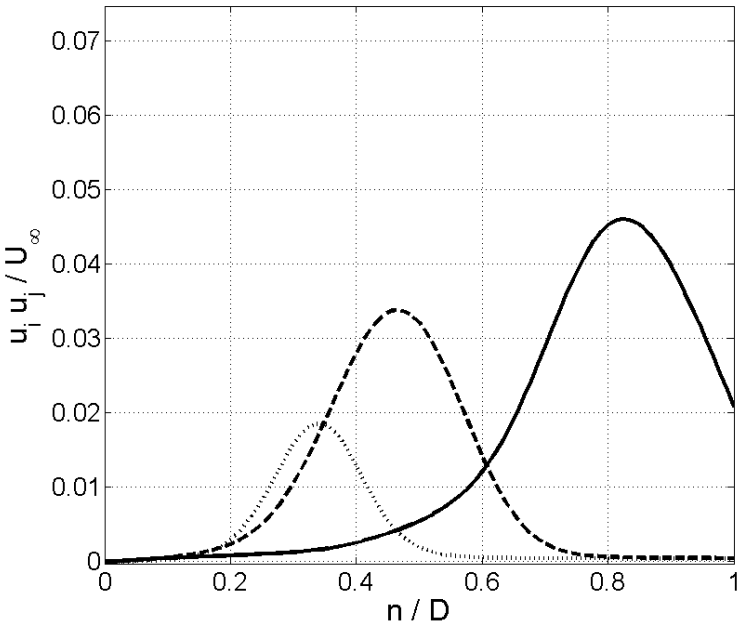

Figure 5.21: Development of *ww* (tangential) Reynolds stress from Location 4-6, $Re = 2.5 \times 10^4$: $\cdots$ *ww*, location 4; $- - -$ *ww*, location 5; — *ww*, location 6.

The Reynolds stress for the subcritical case in Figure 5.21 are consistent with the behavior suggested by the velocity profiles in Figure 5.18. As the flow evolves from the dimple at 84 degrees to 90 degrees (locations 4 and 5, respectively), the *ww* stress (tangential) increases by a factor of two. The largest value of the Reynolds stress tensor (over all sampled locations) is observed at $n/D = 0.82$ in location 6, which is within the detached shear layer. The tangential stress in location 6 does not approach zero as n/D approaches 1 as in locations 4 and 5, due mainly to the truncation of the sampling region along the line normal to the wall. The

increasing momentum transport from the fluctuating velocity field at locations 4 and 5 is consistent with the increasing degree of flow reversal depicted in the mean velocity profiles of Figure 5.18d,e.

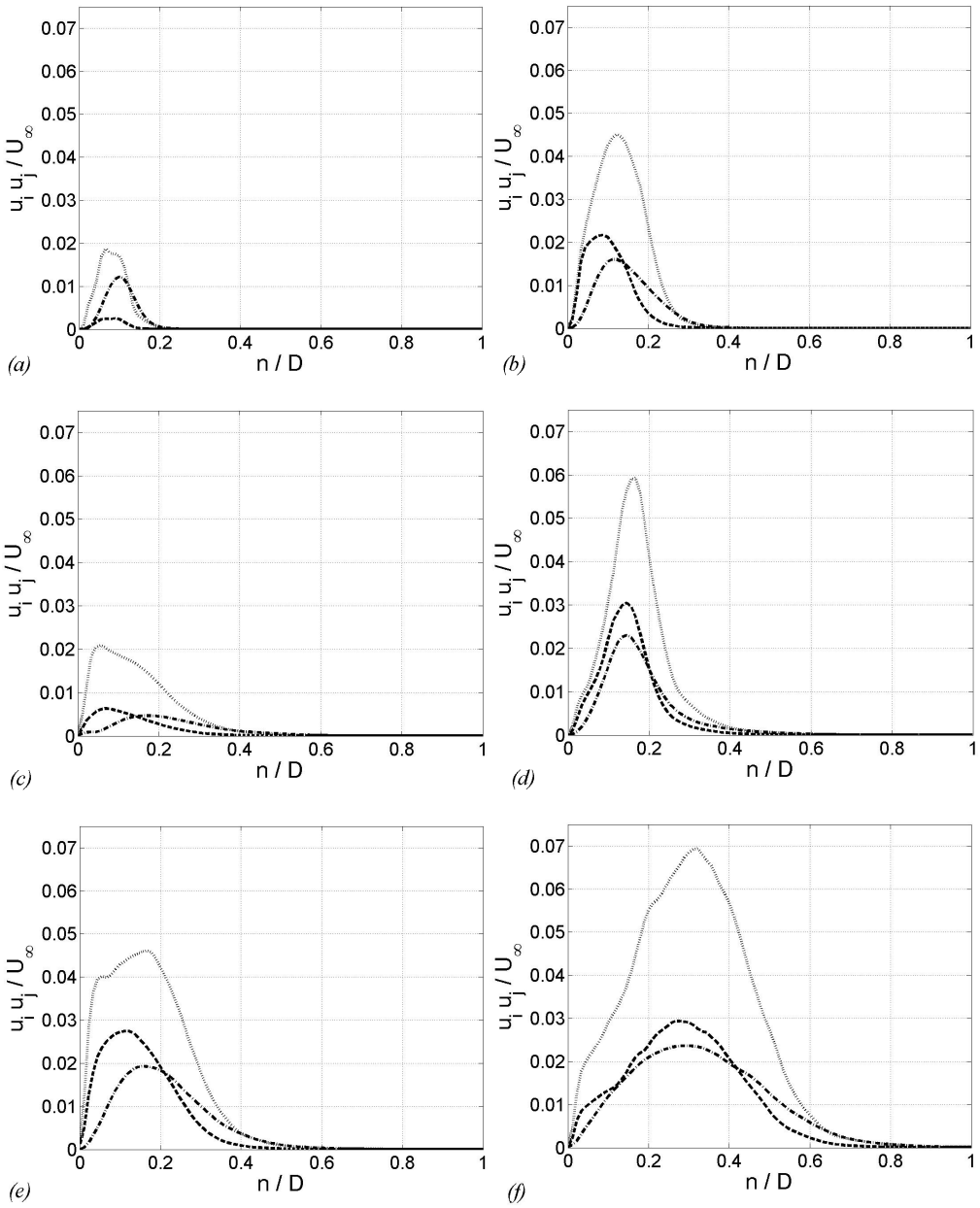

Figure 5.22: Reynolds stress profiles, $Re = 1.1 \times 10^5$, at locations 1-6 in frames (a)-(f), respectively. $\cdots$ *ww*; $- - -$ *vv*; $- \cdot -$ *uu*.

Evolution of the Reynolds stresses for the high Reynolds number flow help illuminate momentum transfer from the fluctuating velocity field within individual dimples. Reynolds stress profiles are largest at locations 2, 4, and 6, as compared with locations 1, 3, and 5. Elevated values of the normal Reynolds stresses are observed as the flow evolves from local attachment near the trailing edge of the dimple in location 1 (Figure 5.22a) to local detachment as it traverses the dimple in location 2 (Figure 5.22b). A similar trend is observed as the flow reaches location 3 (no dimple, c.f., Figure 5.17, 5.22c) and locally detaches over location 4 (Figure 5.22d). The Reynolds stress magnitudes decrease slightly for the results at location 5 (Figure 5.22e) compared with location 4. Location 6 (Figure 5.22f) exhibits higher stress values as the flow again detaches, although the trend occurs further into the flow (away from the surface of the golf ball), indicating the onset of complete flow detachment. The Reynolds stresses are also consistent with the mean velocity contours in Figure 5.6a-c, demonstrating a pattern of periodic increase and decrease in the normal stresses, which seems to correspond to local patterns of attachment and detachment. An increase in the magnitude of the Reynolds stress (moving from location 1 to 6) is accompanied by a broadening of the profiles; e.g., the size of the region affected by momentum transfer of the fluctuations has increased from approximately $n/D = 0.2$ (location 1) to $n/D = 0.8$ (location 6).

5.9 Summary

Direct numerical simulation (DNS) has been used to investigate the flow over a symmetrically-oriented golf ball in the subcritical ($Re = 2.5 \times 10^4$) and supercritical ($Re = 1.1 \times 10^5$) regimes. The simulations were performed using an immersed boundary approach in which the golf ball is represented using forcing applied on a background grid in a cylindrical coordinate system. The immersed boundary approach is attractive for simulations of a moving surface, a current focus, and enables

efficient solvers to be employed. The latter point is critical for efficient application of DNS on grids of the scale used in this work.

The flow over a golf ball itself poses several challenges, beyond those associated with computations using DNS at the Reynolds numbers considered here. The simulations highlight the effects of laminar separation, transition, and the local detachment and reattachment of the flow within dimples.

In particular, flow visualizations reveal small-scale shear layers that develop over dimples, consistent with the proposal of Choi *et al.* [25] as a key contributor to the drag reduction mechanism. The present contribution helps solidify the importance of that mechanism and advance understanding of the effect of shear layer instabilities on the increased momentum transport near the golf ball, critical in delaying complete flow detachment.

Time-averaged traces of the velocity provide insight into the physical processes characterizing the flow, showing that even in the average there is a recirculation within successive dimples for the supercritical regime. The wake is comprised of low-pressure tubes which are associated with coherent vortices, while vorticity contours in crossflow planes reveal asymmetrical behavior of the wake as the flow evolves downstream for the subcritical case. Averaged values of the drag force are in the range of previous measurements for non-rotating golf balls. Statistics of the pressure coefficient highlight regions (upstream of complete flow detachment) in which local increases in pressure correspond to the flow exiting dimples. Pressure coefficients from the present DNS are comparable with those obtained from the previous computations of Constantinescu & Squires [29] and the measurements of Achenbach [3] for a smooth sphere.

Contours of the pressure coefficient on the surface illuminate the behavior of the pressure near the golf ball, as well as the effect of impinging structures due to turbulent motion in the near-wake region. Profiles of the mean velocity provide insight

into the evolution of the flow near the wall, confirming complete flow detachment around 84 degrees for the subcritical regime; while local detachment and reattachment lead to complete flow detachment around 110 degrees for the high Reynolds number flow. Radial and axial velocity spectra indicate secondary peaks at Strouhal numbers ($St = 40, 60$) that appear to correspond to the small-scale structures developing over the dimple near separation. Reynolds stresses quantify the momentum contribution of the fluctuations in the regions of detached shear layers in the subcritical case, and in regions that underlie local attachment and detachment within dimples for the supercritical case.

Chapter 6

Effect of surface roughness on drag reduction

From results reported in the preceding chapters, it is clear that progress has been made in understanding the basic mechanisms of drag reduction in bluff body flows. Central to this process appears to be the development of shear layer instabilities over dimples that increase momentum transport near the surface of the golf ball. There are, however, several outstanding questions: How do instabilities in the shear layer over dimples lead to the formation of complex, three-dimensional vortices which interact with the surface of the golf ball? What is the effect of this interaction on the locally-reattached layer? How is momentum transported into and out of the near-wall region? How does the process of local detachment and reattachment contribute to the overall drag on the golf ball? What is the contribution of the dimples to the change in separation as compared with a smooth sphere? To illuminate these issues, a DNS of the flow over golf ball in the supercritical regime is presented. In the following section, a brief description of the computational approach will be given. The results section will focus on the relationship between evolving flow structures and spatio-temporal statistics in the dimples.

6.1 Geometry and Grid

A golfball comprised of approximately 300 spherical dimples is used in this study. The surface of the ball is discretized with a mesh of $77,764$ surface triangles connected by nodes. The dimple geometry on the golf ball has an axis of one-fifth symmetry, which is aligned with the freestream direction (c.f. Figure 6.1). The existence of the symmetry axis and its alignment with the freestream coordinate is advantageous since the statistical sample can be advanced by averaging over azimuthal planes, as well as time. For the current work, statistics were averaged in time and spatially over the five axes of symmetry as shown in Figure 6.1.

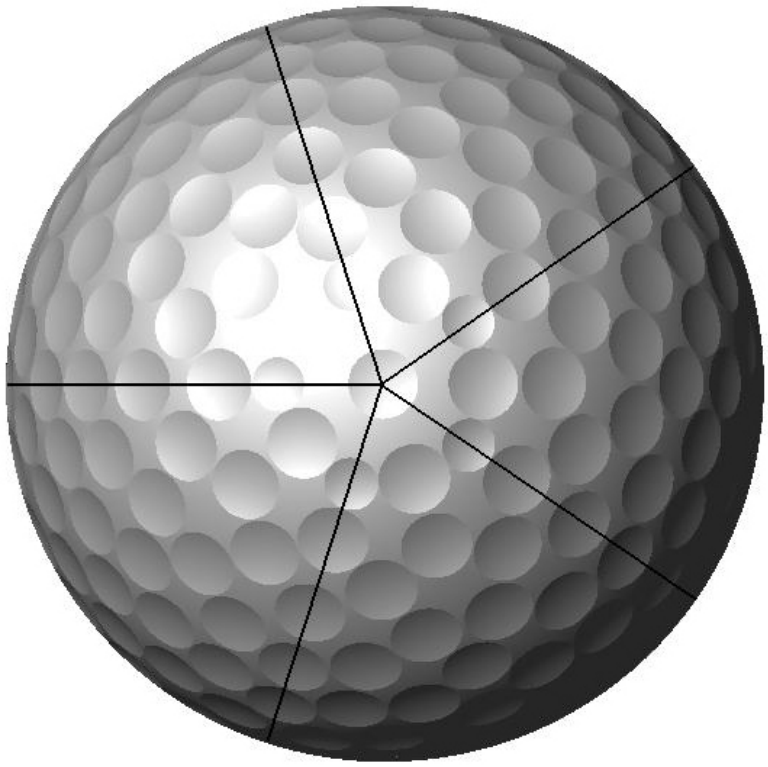

Figure 6.1: One-fifth symmetry of the 300-dimple golfball; present view looking from upstream of the golf ball toward the downwind direction.

Simulations are conducted for a supercritical case at a Reynolds number of 1.1×10^5. The grid sizes in the radial, azimuthal, and axial directions are summarized in table 6.1. Grid refinement studies indicated that qualitative flow features (e.g., visualizations) as well as quantitative measures such as the aerodynamic forces could be accurately captured using the grid resolution presented in Table 6.1.

The radial and axial grid point distributions were clustered to refine the grid near the golf ball. This was accomplished by modifying stretching ratios. The radial and axial grids were then smoothed in order to avoid abrupt changes in spacing using a stencil that weighted the coordinate value of a particular point twice as much as the point before and after it. As depicted in Figure 6.2(a), the grid near the dimple surface maintains an approximately uniform resolution in order to capture

Table 6.1: Grid resolution for present DNS of a golf ball in the supercritical regime ($Re = 1.1 \times 10^5$).

Coordinate	$Re = 1.1 \times 10^5$
Radial (R)	858
Azimuthal (θ)	502
Axial (Z)	3002
Total grid points	1.3×10^9

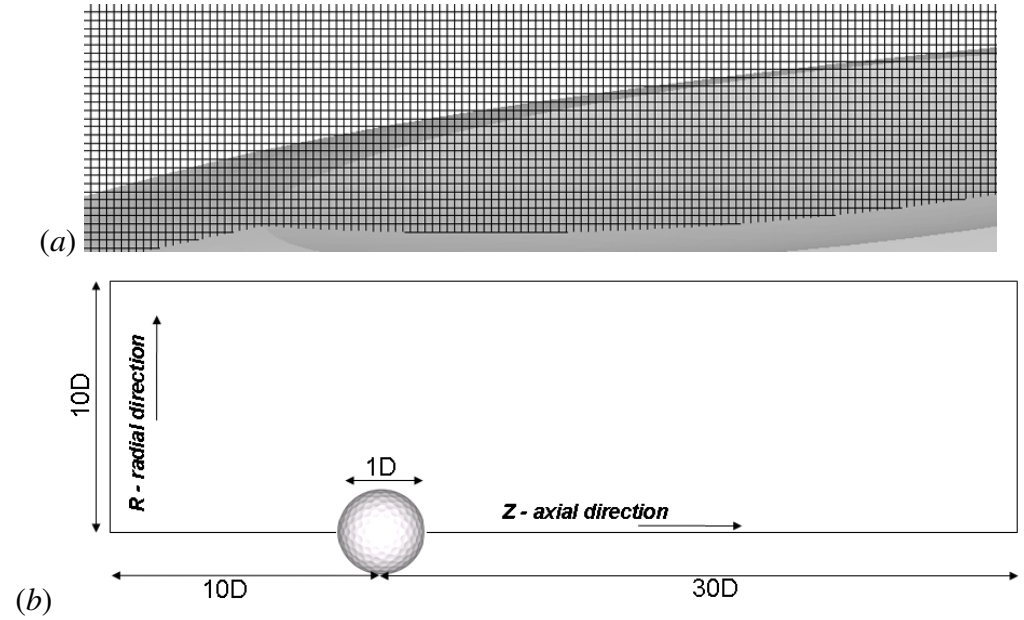

Figure 6.2: (a) Example grid resolution in a dimple near 84 degrees (measured from the stagnation point at the front of the golf ball): $Re = 1.1 \times 10^5$. This mesh refinement level has 160 points across the dimple in the streamwise direction. (b) Computational domain, cylindrical coordinates.

the velocity gradients and small-scale structures that develop over the ball. This approximate uniformity of the grid near the surface is maintained. The azimuthal grid spacing is constant, and the mesh resolution at the top/bottom of the ball is approximately 160 points across the dimple.

Table 6.2: Wall normal (k^+), spanwise (d^+), and mesh (γ^+) lengthscales of roughness elements in terms of wall units. Present DNS of the flow over a dimples on a golf ball in the supercritical regime ($Re = 1.1 \times 10^5$) is compared with the DNS of flow over ribs in a channel of Choi *et al.* [24] at $Re = 4.2 \times 10^3$.

Case	k^+	d^+	γ^+	$NR \times N\theta \times NZ$
Present golf ball DNS	59.7	944	5.9	$858 \times 502 \times 3002$
Ribbed channel DNS of Choi *et al.* [24]	34.6	40	1.3	$16 \times 129 \times 128$

The dimensions of the roughness elements (in this case, the dimples) are presented in terms of the wall units in Table 6.2. The scaling in wall units for an arbitrary roughness lengthscale n^+ is defined using the friction velocity (u_τ) and the molecular viscosity (ν) as shown in equation 6.1. The wall stress (τ_w) is estimated by integrating the mean shear stress distribution shown in Figure 6.7 over the golf ball (since τ_w is implicit in the definition of C_f per equation 3.12).

$$n^+ = \frac{u_\tau n}{\nu}, \qquad u_\tau = \sqrt{\frac{\tau_w}{\rho}} \tag{6.1}$$

Relevant lengthscales for the dimples include the dimple depth (k) and the dimple diameter (d). These values in wall units (k^+, d^+) for the concave dimples are contrasted with similar lengthscales of convex roughness elements (ridges) from the study of Choi *et al.* [24] in Table 6.2. As demonstrated in Table 6.2, the dimples on the golf ball in the present study form roughness elements in which the diameter (d^+, spanwise dimension) is an order of magnitude larger than the depth (k^+, wall normal dimension). This is distinct from the ribbed channel roughness elements of Choi *et al.* [24], where the dimensions of the roughness elements are of the same order of magnitude in both the spanwise and wall normal directions. Effectively, the dimples form very shallow roughness elements, but their effect on the flow is dramatic.

Solutions are obtained in a domain that extends 10 D (where D is the golf ball diameter) in the radial direction and 40 D in the axial direction. The center of the golf ball is 10 D from the inlet to the computational domain (corresponding to the front stagnation point at 9.5 diameters from the inlet), as illustrated in Figure 6.2(b). The R-Z plane shown in Figure 6.2(b) is revolved about the centerline in the azimuthal dimension, θ.

The flow solver is parallelized using domain decomposition and message-passing interface (MPI). The code exhibits linear scaling for computations performed using as many as 500 processors on a range of meshes up to 1.3×10^9 points. Integration of the flow over 96 wall-clock hours on 250 processors yields approximately 2.0 time units of sample (the time unit is non-dimensionalized using $T = D / U$, where U is freestream velocity and D is the diameter of the golf ball).

6.2 Instantaneous flow dynamics

Having established the accuracy of the simulations by presenting validation results, the discussion in this section will focus on the profuse detail provided by the simulations to understand the instantaneous flow dynamics. First, the coherent structures that dominate the local dynamics of the flow will be identified and the evolution of their motion in space and time will be explored. The effect of these structures on the spatio-temporal statistics, and the way that momentum is produced and transported will be presented in the following section.

The primary source of data for this work is a DNS calculation on the 1.3×10^9 point grid. The solution was integrated for approximately 30 D / U time units, and statistics were gathered over the final 17 D / U time units. Flow over a non-rotating golf ball is characterized by local detachment and reattachment as the air traverses subsequent dimples. Visualizations of the instantaneous azimuthal vorticity within individual dimples (representative examples in Figures 6.3, 6.4) reveal

this phenomenon, which has been advanced by Choi *et al.* [25] (based on their measurements) and confirmed by Smith *et al.* [84] (based on their direct simulations). As shown in Figures 6.3 and 6.4, shear layer instabilities form as the flow detaches from the leading edge of a dimple. Development of these instabilities leads to enhanced momentum transfer within the dimple, and the flow often reattaches to the surface of the golf ball directly downstream of a dimple trailing edge. The contour results in Figures 6.3 and 6.4 illustrate the Kelvin-Helmholtz nature of the shear-layers as they roll up over the dimples, while the isosurfaces reveal the three-dimensionality of the flow as it evolves in time from the leading to the trailing edge of the dimple shown.

As the flow over a non-rotating golf ball develops, the shear layers conform to the surface of the golf ball, and remain attached until approximately 50 degrees from the stagnation point at the front of the golf ball. Around 50 degrees, instabilities in the shear layers develop over dimples. The region in which this development occurs is visualized in Figures 6.3 and 6.4 using instantaneous contours of the azimuthal vorticity at subsequent instances in time. At the left (upstream) side of Figure 6.3(a) at $T = 5.0$, the shear layers are attached to the wall of the golf ball. Toward the middle of the figure, the shear layers detach locally due to the geometry of the dimples. In this initial detachment, the vorticity imparted into the shear layers is primarily convected downstream across the dimple. As the flow traverses the dimple, the shear layer begins to curl toward the wall at $T = 5.0125$ (reference Figure 6.3(a),(b),(c); this structure is labeled **A**). The vorticity at the tip of the detached shear layer does roll up into a vortical structure (structure **A**; see Figure 6.3(a),(b),(c)), and this structure gains strength as it convected across the dimple at $T = 5.0375$ and $T = 5.05$ (ref. Figure 6.4). Figure 6.3(a),(b) also show a vortical structure (labeled **B**) detaching from the shear layer as it is advected downstream. As noted above, local reattachment of the shear layer occurs at **C** in Figure 6.3.

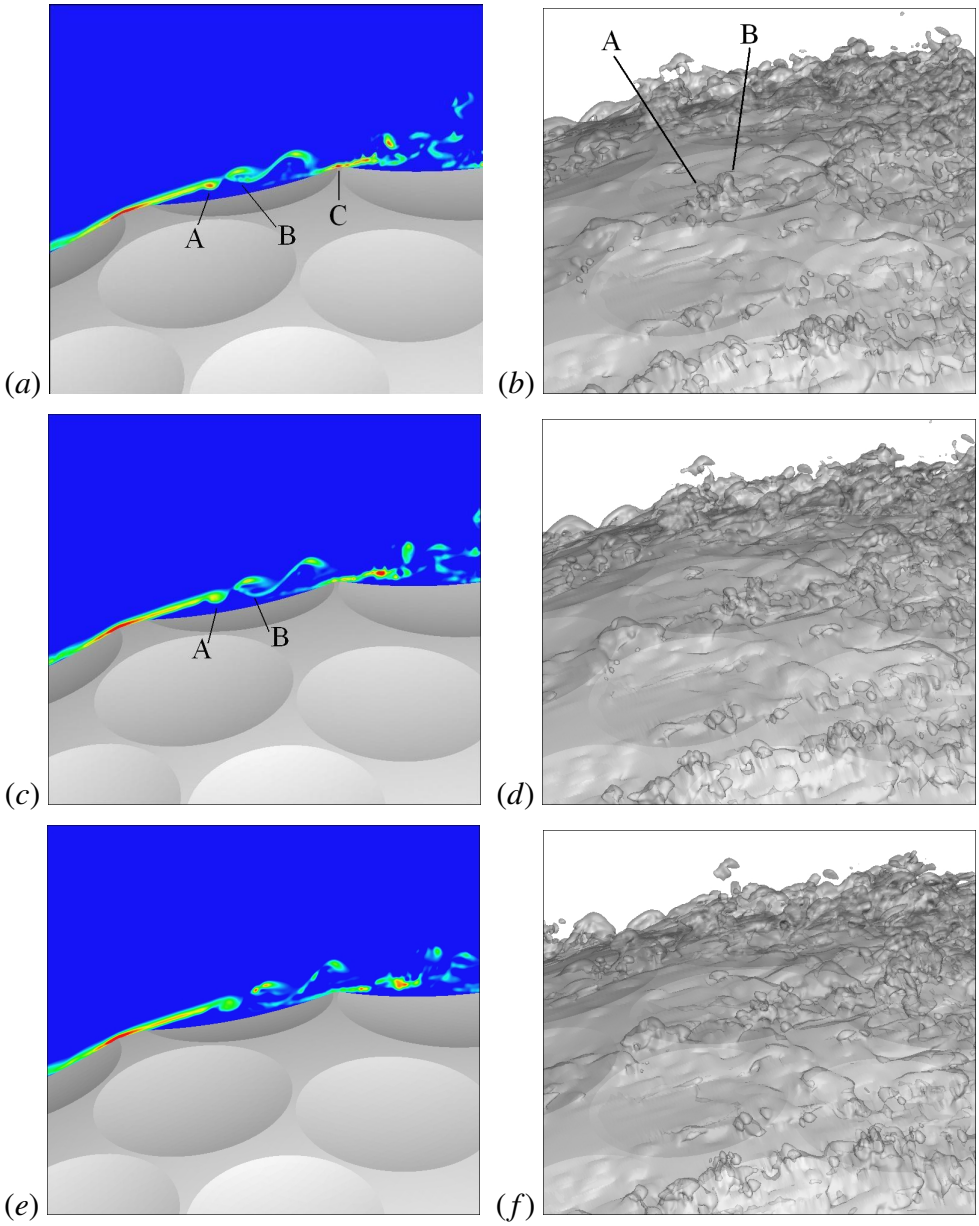

Figure 6.3: Filled isocontours (a, c, e) and isosurfaces (b, d, f) of azimuthal vorticity at five instances during the evolution of flow structures over dimples near 65 degrees (angle measured from the stagnation point at the front of the ball). The viewpoint is the same for the isocontour and isosurface results. (a),(b) $T = 5.0$; (c),(d) $T = 5.0125$; (e),(f) $T = 5.025$.

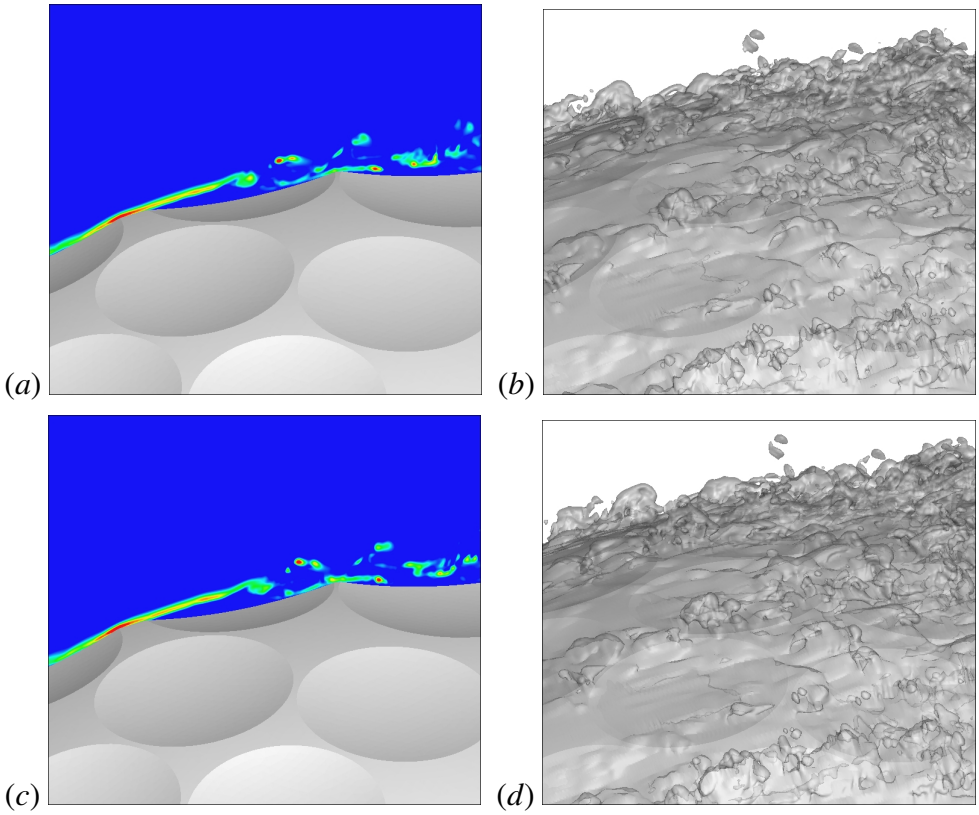

Figure 6.4: Filled isocontours (*a*, *c*) and isosurfaces (*b*, *d*) of azimuthal vorticity at five instances during the evolution of flow structures over dimples near 65 degrees (angle measured from the stagnation point at the front of the ball). The viewpoint is the same for the isocontour and isosurface results. (*a*),(*b*) T = 5.0375; (*c*),(*d*) T = 5.05.

As a possible explanation for the observed behavior, one may speculate that the formation of the leading structure (**B**) and the structure being formed (**A**) share some of the features reported in Spalart & Strelets [92], which involved DNS of transitional flow over a flat plate. In that flow, an attached shear layer along the plate forms vortical structures with a similar mechanism of roll-up that we observe here. The flat plate DNS results of Spalart & Strelets [92] also show regions of local reattachment downstream of the shear layer instability, but the proximity of the reattachment region to the location of the initial instability is greater than that observed in the present work. This is primarily due to the fact that the curvature of

the golf ball surface and the convex nature of the dimples prevent the dynamics of the flow from being dominated by the (non-dimpled) wall, as is the case in Spalart & Strelets [92]. Recent studies of flow over a flat plate with dimples by Mode [62] and Jensen [47] have helped to illuminate the contribution of the surface curvature and the dimples for a golf ball, as structures (**A**) and (**B**) for a dimpled flat plate are formed further downstream of the dimple's leading edge than in the case of the golf ball. In particular, Mode [62] reported qualitative results which show the vortical structures forming around $3/4$ of the dimple diameter downstream of the dimple's leading edge. For the golf ball, similar structures form around around $1/3$ of the dimple diameter from the dimple's leading edge.

Development of streamwise disturbances (also known as Tollmien-Schlichting or "T-S" waves) are difficult to identify in Figures 6.3 and 6.4. Hairpin-type structures do not appear in the flow field over the dimples, though they are present in the near wake of the golf ball. Rather, the local detachment and reattachment mechanism forms streets of spanwise (azimuthal) packet-like vortical structures that evolve and develop as they traverse subsequent dimples. This mechanism appears more similar to bypass transition than the transition mechanism via T-S waves producing instabilities in flat plate flow. A similar mechanism was reported by Mode [62] in the dimpled flat plate case, and confirmed in the work of Piot *et al.* [73] in a study of flow over convex roughness elements. Furthermore, the azimuthal (spanwise) vorticity is complemented by azimuthal rotation in the velocity field, producing Görtler-like vortices the originate over individual dimples. This can be observed in Figure 6.5. Alternating regions of the azimuthal velocity field with changing sign (represented by **E** and **F** in Figure 6.5) implying some level of streamwise vorticity. The magnitude of the azimuthal velocity at **E** and **F** is approximately 50% of the radial and streamwise velocity at the same point, suggesting that these streamwise vortical structures are secondary (in terms of their relative impact

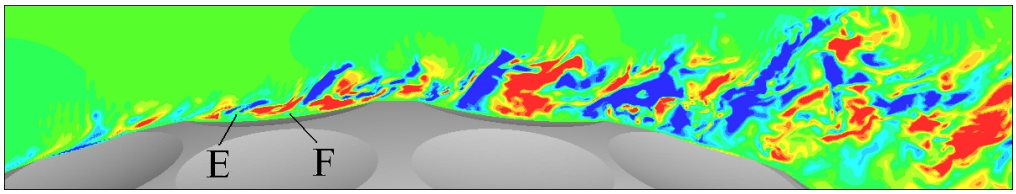

Figure 6.5: Instantaneous contours of azimuthal velocity at dimples near 90 degrees (angle measured from the stagnation point at the front of the ball). **E** denotes velocity with a negative sign (coming out of the plane of the figure); **F** represents velocity with a positive sign (going into the plane of the figure).

on the flow) in nature to the azimuthally-oriented structures already discussed. In the next section, the effect of these coherent structures on statistical quantities and momentum fluxes will be evaluated in order to illuminate the contribution to the overall drag reduction.

6.3 Statistics and fluxes

The current section will focus on the presentation of flow statistics and momentum fluxes for the flow over a non-rotating golf ball. We present statistical results of the aerodynamic forces as well as the pressure and shear stress, and discuss their relationship to the instantaneous flow mechanism over dimples. The concept of momentum flux is introduced and its implementation for analysis in the present work is discussed. Momentum transport contributions are evaluated for instantaneous results, time-averages, and fluctuations.

6.3.1 Statistical results

The simulation of the supercritical Reynolds number was integrated in time until a statistically quasi-stationary state developed around 15 D / U time units. Further integration to 32 D / U time units was performed in order to acquire statistics of the flow. This integration time corresponds to about 11 oscillatory shedding cycles at the dominant frequency. A comparison of the drag coefficient results is presented

Table 6.3: Mean drag coefficient (C_D), dimensionless dimple depth (k/D), and total number of spherical dimples on the golf ball: measurements compared with present DNS.

Results	C_D, $Re = 1.1\times10^5$	k/D	Dimples
Present DNS	0.21	6.0×10^{-3}	300
Bearman & Harvey [11]	0.25	9.0×10^{-3}	336
Choi *et al.* [25]	0.21	4.0×10^{-3}	392

in Table 6.3. The mean drag coefficient is within the range of available measurements (Bearman & Harvey [11] and Choi *et al.* [25]) for golf balls. Especially favorable comparison is achieved with respect to the measurement of Choi *et al.* [25]. Differences in the results may be attributed primarily to differences in the dimple geometry of the cases compared; the dimensionless dimple depth (k, the dimple depth is normalized by the golf ball diameter D) of the present work is 50% larger than that of Choi *et al.* [25], but 30% smaller than that of Bearman & Harvey [11]. Differences in the number and arrangement of the dimples on the golf ball undoubtedly play a role as well.

The force histories in Figure 6.6 quantify the chaotic nature of the vortex shedding around the golf ball. The coherent vortical structures which form over the dimples eventually lead to global flow detachment between 110° and 120° (angle measured from the stagnation point on the front of the golf ball). In addition to the streamwise (drag) component, the lateral force coefficients are also shown. Unlike the behavior associated with laminar separation on bluff bodies, the lateral force coefficients here exhibit oscillations about a non-zero mean. For the present work, which is concerned solely with the turbulent separation in the supercritical regime, there appears to oscillation of the side forces about different equilibrium positions. For example, the mean of C_X (~ -0.047) is clearly different than the mean of C_Y

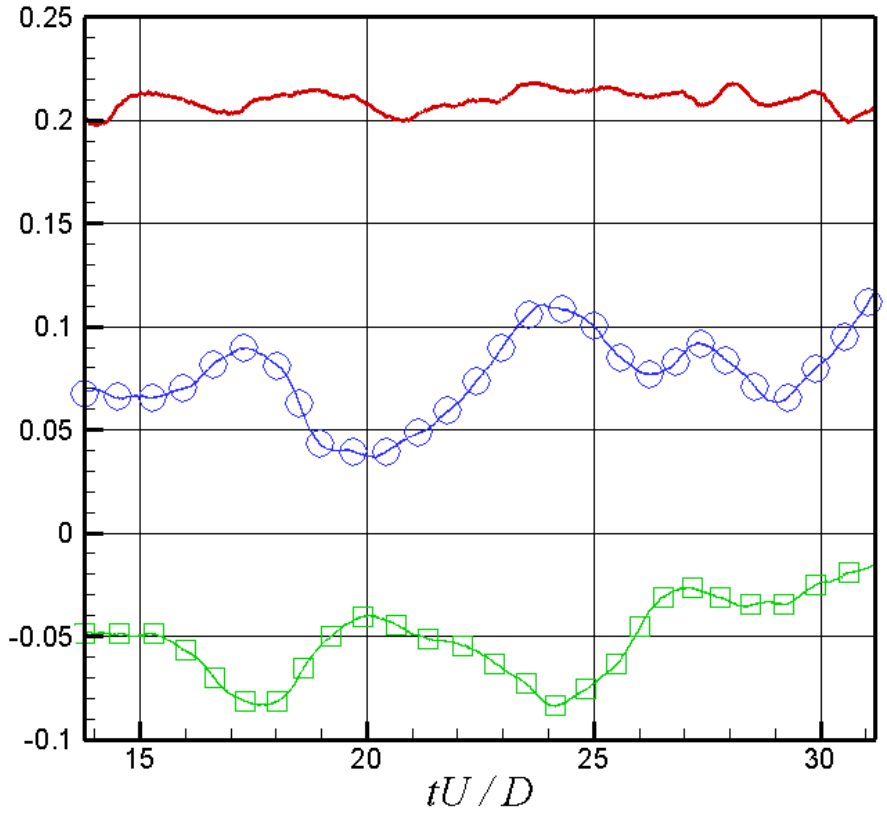

Figure 6.6: Time-history of aerodynamic force coefficients for a non-rotating golf ball at $Re = 1.1 \times 10^5$: $-$ C_D; □ C_X; ◯ C_Y.

(~ 0.082), and C_X assumes negative values throughout the integration history as shown in Figure 6.6. The observation of non-zero side forces was observed in the experiments of Taneda [99] and the calculations of Constantinescu & Squires [29]. It has been suggested by Travin *et al.* [101] (in regard to flow over a cylinder) that the wake may rotate around the body at very low frequency, and thus, if it were possible to statistically sample statistics over thousands of time units the mean side forces may go to zero.

Since the aerodynamic drag is comprised of contributions from the pressure and the shear stress, we present temporal and spatially-averaged results for the pressure

coefficient (C_P) and the friction coefficient (C_f) (reference equations 3.11 and 3.12, respectively for the definitions). These statistics elucidate the mean contribution of the flow at the local (dimples) level and confirm existing knowledge about flow characteristics at the global level. Statistics of the mean flow field were averaged over 17 D/U time units to produce these results. Calculation of the wall stresses from an immersed boundary solution is non-trivial, since the immersed object does not align with the background grid. A local reconstruction approach for the pressure and the viscous stress tensor was employed to recover these mean quantities on the surface of the golf ball. To increase the statistical sample, the mean flow statistics of pressure and shear stress were also averaged spatially over the five symmetry planes (shown in Figure 6.1) to produce the results in Figure 6.7. The shear stress coefficient (C_f) is non-dimensionalized by $\sqrt{Re}$ to allow direct comparison with the smooth sphere measurements of Achenbach [3] in the supercritical regime at $Re = 1.14 \times 10^6$. In order to highlight the differences between mean flow characteristics in the boundary layer, results within all the dimples (blue symbols) are contrasted with the non-dimpled surfaces (red symbols) of the golf ball.

Figure 6.7 reveals information about the flow in the boundary layer as a function of angular position measured from the stagnation point. There exists a clear correspondence between the local trends of the shear stress and pressure. Even as the overall trend of each result progresses from the front stagnation point toward the rear of the golf ball, we observe local changes which align with each other. At twelve distinct angular locations (25°, 32°, 39°, 43°, 50°, 52°, 59°, 65°, 71°, 76°, 85°, 97°), local minima in the shear stress result for the dimples correspond to local maxima in the pressure result in the dimples. The local maxima in the pressure was reported by Smith *et al.* [84], and it was attributed to local flow deceleration as the flow exits dimples near the trailing edge. The existence of the effect in the mean shear stress result confirms this, as local flow deceleration would lead to a

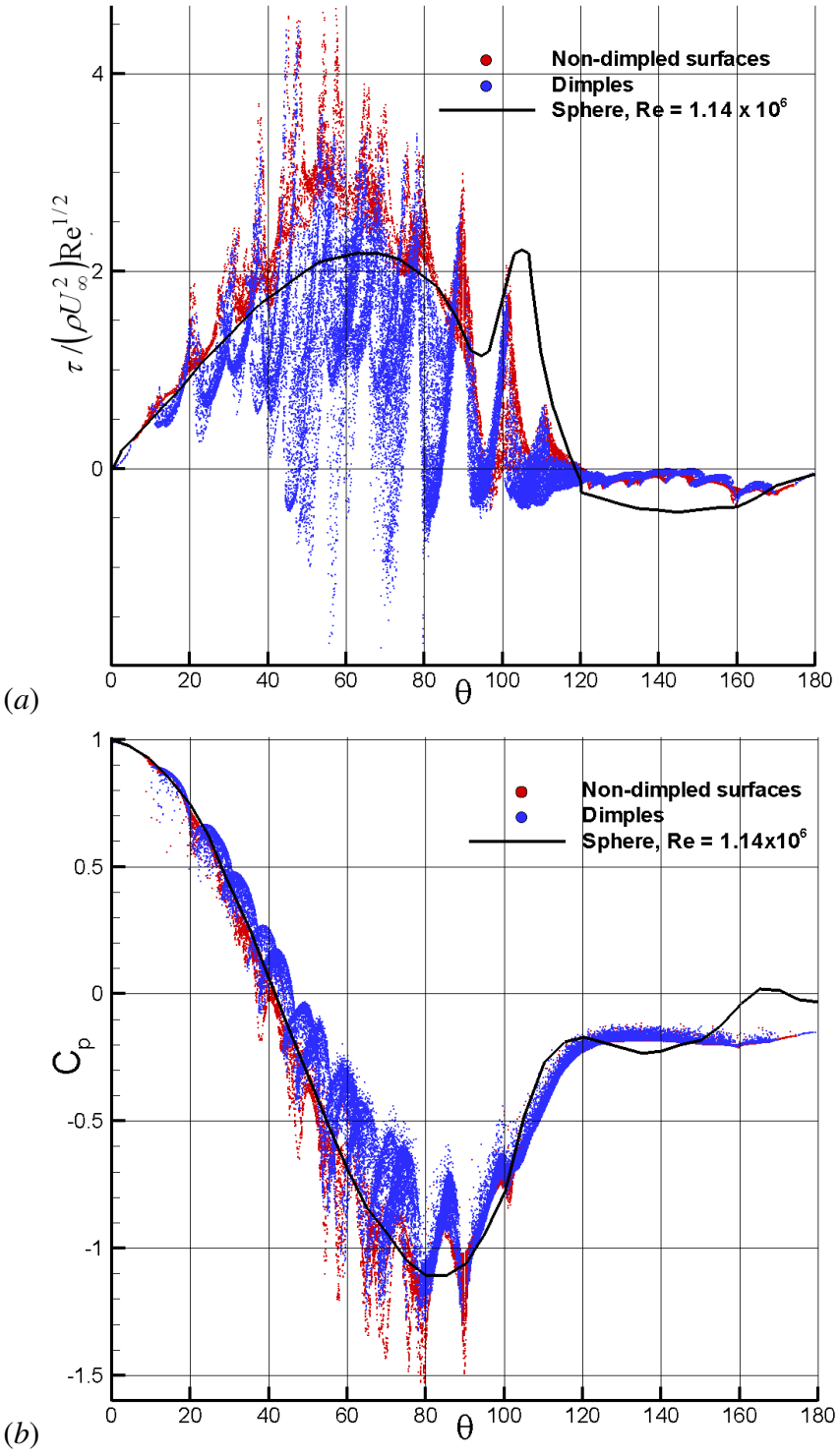

Figure 6.7: Mean distributions of (a) skin friction (shear stress) and (b) pressure: ● present DNS (blue ● represents results within the dimples while red ● represents results on non-dimpled surfaces), $Re = 1.1 \times 10^5$; – smooth sphere measurement of Achenbach [3] in the supercritical regime, $Re = 1.14 \times 10^6$.

local reduction in the velocity gradients normal to the wall, from which the shear stress arises. Local maxima (or "spikes") are present in the mean shear stress result; they precede each local minima, indicating regions of acceleration as the shear layer traverses dimples as early as 22°. Four different regions can be distinguished:

- The local maximum shear stress at 22° has a magnitude of 0.75 (implying its value increases past the mean trend of the shear stress by this amount);
- Between 39° and 59° the magnitude of the local maximum shear stress is 1.75;
- Between 64° and 80° the magnitude of the local maximum is 1.0;
- From 90° to 105° the local maximum of the shear stress reaches its highest magnitude of 2.0.

At 105°, the local maxima of the shear stress is immediately preceded by negative values of the wall shear stress (implying local flow detachment) and this region also corresponds to the local minimum and following increase in the wall shear stress observed for the supercritical smooth sphere. As discussed by Achenbach [3], this effect for the supercritical flow over a smooth sphere is indicative of a laminar intermediate separation followed by transition to turbulent flow (hence the local increase to a value of $C_f = 2.25$). Furthermore, the negative values of the skin friction for the smooth sphere at $Re = 1.14 \times 10^6$ do not occur until 118°. Contrast this with the golf ball, where negative skin friction reveals local flow detachment within dimples as early as 43° (one of the local minima in Figure 6.7), and alternating regions of local detachment persist from 43° until the mean shear stress remains negative consistently past 120°. Although the mean stress trends between the supercritical smooth sphere and the golf ball are similar, some significant distinctions appear. Perhaps most obvious is the difference between the skin friction values of the smooth sphere

and the golf ball between 43° and 80°; as an illustrative point consider 65°: here the smooth sphere C_f curve reaches its first maxima of 2.25 while at the same angular position the golf ball skin friction result is clearly higher. We attribute this primarily to the increased surface area of the golf ball as compared with the smooth sphere. Another important difference is the mechanism of transition and global separation. For the smooth sphere, Achenbach [3] suggested that local minima of skin friction at 95° implied laminar intermediate separation which is proceeded by a transition to turbulent flow in the shear layer (implied by the absolute maximum in the skin friction of 2.3 at 105°) and complete global separation around 118°. For the golf ball, the evidence shown here reveal local minima of the wall shear stress occuring as early as 25°, with alternating regions of flow acceleration and deceleration in the dimples leading to local flow detachment and a subsequent transition to turbulent flow occuring much more quickly (around 43°), with global separation occuring very close to the same angular location as the supercritical smooth sphere.

Contours of the mean shear stress and pressure coefficients are presented Figure 6.8(a)-(d). The skin friction contours provide confirmation of what was observed in Figure 6.7. Local regions of flow detachment produce separation bubbles within individual dimples as early as 43° measured from the stagnation point on the front of the golf ball. Areas displaying local detachment in the dimples appear to be immediately preceded (upstream) by concentrated regions of high shear stress ($C_f \approx 4.5$) on the trailing edge(s) of the dimple(s) that lie upstream. Some dimples even display multiple patches of locally-separated flow in the mean, and many are observed to lie within a band at 70° of the stagnation point (consider Figure 6.8(b)). Moving aft on the golf ball from 70°, the local regions of separation within dimples increase in size from $\approx 25\%$ of the dimple area to $\approx 50\%$ at 80°. Past 90° the regions of local separation are approximately the same diameter as the dimples themselves. The global separation line varies between 110° and 120° based on the dimple pattern in

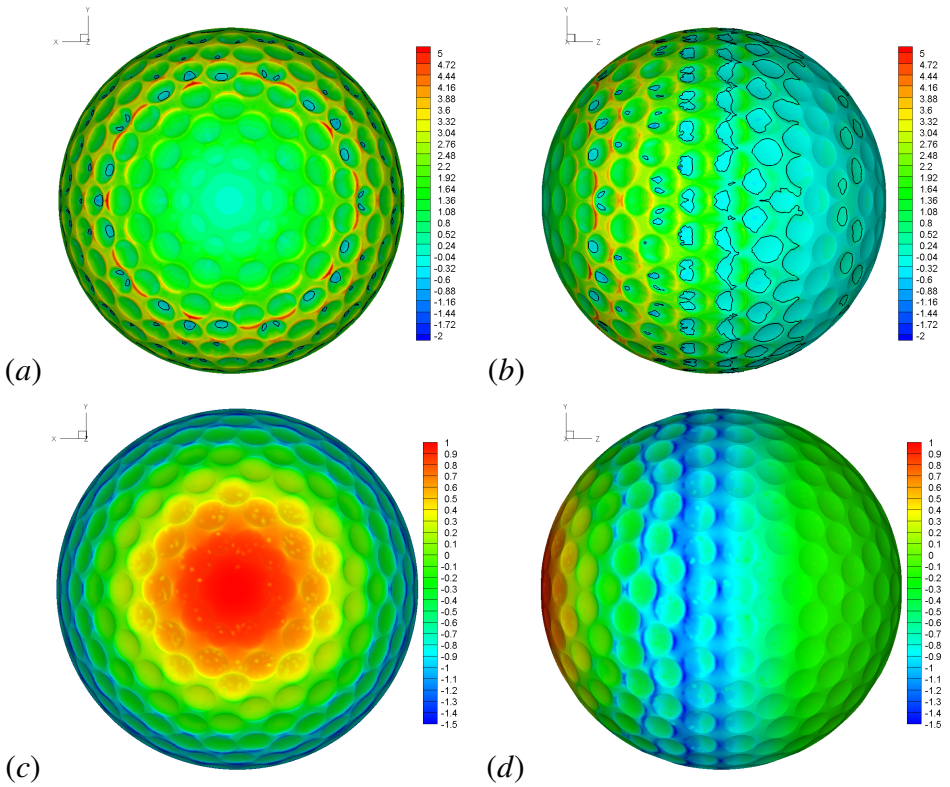

Figure 6.8: Contours of mean skin friction (shear stress) and pressure coefficients. Results are averaged in time and about the five axes of symmetry. Isolines of zero skin friction are superimposed on the shear stress result. (a) Shear stress (C_f), front view (looking aft from upstream of the golf ball); (b) Shear stress (C_f), side view (flow from left to right); (c) Pressure (C_P), front view (looking aft from upstream of the golf ball); (d) Pressure (C_P), side view (flow from left to right).

the azimuth, confirming previous visualizations and mean statistics of the velocity field. Small patches of zero skin friction are evident on the golf ball surface even aft of global flow detachment, indicating the presence of impinging structures on the golf ball surface in the wake.

Contours of the mean pressure coefficient in Figure 6.8(c)-(d) corroborate the two-dimensional findings in Figure 6.7(b). The maximum value of the pressure at the stagnation point is clearly shown, as is the reduction in pressure as the flow accelerates toward the region of adverse pressure gradient in the wake. Regions of low pressure ($C_P \approx -1.2$) are apparent on portions of the non-dimpled golf ball surface

around 52° from the stagnation point. These patches of low pressure correspond exactly to patches of high shear stress ($C_f \approx 4.5$) at the same location, implying the flow is accelerating as it passes over these narrow non-dimpled surfaces between streamwisely-oriented dimples. Interestingly, these regions of low pressure on non-dimpled surfaces appear to lag the regions of zero shear stress shown in Figure 6.8(a)-(b), which are distinctly apparent at 43° from the stagnation point. The pressure coefficient contours display a minimum ($C_P \approx -1.5$) between 80° and 90°, which occurs only on the non-dimpled surfaces (also confirmed in Figure 6.7(b)). Recovery of the pressure coefficient occurs rapidly aft of 100° from the stagnation point, and the results compare very well with the supercritical sphere measurement up to nearly 150°, at which point the sphere result increases to nearly a value of zero for the remainder of the sphere surface (reference Figure 6.7(b)). The recovery value of the golf ball pressure coefficient remains approximately constant at $C_P \approx 0.25$ throughout post-separation region.

For a stationary golf ball, both the pressure and shear stress contribute to the overall drag (these are the only two effects; no induced drag is present since the ball is not rotating). The effect of the dimples on the flow over a non-rotating golf ball in the supercritical regime can be further illuminated by comparing the relative contribution of the pressure and the shear stress to the global drag with the supercritical smooth sphere results of Achenbach [3]. In keeping with the non-dimensional presentation of the forces, the pressure (C_P) and shear stress (C_f) cofficients are integrated over the surface of the golf ball to yield their relative contributions to the drag coefficient (C_D). The results are compared with supercritical smooth sphere results in Table 6.4.

Table 6.4 highlights the viscous penalty of the dimples. The contribution of the viscous stress to the drag is approximately twice as high for the supercritical golf ball (14.3%) as compared with the smooth sphere (6.1%) in the supercritical

Table 6.4: Relative contribution of the mean pressure (C_P) and shear stress (C_f) coefficients to the mean drag coefficient (C_D) for the present DNS of the flow over a golf ball at $Re = 1.1 \times 10^5$ compared with the measurements of Achenbach [3] at $Re = 1.14 \times 10^6$ of the flow over a smooth sphere.

Case	C_P / C_D	C_f / C_D	C_D
Present DNS: $Re = 1.1 \times 10^5$	85.7%	14.3%	0.21
Achenbach [3]: $Re = 1.14 \times 10^6$	93.9%	6.1%	0.13

regime. The dimples clearly have an effect on the contribution of the pressure for the golf ball as well. Though the percentage of the drag contributed by the pressure is lower for the supercritical golf ball (85.7%) than the supercritical smooth sphere at 93.9% (due to the increased viscous stress from the dimples), the actual value of the pressure contribution to the drag for the supercritical golf ball is 0.18, whereas the pressure contribution for the post-drag crisis smooth sphere is 0.12. This is due primarily to the fact that the drag coefficient for the golf ball in the supercritical regime (0.21) is nearly twice the value of the supercritical smooth sphere drag (0.13). Thus, when comparing a dimpled golf ball with a smooth sphere in the supercritical regime, it is clear that the dimples on the golf ball produce a small penalty for the viscous component of the drag force, but the majority of the drag penalty from the dimples is apparent in the additional pressure drag they produce.

6.3.2 Momentum Flux

A contribution of the present work is to explore the connection between the local flow mechanism at the dimples and the global aerodynamic performance. In order to elucidate the contribution of the dimples to the global drag reduction, we present an analysis of momentum transport near and within the dimples on the golf ball. Momentum transport presents a method of understanding the effect(s) of the

dimples on the flow, and therefore has potential as a metric for drag reduction via passive flow control by dimpling. Since the current work is concerned with the dynamics of a Newtonian fluid, the flux of momentum represents a change in the force. Therefore, we attempt to quantify how local momentum transport energizes the flow in the dimples and where this primarily occurs on the golf ball. The term $flux$ is used commonly in reference to transport phenomena. Mathematically, it represents the rate of transfer of a physical quantity across a surface. Details of the method are described in Chapter 2.

Initial statistics of the radial direction (u_r) momentum flux are shown in Figure 6.9. The circled region contains three dimples which are oriented sequentially with respect to the flow (the mean flow direction is along the positive Z axis in the figure). The radial direction momentum flux contours highlight the sign of radial-direction momentum as it is transported across the surfaces on each dimple. A similar trend is clear from around 10° to about 90° (angle is measured from the stagnation point at the front of the golf ball); mean radial momentum is transported into the dimples (represented by the negatively-signed flux with the blue contour colors) on the upstream half of each dimple. Halfway across each dimple in the direction of the flow the flux changes sign, implying momentum is transported out of these dimples (positively-signed flux with red contours) in the mean.

To illustrate how the local flow mechanism in the dimples is related to the momentum flux, instantaneous contours of radial and axial momentum flux are superimposed on isosurfaces of coherent structures identified using the Q-criterion method of Hunt *et al.* [45] in Figure 6.10. The Q-criterion is a vortex identification method which isolates convex, low-pressure tubes that are usually associated with coherent vortices. The two dimples in the center of Figure 6.10(a), (b) were selected for analysis due to their streamwise orientation and their relative location to the stagnation point on the front of the golf ball. These dimples lie along one

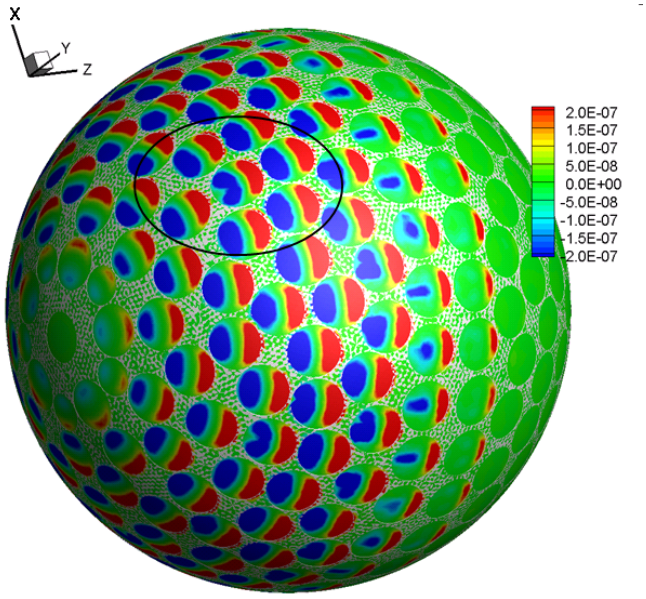

Figure 6.9: Mean momentum flux due to the radial (u_r) velocity component. Circled region highlights dimples oriented sequentially in the axial (Z) direction which have similar flux patterns on the dimple-capping surfaces. The direction of the mean flow is along the positive Z-direction.

of the five symmetry axes of the golf ball at about 50 degrees from the stagnation point at the front of the golf ball, and are aligned axially with the bulk streamwise flow, which is oriented from left to right in Figure 6.10. As expected, the Q-criterion isosurfaces show the azimuthally-oriented, packet-like structures which characterize the local detachment/reattachment mechanism over the two dimples in the figure. The momentum flux contour reveals some interesting characteristics of the flow as it enters the dimples. The radial flux (u_r) result reveals that flow enters the dimple (inward flux has a negative sign and is represented by blue contours) toward the leading edge along the radial (normal) direction, then exits the dimple toward the trailing edge (outward flux has a positive sign and is denoted by the red contours). A similar (entrance - exit) trend for the radial momentum flux can be observed for several of the other dimples in the figure. Contours of the axial flux (v_θ) show that flow oriented axially (in the streamwise direction) enters these

(*a*) 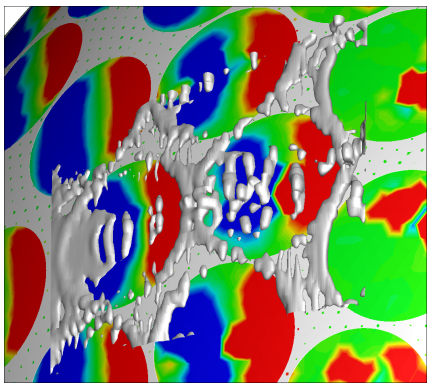 (*b*) 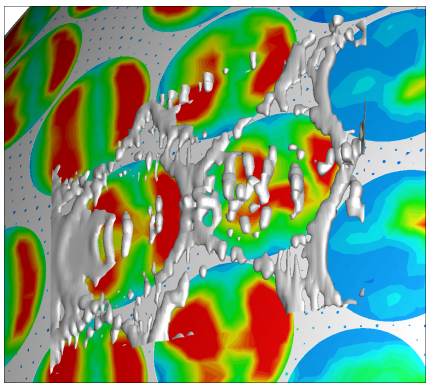

Figure 6.10: Isosurface of the Q-criterion (Hunt *et al.* [45]) superimposed on contours of instantaneous momentum flux in spherical coordinates (a) radial component, u_r; (b) axial component, v_θ. Flow direction is from left to right.

dimples near the trailing edge and then exits toward the aft side of the dimple. The shape and location of the coherent structures appear to be closely correlated with the contours of the radial momentum flux. Some correlation is also apparent in the axial momentum flux result.

Results based on mean and instantaneous fields demonstrate how momentum is transported into the near-wall region within the dimples. The local mechanism (comprised of shear layer instabilities, detachment, roll-up, and reattachment) transports momentum into the dimples by the generation of coherent vortical structures. The fluid velocities in the vicinity of these structures transport their associated momentum into the dimples. The transport of momentum into the near-wall region in the dimples is apparent in the mean and instantaneous velocity fields, but we must also consider how momentum is transported by the fluctuating velocity field. As noted by Cebeci & Bradshaw [20], the momentum transported by the turbulent stresses (the fluctuating momentum flux) in flows with strong shear layers (as is the case in the present work) often exceeds the contribution from the mean flow. Contours of the momentum flux due to the fluctuating velocity field in spherical coordinates are presented in Figure 6.11 plotted on the sphere of the same diameter

as the golf ball. An initial observation is that the momentum transported by the fluctuations is confined to a region between 50° and 110° (the angle is measured from the stagnation point at the front of the golf ball) for the radial (u_r), axial (v_θ), and azimuthal (w_ϕ) flux components. The overall trend of momentum flux from the fluctuations is distinct from the averaged result shown in Figure 6.9, in which the mean flow transports momentum into the dimples in a region between 10° and 110°. Furthermore, the sign of the radial (u_r) momentum flux from the fluctuations (Figure 6.11(a),(b)) is directly opposite to the sign of the radial (u_r) momentum flux from the mean result in Figure 6.9. Inspection of the trend reveals that the radial flux from the fluctuation is *positive* from the leading edge of the dimple to nearly halfway across the dimple face in the direction of the bulk flow. Toward the middle of the dimple, the sign of the radial momentum flux becomes *negative*. For the axial (v_θ) result from the fluctuations (Figure 6.11(c),(d)), distinct regions of positively-signed flux are evident beginning at around 50 degrees from the stagnation point. The momentum flux in the axial direction is nearly an order of magnitude greater (order of 1×10^{-6}) than either the radial or azimuthal components (both of which are of the order of 1×10^{-7}). These large fluxes in the axial result are evident in the 50-110 degree band, but they do not appear past 90 degrees from the stagnation point. The azimuthal (w_ϕ) momentum flux result in Figure 6.11(e),(f) shows alternating patches of positively-signed and negatively signed flux, indicating regions where the flow enters the dimple near the leading edge with a positively signed angular orientation, and then exits with a negatively-signed angular orientation.

In order to interpret the observed behavior, we suggest that the momentum transport from the fluctuations follows a different trend than that observed for the instantaneous or the mean result. The restriction of the momentum flux from the fluctuations to the smaller band from 50 to 110° (from the stagnation point on the front of the golf ball) distinctly reveals the region where the flow begins to transi-

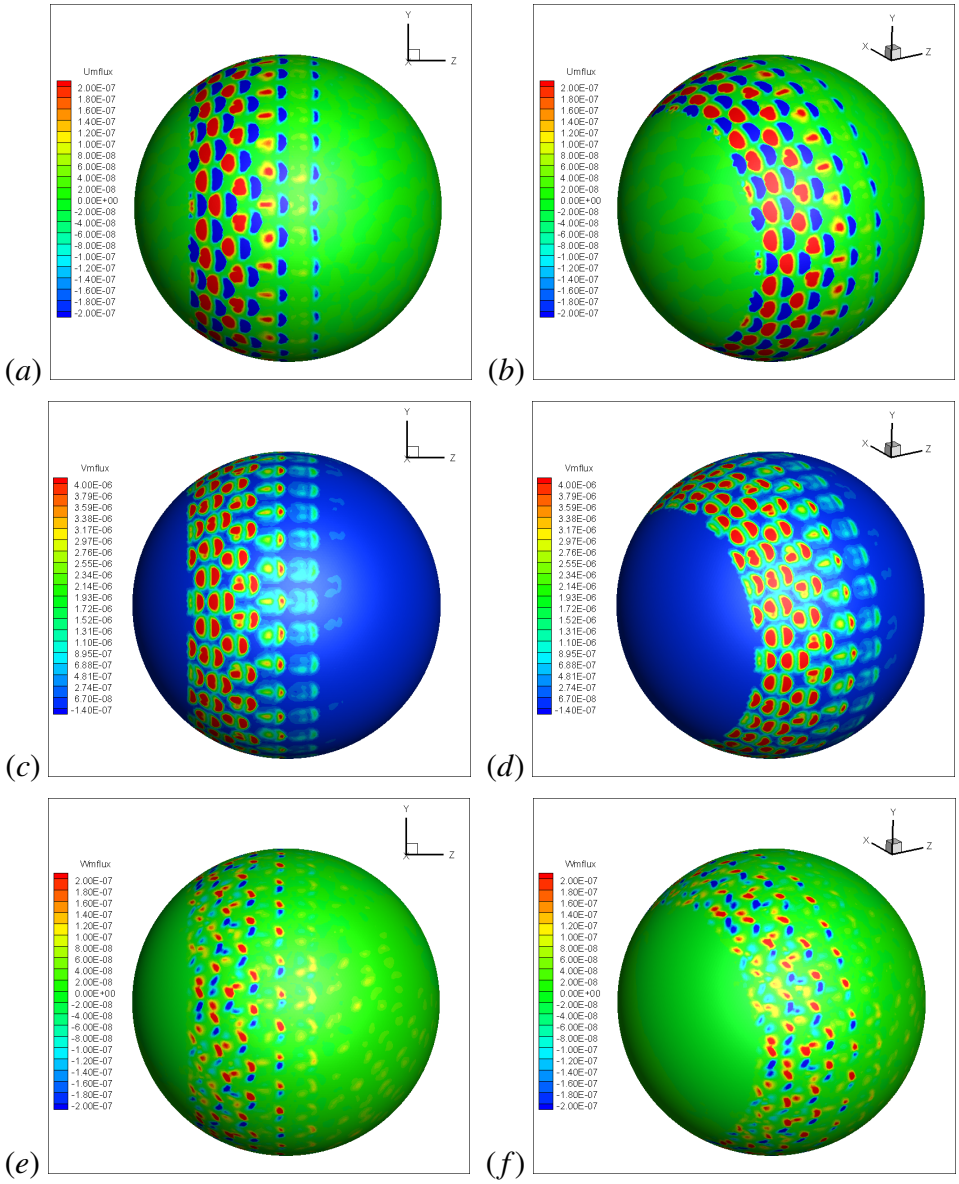

Figure 6.11: Contours of momentum flux due to the fluctuating velocity field (a), (b) Radial momentum flux (u_r); (c), (d) Axial momentum flux (v_θ); (e), (f) Azimuthal momentum flux (w_ϕ). The bulk flow direction is along the positive Z axis in all frames.

tion, as well as where it detaches completely. The distinct reversal of the sign in the radial flux result (evident in Figure 6.11) is the most significant difference, and indicates that the direction of momentum transport from the fluctuating velocity field in the radial direction is the opposite of the mean result. The radial momentum flux from the fluctuation also reveals a connection to the instantaneous mechanism of flow detachment and reattachment in the dimples. The positively-signed momentum flux on the upstream half of the dimple is likely due to the azimuthal vorticity of the coherent vortices as they detach from the shear layer and begin to rotate in the bulk flow. As these vortical structures complete one full rotation, they transport momentum back into the dimple (negatively-signed flux). The axial momentum flux due to the fluctuations displays strong momentum transport even as far as 120 degrees or so aft of the stagnation point, revealing locations where the detached shear layers wrap around and impinge on the golf ball. The azimuthal momentum flux from the fluctuating velocity field reveals how momentum is transported into the dimples in the crossflow direction. The signs of the contours and their location with respect to the dimples suggest that momentum is transported (by the azimuthal fluctuating velocity field) into the dimples near the leading edge with an orientation toward the center; e.g., momentum transport is not purely in the axial direction, but rather has some azimuthal component which guides the flow near the leading edge of the dimple toward its center, and then forces the flow outward away from the dimple center as it approaches the trailing edge of the dimple.

To further illuminate the contribution of the fluctuating velocity field to momentum flux in the dimples, we present a spatially-averaged result for the momentum flux contribution from the fluctuations in Figure 6.12. This result was obtained by taking the azimuthal average of the momentum flux through the spherical - capping surfaces on the dimples from the fluctuating velocity field. The mean location of non-zero flux (which implies transition) is clearly revealed at 50° from the stagna-

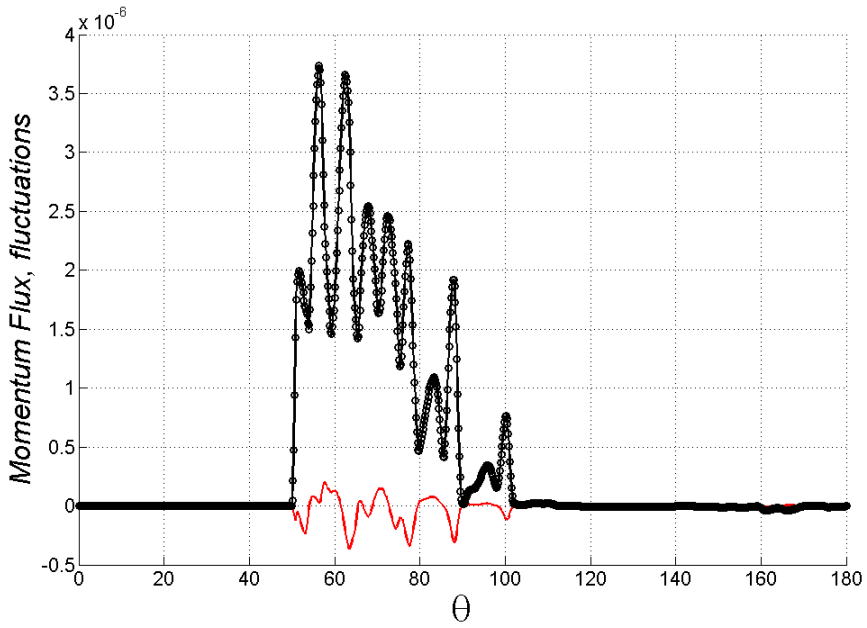

Figure 6.12: Momentum flux due to the fluctuating velocity field: present DNS, $Re = 1.1 \times 10^5$. Results on the surfaces covering the dimples are averaged in the azimuthal (spanwise) direction. − averaged radial (u_r) component of momentum flux; ◯ averaged axial (v_θ) component of momentum flux.

tion point, which correlates very well with observations from the qualitative results presented from the instantaneous and mean contours which reveal the local detachment of coherent vortical structures from the shear layer. Non-zero fluxes are present only between 50 and 110°, as observed previously. The momentum flux due to the radial component shows alternating regions of positive and negative flux, corresponding to the flow leaving and entering the dimples. Momentum flux due to the axial component is primarily positively-signed, implying that momentum transfer is occurring in the positive axial direction (the direction of the bulk flow around the golf ball). The variation in the axial flux result is likely due to the local variation of the dimple pattern at that (angular) location. As noted previously, the axial momentum flux is an order of magnitude greater than that of the radial momentum flux.

6.4 Summary

Direct numerical simulation (DNS) has been used to investigate the effect of surface dimpling on the aerodynamic performance of a non-rotating golf ball in the super-critical regime ($Re = 1.1 \times 10^5$). This simulation was conducted using an immersed boundary approach in which the surface of the golf ball is represented using forcing applied on a background grid in cylindrical coordinates. The immersed boundary approach is attractive for simulations of moving bodies, and it enables efficient flow solvers to be utilized (critical for efficient application of DNS on grids of the scale used in this work).

The flow over a golf ball presents many challenges with respect to the study of bluff body flows, as the physical processes that govern the flow include laminar separation, transition, and local detachment and reattachment within the dimples. Accurate resolution of the physics motivated the DNS, but more importantly we want to illuminate the effect of the dimples, which are a form of passive flow control for drag reduction. Previous work has focused on the flow mechanism within the dimples (Choi *et al.* [25], Smith *et al.* [84]) and the global characteristics of the flow (Bearman & Harvey [11], Smith *et al.* [84]); the contribution of the present work builds on that body of knowledge by investigating the effect of the flow mechanism in the dimples on the global characteristics of the flow. Outstanding questions about the nature of momentum transport in the near-wall region; formation of coherent vortical structures due to instabilities in the shear layer; and the connection between the instantaneous structures, the viscous stresses, and the turbulent stresses are addressed herein.

The mechanism of flow over dimples on a non-rotating golf ball is characterized by development of coherent vortical structures that originate from instabilities in the locally-detached shear layer. Spanwise flow structures form near the leading edge

of dimples and advect momentum into the near-wall region, energizing the flow and often producing local reattachment past the trailing edge of dimples. Local rotation of the flow is observed in the azimuthal velocity field, suggesting that Görtler-like structures are formed as the flow develops over the dimples.

Statistics and momentum fluxes provide quantitative insight into the behavior of the flow within and near individual dimples on a non-rotating golf ball. Time-histories of the aerodynamic forces reveal frequencies of the flow that are directly related to the flow mechanism over the dimples. Mean values of the force coefficents highlight the overall advantage of the dimples and the asymmetrical nature of the shedding mechanism in the wake. Statistics of the shear stress and pressure on the golf ball surface show the mean effect of the instantaneous flow structures. Local regions of increased pressure and decreased shear stress on dimpled surfaces highlight the local acceleration of the flow, which implies an increase in momentum transport. Isolines of zero shear stress show local separation bubbles within individual dimples, and illustrates the line of global separation for the mean flow. Integration of the pressure and shear stress on the golf ball illuminate the relative contribution of each to the overall drag on the golf ball, and the cumulative effect of the dimples as compared with a smooth sphere in the supercritical regime. Transport of momentum into the dimples is quantified using a reconstruction approach to calculate the local flux of momentum through surfaces which cover each dimple. Instantaneous momentum flux results correlate very well with the coherent vortical structures which form over the dimples. Mean momentum flux results confirm trends seen in statistics of the velocity field discussed in detail in Smith *et al.* [84]. Momentum flux through the surfaces covering individual dimples is most significantly affected by the turbulent stresses (the fluctuating velocity field), and visualizations of the momentum flux due to the fluctuations reveal that momentum transported by the fluctuations into the dimples is oppositely-signed when

compared with the instantaneous and mean fluxes. Contours and spatial averages of the momentum flux due to the fluctuations clearly show that the flow undergoes turbulent transition at about 50° from the stagnation point.

Chapter 7

Summary and Recommendations for Future Work

A general methodology was developed for studying the detailed physics of the flow around bluff bodies. The approach utilized Direct Numerical Simulations of the incompressible Navier-Stokes equations. A code for computing the flow around immersed bodies was extended to calculate solutions around complex, three dimensional objects (such as a golf ball in the present study). The simulations were then used to study three topics which concern the flow over a non-rotating golf ball. Detailed summaries of each of these research areas are presented in the final sections of chapters 4, 5, and 6. Section 7.1 is essentially a condensed version of these sections which highlights the significant contributions of the research. Some interesting issues have arisen through the course of this work, leading to suggestions for the future directions of related projects. These recommendations are presented in section 7.2.

7.1 Summary

7.1.1 Subcritical and Supercritical Regimes: arbitrarily-aligned golf ball

One of the most significant accomplishments of this phase of the work was the direct numerical simulation (DNS) of the flow over a non-rotating golf ball for pre-drag crisis ($Re = 1.0 \times 10^4$, $Re = 2.5 \times 10^4$) and post-drag ($Re = 1.1 \times 10^5$) crisis Reynolds numbers. The implementation of an immersed boundary approach allowed for efficient solution of the equations on cylindrical coordinate grids. The golf ball was oriented arbitrarily with respect to the flow, and was represented using momentum forcing applied on the background grid.

Flow visualizations in the near-wall region and in the wake reveal differences in the separation characteristics of the flow. The lengthscales of structures in the subcritical regime are generally larger than the diameter of the dimples, making

local detachment within dimples impossible. Thus, global flow separation occurs further upstream in the subcritical cases. For supercritical flow, the lengthscales of vortical structures are smaller than the geometrical details of the dimples, leading to local detachment within dimples even in the mean. Preliminary spectra of the velocity fluctuations reveal frequencies of small-scale flow structures associated with a shear layer instability over the dimples. Integrated forces for both physical regimes reasonably well with existing measurements.

7.1.2 Subcritical and Supercritical Regimes: symmetrically-aligned golf ball

Results from simulations of the flow in which the major axis of symmetry (of the golf ball) is aligned with the flow direction provided insight into the details of dynamics at the local (dimples) level as well as global trends in the wake. Direct numerical simulation (DNS) has been used to investigate the flow in the subcritical ($\mathrm{Re} = 2.5\times10^4$) and supercritical ($\mathrm{Re} = 1.1\times10^5$) regimes for this non-rotating ball. As in the case of the arbitrarily-aligned golf ball, simulations were performed using an immersed boundary approach in which the surface of the ball is represented using forcing applied on a background grid in a cylindrical coordinate system. The simulations highlight the effects of laminar separation, transition, and the local detachment and reattachment of the flow within dimples.

In particular, flow visualizations reveal small-scale shear layers that develop over dimples, consistent with the proposal of Choi *et al.* [25] as a key contributor to the drag reduction mechanism. This contribution helps solidify the importance of that mechanism and advance understanding of the effect of shear layer instabilities on the increased momentum transport near the golf ball, critical in delaying complete flow detachment. Time-averaged traces of the velocity provide insight into the physical processes characterizing the flow, showing that even in the average there is a recirculation within successive dimples for the supercritical regime.

The wake is comprised of low-pressure tubes which are associated with coherent vortices, while vorticity contours in crossflow planes reveal asymmetrical behavior of the wake. Averaged values of the drag force are in the range of previous measurements for non-rotating golf balls. A key contribution of the present work is the development of an approach for reconstruction of the pressure on the surface of the immersed body. This approach was utilized to investigate contours and statistics of the pressure on the immersed body. Pressure coefficients from the present DNS are comparable with those obtained from the previous computations of Constantinescu & Squires [29] and the measurements of Achenbach [3] for a smooth sphere.

Profiles of the mean velocity provide insight into the evolution of the flow near the wall, confirming complete flow detachment around 84° for the subcritical regime; while local detachment and reattachment lead to complete flow detachment around 110° for the high Reynolds number flow in the symmetry planes. Velocity spectra indicate secondary peaks at Strouhal numbers (St = 40, 60) that appear to correspond to the small-scale structures developing over the dimple near separation. Reynolds stresses quantify the contribution of the fluctuations in the regions of detached shear layers in the subcritical case, and in regions that underlie local attachment and detachment within dimples for the supercritical case.

7.1.3 Effect of surface roughness on drag reduction

Results from a direct numerical simulation (DNS) were used to study the effect of surface dimpling in the supercritical regime ($Re = 1.1 \times 10^5$) for a non-rotating golf ball. The purpose was to illuminate the effect of the dimples, which are a form of passive flow control for drag reduction. Previous work has focused on the flow mechanism within the dimples (Choi *et al.* [25], Smith *et al.* [84]) and the global characteristics of the flow (Bearman & Harvey [11], Smith *et al.* [84]); the contribu-

tion of this phase of the work builds on that body of knowledge by investigating the effect of the flow mechanism in the dimples on the global characteristics of the flow. Outstanding questions about the nature of momentum transport in the near-wall region; formation of coherent vortical structures due to instabilities in the shear layer; and the connection between the instantaneous structures, the viscous stresses, and the turbulent stresses are addressed in this phase of the work.

The mechanism of flow over dimples on a non-rotating golf ball is characterized by development of coherent vortical structures that originate from instabilities in the locally-detached layers. Flow structures form near the leading edge of dimples, and they advect momentum into the near-wall region, energizing the flow and often producing local reattachment. Local rotation of the flow in the dimples is also observed in the streamwise direction, implying that Görtler-like structures are forming during the spatio-temporal development of the flow.

Statistics and momentum fluxes provide quantitative insight into the behavior of the flow within and near individual dimples on a non-rotating golf ball. Mean values of the force coefficents highlight the overall advantage of the dimples and the asymmetrical nature of the shedding mechanism in the wake. A key contribution of this portion of the work is the implementation of a method for reconstructing the viscous stress field on an immersed body. The approach was used to evaluate statistics of the shear stress on the golf ball surface, which show the mean effect of instantaneous flow structures. Integration of the mean shear stress and the pressure on the golf ball illuminate the relative contributions of each to the overall drag force. Comparision of the integrals of pressure and shear stress with similar results for a supercritical smooth sphere demonstrate the penalty of the dimples with respect to the viscous and pressure components of the drag force. Isolines of zero shear stress show local separation bubbles within individual dimples, and illustrate where the flow globally detaches from the golf ball (this point varies between 110°

and 120° due to variations in the dimple pattern azimuthally). Transport of momentum into the dimples is quantified by calculating the local flux of momentum through surfaces which cover each dimple. Instantaneous momentum flux results correlate very well with the coherent vortical structures which form over the dimples. Mean momentum flux results confirm trends seen in statistics of the velocity field discussed in detail in Smith *et al.* [84]. Momentum fluxes due to the fluctuations clearly show that the flow undergoes turbulent transition at about 50° from the stagnation point. Contributions of the fluctuating velocity field to momentum transport within the dimples are greater than the momentum transport in the mean.

7.2 Recommendations for Future Work

Through the course of this study some interesting questions have arisen. Surface roughening using dimples is an effective means of passive flow control, and the present study illuminates the connection between flow in the dimples and the characteristic drag reduction. Dimpling as a means of passive flow control is advantageous in a range of engineering applications, beyond sports equipment. The present study advances understanding of how this means of control contributes to drag reduction. Studies of the flow over golf balls in which the key geometric features of the dimples are varied would be enlightening. The metrics employed in the present work (statistics of the shear stress, pressure, and momentum flux) could be used to evaluate the relative effects of geometrical parameters such as dimple depth, dimple diameter, as well as dimple patterns. A key contribution would be to explore the geometric parameter space of the dimples while including the effects of rotation.

Since the flow over a golf ball includes laminar separation, transition and global separation, it presents a challenge to any empirical approach. A possible extension of this work may be the calibration of turbulence models; existing models could be tested in the same physical regime as those resolved in the present contribution.

REFERENCES

[1] Achenbach, E. 1968 Distribution of local pressure and skin friction around a circular cylinder in cross-flow up to $re = 5x10^6$. *Journal of Fluid Mechanics* **34** (04), 625.

[2] Achenbach, E. 1971 Influence of surface roughness on the cross-flow around a circular cylinder. *Journal of Fluid Mechanics* **46** (02), 321.

[3] Achenbach, E. 1972 Experiments on the flow past spheres at very high reynolds numbers. *Journal of Fluid Mechanics* **54** (03), 565.

[4] Achenbach, E. 1974 The effects of surface roughness and tunnel blockage on the flow past spheres. *Journal of Fluid Mechanics* **65** (1), 113.

[5] Akselvoll, K. & Moin, P. 1996 Large-eddy simulation of turbulent confined coannular jets. *Journal of Fluid Mechanics* **315** (-1), 387.

[6] Arya, S., Mount, D., Netanyahu, N. & Silverman, R. 1994 An optimal algorithm for approximate nearest-neighbor searching in fixed dimensions. In *Proceedings of the Fifth Annual ACM-SIAM Symposium on Discrete Algorithms*, pp. 573–582.

[7] Ausas, R., Buscaglia, G., Leiva, J., Jai, M., Bayada, G. & Ragot, P. 2006 The impact of the cavitation model in the analysis of micro-textured lubricated journal bearings. *Mecanica Computacional* **25**, 1247–1258.

[8] Balaras, E. 2002 Large eddy simulation of high reynolds number wall bounded shear layers. PhD thesis, Swiss Federal Institute of Technology (EPFL).

[9] Balaras, E. 2004 Modeling complex boundaries using an external force field on fixed cartesian grids in large-eddy simulations. *Computers and Fluids* **33** (3), 375.

[10] Balaras, E. & Yang, J. 2005 Nonboundary conforming methods for large-eddy simulations of biological flows. *Journal of Fluids Engineering* **127** (5), 851.

[11] Bearman, P. W. & Harvey, J. K. 1976 Golf ball aerodynamics. *Aeronautical Quarterly* **27** (2), 112–122.

[12] Beratlis, N. 2006 Eddy flow solver. *Personal Communication* p. 1147.

[13] Beratlis, N. 2011 A wall model for immersed boundary methods. *Personal Communication* p. 1.

[14] Beratlis, N., Balaras, E. & Kiger, K. 2007 Direct numerical simulations of transitional pulsatile flow through a constriction. *Journal of Fluid Mechanics* **587**, 425–451.

[15] Beratlis, N., Balaras, E., Parvinian, B. & Kiger, K. 2005 A numerical and experimental investigation of transitional pulsatile flow in a stenosed channel. *Journal of Biomechanical Engineering* **127** (7), 1147.

[16] Beyer, R. P. 1992 A computational model of the cochlea using the immersed boundary method. *Journal of Computational Physics* **98** (1), 145.

[17] Bower, Alan F. 2010 *Applied mechanics of solids*. Boca Raton, FL: Taylor and Francis.

[18] Brizmer, V., Kligerman, Y. & Etsion, I. 2003 A laser surface textured parallel thrust bearing. *Tribology Transactions* **46** (3), 397.

[19] Bunker, R. S. & Donnellan, K. F. 2003 Heat transfer and friction factors for flows inside circular tubes with concavity surfaces. *Journal of Turbomachinery* **125** (4), 665.

[20] Cebeci, T. & Bradshaw, P. 1977 *Momentum Transfer in Boundary Layers*. Washington: Hemisphere Publishing Corporation.

[21] Chesnakas, C. J. & Simpson, R. L. 1994 Full three-dimensional measurements of the cross-flow separation region of a 6:1 prolate spheroid. *Experiments in Fluids* **17** (1-2), 68–74.

[22] Chesnakas, C. J. & Simpson, R. L. 1997 Detailed investigation of the three-dimensional separation about a 6: 1 prolate spheroid. *AIAA Journal* **35** (6), 990.

[23] Choi, Haecheon 2008 Control of flow over a bluff body. *Annual Review of Fluid Mechanics* **40** (1), 113–139.

[24] Choi, H., Moin, P. & Kim, J. 1993 Direct numerical simulation of turbulent flow over riblets. *Journal of Fluid Mechanics* **255** (1), 503–539.

[25] Choi, Jin J., Jeon, W. & Choi, H. 2006 Mechanism of drag reduction by dimples on a sphere. *Physics of Fluids* **18** (4), 041702.

[26] Constantinescu, G.S. & Squires, K.D. 2000 Les and des investigations of turbulent flow over a sphere. *AIAA Journal, 2000-0540* .

[27] Constantinescu, George S., Pasinato, H., Wang, Y., Forsythe, J. & Squires, K. 2002 Numerical investigation of flow past a prolate spheroid. *Journal of Fluids Engineering* **124** (4), 904.

[28] Constantinescu, George S. & Squires, K. D. 2003 Les and des investigations of turbulent flow over a sphere at re = 10,000. *Flow, Turbulence and Combustion* **70**, 267–298.

[29] Constantinescu, George S. & Squires, K. D. 2004 Numerical investigations of flow over a sphere in the subcritical and supercritical regimes. *Physics of Fluids* **16** (5), 1449.

[30] Davies, John M. 1949 The aerodynamics of golf balls. *Journal of Applied Physics* **20** (9), 821.

[31] Diasinos, S. S. & Gatto, A. 2008 Experimental investigation into wing span and angle-of-attack effects on sub-scale race car wing/wheel interaction aerodynamics. *Experiments in Fluids* **45** (3), 537–546.

[32] Eggels, J. G. M., Unger, F., Weiss, M., Westerweel, J., Adrian, R., Friedrich, R. & Nieuwstadt, F. 1994 Fully developed turbulent pipe flow: a comparison between direct numerical simulation and experiment. *Journal of Fluid Mechanics* **268** (1), 175.

[33] Fadlun, E. A., Verzicco, R., Orlandi, P. & Mohd-Yusof, J. 2000 Combined immersed-boundary finite-difference methods for three-dimensional complex flow simulations. *Journal of Computational Physics* **161** (1), 35.

[34] Forsythe, J.R. & Woodson, S.H. 2003 Unsteady cfd calculations of abrupt wing stall using detached-eddy simulation. *AIAA Journal, 2003-0594* .

[35] Forsythe, J. R., Squires, K. D., Wurtzler, K. E. & Spalart, P. R. 2002 Detached-eddy simulation of fighter aircraft at high alpha. In *AIAA Aerospace Sciences Meeting*, pp. 1–11. Reno, NV: AIAA.

[36] Fu, T. C. 1994 The flow structure in the lee of an inclined 6: 1 prolate spheroid. *Journal of Fluid Mechanics* **269** (1), 79.

[37] Gee, K. 1992 Turbulence model effects on separated flow about a prolate spheroid. *AIAA Journal* **30** (3), 655.

[38] Gerrard, J. H. 1978 The wakes of cylindrical bluff bodies at low reynolds number. *Philosophical Transactions of the Royal Society of London. Series A, Mathematical and Physical Sciences* **288** (1354), pp. 351–382.

[39] Ghias, R., Mittal, R. & Lund, T. S. 2004 A non-body conformal grid method for simulation of compressible flows with complex immersed boundaries. *AIAA Journal* (0080).

[40] Gilmanov, A., Sotiropoulos, F. & Balaras, E. 2003 A general reconstruction algorithm for simulating flows with complex 3d immersed boundaries on cartesian grids. *Journal of Computational Physics* **191** (2), 660.

[41] Gottlieb, J.J. & Groth, C.P.T. 1988 Assessment of riemann solvers for unsteady one-dimensional inviscid flows of perfect gases. *Journal of Computational Physics* **78**, 437–458.

[42] Hemida, Hassan H. & Krajnovic, S. 2008 L e s study of the influence of a train-nose shape on the flow structures under cross-wind conditions. *Journal of Fluids Engineering* **130** (9), 091101.

[43] Henderson, Ronald D. 1995 Details of the drag curve near the onset of vortex shedding. *Physics of Fluids* **7** (9), 2102.

[44] Hiemenz, K. 1911 Die grenzschict an einem in den gleichformigen flussigkeitsstrom eingetauchten geraden kreiszylinder. *Dingler's Polytech J.* **326**, 321.

[45] Hunt, J. C. R., Wray, A. & Moin, P. 1988 Eddies, stream, and convergence zones in turbulent flows. *Tech. Rep.*. Stanford University.

[46] Iaccarino, G., Kalitzin, G. & Elkins, C. J. 2003 Numerical and experimental investigation of the turbulent flow in a ribbed serpentine passage. *Center for Turbulence Research Report* pp. 379–388.

[47] Jensen, Jeremy Gutierrez 2010 Direct numerical simulation of turbulent flow over a dimpled flat plate using immersed boundary technique. Master's thesis, Arizona State University, Tempe, Arizona.

[48] Johnson, T. A. & Patel, V. C. 1999 Flow past a sphere up to a reynolds number of 300. *Journal of Fluid Mechanics* **378** (-1), 19.

[49] Kalitzin, G., Iaccarino, G. & Khaligi, B. 2003 Towards an immersed boundary solver for rans simulations. *AIAA Journal* (0770).

[50] Karniadakis, G. E. & Triantafyllou, G. S. 1992 Three-dimensional dynamics and transition to turbulence in the wake of bluff objects. *Journal of Fluid Mechanics* **238** (1), 1.

[51] Karypis, G., Schloegel, K. & Kumar, V. 1997 *ParMETIS: Parallel Graph Partioning and Sparse Matrix Ordering Library Version 1.0*. Minneapolis, MN: University of Minnesota, Department of Computer Science.

[52] Katz, Joseph J. 2006 Aerodynamics of race cars. *Annual Review of Fluid Mechanics* **38** (1), 27–63.

[53] Kim, D. & Choi, H. 2002 Laminar flow past a sphere rotating in the streamwise direction. *Journal of Fluid Mechanics* **461**, 365.

[54] Kim, J., Kim, D. & Choi, H. 2001 An immersed-boundary finite-volume method for simulations of flow in complex geometries. *Journal of Computational Physics* **171** (1), 132.

[55] Krishnan, V., Squires, K. D. & Forsythe, J. R. 2004 Prediction of separated flow characteristics over a hump using rans and des. In *2nd AIAA Flow Control Conference*. AIAA.

[56] Lin, J. C., Towfighi, J. & Rockwell, D. 1995 Instantaneous structure of the near-wake of a circular cylinder: on the effect of reynolds number. *Journal of Fluids and Structures* **9** (4), 409–418.

[57] Maxworthy, T. 1969 Experiments on the flow around a sphere at high reynolds numbers. *Journal of Applied Mechanics* **36**, 598.

[58] Menter, F. & Kuntz, M. 2003 Adaptation of eddy-viscosity turbulence models to unsteady separated flow behind vehicles. In *The Aerodynamics of Heavy Vehicles: Trucks, Buses, and Trains*, pp. 339–352. Berlin: Springer-Verlag.

[59] Mittal, R. & Balachandar, S. 1995 Effect of three-dimensionality on the lift and drag of nominally two-dimensional cylinders. *Physics of Fluids* **7** (8), 1841.

[60] Mittal, R. & Iaccarino, G. 2005 Immersed boundary methods. *Annual Review of Fluid Mechanics* **37** (1), 239–261.

[61] Mittal, R., Seshadri, V. & Udaykumar, H. S. 2004 Flutter, tumble and vortex induced autorotation. *Theoretical and Computational Fluid Dynamics* **17** (3), 165–170.

[62] Mode, Jeffrey M. 2010 Simulation of the flow over a flat dimpled plate. Master's thesis, Arizona State University, Tempe, Arizona.

[63] Moon, H. K., O'Connell, T. & Glezer, B. 2000 Channel height effect on heat transfer and friction in a dimpled passage. *Journal of Engineering for Gas Turbines and Power* **122** (2), 307.

[64] Morinishi, Y., Vasilyev, O. & Ogi, T. 2004 Fully conservative finite difference scheme in cylindrical coordinates for incompressible flow simulations. *Journal of Computational Physics* **197** (2), 686.

[65] Norberg, C. 2003 Fluctuating lift on a circular cylinder: review and new measurements. *Journal of Fluids and Structures* **17** (1), 57.

[66] Orlanski, I. 1976 A simple boundary condition for unbounded hyperbolic flows. *Journal of Computational Physics* **21** (3), 251.

[67] O'Rourke, J. 1998 *Computational Geometry in C*. NY: Cambridge University Press.

[68] Osher, S. & Fedkiw, R. P. 2003 *Level set methods and dynamic implicit surfaces*. NY: Springer-Verlag.

[69] Pauley, H., Ralston, J. & Dickes, E. 1995 Experimental study of the effects of reynolds number on high angle of attack aerodynamic characteristics of forebodies during rotary motion. *NASA CR 195033* .

[70] Peskin, C. S. 1972 Flow patterns around heart valves: a digital computer method for solving the equations of motion. PhD thesis, Albert Einstein College of Medicine, University Microfilms, 378:72-30.

[71] Peskin, C. S. 1982 The fluid dynamics of heart valves: Experimental, theoretical, and computational methods. *Annual Review of Fluid Mechanics* **14** (1), 235–259.

[72] Pierce, C. 2001 Progress-variable approach for large eddy simulation of turbulent combustion. PhD thesis, Stanford University, Stanford, CA.

[73] Piot, E., Casalis, G. & Rist, U. 2008 Stability of the laminar boundary layer flow encountering a row of roughness elements: Biglobal stability approach and dns. *European Journal of Mechanics, B, Fluids* **27** (6), 684.

[74] Pope, Stephen B. 2000 *Turbulent Flows*. New York: Cambridge University Press.

[75] Press, W., Teukolsy, S., Vetterling, W. & Flannery, B. 1992 *Numerical Recipes in Fortran 77: The Art of Scientific Computing*. NY: Cambridge University Press.

[76] Roache, P. J. 1994 Perspective: a method for uniform reporting of grid refinement studies. *Journal of Fluids Engineering* **116** (3), 405.

[77] Roache, P. J. & Knupp, P. M. 1993 Complete richardson extrapolation. *Communication in Numerical Methods in Engineering* **9**, 365.

[78] Roos, F. W. & Willmarth, W. 1971 Some experimental results on sphere and disk drag. *AIAA Journal* **9** (2), 285–291.

[79] Roshko, A. 1961 Experiments on the flow past a circular cylinder at very high reynolds number. *Journal of Fluid Mechanics* **10** (03), 345.

[80] Schetz, Joseph J. A. 2001 Aerodynamics of high-speed trains. *Annual Review of Fluid Mechanics* **33** (1), 371–414.

[81] Schlichting, H. 1979 *Boundary-Layer Theory*, seventh edn. McGraw-Hill.

[82] Shur, M., Spalart, P.R., Stretlets, M. & Travin, A. 1999 Detached-eddy simulation of an airfoil at high angle of attack. In *4th International Symposium of Engineering Turbulence Modeling and Measurements*. Corsica.

[83] Smagorinsky, J. 1963 General circulation experiments with the primitive equations: I. the basic equations. *Mon. Weather Rev.* **91** (1), 99–164.

[84] Smith, C. E., Beratlis, N., Balaras, E., Squires, K. D. & Tsunoda, M. 2010 Numerical investigation of the flow over a golf ball in the subcritical and supercritical regimes. *The International Journal of Heat and Fluid Flow* **31** (3), 262.

[85] Smits, A. & Ogg, S. 2004 *Aerodynamics of the Golf Ball*. Kluwer Academic Publishers.

[86] Smits, A. & Smith, D. 1994 A new aerodynamic model of a golf ball in flight. In *Science and Golf II: Proceedings of the World Scientific Congress of Golf II*, , vol. II, p. 340.

[87] Son, K., Choi, J., Jeon, W. P. & Choi, H. 2011 Mechanism of drag reduction by a surface trip wire on a sphere. *Journal of Fluid Mechanics* **672** (1), 411.

[88] Spalart, P.R. & Allmaras, S.R. 1994 A one-equation turbulence model for aerodynamic flows. *La Recherche Aerospatiale* pp. 5–21.

[89] Spalart, Philippe R. 2003 Simulation of active flow control on a stalled airfoil. *Flow, Turbulence and Combustion* **71** (1-4), 361–373.

[90] Spalart, Philippe R. 2008 On the far wake and induced drag of aircraft. *Journal of Fluid Mechanics* **603**, 413.

[91] Spalart, P. R., Deck, S., Shur, M. L., Squires, K. D., Strelets, M. Kh. & Travin, A. 2006 A new version of detached-eddy simulation, resistant to ambiguous grid densities. *Theo. Comp. Fluid Dynamics* **20** (3), 181.

[92] Spalart, P. R. & Strelets, M. K. 2000 Mechanisms of transition and heat transfer in a separation bubble. *Journal of Fluid Mechanics* **403** (1), 329.

[93] Squires, K.D., Forsythe, J.R. & Spalart, P.R. 2001 *Detached-Eddy Simulation of the separated flow around a forebody cross-section*. Kluwer Academic Press.

[94] Squires, K. D., Forsythe, J. R., Morton, S. A., Blake, D. C., Serrano, M., Wurtzler, K. E., Strang, W. Z., Tomaro, R. F. & Spalart, P. R. 2002 Analysis of full aircraft with massive separation using detached eddy simulation. In *Proceedings of the High Performance Computing Modernization Programme, Users Group Conference*.

[95] Squires, K. D., Krishnan, V. & Forsythe, J. R. 2008 Prediction of the flow over a circular cylinder at high reynolds number using detached-eddy simulation. *Journal of Wind Engineering and Industrial Aerodynamics* **96** (10-11), 1528.

[96] Strang, W.Z., Tomaro, R.F. & Grismer, M.J. 1999 The defining methods of cobalt$_{60}$: a parallel, implicit, unstructured euler/navier-stokes flow solver. *AIAA Journal, 99–0786* .

[97] Swarztrauber, P. 1974 Direct method for the discrete solution of separable elliptic equations. *Siam Journal of Numerical Analysis* **11**, 1136.

[98] Swarztrauber, P. 1984 Fast fourier transforms algorithms for vector computers. *Parallel Computing* pp. 45–64.

[99] Taneda, S. 1978 Visual observations of the flow past a sphere at reynolds numbers between 10^4 and 10^6. *Journal of Fluid Mechanics* **85** (1), 187.

[100] Thoman, David Charles 1966 Numerical solutions of time dependent two dimensional flow of a viscous, incompressible fluid over stationary and rotating cylinders. PhD thesis, University of Notre Dame, Indiana.

[101] Travin, A., Shur, M., Strelets, M. & Spalart, P.R. 1999 Detached-eddy simulations past a circular cylinder. *Flow, Turbulence, and Combustion* **63**, 293–313.

[102] Unal, M. F. & Rockwell, D. 1988 On vortex formation from a cylinder. part 1. the initial instability. *Journal of Fluid Mechanics* **190** (-1), 491.

[103] Unverdi, S. O. & Tryggvason, G. 1992 A front-tracking method for viscous, incompressible, multi-fluid flows. *Journal of Computational Physics* **100** (1), 25.

[104] Verzicco, R., Fatica, M., Iaccarino, G. & Moin, P. 2002 Large eddy simulation of a road vehicle with drag reduction devices. *AIAA Journal* **40** (12).

[105] Verzicco, R., Mohd-Yusof, J., Orlandi, P. & Haworth, D. 1999 Les in complex geometries using boundary body forces. *Center for Turbulence Research Report* pp. 379–388.

[106] Verzicco, R. & Orlandi, P. 1996 A finite-difference scheme for three-dimensional incompressible flows in cylindrical coordinates. *Journal of Computational Physics* **123** (2), 402.

[107] Viswanathan, A., Klismith, K., Forsythe, J. & Squires, K. 2003 Detached-eddy simulation around a rotating forebody. *AIAA Journal, 2003-0263* .

[108] Wetzel, T. G. 1998 Measurement of three-dimensional crossflow separation. *AIAA Journal* **36** (4), 557.

[109] Williamson, C. H. K. 1996 Vortex dynamics in the cylinder wake. *Annual Review of Fluid Mechanics* **28** (1), 477–539.

[110] Wurtzler, K.E. 1999 An effectivness study of f-15 forebody flow analysis using cobalt. *AIAA Journal 99-0536* .

[111] Wygnanski, Israel 2006 Iutam symposium on one hundred years of boundary layer research - a century of active control of boundary layer separation: A personal view. *Proceedings of the IUTAM symposium held at DLR-Gottingen, Germany, August 12-14, 2004* **129**, 155–165.

[112] Yang, J. 2005 An embedded-boundary formulation for large-eddy simulation of turbulent flows interacting with moving boundaries. PhD thesis, University of Maryland, Maryland.

[113] Yang, J. & Balaras, E. 2006 An embedded-boundary formulation for large-eddy simulation of turbulent flows interacting with moving boundaries. *Journal of Computational Physics* **215** (1), 12.

[114] Ye, T., Mittal, R., Udaykumar, H. S. & Shyy, W. 1999 An accurate cartesian grid method for viscous incompressible flows with complex immersed boundaries. *Journal of Computational Physics* **156**, 209–240.

[115] Zhu, Luoding L. & Peskin, C. 2003 Interaction of two flapping filaments in a flowing soap film. *Physics of Fluids* **15** (7), 1954, doi:10.1063/1.1582476 pmid:.

APPENDIX A

PARAMETER STUDY - PREDICTION OF THE FLOW OVER A GOLF BALL WITH DIFFERING GEOMETRY, MESHES, AND TURBULENCE MODELS

In the following appendix, preliminary results from a study of the flow over a golf ball using a boundary conforming approach are presented. The primary goal is to assess the capability of the turbulence treatments to predict the flight performance of the golf ball and to resolve the turbulent flow structures that contribute to delayed separation.

In particular, a boundary conforming approach within the framework of turbulence modeling has been applied to the study of the flow over a golf ball with and without rotation. Three different approaches are applied: Spalart-Allmaras Reynolds-averaged Navier-Stokes (RANS) (Spalart & Allmaras [88]), detached-eddy simulation (DES) (Spalart *et al.* [91]), and no (turbulence) model. Preliminary results motivated a modification for the DES approach, in which the transition of the model from RANS to LES (large-eddy simulation) is delayed in order to preserve the model length scale in the boundary layer. Solutions are calculated on unstructured grids ranging from 3×10^6 points to 10×10^6 points, with most solutions calculated using baseline grids of 6.4×10^6 and 6.7×10^6 points. Computations are performed for a post-drag crisis Reynolds number (based on the diameter of the golf ball and the freestream velocity) of 1.6×10^5. Flow visualization reveals the turbulent characteristics of the wake, which appear to be affected by the geometry of the surface. Time-averaged statistics of velocity, pressure, and shear stress indicate the location of complete flow detachment. Predictions of the lift and drag appear to be in reasonable agreement with the measurements of Bearman & Harvey [11] and Choi *et al.* [25].

A.1 Simulation Overview

The compressible Navier-Stokes equations are solved on unstructured grids using *Cobalt* (Strang *et al.* [96]). The numerical method is a cell-centered finite volume approach applicable to arbitrary cell topologies (e.g, hexahedron, prisms, tetrahe-

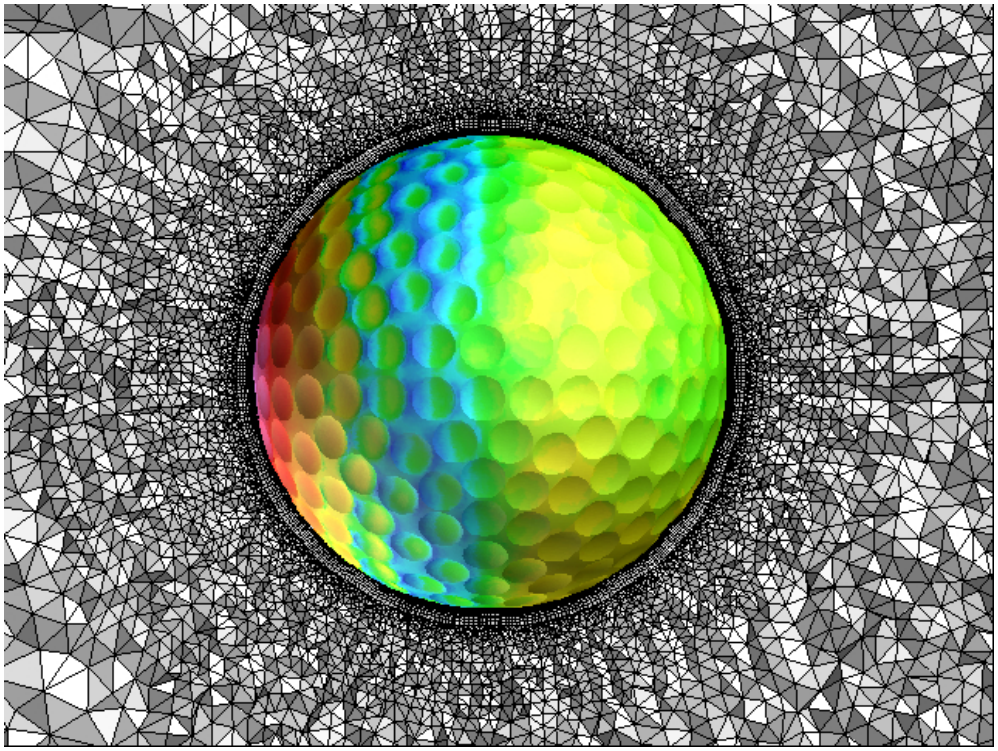

Figure A.1: Contours of the mean pressure coefficient C_p superimposed on a cross-section of the grid in the vicinity of the golf ball, $Re = 1.6 \times 10^5$.

dron). The spatial operator uses the exact Riemann solver of Gottlieb & Groth [41], least squares gradient calculations using QR factorization to provide second order accuracy in space, and TVD flux limiters to limit extremes at cell faces. A point implicit method using analytical first-order inviscid and viscous Jacobians is used for advancement of the discretized system. For time-accurate computations, a Newton sub-iteration scheme is employed, the method is second order accurate in time. The domain decomposition library ParMETIS (Karypis *et al.* [51]) is used for parallel implementation and communication between processors is achieved using Message Passing Interface.

The computations have been performed on unstructured grids comprised of 6.4×10^6 cells. A cross-section in the vicinity of the non-rotating golf ball is shown in Figure A.1. The grids were created using *Gridgen* and are comprised of prisms

near the ball surface and tetrahedra away from the wall. Farfield conditions are applied at the outer boundaries of the computational domain that lie in the plane of the freestream velocity vector. The outer boundaries are located 14 diameters from the golf ball surface. The Reynolds number based on golf ball diameter and freestream velocity for the results presented in the next section is 1.6×10^5. The separated flow is approximated by computing fully-turbulent solutions.

The baseline version DES97 is formulated using the Spalart-Allmaras (referred to as 'S-A' throughout) one-equation model (Spalart & Allmaras [88]), which solves solves a single partial differential equation for a variable $\widetilde{\nu}$ which is related to the turbulent viscosity. The model includes a wall destruction term that reduces the turbulent viscosity in the log layer and laminar sublayer and trip terms that provides a smooth transition from laminar to turbulent flow.

The baseline formulation, DES97, is based on a modification to the Spalart-Allmaras RANS model such that the model reduces to its RANS formulation near solid surfaces and to a subgrid model away from the wall. The basis is to attempt to take advantage of the usually adequate performance of RANS models in the thin shear layers where these models are calibrated and LES for resolution of geometry-dependent and three-dimensional eddies. The DES formulation is obtained by replacing in the S-A model the distance to the nearest wall, d, by $\widetilde{d}$, where $\widetilde{d}$ in DES97 is defined as,

$$\widetilde{d} \equiv \min(d, \Delta) \tag{A.1}$$

where the lengthscale Δ is the largest distance between the cell center under consideration and the cell center of the neighbors (i.e., those cells sharing a face with the cell in question). In "natural" applications of DES, the wall-parallel grid spacings (e.g., streamwise and spanwise) are typically on the order of the boundary layer thickness and the S-A RANS model is retained throughout the boundary layer, i.e.,

$\widetilde{d} = d$. Consequently, prediction of boundary layer separation is determined in the "RANS mode" of DES. Away from solid boundaries, the closure is a one-equation model for the SGS eddy viscosity. The constant $C_{DES} = 0.65$ was set in homogeneous turbulence (Shur *et al.* [82]) and is used without modification in this study.

The new version of the model, DDES, modifies the formula (A.1) in order to preserve RANS treatment of the boundary layer. Essentially, the spirit of the modification (A.1) is to utilize information concerning the lengthscale of the turbulence as predicted by the model, in addition to the wall distance and local grid spacing. As reported by Spalart *et al.* [91], the modification is analogous to that developed by Menter and Kuntz which uses the blending function F_2 of the SST model to shield the boundary layer and "delay LES function" (Menter & Kuntz [58]). The argument of this function is $\sqrt{k}/(\omega \mathrm{y})$, which is the ratio between the internal length scale $\sqrt{k}/\omega$ of the k-ω turbulence model and the distance to the wall (y or d). The F function equals 1 in the boundary layer and falls to 0 rapidly at the edge of the boundary layer. The S-A model does not use an internal length scale such as $\sqrt{k}$ / ω but instead involves the parameter r, which is also the squared ratio of a model length scale to the wall distance (the length scale is not internal in that it involves the mean shear rate). For DDES, the parameter r is slightly modified relative to the S-A definition, in order to apply to any eddy-viscosity model, and be slightly more robust in irrotational regions, where ν_t is the kinematic eddy viscosity, ν the molecular viscosity, $U_{i,j}$ the velocity gradients, κ the Karman constant, and d the distance to the wall. Similar to r in the S-A model, this parameter equals 1 in a logarithmic layer, and falls to 0 gradually towards the edge of the boundary layer. The addition of ν in the numerator corrects the very near-wall behavior by ensuring that r_d remains away from 0. In the S-A model, $\widetilde{\nu}$ can be used instead of $\nu_t + \nu$. The subscript "d" represents "delayed."

$$r_d \equiv \frac{\nu_t + \nu}{\sqrt{U_{i,j}U_{i,j}}\kappa^2 d^2} \tag{A.2}$$

The quantity r_d is used in the function, which is designed to be 1 in the LES region, where $r_d << 1$, and 0 elsewhere (and to be insensitive to r_d exceeding 1 very near the wall). It is similar to 1 - F_2, and rather steep near $r_d = 0.1$.

$$f_d \equiv 1 - tanh([8r_d]^3) \tag{A.3}$$

The values 8 and 3 for the constants in (A.3) are based on intuitive shape requirements for f_d, and on tests of DDES in the flat-plate boundary layer. These values for the coefficients ensure that the solution is essentially identical to the RANS solution, even if Δ is much less than δ. A value larger than 8 would delay LES in even larger regions, which would be safer in the sense of avoiding Modeled Stress Depletion (MSD), but is undesirable overall. It is conceivable that models very different from S-A would make r_d approach 0 at $d = \delta$ differently enough to require a modest adjustment of f_d.

The application of the above procedures to S-A-based DES, which is used from here on, proceeds by re-defining the DES length scale $\tilde{d}$, setting f_d to 0 yields RANS ($\tilde{d} = d$), while setting it to 1 gives DES97 ($\tilde{d} = \min(d, C_{DES}\Delta)$). For DES based on most of the possible RANS models, DDES will consist in multiplying by f_d the term that constitutes the difference between RANS and DES, as in (A.4).

$$\tilde{d} \equiv d - f_d max(0, d - C_{DES}\Delta) \tag{A.4}$$

A.2 Results

Instantaneous contours of vorticity and pressure illustrate the differences between the simulation strategies by comparing the flow before and after detachment. Isosurfaces of the instantaneous vorticity magnitude colored by pressure are shown in

Figure A.2a for Spalart-Allmaras RANS, Figure A.2b for DES, and Figure A.2c for the no-model case. All three simulation strategies exhibit similarity in the capture of small-scale striations in the isosurface near the point of flow detachment. These disturbances have a width roughly of the same length-scale as the diameter of the dimples. Figure A.2a,b show that isosurfaces upstream of separation are smooth, consistent with the RANS treatment of the attached boundary layers in both cases. The no-model case (Figure A.2c) also displays smooth isosurfaces before separation, which is due to the laminar-like behavior of the attached boundary layer. Owing to the strong instabilities governing the flow, the unsteady DES and no-model approaches exhibit wake structures that quickly develop a complex, three-dimensional character. Furthermore, interesting differences in the location of complete flow detachment are observed between the DES calculation and the no-model result; e.g., the flow appears to remain attached further into the wake in the no-model calculation, whereas DES displays detachment around 95 degrees (measured from the stagnation point on the front of the golf ball).

Mean-flow properties such as velocity and pressure yield insight into the understanding of the separation properties (and thus, indirectly, the aerodynamic forces) for each predictive approach. Isosurfaces of the mean streamwise velocity at a value of zero (useful for isolating the regions where flow reversal is occuring) are displayed for each case in Figure A.3.

Time histories of the drag coefficient are plotted in Figure A.4a, respectively. The black curve shown is the modified version of DES in which the LES region is not activated until approximately $r/D = 1.025$. It is noteworthy to observe that the mean drag coefficient for the modified DES is approximately 0.25, in good agreement with the experimental predictions of Bearman & Harvey [11] and Choi *et al.* [25]. The lift force oscillations in Figure A.4b display the modulation characteristic of bluff body flows and reflect the complex processes governing the wake.

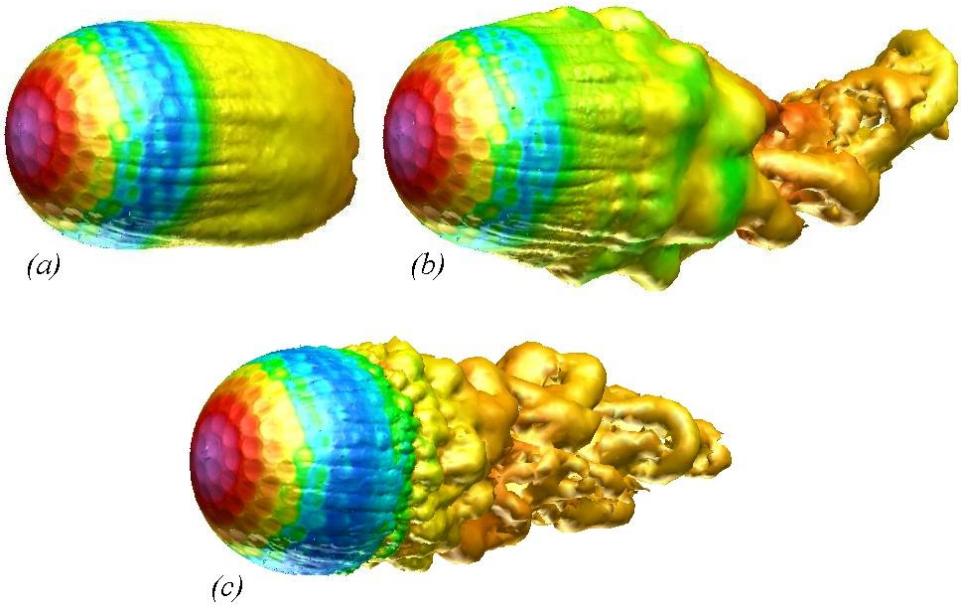

Figure A.2: Isosurfaces of the instantaneous vorticity magnitude colored by pressure. (*a*) S-A RANS; (*b*) DES; (*c*) No-model.

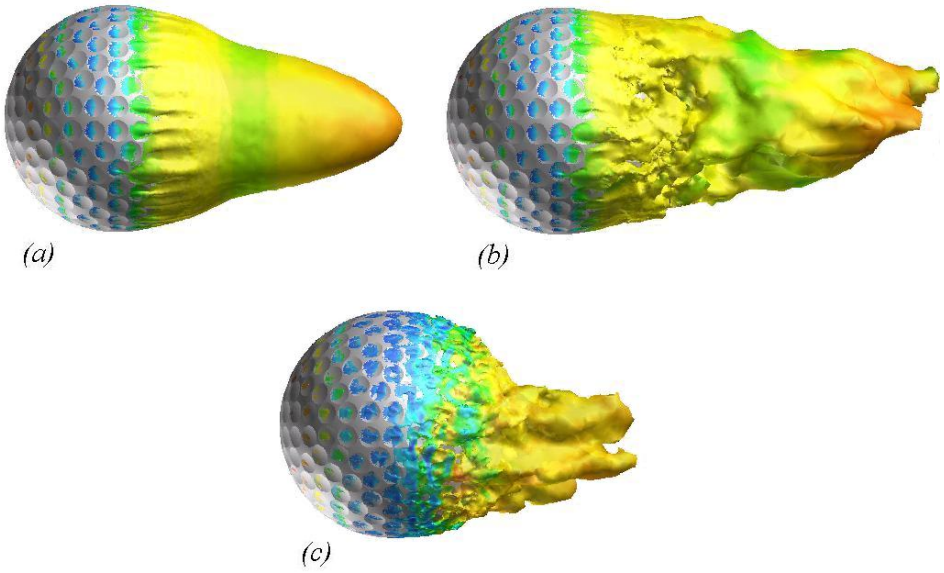

Figure A.3: Isosurface of instantaneous streamwise velocity (colored by pressure) where the isovalue is equal to zero. (*a*) S-A RANS; (*b*) DES; (*c*) No-model.

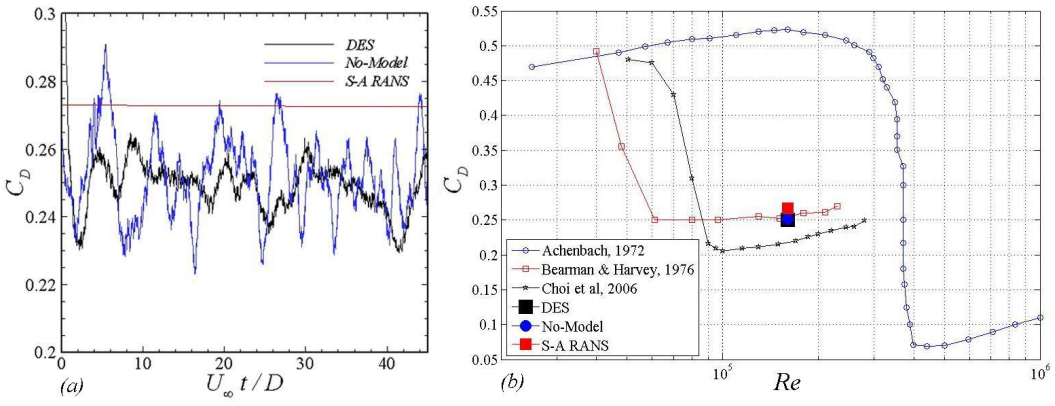

Figure A.4: Aerodynamic force results for the supercritical Reynolds number ($Re = 1.6 \times 10^5$) and three different modeling approaches (*a*) Time history of the drag coefficient; (*b*) Drag coefficient versus Reynolds number.

A.3 Summary

Predictions of the flow over a golf ball have been conducted using turbulence modeling. One objective of the current contribution is the application of detached eddy simulation (DES) to study the flow over a golf ball in order to understand the behavior of the model. This application of DES provides accurate calculation of the aerodynamic forces, but its limitations in predicting flows with turbulent transition and separation (such as the flow over a golf ball) motivate a higher-fidelity approach.

APPENDIX B

CONTINUOUS FORM OF DIFFERENTIAL OPERATORS FOR CONVECTIVE AND VISCOUS TERMS WITH THE IMPLICIT CRANK NICHOLSON TIME ADVANCE

Since the discrete forms of these operators are reported in Chapter 2 in computational space, some readers may be interested in the continuous form in physical space.

$$\left[1-\frac{\alpha_k\Delta t}{2}\frac{1}{Re}\frac{1}{r^2}\frac{\partial^2}{\partial\theta^2}\right]\widehat{u_r^k} = RHS_r{}^{k-1}$$
$$= u_r{}^{k-1}+\gamma_k\Delta t A_r{}^{k-1}+\rho_k\Delta t A_r{}^{k-2}+\frac{\alpha_k\Delta t}{2}B_r{}^{k-1}-\alpha_k\Delta t\frac{\partial p^{k-1}}{\partial r} \qquad \text{(B.1)}$$

$$\left[1-\frac{\alpha_k\Delta t}{2}\frac{1}{Re}\frac{1}{r^2}\frac{\partial^2}{\partial\theta^2}\right]\widehat{u_\theta^k} = RHS_\theta{}^{k-1}$$
$$= u_\theta{}^{k-1}+\gamma_k\Delta t A_\theta{}^{k-1}+\rho_k\Delta t A_\theta{}^{k-2}+\frac{\alpha_k\Delta t}{2}B_\theta{}^{k-1}-\alpha_k\Delta t\frac{1}{r}\frac{\partial p^{k-1}}{\partial\theta} \qquad \text{(B.2)}$$

$$\left[1-\frac{\alpha_k\Delta t}{2}\frac{1}{Re}\frac{1}{r^2}\frac{\partial^2}{\partial\theta^2}\right]\widehat{u_z^k} = RHS_z{}^{k-1}$$
$$= u_z{}^{k-1}+\gamma_k\Delta t A_z{}^{k-1}+\rho_k\Delta t A_z{}^{k-2}+\frac{\alpha_k\Delta t}{2}B_z{}^{k-1}-\alpha_k\Delta t\frac{\partial p^{k-1}}{\partial z} \qquad \text{(B.3)}$$

The coefficients are the same as were defined above in Section 2.1.3.1, and the A and B operators are defined as follows:

$$A_r = -\left[\frac{1}{r}\frac{\partial(ru_ru_r)}{\partial r}+\frac{1}{r}\frac{\partial(u_\theta u_r)}{\partial\theta}+\frac{\partial(u_zu_r)}{\partial z}-\frac{{u_\theta}^2}{r}\right]$$
$$+\frac{1}{Re}\left[\frac{\partial}{\partial r}\left(\frac{1}{r}\frac{\partial(ru_r)}{\partial r}\right)+\frac{\partial^2u_r}{\partial z^2}-\frac{2}{r^2}\frac{\partial u_\theta}{\partial\theta}\right] \qquad \text{(B.4)}$$

$$A_\theta = -\left[\frac{1}{r}\frac{\partial(ru_ru_\theta)}{\partial r}+\frac{1}{r}\frac{\partial(u_\theta u_\theta)}{\partial\theta}+\frac{\partial(u_zu_\theta)}{\partial z}+\frac{u_ru_\theta}{r}\right]$$
$$+\frac{1}{Re}\left[\frac{1}{r}\frac{\partial}{\partial r}\left(r\frac{\partial u_\theta}{\partial r}\right)+\frac{\partial^2u_\theta}{\partial z^2}+\frac{2}{r^2}\frac{\partial u_r}{\partial\theta}-\frac{u_\theta}{r^2}\right] \qquad \text{(B.5)}$$

$$A_z = -\left[\frac{1}{r}\frac{\partial(ru_ru_z)}{\partial r} + \frac{1}{r}\frac{\partial(u_\theta u_z)}{\partial \theta} + \frac{\partial(u_z u_z)}{\partial z}\right] + \frac{1}{Re}\left[\frac{1}{r}\frac{\partial}{\partial r}\left(r\frac{\partial u_z}{\partial r}\right) + \frac{\partial^2 u_z}{\partial z^2}\right] \tag{B.6}$$

$$B_r = \frac{1}{r^2}\frac{1}{Re}\frac{\partial^2 u_r}{\partial \theta^2} \tag{B.7}$$

$$B_\theta = \frac{1}{r^2}\frac{1}{Re}\frac{\partial^2 u_\theta}{\partial \theta^2} \tag{B.8}$$

$$B_z = \frac{1}{r^2}\frac{1}{Re}\frac{\partial^2 u_z}{\partial \theta^2} \tag{B.9}$$

APPENDIX C

PARALLEL INTERFACE-TRACKING ALGORITHM

The parallelization of the interface-tracking (tagging) algorithm is presented in detail. The interface-tracking is completed in parallel using MPI (Message-Passing Interface) and a *slice* domain decomposition of the azimuthal direction in cylindrical coordinates. However, since the flow solver is parallelized with a *slab* domain decomposition in the axial (flow) direction, the output of the interface-tracking must be re-organized to correspond to the flow solver, which is accomplished by communication of the data between processors. An overview of the fundamental algorithm structure is discussed, including a description of the proposed domain decomposition and the subsequent changes in the algorithm that are required, the inter-processor communication or swap, followed by the approach used to re-assemble the data in the domain decomposition of the flow solver.

C.1 Algorithm Structure

The interface-tracking algorithm is comprised of four basic subroutines which generate the data used by the flow solver to account for the effect of an object in the flow.

These subroutines are called in the order they are discussed by each processor during the interface-tracking process. A brief description of each subroutine is presented, followed by operational details of each subroutine. The input and output variables for each subroutine are listed in the following format in the accompanying tables: NAME - Description (TYPE).

C.1.1 TAG_3D

The purpose of TAG_3D is to classify Eulerian (fluid) grid points as either inside or outside the immersed boundary. The inputs and outputs of TAG_3D are listed in Tables C.1 and C.2.

Table C.1: Input Variables, Description, and Data Types: Interface tracking subroutine TAG_3D.

Variable	Description	Type
X_CART	Cartesian X-coordinates, Eulerian grid	REAL
Y_CART	Cartesian Y-coordinates, Eulerian grid	REAL
Z	Cartesian Z-coordinates, Eulerian grid	REAL
IBMIN,IBMAX	Eulerian X-indices with Lagrangian body	INTEGER
JBMIN,JBMAX	Eulerian Y-indices with Lagrangian body	INTEGER
KBMIN,KBMAX	Eulerian Z-indices with Lagrangian body	INTEGER
NX	Size of X-coordinate array	INTEGER
NY	Size of Y-coordinate array	INTEGER
NZ	Size of Z-coordinate array	INTEGER
VERTEX	Vertex coordinates, Lagrangian body	REAL
VERTEXC	Centroid coordinates, Lagrangian body	REAL
NFACET	Number of triangles, Lagrangian body	INTEGER

Table C.2: Output Variables, Description, and Data Types: Interface tracking subroutine TAG_3D.

Variable	Description	Type
FLAG	Eulerian points inside (1) or outside (-1) body	INTEGER

C.1.2 FLAGU

The purpose of FLAGU is to create third and fourth Eulerian point classifications. These are obtained using the information obtained from TAG_3D, which classified the Eulerian grid points as **inside points**, which have a flag of 1, indicating they are inside the Lagrangian body; or **outside points**, which have a flag of -1, indicating they are outside the the Lagrangian body. Using this information, FLAGU creates one integer array representing **outside points**, **inside points**, and **forcing points**

(the Eulerian fluid points closest to the Lagrangian body surface); and another integer array representing **outside points**, **inside points**, and **field-extension points** (the Eulerian solid points closest to the Lagrangian body surface). The inputs and outputs of FLAGU are listed in Tables C.3 and C.4.

Table C.3: Input Variables, Description, and Data Types: Interface tracking subroutine FLAGU.

Variable	Description	Type
IBMIN,IBMAX	Eulerian X-indices with body	INTEGER
JBMIN,JBMAX	Eulerian Y-indices with body	INTEGER
KBMIN,KBMAX	Eulerian Z-indices with body	INTEGER
NX	Size of X-coordinate array	INTEGER
NY	Size of Y-coordinate array	INTEGER
NZ	Size of Z-coordinate array	INTEGER
FLAG	Points inside (1), outside (-1) body	INTEGER

Table C.4: Output Variables, Description, and Data Types: Interface tracking subroutine FLAGU.

Variable	Description	Type
FLAGO	Fluid (0), solid (1), forcing points(-1)	INTEGER
FLAGI	Fluid (0), solid (1), field-extension points(-1)	INTEGER

C.1.3 GEOM

The purpose of GEOM is to obtain information about the relationship between the **forcing / field-extension** points and the immersed boundary. First, the integer flag information (FLAGO/FLAGI) is used to store the indices of the **forcing / field-extension** points and to count the number of total **forcing / field-extension**

points (NIMU). At this point in the algorithm, a transition occurs in the organization of the data structure for the interface-tracking: the count of **forcing / field-extension** points using three-dimensional integer flag arrays is used to change to a one-dimensional structure based on the number of **forcing / field-extension** points. For the rest of the algorithm, all the arrays are organized (indexed) according to the **forcing / field-extension** points.

Second, for each **forcing / field-extension** point, a search is done over all the triangle vertices to determine which ones may have a relationship with the **forcing / field-extension** point. Here, the ANN (Approximate Nearest Neighbor) approach is used to improve performance by providing a small set of "nearest neighbor" vertices for each **forcing / field-extension** point.

Third, two rays are projected along a radial (R) and axial (Z) gridline from Eulerian **forcing/field-extension** points toward the Lagrangian body. A set of geometric conditions (O'Rourke [67]) are used to determine if the ray actually intersects the Lagrangian body. Assuming an intersection is found from the projected ray(s) along the radial and axial gridlines, the shortest distance from the Eulerian point to the Lagrangian body is stored and used to generate a unit vector from the Lagrangian surface toward the closest Eulerian point (the unit vector has a magnitude of 1 in either the radial or axial direction).

Finally, the intersection point coordinates (XNU,YNU,ZNU) of the closest ray (the ray which corresponds to the shortest distance) with the Lagrangian body are stored. The inputs and outputs of GEOM are listed in Tables C.5 and C.6.

C.1.4 MTRX

The purpose of MTRX is to compute and store the interpolation stencil used for the reconstruction of the solution at the **forcing points / field-extension points**. Using the coordinates of the intersection point (XNU,YNU,ZNU), the indices of

Table C.5: Input Variables, Description, and Data Types: Interface tracking subroutine GEOM.

Variable	Description	Type
X_CART	Cartesian X-coordinates, Eulerian grid	REAL
Y_CART	Cartesian Y-coordinates, Eulerian grid	REAL
Z	Cartesian Z-coordinates, Eulerian grid	REAL
IBMIN,IBMAX	Eulerian X-indices with body	INTEGER
JBMIN,JBMAX	Eulerian Y-indices with body	INTEGER
KBMIN,KBMAX	Eulerian Z-indices with body	INTEGER
NX	Size of X-coordinate array	INTEGER
NY	Size of Y-coordinate array	INTEGER
NZ	Size of Z-coordinate array	INTEGER
FLAG	Points inside (1), outside (-1) body	INTEGER
FLAGO	Fluid (0), solid (1), forcing points(-1)	INTEGER
FLAGI	Fluid (0), solid (1), field-extension points(-1)	INTEGER
VERTEX	Vertex coordinates, Lagrangian body	REAL
VERTEXC	Centroid coordinates, Lagrangian body	REAL
NFACET	Number of triangles on Lagrangian body	INTEGER

the **forcing/field-extension** point (IU,JU,KU), and the unit vector pointing from the Lagrangian surface toward the closest fluid point, MTRX calculates the indices of the nearest fluid point (IUMTRX,JUMTRX,KUMTRX), and an interpolation stencil (UMTRX) is calculated and stored for each **forcing/field-extension** point. The inputs and outputs of MTRX are listed in Tables C.7 and C.8.

C.2 Parallel Implementation

Since the parallel approach used for the flow solver causes a load imbalance when the solution is integrated in time, a different parallelization scheme (domain de-

Table C.6: Output Variables, Description, and Data Types: Interface tracking subroutine GEOM.

Variable	Description	Type
IU	Eulerian X-index of forcing points	INTEGER
JU	Eulerian Y-index of forcing points	INTEGER
KU	Eulerian Z-index of forcing points	INTEGER
NXU	Radial unit vector, intersection to forcing point	REAL
NYU	Azimuthal unit vector, intersection to forcing point	REAL
NZU	Axial unit vector, intersection to forcing point	REAL
XNU	X coordinate, ray intersection with body	REAL
YNU	Y coordinate, ray intersection with body	REAL
ZNU	Z coordinate, ray intersection with body	REAL
LIMU	Start indices of new, one-dimensional arrays	INTEGER
MIMU	End indices of new, one-dimensional arrays	INTEGER
NIMU	Total number of forcing/field-extension points	INTEGER

composition) is developed in the current work for the interface-tracking. The new parallelization is based on an even division of work among all processors. This is accomplished using a "slice" decomposition of the domain in the azimuthal direction. The original parallel scheme was designed so that each processor would have an equal portion of the Eulerian grid points, and decomposing the domain along the streamwise direction was the most logical choice since this direction has the most points. However, since the interface-tracking scheme is concerned only with the Lagrangian immersed body, then the logical outcome of the original parallel scheme is the imbalance of work and subsequent slow-down as the code is scaled up onto larger processor counts.

Table C.7: Input Variables, Description, and Data Types: Interface tracking subroutine MTRX.

Variable	Description	Type
X_CART	Cartesian X-coordinates, Eulerian grid	REAL
Y_CART	Cartesian Y-coordinates, Eulerian grid	REAL
Z	Cartesian Z-coordinates, Eulerian grid	REAL
NX	Size of X-coordinate array	INTEGER
NY	Size of Y-coordinate array	INTEGER
NZ	Size of Z-coordinate array	INTEGER
VERTEX	Vertex coordinates, Lagrangian body	REAL
VERTEXC	Centroid coordinates, Lagrangian body	REAL
NFACET	Number of triangles on Lagrangian body	INTEGER
IU	Eulerian X-index of forcing points	INTEGER
JU	Eulerian Y-index of forcing points	INTEGER
KU	Eulerian Z-index of forcing points	INTEGER
NXU	Radial unit vector, intersection to forcing point	REAL
NYU	Azimuthal unit vector, intersection to forcing point	REAL
NZU	Axial unit vector, intersection to forcing point	REAL
XNU	X coordinate, ray intersection with body	REAL
YNU	Y coordinate, ray intersection with body	REAL
ZNU	Z coordinate, ray intersection with body	REAL
LIMU	Start indices of new, one-dimensional arrays	INTEGER
MIMU	End indices of new, one-dimensional arrays	INTEGER
NIMU	Total number of forcing/field-extension points	INTEGER

Table C.8: Output Variables, Description, and Data Types: Interface tracking subroutine MTRX.

Variable	Description	Type
IUMTRX	Eulerian X-index of nearest fluid point	INTEGER
JUMTRX	Eulerian Y-index of nearest fluid point	INTEGER
KUMTRX	Eulerian Z-index of nearest fluid point	INTEGER
UMTRX	Interpolation stencil at forcing point	REAL

A few changes are required in the four subroutines which comprise the interface-tracking scheme. The Cartesian coordinates of the Eulerian grid in the X and Y directions (X_CART,Y_CART) must be divided up according to the size of the grid and the number of processors. The arrays which contain the integer flags (FLAG, FLAGO, FLAGI) representing fluid points (0), **forcing/field-extension** points (-1), and solid points (1) are also organized according to the azimuthal domain decomposition.

Additionally, the periodic boundary condition for the azimuthal grid points must be accounted for. This is required in the first two subroutines (TAG_3D and FLAGU), where the exterior (fluid), interior (solid), and **forcing/field-extension** points are indentified.

C.3 Parallel Communication

Since the computational domain (with respect to the interface tracking) is organized in an azimuthal "slice" decomposition, while the computational domain in the flow solver is organized in a streamwise "slab" decomposition, communication must be implemented in order to maintain consistency with the interface-tracking information as used in the flow solver. Each processor determines how the data in its particular "slice" of the domain should be divided up according to the "slab" decomposition. Since the interface-tracking data is now of a one-dimensional structure

in which it is organized by the number of **forcing/field-extension** points, the data which belongs on different processors in the streamwise domain decomposition can be determined by testing the local value of KU(INTEGER streamwise index of a **forcing/field-extension** point) with respect to the global streamwise indices. The indices which belong to each process in the streamwise decomposition are then stored in an INTEGER array on each process in the azimuthal decomposition. Thus, the indices are used to organize the output data (from the interface-tracking) into "buckets" which belong to each process in the streamwise decomposition.

Each process has a set of "buckets" equal to the number of processors (*MYSIZE*, in MPI terminology). These "buckets" are consolidated in one-dimensional storage arrays which are used directly in the communication process. Since the interface-tracking process (TAG_3D, FLAGU, GEOM, MTRX) is called three times within each time-integration (due to the 3rd-order Runge-Kutta time-advance) after the Lagrangian body moves, the number of **forcing/field-extension** points will differ each time. This implies that it is impossible to know the size of the storage arrays and the "bucket" size *a priori*. In order to overcome this problem, the size of the dummy arrays is estimated to be the maximum number of **forcing/field-extension** points possible on that particular process; essentially, the complete size of the Eulerian grid on that process. This is a robust approach because the number of usable **forcing/field-extension** points will always be less than the number of Eulerian grid points. The "bucket" size is simply then the total number of Eulerian grid points on that process divided by the number of processors.

This approach is illustrated in Figure C.1. Consider the stencil array IU, which contains the X-coordinate indices of the **forcing/field-extension** points in the Eulerian grid. After the interface-tracking is complete, IU will contain X-indices of **forcing/field-extension** points in some azimuthal "slice" of the computational domain. Comparison of the Z-coordinate indices of the **forcing/field-extension** points

with the global Z-coordinate indices in the streamwise decomposition determines which portions of IU will belong to each process in the streamwise decomposition. This information is pivotal in the parallel communication process, and is stored in the INTEGER array ILIM.

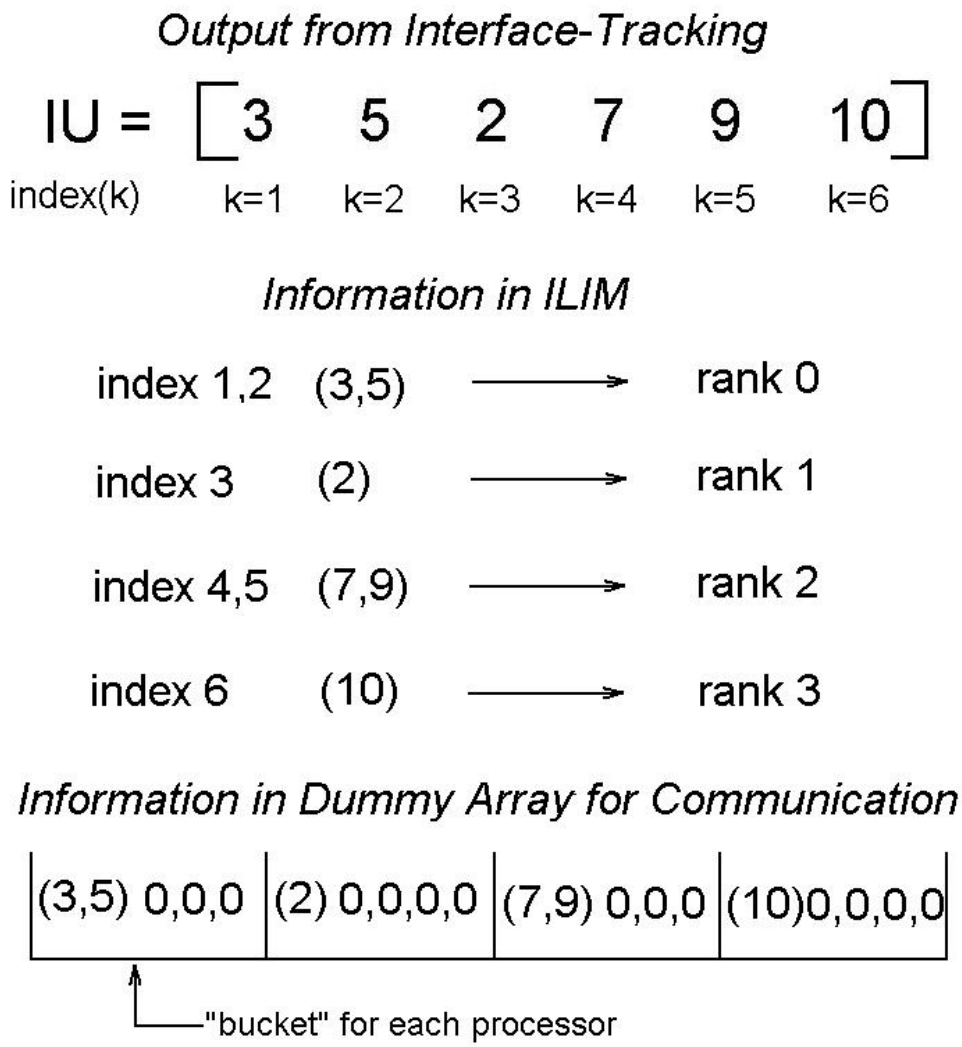

Figure C.1: Data organization for communication of interface tracking arrays back to the slab (streamwise) domain decomposition.

The INTEGER array ILIM is then used to fill up the "buckets" of data in the dummy array which will be used for communication of the data between processors. As indicated in the figure, the "bucket" size is pre-determined by the size of the

Eulerian grid, and the remainder (after being filled by results from IU) is comprised of zeros. Thus, the dummy array is organized such that the first "bucket" contains the information designated for the first processor (rank 0, in MPI terminology), the second processor contains information designated for the second processor (rank 1), and so on. Once this crucial step is completed for the interface-tracking arrays, the results in the dummy arrays are communicated between the processors using *MPI_ALLTOALLV*. On the receiving end of the swap, the pieces from respective processor are assembled in another one-dimensional dummy array.

C.4 Data Reassembly

After the swap of the interface-tracking information from the azimuthal "slice" domain decomposition to the streamwise "slab" domain decomposition, the results contained in the dummy array must be reorganized into their original form. Additionally, since the dummy arrays before being communicated contained zeros that fill it up to the prescribed "bucket" size, these extra zeros are therefore present in the dummy arrays that are the result of the communication, and must be removed in order to avoid problems when using the interface-tracking results in the flow solver.

The method of implementation in the code is actually accomplished by first removing the extra zeros in the one-dimensional dummy arrays, then reassembling the arrays according to their original structure. For one-dimensional arrays (IU,JU,KU, etc.), this process is straightforward, since no data reassembly is required; the data are already of one-dimensional form. However, for the two or three-dimensional arrays (UMTRX,UINDX), precaution must be used in order to reassemble the data correctly.

After the data is properly reassembled, it is stored and prepared for transfer back to the flow solver for usage after the predictor step in the time-advancing scheme.

APPENDIX D

GRID GENERATION

The purpose of this appendix is to provide detailed procedures for using the commercial grid generation tool *Gridgen* to create geometry and meshes.

D.1 Creation of Smooth Sphere Geometry and Mesh using *Gridgen*

1. CREATE SPHERE GEOMETRY FOR DATABASE

   DB

2. CREATE DOMAINS FOR SURFACE MESH

   Create Unstructured

   On DB entities

   Run Solver - Unstrctrd

   Pick All

   Initialize

3. CREATE 1ST HALF OF PRISM LAYER

   Blocks

   Create unstructured

   Extrude From Doms

   Pick Domains 1 and 2

   Set Attributes

   March Flip

   Growth Rate Set 1.3

   delta s Init 2.0e-6

   Done

   Run N 22

4. CREATE 2ND HALF OF PRISM LAYER

   Blocks

   Create structured

Extrude From Doms

Pick Domains 3 and 4

Set Attributes

March Flip

Growth Rate Set 1.3

delta s Init 2.0e-6

Done

Run N 22

5. COPY AND SCALE CONNECTORS ON OUTER EDGE OF PRISM LAYER

   Cons

   Copy

   Select connectors on outside of prism layer, NOT the ones on the surface of the ball

   Done

   Abort - Don't Translate

   Scale

   Enter Anchor via Keyboard = 0, 0, 0

   Enter

   Enter Scaling Factors = 1.3099711392, 1.3099711392, 1.3099711392

   Enter

   Done - Scale

   Done - Save Connectors

6. CREATE DB ENTITIES (SURFACE of REVOLUTION) FOR 1ST UN-STRUCTURED BLOCK

   DB

   Create

Line

Enter Starting Point

via Keybrd = 0.0300024, 0, 0

Enter

Enter Ending Point

via Keybrd = -0.0300024, 0, 0

Enter

Save DB Curve

Create

Circle

Enter Starting Point

via Keybrd = 0.0300024, 0, 0

Enter

Enter Ending Point

via Keybrd = -0.0300024, 0, 0

Enter

Enter Center Point

via Keybrd = 0, 0, 0.0300024

Enter

Save DB Curve

Create

Surface

Revolution

Use the right mouse to select the DB arc just created

Use the right mouse to select the DB line as the axis spine curve

Save DB Curve

Done

7. CREATE DOMAINS FOR FIRST UNSTRUCTURED BLOCK

   Doms

   Create

   Cell Type - unstructured

   Assemble Edges

   Select (in order) the connectors comprising 1/4 of the sphere traced by the scaled connectors (follow the instructions in the Dialogue Window regarding the open circle node)

   Save Domain

   Done

   Modify

   Use the right mouse to select the domain just created

   Done

   Project

   Spherical

   Enter Source via Keybrd = 0, 0, 0

   Enter

   Proj Out

   Int Pts

   Done - Project

   Replace Domains

8. REPEAT FOR OTHER 3 ”SLICES” OF THE SPHERE THAT COMPRISE THE OUTSIDE BOUNDARY OF THE FIRST UNSTRUCTURED BLOCK

9. CREATE 1ST UNSTRUCTURED BLOCK FROM DOMAINS

   Blks

   Create

Cell Type - unstructured

Assemble Faces

Add 1st Face

Use the right mouse to select the domains on the surface of the prism layer

Save the Face

If the direction arrows are pointing inward: select Reorient Faces so that they are outward

Add 2nd Face

Use the right mouse to select the domains at the edge of the first unstructured block

Save the Face

If the direction arrows are pointing outward: select Reorient Faces so that they are inward

Done - Save Blocks

10. RUN SOLVER TO GENERATE POINTS BETWEEN PRISM LAYER AND THE EDGE OF FIRST UNSTRUCTURED BLOCK

    Blks

    Run Solver - Unstrctrd

    Select the empty block that was just created above

    Done

    Set Solver Attributes

    Grid Control Parameters

    Memory Size = 1000 mbytes

    Done Setting Attributes

    Initialize

    Done - Save

11. COPY/SCALE THE DB SURFACE OF REVOLUTION TO THE NEXT BLOCK BOUNDARY

    DB

    Copy

    Select srfrv GG-surf-rev-1

    Done

    Scale

    Enter Anchor via Keybrd = 0, 0, 0

    Enter

    Enter the Scaling Factors = 2.5005266245, 2.5005266245, 2.5005266245

    Enter

    Done - Save

    Done

12. COPY AND SCALE CONNECTORS ON OUTER EDGE OF 1ST UN-STRUCTURED BLOCK

    Cons

    Copy

    Select connectors on outside of the 1st unstructured layer

    Done

    Abort - Don’t Translate

    Scale

    Enter Anchor via Keyboard = 0, 0, 0

    Enter

    Enter Scaling Factors = 2.5005266245, 2.5005266245, 2.5005266245

    Enter

    Done - Scale

Done - Save Connectors

13. SET AVG DELTA S FOR THE SECOND UNSTRUCTURED BLOCK

    Dflt

    Con Dim - avg delta s

    Enter 2.9573

    Done

14. CREATE DOMAINS FOR SECOND UNSTRUCTURED BLOCK

    Doms

    Create

    Cell Type - unstructured

    Assemble Edges

    Select (in order) the connectors comprising 1/4 of the sphere traced by the scaled connectors (follow the instructions in the Dialogue Window regarding the open circle node)

    Save Domain

    Done

    Modify

    Use the right mouse to select the domain just created

    Done

    Project

    Spherical

    Enter Source via Keybrd = 0, 0, 0

    Enter

    Proj In

    Int Pts

Done - Project

Replace Domains

15. REPEAT FOR OTHER 3 ”SLICES” OF THE SPHERE THAT COMPRISES THE OUTSIDE BOUNDARY OF THE SECOND UNSTRUCTURED BLOCK

16. CREATE 2ND UNSTRUCTURED BLOCK FROM DOMAINS

    Blks

    Create

    Cell Type - unstructured

    Assemble Faces

    Add 1st Face

    Use the right mouse to select the domains on the surface of the prism layer

    Save the Face

    If the direction arrows are pointing inward: select Reorient Faces so that they are outward

    Add 2nd Face

    Use the right mouse to select the domains at the edge of the first unstructured block

    Save the Face

    If the direction arrows are pointing outward: select Reorient Faces so that they are inward

    Done - Save Blocks

17. RUN SOLVER TO GENERATE POINTS BETWEEN 1ST UNSTRUCTURED BLOCK AND THE EDGE OF THE SECOND UNSTRUCTURED BLOCK

    Blks

    Run Solver - Unstrctrd

    Select the empty block that was just created above

Done

Set Solver Attributes

Grid Control Parameters

Memory Size = 1000 mbytes

Done Setting Attributes

Initialize

Done - Save

18. COPY/SCALE THE DB SURFACE OF REVOLUTION TO THE NEXT BLOCK BOUNDARY

    DB

    Copy

    Select srfrv GG-surf-rev-1

    Done

    Scale

    Enter Anchor via Keybrd = 0, 0, 0

    Enter

    Enter the Scaling Factors = 2.9998080557, 2.9998080557, 2.9998080557

    Enter

    Done - Save

    Done

19. COPY AND SCALE CONNECTORS ON OUTER EDGE OF 2ND UN-STRUCTURED BLOCK

    Cons

    Copy

    Select connectors on outside of the 2nd unstructured layer

    Done

Abort - Don't Translate

Scale

Enter Anchor via Keyboard = 0, 0, 0

Enter

Enter Scaling Factors = 2.9998080557, 2.9998080557, 2.9998080557

Enter

Done - Scale

Done - Save Connectors

20. SET AVG DELTA S FOR THE THIRD UNSTRUCTURED BLOCK

    Dflt

    Con Dim - avg delta s

    Enter 9.8615

    Done

21. CREATE DOMAINS FOR THIRD UNSTRUCTURED BLOCK

    Doms

    Create

    Cell Type - unstructured

    Assemble Edges

    Select (in order) the connectors comprising 1/4 of the sphere traced by the scaled connectors (follow the instructions in the Dialogue Window regarding the open circle node)

    Save Domain

    Done

    Modify

    Use the right mouse to select the domain just created

    Done

Project

Spherical

Enter Source via Keybrd = 0, 0, 0

Enter

Proj In

Int Pts

Done - Project

Replace Domains

22. REPEAT FOR OTHER 3 ”SLICES” OF THE SPHERE THAT COMPRISES THE OUTSIDE BOUNDARY OF THE THIRD UNSTRUCTURED BLOCK

23. CREATE THIRD UNSTRUCTURED BLOCK FROM DOMAINS

    Blks

    Create

    Cell Type - unstructured

    Assemble Faces

    Add 1st Face

    Use the right mouse to select the domains on the surface of the prism layer

    Save the Face

    If the direction arrows are pointing inward: select Reorient Faces so that they are outward

    Add 2nd Face

    Use the right mouse to select the domains at the edge of the first unstructured block

    Save the Face

    If the direction arrows are pointing outward: select Reorient Faces so that

they are inward

Done - Save Blocks

24. RUN SOLVER TO GENERATE POINTS BETWEEN 2ND UNSTRUCTURED BLOCK AND THE EDGE OF THE 3RD UNSTRUCTURED BLOCK

    Blks

    Run Solver - Unstrctrd

    Select the empty block that was just created above

    Done

    Set Solver Attributes

    Grid Control Parameters

    Memory Size = 1000 mbytes

    Done Setting Attributes

    Initialize

    Done - Save

25. COPY/SCALE THE DB SURFACE OF REVOLUTION TO THE NEXT BLOCK BOUNDARY

    DB

    Copy

    Select srfrv GG-surf-rev-1

    Done

    Scale

    Enter Anchor via Keybrd = 0, 0, 0

    Enter

    Enter the Scaling Factors = 2.6660623591, 2.6660623591, 2.6660623591

    Enter

Done - Scale

Done

26. COPY AND SCALE CONNECTORS ON OUTER EDGE OF 3RD UNSTRUCTURED BLOCK

    Cons

    Copy

    Select connectors on outside of the 3rd unstructured layer

    Done

    Abort - Don’t Translate

    Scale

    Enter Anchor via Keyboard = 0, 0, 0

    Enter

    Enter Scaling Factors = 2.6660623591, 2.6660623591, 2.6660623591

    Enter

    Done - Scale

    Done - Save Connectors

27. SET AVG DELTA S FOR THE FOURTH UNSTRUCTURED BLOCK

    Dflt

    Con Dim - avg delta s

    Enter 23.064

    Done

28. CREATE DOMAINS FOR FOURTH UNSTRUCTURED BLOCK

    Doms

    Create

    Cell Type - unstructured

    Assemble Edges

Select (in order) the connectors comprising 1/4 of the sphere traced by the scaled connectors (follow the instructions in the Dialogue Window regarding the open circle node)

Save Domain

Done

Modify

Use the right mouse to select the domain just created

Done

Project

Spherical

Enter Source via Keybrd = 0, 0, 0

Enter

Proj In

Int Pts

Done - Project

Replace Domains

29. REPEAT FOR OTHER 3 ”SLICES” OF THE SPHERE THAT COMPRISES THE OUTSIDE BOUNDARY OF THE THIRD UNSTRUCTURED BLOCK

30. CREATE FOURTH UNSTRUCTURED BLOCK FROM DOMAINS

    Blks

    Create

    Cell Type - unstructured

    Assemble Faces

    Add 1st Face

    Use the right mouse to select the domains on the surface of the prism layer

    Save the Face

If the direction arrows are pointing inward: select Reorient Faces so that they are outward

Add 2nd Face

Use the right mouse to select the domains at the edge of the first unstructured block

Save the Face

If the direction arrows are pointing outward: select Reorient Faces so that they are inward

Done - Save Blocks

31. RUN SOLVER TO GENERATE POINTS BETWEEN 3RD UNSTRUCTURED BLOCK AND THE EDGE OF THE 4TH UNSTRUCTURED BLOCK

    Blks

    Run Solver - Unstrctrd

    Select the empty block that was just created above

    Done

    Set Solver Attributes

    Grid Control Parameters

    Memory Size = 1000 mbytes

    Done Setting Attributes

    Initialize

    Done - Save